Fermilab FERMILAB-THESIS-1997-41

CDF/ANAL/TOP/CDFR 4280

OBSERVATION OF TOP QUARK PAIRS IN THE DILEPTON DECAY CHANNEL USING ELECTRONS, MUONS, AND TAUS

A DISSERTATION SUBMITTED TO
THE FACULTY OF THE DIVISION OF THE PHYSICAL SCIENCES
IN CANDIDACY FOR THE DEGREE OF
DOCTOR OF PHILOSOPHY

DEPARTMENT OF PHYSICS

BY
MARCUS HOHLMANN

CHICAGO, ILLINOIS
AUGUST 1997

CONTENTS

LIST OF TABLES **v**

LIST OF ILLUSTRATIONS **x**

ABSTRACT **xxi**

1 INTRODUCTION **1**

1.1 Dilepton events 4
1.2 Organisation of thesis 7
1.3 Top production in the Standard Model 7
1.4 Top quark decay in the Standard Model 9
1.5 Overview of the CDF detector 13
1.6 Calorimetry 15
1.6.1 Fiducial CEM coverage 15
1.6.2 CEM energy resolution 18
1.6.3 Jets 22
1.6.4 Missing transverse energy 24
1.7 B-tagging 27
1.8 Muon Chambers 29
1.8.1 Detector Coverage 29
1.8.2 Momentum resolution 33

2 DILEPTONS WITH ELECTRONS AND MUONS ONLY **37**

2.1 Acceptance and efficiencies 38
2.1.1 Geometrical and kinematical acceptance $A_{geom \cdot P_T}$ . . . 38
2.1.2 Lepton identification 43
2.1.3 Dilepton selection 49
2.1.4 Topological selection 50
2.1.5 Total Acceptance 52

2.1.6 Expected number of events in 109 pb^{-1} 52
2.1.7 Acceptance for $t\bar{t}$ events with both W's decaying into leptons 53
2.1.8 Origin and relative fraction of ee, $\mu\mu$, and $e\mu$ events . . 55
2.2 Correlation with lepton + jets channel 58
2.3 Backgrounds 62
2.4 Observation in the data 63
2.4.1 Data samples 63
2.4.2 Final dilepton selection 66

3 TAU DILEPTONS 73
3.1 Starting the τ search 74
3.1.1 τ decays 74
3.1.2 Finding τ clusters in the calorimeter 74
3.1.3 Identification of π^0's in the CES 76
3.2 Geometrical and kinematical acceptance 78
3.2.1 p_T spectra 81
3.2.2 Calculation of $A_{geom \cdot P_T}$ 81
3.3 τ lepton identification 82
3.3.1 Identification variables 82
3.3.2 τ identification efficiency for $t\bar{t}$ events 88
3.4 Check of τ identification efficiency with $W \to \tau\nu$ data 92
3.4.1 Data samples 95
3.4.2 $W \to \tau\nu$ cross section 98
3.4.3 Comparison of τ identification variables 99
3.4.4 Uncertainty on the τ identification efficiency 111
3.5 Z^0 removal 112
3.6 Topology cuts 113
3.6.1 z–vertex 113
3.6.2 Jets 114
3.6.3 H_T 114
3.6.4 $\not{E}_T$, $S_{\not{E}_T}$ and $\Delta\phi\,(\not{E}_T, jl)$ 117
3.7 Total Acceptance $\times$ Efficiency 119
3.7.1 Calculating A_{tot} 119
3.7.2 Systematic uncertainty on A_{tot} 120
3.7.3 Expected number of events in 109 pb^{-1} 134
3.8 Backgrounds 135
3.8.1 Fakes 135
3.8.2 Physics backgrounds 142
3.9 Observation in the data 155

3.9.1 Final candidates 155
3.9.2 Same-sign events 163
3.10 B–tagging 165
3.11 Significance 174
3.12 Cross section 175
3.13 Summary and Conclusion 175

4 KINEMATICS AND TOPOLOGY OF THE CANDIDATE EVENTS 181
4.1 Kinematics of specific particles 182
4.1.1 Charged leptons 182
4.1.2 Neutrinos 186
4.1.3 Jets 193
4.1.4 Summary of distributions with events in the tails . . . 193
4.2 Global event kinematics 195
4.2.1 Total transverse energy H_T 195
4.2.2 Thrust analysis 197
4.3 Discussion of unusual candidate events 208
4.3.1 The $ee\mu$ trilepton event (Run 67581/Event 129896) . . 208
4.3.2 The $e\mu\mu$ trilepton event (Run 57621/Event 45230) . . . 211
4.3.3 The $\mu\mu\gamma$ event (Run 58281/Event 4805) 212
4.4 Conclusions 213

5 CONCLUSIONS 217
5.1 Summary of results 217
5.2 Future Prospects 219

REFERENCES 225

LIST OF TABLES

1.1 Branching ratios of final states for $t\bar{t}$ decay in the Standard Model. The number of jets actually detected may vary from this naive prediction due to effects such as initial state and final state gluon radiation, jet merging etc. 12

1.2 Coverage and energy resolution of hadronic calorimeters from testbeam measurements for incident isolated pions[16]. 22

2.1 Absolute geometric and kinematic acceptance $A_{geom \cdot P_T}$ for dileptons using PYTHIA+TAUOLA+CLEO+QFL ($m_{top} = 175$ GeV). All numbers are in percent and include all branching ratios. Rows refer to the reconstructed dilepton type (CE: central electron, MU: central muon, CMU(P): non-CMX muon, CMX: CMX muon, MI: isolated minimum ionizing track). Columns refer to the parent particles of the 2 leptons. 'Charm' ('π^0, η') means that at least one lepton is from a charm (π^0 or η) decay. 42

2.2 Identification cuts for tight central electrons (TCE) and loose central electrons (LCE) and their efficiencies as measured from Z events [20]. Note that the E_T cut is not considered a proper identification cut; it rather determines the kinematic acceptance of the electron selection. It is listed here for completeness. . . 44

2.3 Identification cuts for tight central muons (TCM) and CMI muons and their efficiencies as measured from Z events [20]. For CMU-CMUP tight central muons only one $|\Delta x|$ cut needs to be satified. Note that the p_T cut is not considered a proper identification cut; it rather determines the kinematic acceptance of the muon selection. It is listed here for completeness. Note that CMI muons are by definition isolated, even though the isolation is rather a topological cut than an identification cut. 47

2.4 Valid dilepton categories. 50

2.5 Summary of efficiencies that give the total acceptance for ee, $\mu\mu$, and $e\mu$ dilepton events using 80,000 PYTHIA $t\bar{t}$ Monte Carlo events ($m_{top} = 175$ GeV/c^2). Each efficiency is calculated using only the events that pass the preceding cuts. The values for $\epsilon_{trigger}, \epsilon_{ID}$, and ϵ_{Iso} are taken from Ref. [20]. 51
2.6 Percentages of canonical dilepton events in the PYTHIA $t\bar{t}$ MC that survive the successive selection cuts. The last column lists the efficiency of each cut with respect to the events passing the previous cut. The lepton p_T and η information are evaluated at the generator level. 54
2.7 Contribution of various W^+W^- decay modes to events identified as dilepton events in the $t\bar{t}$ Monte Carlo (statistical uncertainties only). 56
2.8 Contribution of various W^+W^- decay modes to lepton + jets events (statistical uncertainties only). The column on the right gives the contributions if a fourth jet with $|\eta_{det}| < 2.4$ and $E_T > 8$ GeV is required as in the top mass analysis. 59
2.9 Percentages of $t\bar{t}$ MC events with both W's decaying into $e\nu$ or $\mu\nu$ ($W^+ \to \ell^+\nu$, $W^- \to \ell^{-\prime}\nu'$ $\ell = e, \mu$ $\ell' = e, \mu$) that get accepted by the dilepton analysis and the lepton + jets analysis. Events are counted either in the dilepton channel or in the lepton + jets channel, but not in both, i.e. the percentages are exclusive. 61
2.10 Summary of backgrounds in the ee, $\mu\mu$, and $e\mu$ analysis after all cuts [20]. 63
2.11 Cuts for selecting the inclusive electron data sample. All values are taken from the ELES bank. 64
2.12 Cuts for selecting the inclusive muon sample. All values are taken from the CMUO bank. 65
2.13 Breakdown of events in the dilepton sample, (CMU=incl. central muon sample, ICE=incl. central electron sample). 66
2.14 The number of events observed in the data after successive cuts for the different dilepton categories. To qualify as a dilepton at least one tight lepton (TCE or TCM) must be isolated. 67
2.15 Top dilepton candidates with b-tags. Jets are ordered by E_T, i.e. 'j1' is the jet with the highest E_T , 'j2' is the jet with the second–highest E_T, etc. 71

3.1 Current world averages for the branching ratios of dominant decay modes of the τ^- lepton [52]. 75

3.2 Loose requirements for creating a tau cluster. 76
3.3 The geometrical and kinematic acceptance $A_{geom \cdot P_T}$ for tau dilepton events with $|\eta^{\tau}_{det}| < 1.2$ and $p_T^{trk+\pi^0} > 15$ GeV calculated from the PYTHIA $t\bar{t}$ Monte Carlo. All numbers are given *in percent*. They are relative to all 80,000 generated $t\bar{t}$ events, i.e. all branching ratios are included in these numbers. Here ℓ stands for e or μ only. The acceptance is broken down by track multiplicity of the τ's (rows) and by the parent particles of the leptons (columns). 83
3.4 Same as Table 3.3, except using $p_T^{trk} > 15$ GeV instead of $p_T^{trk+\pi^0} > 15$ GeV. All numbers are given *in percent*. They are relative to all 80,000 generated $t\bar{t}$ events, i.e. all branching ratios are included in these numbers. Here ℓ stands for e or μ only. The acceptance is broken down by track multiplicity of the τ's (rows) and by the parent particles of the leptons (columns). . 84
3.5 Summary of τ identification variables and cuts. 85
3.6 Efficiency of τ identification cuts in MC top dilepton events for τ's from W's. 93
3.7 Efficiency of τ identification cuts in MC top events for τ's from b's. 93
3.8 Cuts on calorimeter clusters for calorimeter-based $Z^0 \rightarrow e^+e^-$ removal from the $e\tau$ search. 113
3.9 Cuts on tracks for track-based $Z^0 \rightarrow e^+e^-$ removal from the $e\tau$ search. 113
3.10 Summary of efficiencies needed for calculating A_{tot} . Note that $A_{geom \cdot P_T}$ includes all branching ratios. 120
3.11 Summary of all systematic uncertainties on the tau dilepton acceptance. Uncertainties marked by * have been adopted from the calculations for $ee, \mu\mu$, and $e\mu$ dileptons in Ref. [20]. . . . 134
3.12 Rejection power of τ identification cuts for jets in the JET20 sample, i.e. with $E_T^{jet} > 20$. The percentages are relative to the total number of jets in the sample (101713). 141
3.13 Comparison of the background calculation and data for relaxed topological and kinematical cuts. Note that the column in the top table for ≥ 2 jets and after all cuts summarizes the background calculation in the signal region. In those cases where no Monte Carlo events pass the cuts, an upper limit at the 1σ level is given. 156
3.14 Comparison of the background calculation and data for relaxed topological and kinematical cuts (continued). 157

3.15 Characteristics of the 4 tau dilepton candidate events. 159
3.16 The jet 4-vectors of the tau dilepton candidates. Standard jet corrections are applied [42]. 162
3.17 Comparison of fake background calculation and observed same-sign (ss) events in the data for relaxed topological and kinematical cuts. 163
3.18 Expected number of SVX-tagged events per generic W event due to heavy flavor as a function of jet multiplicity. 165
3.19 Expected number of tagged events among the four candidate events compared to the observation in the data. 165
3.20 Values of the soft electron tag variables for the two tau dilepton candidate events with soft electron tags, and the cuts. 172
3.21 Values of the soft muon tag variables for the tau dilepton candidate event with a soft muon tag, and the cuts. 172
3.22 B-tagging results for relaxed topological and kinematical cuts. Note that the table for ≥ 2 jets and after all cuts gives the result for the signal region. 173
3.23 The probabilities $\mathcal{P}$ in % for the expected mean background (B) and for the expected mean background plus $t\bar{t}$ signal ($B+t\bar{t}$) to have fluctuated to the number of observed events (N_{obs}) or more. For the expected $t\bar{t}$ signal we use two cross sections. One is based on the theoretical calculation (4.8$\pm$0.7 pb), the other on the combined CDF measurement (7.7$\pm$2 pb). Uncertainties are taken into account via Gaussian smearing of the mean expected numbers. 176

4.1 Kinematic properties of the 14 top dilepton candidates. For electrons we list the corrected E_T^e in parentheses. The modified significance $S_{\not{E}_T}{}'$ is defined in equ. 4.1. 194
4.2 Summary of the information for the kinematic distributions in which events are found in the tails. We give the mean expected number of events (m) above a kinematic threshold, the observed number of events (N), and the Poisson probability $P(\geq N, m)$ to observe $\geq N$ events when m events are expected. 197
4.3 Thrust, oblateness and invariant masses for the 14 top dilepton candidates. 199
4.4 Probability for the compatibility of the data with the $t\bar{t}$ Monte Carlo for the variables in the thrust analysis using the Kolmogorov–Smirnov test. 207

5.1 Current total acceptances including all efficiencies and branching ratios in Run I and expected acceptance increases in Run II for top dilepton events. The numbers of expected events for Run I are based on the theoretical cross section at a c.m. energy of 1.8 TeV, $\sigma_{t\bar{t}}^{theory} = 4.75\ pb$ [25]. Estimates for Run II are based on $\sigma_{t\bar{t}}^{theory} = 6.65\ pb$ at a c.m. energy of 2 TeV and a data sample of 2 fb^{-1}. Numbers in parentheses for tau dileptons assume that tau identification in the plug region up to $|\eta| = 2.0$ is possible with efficiencies similar to those in the central region. All other numbers assume only extension of the acceptance region for electrons and muons. 220

5.2 The expected statistical uncertainty for the measurement of the $t\bar{t}$ cross section, $(\frac{\Delta\sigma_{t\bar{t}}}{\sigma_{t\bar{t}}})^{stat}$, and the expected sensitivity to new physics in the dilepton channels in Run II for 2 fb^{-1} of data. The listed 95% confidence limits N_{95} on the numbers of events due to new physics in the dilepton channels are calculated assuming that the expected number of $t\bar{t}$ events, based on the theoretical cross section, and background events will be observed. For the numbers in parentheses systematic uncertainties are ignored, for the numbers outside of parentheses we assume systematic uncertainties on the integrated luminosity (8%), acceptance (10% for ee, $\mu\mu$, and $e\mu$, 14% for $e\tau, \mu\tau$), and background (20%) similar to the results in Run I. The limits on the numbers of events are converted to cross section limits assuming that the acceptance for new physics is similar to the acceptance for $t\bar{t}$ events. 223

LIST OF ILLUSTRATIONS

1.1 Lowest-order Feynman diagrams for $t\bar{t}$ production via strong parton interaction in $p\bar{p}$ collisions. 8

1.2 Theoretical predictions for the $t\bar{t}$ cross section in $p\bar{p}$ collisions at the Tevatron from NLO calculations that also employ soft gluon resummation for higher orders. In each set of 3 curves the middle curve represents the central values and the upper and lower curves the $\pm 1\sigma$ envelope. 10

1.3 Matrix of $t\bar{t}$ final states in the Standard Model. We distinguish 5 final states: 'Standard dileptons' (diagonal hatch), 'Lepton + jets' (vertical hatch), 'All-Hadronic' (horizontal hatch), 'Tau dileptons' (dense hatch), and 'Tau + jets' (no hatch). 11

1.4 Schematic drawing of one quadrant of the CDF central detector. The projective tower geometry of the calorimeters is indicated. Note that the forward calorimeters are actually located further upstream and downstream than shown here. CES stands for Central Electromagnetic Shower-maximum detector and CPR for Central Pre-Radiator. 14

1.5 Position of fiducial tight central electrons in the Run Ia inclusive central electron sample as measured by the CES. 16

1.6 Position of fiducial tight central electrons in the Run Ib inclusive central electron sample as measured by the CES. 17

1.7 Dielectron mass of $Z/\gamma \rightarrow ee$ events. For the data (points) masses are calculated using *raw* electron energies, i.e. the calibration to flatten out the CEM response is *not* applied. This is compared with a Monte Carlo template (histogram) generated using a CEM resolution $\Delta E/E = 13.5\%/\sqrt{E[\mathrm{GeV}]} \oplus 5.0\%$. Also shown is a Gaussian fit to the data. 19

1.8 Cubic fit of the χ^2 obtained from comparing $Z/\gamma \to ee$ data using *uncorrected* electron energies in the peak region 80-100 GeV/c^2 to Monte Carlo templates with different constant terms κ for the energy resolution $\Delta E/E = 13.5\%/\sqrt{E[\mathrm{GeV}]} \oplus \kappa$ %. The fit returns $\kappa = (4.8 \pm 0.9)\%$. 19
1.9 Dielectron mass of $Z/\gamma \to ee$ events. For the data (points) masses are calculated using *corrected* electron energies, i.e. the calibration to flatten out the CEM response is applied. This is compared with a Monte Carlo template (histogram) generated using a CEM resolution $\Delta E/E = 13.5\%/\sqrt{E[\mathrm{GeV}]} \oplus 2.0\%$. Also shown is a Gaussian fit to the data. 20
1.10 Cubic fit of the χ^2 obtained from comparing $Z/\gamma \to ee$ data using *corrected* electron energies in the peak region 80-100 GeV/c^2 to Monte Carlo templates with different constant terms κ for the energy resolution $\Delta E/E = 13.5\%/\sqrt{E[\mathrm{GeV}]} \oplus \kappa$ %. The fit returns $\kappa = (2.3 \pm 0.8)\%$. 20
1.11 Jet energy resolution as a function of jet E_T for central jets with $0.2 < |\eta_{jet}| < 0.8$ measured from dijet balancing. For comparison a parameterization of the CHA resolution $\Delta E_T^{jet}/E_T^{jet} = 80\%/(E_T[GeV])^{1/2} \oplus 4\%$ is shown. Note that this is not a fit. . 23
1.12 Components of $\not\!\!E_T$ in $Z \to ee$ and $Z \to \mu\mu$ events. 25
1.13 Resolution of $\not\!\!E_T$ components vs $\sum E_T$ for $Z \to ee$ and $Z \to \mu\mu$ events. The $\not\!\!E_T$ data are placed in bins of $\sum E_T$; $\not\!\!E_T^x$ and $\not\!\!E_T^y$ are fitted to Gaussians for each bin and the resulting σ's plotted vs $\sum E_T$. The curves are fits to the functional form $\sigma = P_1 + P_2 \cdot \sqrt{\sum E_T}$. 26
1.14 The $\not\!\!E_T$ significance $S_{\not\!\!E_T}$, as defined in the tau dilepton analysis (chapter 3), for Z events. 27
1.15 Impact parameter with respect to the primary interaction vertex and the impact parameter significance for electron tracks in the SVX using $Z \to ee$ events. 28
1.16 Position of isolated, tight central muons in the Run Ib inclusive central muon sample as measured from the muon track. a) All muons, b) CMU only, c) CMP only, d) CMU-CMP, e) CMX only, f) CMU-CMX. 30
1.17 Position of isolated, tight central muons in the Run Ia inclusive central muon sample as measured from the muon track. a) All muons, b) CMU only, c) CMP only, d) CMU-CMP, e) CMX only, f) CMU-CMX. 31

1.18 Dimuon mass of $Z/\gamma \rightarrow \mu\mu$ events. Data (points) are compared with a Monte Carlo template (histogram) generated using a tracking resolution $\Delta p_T/p_T = 0.09\% \times p_T[\mathrm{GeV}/c] \oplus 0.66\%$. Also shown is a Gaussian fit to the data in the peak region. 34
1.19 Cubic fit of the χ^2 obtained from comparing $Z \rightarrow \mu\mu$ data in the Z peak region (80-100 GeV/c^2). Monte Carlo templates are used with different parameters α for the track momentum resolution $\Delta p_T/p_T = [(\alpha/100) \times p_T[\mathrm{GeV}/c] \oplus 0.66]\%$. The fit returns $\alpha = 0.091 \pm 0.015$. 34

2.1 Branching ratios of W's, τ's , and b's into electrons, muons, and hadrons in the PYTHIA $t\bar{t}$ MC at the generator level. 40
2.2 The ΔR distributions for matching of e, μ and τ at the generator level (GENP bank) to fully reconstructed e, μ and τ (ELES, CMUO, CMIO and TAUO banks). 41
2.3 Distribution of central electron identification variables for the unbiased second leg in $Z \rightarrow ee$ decays. The first electron is required to pass tight cuts. The dotted lines indicate the cuts used for tight central electrons (TCE) in the dilepton analysis. 46
2.4 Distribution of central muon (CMUO) identification variables for the unbiased second leg in $Z \rightarrow \mu\mu$ decays. The first muon is required to pass tight cuts. The dotted lines indicate the cuts used for tight central muons (TCM) in the dilepton analysis. . 48
2.5 Percentages of dilepton events in the $t\bar{t}$ MC with both W's decaying leptonically that survive the successive selection cuts. The lepton p_T and η information are evaluated at the generator level. 55
2.6 W^+ decay mode vs W^- decay mode as obtained at the generator level for 80,000 generated $t\bar{t}$ MC events. A total of 9569 events pass the dilepton selection or the lepton + jets selection. Dilepton events are shown on the left; lepton + jets events on the right. The numbers indicate the number of events found for each combination. 56
2.7 Contribution of various W^+W^- decay modes to events identified as dilepton events in the $t\bar{t}$ Monte Carlo. For the cases where not both leptons are from W decays the origin of the lepton that is not from a W is indicated. 57
2.8 Contribution of various W^+W^- decay modes to events identified as lepton +jet events in the $t\bar{t}$ Monte Carlo. For the cases where τ's are involved the decay mode of the τ is indicated. . 60

2.9 Percentages of $t\bar{t}$ MC events with both W's decaying into $e\nu$ or $\mu\nu$ ($W^+ \to \ell^+\nu$, $W^- \to \ell^{-\prime}\nu'$ $\ell = e, \mu$ $\ell' = e, \mu$) that get accepted by the dilepton analysis and the lepton + jets analysis. Events are counted either in the dilepton channel or in the lepton + jets channel, but not in both, i.e. the percentages are exclusive. 62
2.10 Schematic (r, ϕ) display of ee, $\mu\mu$, and $e\mu$ top dilepton candidates. The vector lengths represent the transverse momenta of the objects. Note that we plot quantities as used for the dilepton selection; i.e. electron and jet energies are not corrected, but $\not\!\!E_T$ is corrected for muons and jets. The dashed lines represent the thrust axes of the events (see Chapter 4). 69
2.11 Schematic (r, ϕ) display of ee, $\mu\mu$, and $e\mu$ top dilepton candidates. The vector lengths represent the transverse momenta of the objects. Note that we plot quantities as used for the dilepton selection; i.e. electron and jet energies are not corrected, but $\not\!\!E_T$ is corrected for muons and jets. The dashed lines represent the thrust axes of the events (see Chapter 4). 70

3.1 Top: The p_T spectra of τ's at the generator level (GENP) and of their reconstructed charged decay products in $e\tau$ and $\mu\tau$ $t\bar{t}$ MC events ($m_{top} = 175$). Center: One-prong τ decays only. Bottom: Three-prong τ decays only. 79
3.2 Comparison of reconstructed p_T spectra of tracks only and tracks + π^0's for τ decays in $e\tau$ and $\mu\tau$ $t\bar{t}$ MC events ($m_{top} = 175$). . 80
3.3 Comparison of τ identification variables in the $t\bar{t}$ MC (hatched) and for QCD jets from the unbiased JET20(solid histogram) and JET70(dots) samples. All three histograms for a particular variable are normalized to equal area. 89
3.4 The distribution of E/p using p_T^{trk} and $p_T^{trk+\pi^0}$ for one-prong and three-prong τ decays in the PYTHIA $t\bar{t}$ MC. 90
3.5 The RMS cluster width σ_{cl} vs E_T of the τ jet for matched, hadronically decaying (as determined at the generator level) τ's from $W's$ in the PYTHIA $t\bar{t}$ MC. Top: 1-prongs, Center: 3-prongs, Bottom: all track multiplicities. 91
3.6 Efficiency of τ identification cuts as a function of $p_T^{trk+\pi^0}$. Top: One-prongs only. Center: Three-prongs only. Bottom: Both combined. 94
3.7 The $\not\!\!E_T$ distribution in simulated central $W \to \tau\nu$ and $W \to e\nu$ events. 97

3.8 The E_T spectrum in the monojet sample before (top) and after (bottom) requiring the Level 2 MET35 trigger. 100
3.9 Track multiplicity in the monojet data sample. a) No τ identification cuts applied. b) After applying all τ identification cuts except track multiplicity. 101
3.10 Calorimeter RMS cluster width in the monojet sample for *one-prongs*. Top: No τ identification cuts applied. Bottom: After applying all τ identification cuts except for the cluster width cut. The numbers of entries refer to the monojet data. The maximum and minimum of the sliding cut for the E_T range $20 < E_T < 40$ GeV are indicated by the 2 vertical lines. . . . 103
3.11 Calorimeter RMS cluster width in the monojet sample for *three-prongs*. Top: No τ identification cuts applied. Bottom: After applying all τ identification cuts except for the cluster width cut. The numbers of entries refer to the monojet data. The maximum and minimum of the sliding cut for the E_T range $20 < E_T < 40$ GeV are indicated by the 2 vertical lines. . . . 104
3.12 The E/p distribution in the monojet sample for *one-prongs*. Top: No τ identification cuts applied. Bottom: After applying all τ identification cuts except for the E/p cut. The numbers of entries refer to the monojet data. 105
3.13 The E/p distribution in the monojet sample for *three-prongs*. Top: No τ identification cuts applied. Bottom: After applying all τ identification cuts except for the E/p cut. The numbers of entries refer to the monojet data. 106
3.14 Number of π^0's in the monojet sample. Top: No τ identification cuts applied. Bottom: After applying all τ identification cuts except for the cut on the number of π^0's. The numbers of entries refer to the monojet data. 108
3.15 The τ mass distribution in the monojet sample. Top: No τ identification cuts applied. Bottom: After applying all τ identification cuts except for the τ mass cut. The numbers of entries refer to the monojet data. 109
3.16 Track isolation in the monojet sample. Top: No τ identification cuts applied. Bottom: After applying all τ identification cuts except for the track isolation cut. The numbers of entries refer to the monojet data. 110
3.17 The E_T spectrum of the leading and the second jet and jet multiplicity for PYTHIA $e\tau$ and $\mu\tau$ $t\bar{t}$ MC events ($m_{top} = 175$ GeV). 115

3.18 The distribution of the H_T variable for PYTHIA $e\tau$ and $\mu\tau$ $t\bar{t}$ MC events passing the jet cut. 116

3.19 Topology cuts for PYTHIA $e\tau$ and $\mu\tau$ $t\bar{t}$ MC events. Top: $\Delta\phi\,(\not{E}_T, jl)$ vs $\not{E}_T$. Bottom: $S_{\not{E}_T}$ vs $\not{E}_T$. In the plots on the right hand side the topology cuts are imposed. 118

3.20 Acceptance $A_{geom \cdot P_T}$ and efficiencies ϵ_{jets}, ϵ_{H_T}, and $\epsilon_{topology}$ versus top mass from PYTHIA $t\bar{t}$ Monte Carlo. 122

3.21 Total Acceptance A_{tot} versus top mass using $t\bar{t}$ MC sets. . . . 123

3.22 Track isolation for tau candidates in pure ISAJET Monte Carlo and in ISAJET Monte Carlo with additional minimum bias data mixed in. 125

3.23 Track isolation for tau candidates in $t\bar{t}$ ISAJET Monte Carlo and in PYTHIA Monte Carlo. Top: Logarithmic scale, Bottom: Linear scale. 127

3.24 Track isolation for central electrons in $t\bar{t}$ ISAJET Monte Carlo and in PYTHIA Monte Carlo. Top: Logarithmic scale, Bottom: Linear scale. 129

3.25 Track isolation for electrons from central-central Z's in data and in PYTHIA Monte Carlo. Top: Logarithmic scale, Bottom: Linear scale. 130

3.26 The E_T spectrum of jets in the QCD dijet sample with minimal trigger bias used for estimating the τ fake rate. 138

3.27 The τ fake rate per jet for QCD jets as a function of jet E_T and η_{det} as measured in the dijet sample with minimal trigger bias. 140

3.28 The E_T spectrum of jets in a $W+ \geq 3$ jets data sample with dilepton jet cuts and τ analysis topological cuts (109 pb^{-1}). . . 143

3.29 Comparison of jet multiplicity and jet E_T spectra in $Z \rightarrow e^+e^- + \geq 2jets$ events. Points are data (109 pb^{-1}); histograms are VECBOS Monte Carlo. For the jet multiplicity VECBOS is normalized to the 2 jet bin. The VECBOS Monte Carlo is expected to have fewer events than the data in the 0–jet and 1–jet bin because only $Z \rightarrow e^+e^- + 2$ *partons* were generated. For the jet E_T spectra VECBOS is normalized to 76 data events with 2 or more jets. The number of entries in all plots are for the VECBOS Monte Carlo. 145

3.30 Comparison of $\not\!\!E_T$ in $Z \to e^+e^- + jets$ events. Points are data (109 pb^{-1}); histograms are VECBOS Monte Carlo. VECBOS is normalized to 1822(335;76) data events with 0 (1;$\geq$ 2) jets. The number of entries are for the VECBOS Monte Carlo. The VECBOS Monte Carlo is not expected to model the data well in the 0–jet bin because only $Z \to e^+e^- + 2\ partons$ were generated. 146
3.31 Scatterplot of $S_{\not\!\!E_T}$ vs $\not\!\!E_T$ for the Monte Carlo $Z \to e^+e^- + jets$ sample (1200 pb^{-1}). Top: after identifying a primary e or μ and a τ lepton. Center: after requiring 2 jets. Bottom: after requiring 2 jets and $H_T > 180$ GeV. Plots on the left show all events; plots on the right show only events that survive the $S_{\not\!\!E_T} > 3$ GeV$^{1/2}$ cut. 148
3.32 Scatterplot of $S_{\not\!\!E_T}$ vs $\not\!\!E_T$ for the Monte Carlo $Z \to \tau^+\tau^- + jets$ sample (1200 pb^{-1}). Top: after identifying a primary e or μ and a τ lepton. Center: after requiring 2 jets. Bottom: after requiring 2 jets and $H_T > 180$ GeV. Plots on the left show all events; plots on the right show only events that survive the $S_{\not\!\!E_T} > 3$ GeV$^{1/2}$ cut. 150
3.33 Scatterplot of $\Delta\phi\,(\not\!\!E_T, jl)$ vs $\not\!\!E_T$ for the Monte Carlo $Z \to \tau^+\tau^- + jets$ sample (1200 pb^{-1}). Top: after identifying a primary e or μ and a τ lepton. Center: after requiring 2 jets. Bottom: after requiring 2 jets and $H_T > 180$ GeV. Plots on the left show all events; plots on the right show only events that survive the topological cut indicated by the line. 151
3.34 Scatterplot of $S_{\not\!\!E_T}$ vs $\not\!\!E_T$ for the VECBOS+TAUOLA+QFL $Z \to \mu^+\mu^- + jets$ sample (1200 pb^{-1}). Top: after identifying a primary e or μ and a τ lepton. Center: after requiring 2 jets. Bottom: after requiring 2 jets and $H_T > 180$ GeV. Plots on the left show all events; plots on the right show only events that survive the $S_{\not\!\!E_T} > 3$ GeV$^{1/2}$ cut. 153
3.35 Scatterplot of $S_{\not\!\!E_T}$ vs $\not\!\!E_T$ for the PYTHIA WW sample (2500 pb^{-1}). Top: after identifying a primary e or μ and a τ lepton. Center: after requiring 2 jets. Bottom: after requiring 2 jets and $H_T > 180$ GeV. Plots on the left show all events; plots on the right show only events that survive the $S_{\not\!\!E_T} > 3$ GeV$^{1/2}$ cut. 154
3.36 Scatterplot of $S_{\not\!\!E_T}$ vs $\not\!\!E_T$ for CDF data (109 pb^{-1}). Top: after identifying a primary e or μ and a τ lepton. Center: after requiring 2 jets. Bottom: after requiring 2 jets and $H_T > 180$ GeV. Plots on the left show all events; plots on the right show only events that survive the $S_{\not\!\!E_T} > 3$ GeV$^{1/2}$ cut. 158

3.37 The distribution of $S_{\not E_T}$ vs $\not E_T$ for events with a primary lepton and a tau candidate in the CDF data compared with the $t\bar{t}$ Monte Carlo. Three of the four final candidate events (stars) have b-tagged jets. 160
3.38 The distribution of the signed impact parameter d for SVX tracks from τ's (top) and W electrons (bottom) in the $t\bar{t}$ Monte Carlo. The arrows indicate the measured impact parameters for those τ's in the τ dilepton candidates that have tracks in the SVX. 161
3.39 Scatterplot of $\Delta\phi\,(\not E_T, jl)$ vs $\not E_T$ for CDF data (109 pb^{-1}). Top: after identifying a primary e or μ and a τ lepton. Center: after requiring 2 jets. Bottom: after requiring 2 jets and $H_T > 180$ GeV. Plots on the left show all events; plots on the right show only events that survive the topology cut indicated by the line. 164
3.40 Scatterplot of $S_{\not E_T}$ vs $\not E_T$ for same-sign events in CDF data (109 pb^{-1}). Top: after identifying a primary e or μ and a τ lepton. Center: after requiring 2 jets. Bottom: after requiring 2 jets and $H_T > 180$ GeV. Plots on the left show all events, plots on the right only show events that survive the $S_{\not E_T} > 3$ GeV$^{1/2}$ cut. See text for details on the four event passing all cuts. 166
3.41 The $e^-\tau^+$ candidate 45880/31838. The hadronic τ is at $\phi = 356^o$ and $\eta_{det} = -0.25$. The jet at $\phi = 66^o$ and $\eta_{det} = -0.38$ is b–tagged by a soft electron. 167
3.42 The $\mu^+\tau^-$ candidate 64721/229200. The hadronic τ is at $\phi = 70^o$ and $\eta_{det} = 1.09$. The jet at $\phi = 19^o$ and $\eta_{det} = -0.09$ is b–tagged by a soft muon and the jet at $\phi = 131^o$ and $\eta_{det} = 0.29$ is b–tagged by a soft electron. 168
3.43 The $e^-\tau^+$ candidate 64934/416715. The hadronic τ is at $\phi = 275^o$ (behind a small cluster) and $\eta_{det} = -0.03$. The jet at $\phi = 345^o$ and $\eta_{det} = -0.27$ is b–tagged by the SVX. 169
3.44 The $\mu^+\tau^-$ candidate 65471/47719. The hadronic τ is at $\phi = 81^o$ (behind a jet) and $\eta_{det} = 0.12$. There are no b–tags in this event. 170
3.45 Comparison of $t\bar{t}$ cross sections measured in different channels. 178

4.1 The E_T and p_T spectra of electrons and muons in the candidate events compared with the expected spectra. Electron energies are not corrected. Left: ee, $\mu\mu$, $e\mu$ candidates. There are 2 entries per event. Right: $e\tau$, $\mu\tau$ candidates. Background and top contributions have been normalized to the expected number of events. 184

4.2 The p_T spectrum of τ's in the tau dilepton candidate events compared with the expected spectrum. Background and top contributions have been normalized to the expected number of events. 184

4.3 The invariant mass $m_{\ell\ell}$ formed by the leptons in the candidate events compared with the expected spectra. Left: ee, $\mu\mu$, $e\mu$ candidates. Right: $e\tau$, $\mu\tau$ candidates. Background and top contributions have been normalized to the expected number of events. 185

4.4 The $\vec{p}_T^{\,\ell\ell} = \vec{p}_T^{\,\ell_1} + \vec{p}_T^{\,\ell_2}$ spectrum of the dilepton system in the candidate events compared with the expected spectra. Left: ee, $\mu\mu$, $e\mu$ candidates. Right: $e\tau$, $\mu\tau$ candidates. Background and top contributions have been normalized to the expected number of events. 185

4.5 The $\not{E}_T$ spectrum without accounting for jet corrections for the candidate events compared with the expected spectra. Left: ee, $\mu\mu$, $e\mu$ candidates. Right: $e\tau$, $\mu\tau$ candidates. Background and top contributions have been normalized to the expected number of events. 187

4.6 The $\not{E}_T$ spectrum after accounting for jet corrections for the candidate events compared with the expected spectra. Left: ee, $\mu\mu$, $e\mu$ candidates. Right: $e\tau$, $\mu\tau$ candidates. Background and top contributions have been normalized to the expected number of events. 187

4.7 Scatterplot of the angle $\Delta\phi(\not{E}_T, \ell j)$ between the corrected $\not{E}_T$ and the closest lepton or jet versus corrected $\not{E}_T$ for the ee, $\mu\mu$, and $e\mu$ candidate events, compared with the expected distributions for $t\bar{t}$ and background. Background and top contributions are *not* normalized to the expected number of events. 188

4.8 Scatterplot of the angle $\Delta\phi(\not{E}_T, \ell j)$ between the corrected $\not{E}_T$ and the closest lepton or jet versus corrected $\not{E}_T$ for the $e\tau$, and $\mu\tau$ candidate events, compared with the expected distributions for $t\bar{t}$ and background. Background and top contributions are *not* normalized to the expected number of events. 189

4.9 The spectrum of the $\not{E}_T$ significance after accounting for jet corrections for the candidate events compared with the expected spectra. Left: ee, $\mu\mu$, $e\mu$ candidates. Right: $e\tau$, $\mu\tau$ candidates. Background and top contributions have been normalized to the expected number of events. 191

4.10 The spectrum of the modified $\not\!\!E_T$ significance (see equ. 4.1) after accounting for jet corrections for the candidate events compared with the expected spectra. Left: ee, $\mu\mu$, $e\mu$ candidates. Right: $e\tau$, $\mu\tau$ candidates. Background and top contributions have been normalized to the expected number of events. 191

4.11 Scatterplot of the $\not\!\!E_T$ significance, $S_{\not\!\!E_T}$, versus $\not\!\!E_T$ for the candidate events compared with the expected distributions for top and background. Jet corrections are taken into account for calculating the $\not\!\!E_T$. Left: ee, $\mu\mu$, $e\mu$ candidates. Right: $e\tau$, $\mu\tau$ candidates. Background and top contributions are *not* normalized to the expected number of events. 192

4.12 The number of jets with $E_T > 10$ GeV, $|\eta| < 2.0$ in the candidate events compared with the expected spectra. Left: ee, $\mu\mu$, $e\mu$ candidates. Right: $e\tau$, $\mu\tau$ candidates. Background and top contributions have been normalized to the expected number of events. 195

4.13 The E_T spectrum of the leading jet in the candidate events compared with the expected spectrum. No jet corrections are applied. Left: ee, $\mu\mu$, $e\mu$ candidates. Right: $e\tau$, $\mu\tau$ candidates. Background and top contributions have been normalized to the expected number of events. 196

4.14 The E_T spectrum of the second jet in the candidate events compared with the expected spectrum. No jet corrections are applied. Left: ee, $\mu\mu$, $e\mu$ candidates. Right: $e\tau$, $\mu\tau$ candidates. Background and top contributions have been normalized to the expected number of events. 196

4.15 The H_T spectrum of candidate events compared with the expected spectrum. Left: ee, $\mu\mu$, $e\mu$ candidates. Right: $e\tau$, $\mu\tau$ candidates. Background and top contributions have been normalized to the expected number of events. 198

4.16 Schematic (r, ϕ) view of the topology for $e\tau$ and $\mu\tau$ top dilepton candidates including thrust axes (dashed line). The vector lengths represent the transverse momenta of the objects. Note that we plot quantities as used for the dilepton selection, i.e. electron and jet energies are not corrected, but $\not\!\!E_T$ is corrected for muons and jets. 200

4.17 Thrust and oblateness of top dilepton candidates compared with $t\bar{t}$ 175 MC (dashed). Left: $e\mu, ee, \mu\mu$ candidates. Right: $e\tau$, $\mu\tau$ candidates. KS probability for thrust is 70.2% (93.3%), for oblateness is 53.4% (70.3%). Values in parentheses are for tau dileptons. 202
4.18 Top: Invariant mass in thrust hemisphere vs thrust [KS P = 25.1%, (P = 83.1%)]. Bottom: Invariant mass in hemisphere opposite the thrust vs thrust [KS P = 24.1%, (P = 98.6%)]. Left: $e\mu, ee, \mu\mu$ candidates. Right: $e\tau, \mu\tau$ candidates. Values in parentheses are for tau dileptons. Large dots are data, smaller dots are $t\bar{t}$ 175 MC. 203
4.19 Top: Invariant mass in thrust hemisphere vs invariant mass in hemisphere opposite the thrust [KS P = 3.7% (P = 95.3%)]. Center: $m_{thrust} - m_{opp}$ [KS P = 44.1% (P = 95.4%)]. Bottom: $m_{thrust} - m_{opp}$ vs thrust [KS P = 51.9% (P = 87.5%)]. Left: $e\mu, ee, \mu\mu$ candidates. Right: $e\tau, \mu\tau$ candidates. Values in parentheses are for tau dileptons. Large dots are data, smaller dots are $t\bar{t}$ 175 MC. 204
4.20 Same as previous figure, except with additional requirement $H_T > 220$ GeV. Left: $e\mu$ candidates. Right: $e\tau$, $\mu\tau$ candidates. Top: Invariant mass in thrust hemisphere vs invariant mass in hemisphere opposite the thrust [KS P = 25.6% (P = 93.9%)]. Center: $m_{thrust} - m_{opp}$ [KS P = 81.7% (P = 97.5%)]. Bottom: $m_{thrust} - m_{opp}$ vs thrust [KS P = 59.7% (P = 81.9%)]. Values in parentheses are for tau dileptons. Large dots are data, smaller dots are $t\bar{t}$ 175 MC. 206
4.21 CTC display for the "trilepton" event (Run 67581/Event 129896). The additional third lepton is at $\phi = 359°$ (right). It is isolated and passes all TCE identification requirement, except the fiducial cut (because it is too close to the wedge boundary in ϕ). . 209
4.22 Lego display of transverse calorimeter energies for the "other" trilepton event (Run 57621/Event 45230). The p_T of the muons are also indicated (in medium gray scale). The additional third lepton, a muon, is very close to the jet at $\phi = 254, \eta = 0.5$, which is also b–tagged by the SVX. 211
4.23 CTC display for the $\mu\mu\gamma$ event (Run 58281/Event 4805). The photon-like jet is near 180° (left) and forms a mass $m_{\mu\mu\gamma}$ = 87.2 GeV/c^2 with the muon pair. The event is interpreted as a radiative Z decay. 213

ABSTRACT

This thesis presents a search for top quark pair production via the process $p\overline{p} \rightarrow t\overline{t} + X \rightarrow W^+W^-b\overline{b} + X \rightarrow (\ell^+\nu_\ell)\ (\ell^-\overline{\nu}_\ell)\ b\overline{b} + X$, where ℓ is either e, μ, or τ. Using a sample of $109 \pm 7\ pb^{-1}$ of $p\overline{p}$ collisons at $\sqrt{s} = 1.8$ TeV collected by the CDF detector at the Fermilab Tevatron we find a clear signal for $t\overline{t}$ production in the ee, $\mu\mu$, and $e\mu$ dilepton channels. We observe 9 events where we expect 3.9 ± 0.7 $t\overline{t}$ events (based on the theoretical production cross section) and 2.1 ± 0.4 background events. The $t\overline{t}$ production cross section measured from this channel is $\sigma_{t\overline{t}} = 8.5^{+4.1}_{-3.3}(stat)^{+1.6}_{-0.8}(syst)$ pb. Using a method developed in this thesis to identify hadronically decaying τ leptons we also search for $e\tau$ and $\mu\tau$ dilepton events from $t\overline{t}$ production and decay. We observe 4 events and expect 2.5 ± 0.4 background events. In 3 of the 4 events at least one jet is tagged as due to a b quark decay. We expect 0.28 ± 0.02 tagged events from background processes. Based on the 4 tau dilepton events we calculate the $t\overline{t}$ production cross section to be $\sigma_{t\overline{t}} = 10.2^{+16.3}_{-10.2}(stat) \pm 1.6(syst)$ pb. The kinematics and topology of the candidate events are generally consistent with the expectations, with two exceptions. Five of the 14 candidate events have unusually large missing transverse energy. One $e\mu$ event contains an electron with very high E_T (182 GeV) and an additional high–E_T (23 GeV) isolated positron. In 109 pb^{-1} we expect $(2.4 \pm 0.9) \times 10^{-6}$ such "trilepton" events from $t\overline{t}$ production and decay.

Chapter 1

INTRODUCTION

Grau, teurer Freund, ist alle Theorie,
Und grün des Lebens goldner Baum.

J.W. v. Goethe, *Faust I, Studierzimmer*

Soon after the bottom quark [1] had been discovered at Fermilab in 1977 the search for its partner, aptly named the 'Top quark', was on. Theoretical considerations within the Standard Model of particle physics in conjunction with experimental results led to the general expectation that this additional, sixth quark flavor had to exist. For example, the observation that the forward-backward asymmetry A_{FB} in the scattering process $e^+e^- \to Z/\gamma \to b\bar{b}$ is non-zero indicates that the b quark is in fact not a weak isospin singlet but rather a member of an isospin doublet. This asymmetry is directly proportional to the third component T_3^f of the weak isospin of the left-handed b-quark, so that one would expect A_{FB} to vanish if the b-quark were a weak isospin singlet.

In 1984 the JADE collaboration reported a measurement of $A_{FB}^{b\bar{b}} = -22.8 \pm 6.0 \pm 2.5\%$ [2] at the e^+e^--collider PETRA running at a c.m. energy of 34.6 GeV. This indicated that indeed A_{FB} and T_3^f do not vanish, while for a b-quark with $T_3^f = -1/2$ the Standard Model predicted $A_{FB}^{b\bar{b}} = -25.2\%$. The

early measurements at the Z-pole from LEP reported in 1991, e.g. $A_{FB}^{b\bar{b}} = 12.6 \pm 2.8 \pm 1.2\%$ from ALEPH [3], were in agreement with the Standard Model value at the pole of $A_{FB}^{b\bar{b}} = 9.97\%$. The currently measured value $A_{FB}^{b\bar{b}} = 9.92 \pm 0.35\%$ [4] from LEP is in excellent agreement with the Standard Model. Therefore, a top quark is required as the $T_3^f = +1/2$ partner of the bottom quark to complete the third generation isospin doublet of quarks.

A similar argument for the existence of the top quark comes from the absence of flavor-changing neutral currents (FCNC) in B decays. The experimental limits on the FCNC decay $B^0 \to \mu^+\mu^-$ in 1984 were , $(B^0 \to \mu^+\mu^-)/, (B^0 \to all) < 7 \cdot 10^{-3}$ [5]. Today the limit has been improved to , $(B^0 \to \mu^+\mu^-)/, (B^0 \to all) < 5.9 \cdot 10^{-6}$ [4]. This strong FCNC–suppression in the B sector indicates that a mechanism is at work for the third quark generation that is analogous to the GIM mechanism [6] for the second quark generation. Just as the GIM mechanism required a charm quark to cancel unobserved FCNC transitions between first and second generations, a weak isopartner for the b quark is needed for the third generation.

Since the electroweak interaction is chiral, i.e. distinguishes between left–handed and right–handed particles, a theoretical problem known as the 'chiral anomaly' can arise for the coupling of three electroweak bosons to each other, e.g. $Z \to \gamma\gamma$, via triangular fermion loops. The contribution of each fermion (quark or lepton) in the loop is proportional to $T_3^f Q_f^2$ where Q_f is the charge of the fermion. The total amplitude is proportional to $\sum_f T_3^f Q_f^2$ and diverges unless the contributions from all fermions exactly cancel each other and $\sum_f T_3^f Q_f^2$ vanishes. The divergence cannot be removed by the standard renormalization procedures to remove infinities, which is why this effect is called an anomaly. This would leave the electroweak model unrenormalizable. Fortunately, the cancellation is possible provided there are two lepton and

quark doublets in each generation and if we take into account the 3 quark colors:

$$\sum_f T_3^f Q_f^2 = \frac{1}{2}(0)^2 + \left(-\frac{1}{2}\right)(-1)^2 + 3\frac{1}{2}\left(\frac{2}{3}\right)^2 + 3\left(-\frac{1}{2}\right)\left(-\frac{1}{3}\right)^2 = 0.$$

Again, this means that a weak isopartner for the b quark is needed for this cancellation to work in the third generation of quarks and leptons and to render the electroweak theory anomaly–free and renormalizable. In summary, these theoretical arguments supported by experimental results made a strong case for the existence of the top quark.

The earliest searches for the top were conducted in the late 70's at the e^+e^- collider PETRA at DESY [7, 8]. The idea was to look for a step in the ratio of the total hadronic cross section to the dimuon cross section $R = \sigma(e^+e^- \to \gamma \to hadrons)/\sigma(e^+e^- \to \gamma \to \mu^+\mu^-)$ as the c.m. energy increased. The pair production of a top quark and an antitop quark would produce such a step near threshold, in analogy to what had been found near the thresholds for $c\bar{c}$ and $b\bar{b}$ production. No step was observed up to the highest energies that PETRA could reach; a limit of basically half the c.m. energy was set, $m_{top} > 23.3$ GeV at 95% C.L.. This approach was continued in the 80's at the e^+e^- collider TRISTAN at KEK, which reached a c.m. energy of 61.4 GeV and extended the limit to $m_{top} > 30.2$ GeV at 95% C.L. [9].

In 1984 the UA1 collaboration claimed a positive result in a search for top quarks via the decay chain $W \to t\bar{b}$, $t \to \ell\nu b$ at the CERN S$p\bar{p}$S collider ($\sqrt{s} = 630$ GeV) [10]. In a data sample of 0.2 pb^{-1}, 12 'isolated lepton + 2 jet' events had been found with an expected background of 3.5 events. In addition, the invariant mass of the lepton, neutrino and one of the jets had appeared to be clustered around 40 GeV/c^2. In this initial analysis no missing transverse energy $\not{E}_T$ had been required so that J/ψ, Υ and Drell-Yan $\to \ell^+\ell^- + jets$

($\ell = e$ or μ) processes were significant sources of background. However, they had not been included in the analysis. Also, the background contribution from $b\bar{b}, c\bar{c}$ had been underestimated by about a factor of four, and the contribution from $W + jets$ events had been neglected [11]. Later UA1 analyses with more data and improved background calculations showed that the oberved number of events could be explained by background alone.

Further searches at the CERN S$p\bar{p}$S by UA1 and UA2 and later at the Fermilab Tevatron by CDF (Collider Detector at Fermilab) all produced negative results and increasing limits [12, 13, 14, 15] on the mass of this expected, albeit seemingly elusive new quark type. It wasn't until 1994 when the CDF collaboration turned up the first hard evidence for the existence of top quarks [16]. This was possible because of a successful high statistics run of the Tevatron collider in 1992-1993 (Run Ia) when CDF collected data corresponding to 20 pb^{-1}. After increasing the total accumulated data to 67 pb^{-1} in Run Ib during 1994-95 the mounting evidence finally led to the firm establishment of the existence of the top quark by CDF [17]. At this time the D0 collaboration also observed top quarks [18].

1.1 Dilepton events

One key element of the discovery of the top quark is the observation of events with 2 high-p_T leptons (e or μ), at least 2 jets and large missing transverse energy. These so-called 'dilepton' events are interpreted as the production of $t\bar{t}$ pairs via the strong interaction and the subsequent decay of each top quark[1] into a b quark and a W boson via the weak force. If both W bosons in turn decay leptonically into $e\nu$ or $\mu\nu$, 2 high-p_T leptons and

[1]For simplicity we will often refer to top and antitop quarks generically as 'top quarks'.

missing transverse energy due to escaping neutrinos can be observed. The fragmentation of the b quarks gives rise to high-p_T jets. The advantage of a search for dilepton events is that they are expected to have the smallest background of all $t\bar{t}$ decay channels. However, this channel also has a very small acceptance.

The standard CDF analysis of top dilepton events is well established, has been widely presented and is extensively documented. The most comprehensive documentations of the analysis to date are the Ph.D. theses by James Romano [19] for Run Ia and Mark Kruse [20] for Run Ia+Ib. A detailed publication in Physical Review D is forthcoming.

However, some results of the top dilepton analysis invite further questions, which this thesis attempts to address as a way towards further understanding in a 'second-generation' CDF top dilepton analysis. For instance, Monte Carlo simulations show that a significant fraction of events with both W's decaying leptonically are not reconstructed as top dilepton events but rather as 'lepton plus jets' events that contain only one high-pt lepton plus a tagged b-jet. Also, it is interesting that the $t\bar{t}$ cross section based on the final set of 9 candidate events is about twice as big as what is expected from theory, even if it is a statistically limited measurement. Furthermore, the topology and kinematics of some candidate events appear somewhat unusual. In this thesis we address these issues after a brief review of the methods and results of the standard dilepton analysis.

Another aspect of a second-generation analysis is how the scope of the dilepton analysis can be increased. One avenue is the incorporation of decays that involve the third lepton, i.e. the tau lepton. At the center of this thesis is a search for dilepton events from $t\bar{t}$ decays with one electron or muon and one *hadronically* decaying tau lepton:

$$t\bar{t} \rightarrow W^+W^-b\bar{b} \rightarrow (\ell\nu_\ell)(\tau\nu_\tau)\ b\bar{b} \qquad (\ell = e \text{ or } \mu)$$
$$\hookrightarrow hadrons + \nu_\tau.$$

This decay mode of the top quark is predicted by the Standard Model and the first and obvious motivation of the measurement is to test that prediction. A second motivation is that this decay channel – which we will simply refer to as the 'τ dilepton' channel throughout this thesis – is especially interesting as the top decay into a b quark, a τ lepton and a tau neutrino ν_τ involves exclusively members of the third lepton and quark families and one should always be on the lookout for unexpected behaviour. For instance, the existence of a charged Higgs boson $H^\pm$ with a mass below the top mass could enhance the production of this type of event through the decay chain $t\bar{t} \rightarrow H^\pm W^\mp b\bar{b}$, $H^\pm \rightarrow \tau^\pm\nu_\tau$. As the coupling of the $H^\pm$ to fermions is proportional to the fermion mass, the leptonic decays of the $H^\pm$ are expected to be dominated by decays into τ's. The existence of a charged Higgs boson would be much less visible in dilepton events containing only electrons and muons.

On a more pragmatic level, the motivation for this analysis is the fact that most studies of the top system (e.g. kinematics, mass, cross sections) are currently statistically limited – this is especially true for studies using dilepton events due to the small branching ratio (BR) for this mode. Therefore, the acceptance of the CDF dilepton analysis needs to be increased. Opening up a new decay channel is one way of achieving that goal. As discussed below the Standard Model BR for $e\tau$ and $\mu\tau$ events is 4/81, i.e. the same as for the standard ee, $e\mu$ and $\mu\mu$ dileptons combined. In principle the number of dilepton events could be doubled by including τ's . However, the branching ratio for hadronic τ decays is about 64% and each τ decay involves an undetectable neutrino ν_τ, which decreases the kinematic acceptance for the detectable τ

decay products. Also, τ identification is not as efficient as electron or muon identification. This means that the total acceptance for τ dileptons is about five times smaller than for the standard dileptons. However, CDF has collected enough data in Run I that τ dileptons from top decays can be observed and become useful for studies of the top system. As will be shown in the last chapter we expect that the 20-fold increase of data in Run II will firmly establish this decay channel.

1.2 Organisation of thesis

In the remainder of this introductory chapter we will give the Standard Model predictions for top quark production and decay, and discuss the properties of the CDF detector that are relevant for the top dilepton analysis. Chapter 2 gives a brief description of the methods and results of the standard dilepton analysis for electrons and muons and addresses related questions such as the correlations with the lepton +jet channel. In Chapter 3 the dilepton analysis using hadronic τ decays is presented in detail. The kinematics of all dilepton candidate events are examined in Chapter 4 to check if the selected events actually look 'top-like'. Chapter 5 summarizes the analysis and gives an outlook for top physics with dilepton events in Run II.

1.3 Top production in the Standard Model

In $p\overline{p}$ collisions top quarks can be produced in $t\overline{t}$ pairs or as a single top quark in association with a $\overline{b}$. 'Single top' production occurs only via the weak interaction in processes such as the s-channel production of off-shell W's ($q\overline{q}' \rightarrow W^{+*} \rightarrow t\overline{b}$), or via t-channel 'W-gluon fusion' ($qg \rightarrow q'Wg \rightarrow q't\overline{b}$).

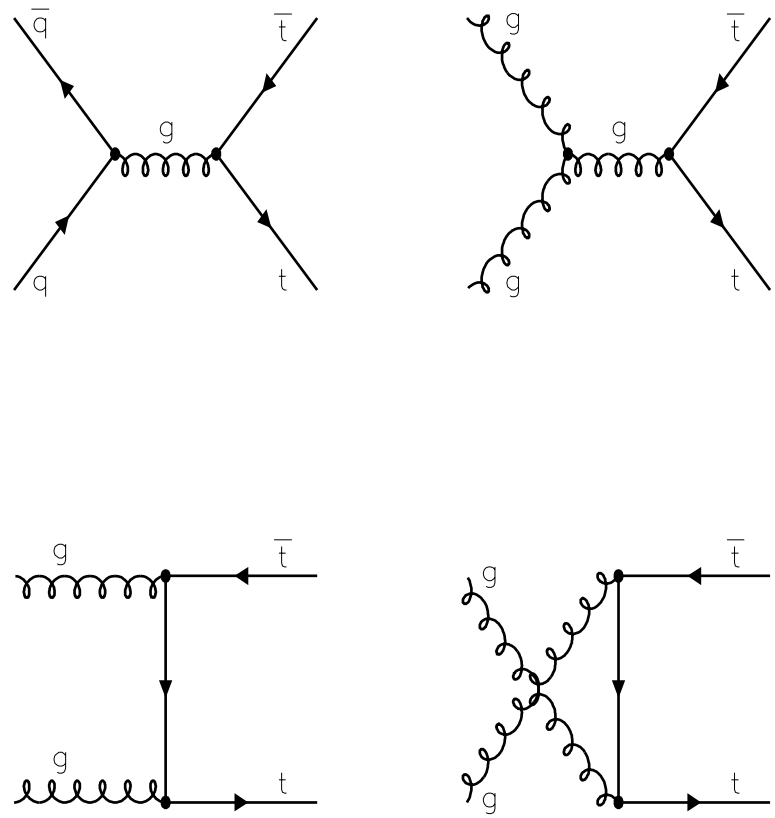

Figure 1.1: Lowest-order Feynman diagrams for $t\bar{t}$ production via strong parton interaction in $p\bar{p}$ collisions.

On the other hand, $t\bar{t}$ pairs can be produced via the strong interaction. For heavy top quarks ($60 < m_{top} < 220$ GeV/c^2) this production mechanism dominates at the Tevatron. The tree-level s-channel and t-channel Feynman diagrams for strong $t\bar{t}$ production are shown in Figure 1.1. The corresponding leading order parton $\mathcal{O}(\alpha_s^2)$ cross sections are given by [22]:

$$\sigma_{q\bar{q}} = \frac{\alpha_s^2}{m_t^2}\frac{\pi\beta\rho}{27}(2+\rho) \quad \sigma_{g\bar{g}} = \frac{\alpha_s^2}{m_t^2}\frac{\pi\beta\rho}{192}\left(\frac{1}{\beta}(\rho^2+16\rho+16)\ln\left(\frac{1+\beta}{1-\beta}\right) - 28 - 31\rho\right) \tag{1.1}$$

$$\text{with} \qquad \beta = \sqrt{1-\rho} \qquad \rho = \frac{4m_t^2}{\hat{s}}, \tag{1.2}$$

and where α_s is the strong coupling constant evaluated at the top mass m_t and $\hat{s}$ is the center of mass energy of the parton system. To get the total tree-level $t\bar{t}$ cross section in $p\bar{p}$ collisions this parton cross section is convoluted with the momentum distributions of the partons inside the proton and antiproton. At Tevatron energies ($\sqrt{s} = 1.8$ TeV) the '$q\bar{q}$ luminosity' [21] exceeds the gg luminosity for $\sqrt{\hat{s}} > 220$ GeV so that the production of heavy top quark pairs is dominated by the $q\bar{q}$ process, even though the parton cross section for $gg \to t\bar{t}$ is about three times larger than for $q\bar{q} \to t\bar{t}$ near production threshold ($\sqrt{\hat{s}} \sim 2m_t$).

Higher-order corrections to the tree-level parton calculation are not negligible. Full next-to-leading order calculations for heavy quark pair production were published in the late eighties [22, 23]. The next-to-leading order corrections $\mathcal{O}(\alpha_s^3)$ were found to be on the order of 30%. The largest effects are due to diagrams with t-channel gluon propagators [22]. Corrections beyond $\mathcal{O}(\alpha_s^3)$ have since been calculated by several groups using soft gluon resummation techniques for initial state gluons [24, 25, 26]. The resulting theoretical predictions for the $t\bar{t}$ cross section are shown in Figure 1.2.

1.4 Top quark decay in the Standard Model

The Standard Model predicts that the top quark decays into a W boson plus a quark q via the weak force. Since $m_t > m_W + m_q$, the W is real. From unitarity constraints on the CKM matrix, which connects the weak eigenstates and the mass eigenstates for the quarks, one expects the CKM matrix element V_{tb} to be very close to unity, $V_{tb} \sim 1$, so that nearly 100% of

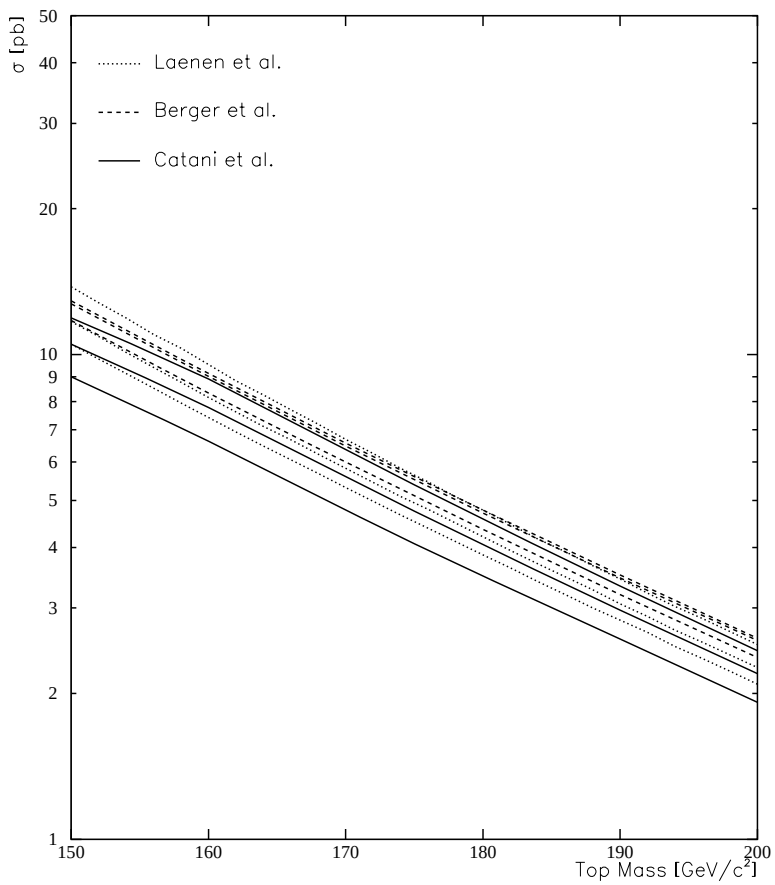

Figure 1.2: Theoretical predictions for the $t\bar{t}$ cross section in $p\bar{p}$ collisions at the Tevatron from NLO calculations that also employ soft gluon resummation for higher orders. In each set of 3 curves the middle curve represents the central values and the upper and lower curves the $\pm 1\sigma$ envelope.

top quarks decay to b quarks: $t \to Wb$. The other allowed decays $t \to Wd$ and $t \to Ws$ are expected to be suppressed at the levels $\frac{|V_{td}|^2}{|V_{tb}|^2} \approx 5 \cdot 10^{-4}$ and $\frac{|V_{ts}|^2}{|V_{tb}|^2} \approx 10^{-3}$, respectively [4]. The partial decay width for $t \to Wb$ [27] is:

$$, (t \to Wb) = \frac{G_F |V_{tb}|^2}{8\sqrt{2}\pi} \frac{m_W^2}{m_t^2} \left(\frac{(m_t^2 - m_b^2)^2}{m_W^2} + m_t^2 + m_b^2 - 2m_W^2 \right) \times 2k, \quad (1.3)$$

where

$$k = \frac{\sqrt{(m_t^2 - (m_W + m_b)^2)(m_t^2 - (m_W - m_b)^2)}}{2\ m_t} \quad (1.4)$$

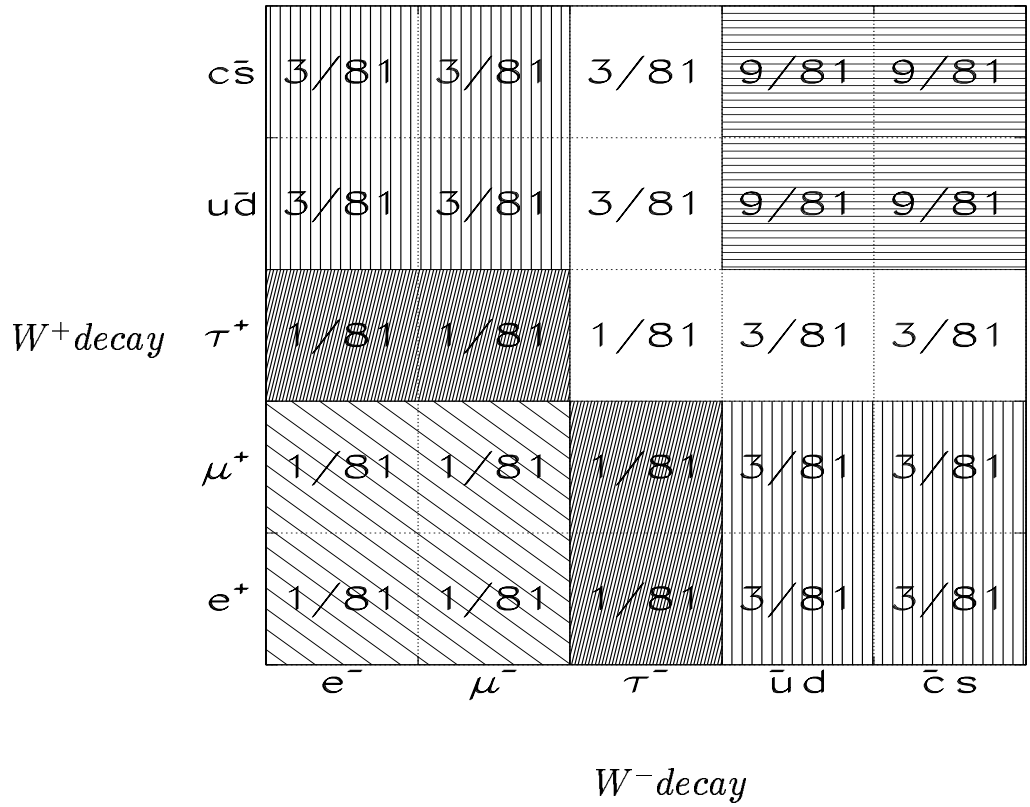

Figure 1.3: Matrix of $t\bar{t}$ final states in the Standard Model. We distinguish 5 final states: 'Standard dileptons' (diagonal hatch), 'Lepton + jets' (vertical hatch), 'All-Hadronic' (horizontal hatch), 'Tau dileptons' (dense hatch), and 'Tau + jets' (no hatch).

is the W momentum in the rest frame of the top quark. Using $V_{tb} = 1$, $m_W = 80.4$ GeV/c^2 and $m_t = 175$ GeV/c^2 one finds , $(t \to Wb) \equiv \frac{1}{\tau} \approx 1.55$ GeV. The top life-time is thus $\tau \approx 4 \times 10^{-25} s$.

Comparing this to the typical time scale $\Lambda_{QCD}^{-1} \sim \mathcal{O}((100\text{MeV})^{-1})$ $\sim \mathcal{O}(10^{-23} s)$ of quark hadronization, which is a non-perturbative process, the weak decay of the top is predicted to occur before hadronization starts. Effects due to hadronization would be expected to play a significant role only if the top quark mass were below 120 GeV [28].

The Standard Model picture then is that $t\bar{t}$ pairs are produced strongly

Channel	Signature	BR
Standard dilepton	$ee, \mu\mu, e\mu$ + 2 b jets	4/81
Tau dilepton	$e\tau, \mu\tau + 2\ b\ jets$	4/81
Lepton + jets	$e + jets, \mu + jets$ +2 b jets	24/81
Tau + jets	$\tau + jets$ + 2 b jets	12/81
All-Hadronic	$jets, jets$ + 2 b jets	36/81

Table 1.1: Branching ratios of final states for $t\bar{t}$ decay in the Standard Model. The number of jets actually detected may vary from this naive prediction due to effects such as initial state and final state gluon radiation, jet merging etc.

with the top and anti-top quark each subsequently decaying via the weak force into a real W and a b ($\bar{b}$) quark: $t\bar{t} \rightarrow (W^+b)(W^-\bar{b})$. Consequently, the observed final states are distinguished by the decay modes of the W's. If both W's decay leptonically the final state is an event that contains two leptons, i.e. a dilepton event. If one W decays leptonically and the other one hadronically, we have a final state with one lepton plus jets. Finally, if both W's decay hadronically the final state contains only jets, refered to as the 'all hadronic' final state.

We estimate the branching ratios for the different final states: The partial decay width of the W into fermion pairs is given to lowest-order by $,_0(W \rightarrow ff') = |V_{ff'}|^2 N_c \frac{G_F m_W^3}{6\sqrt{2}\pi}$, where the color factor N_c equals 3 for quarks and 1 for leptons. The CKM element $|V_{ff'}| = 1$ for leptons. For the dominating quark decays $W^+ \rightarrow u\bar{d}$, $W^+ \rightarrow c\bar{s}$ we also have $|V_{ff'}| \approx 1$ [4], so that $,_0(W \rightarrow ff') \approx C \cdot N_c$ with a common constant C for all fermion pairs. Since there are 9 different fermion pairs available for W decays – taking color into account – the branching ratio $,_0(W \rightarrow ff')/,_0(W \rightarrow all)$ is $\approx 1/9$ for all leptonic decay modes and $\approx 3/9$ for each of $W^+ \rightarrow u\bar{d}$, $W^+ \rightarrow c\bar{s}$. The branching ratios for the different final states of $t\bar{t} \rightarrow (W^+b)(W^-\bar{b})$ can be easily read off of Figure 1.3 in which we plot all possible combinations of W^+ decay

modes and W^- decay modes including their branching ratios. In Table 1.1 we list the branching ratios for the different final states. As noted above, the BR of 4/81 for tau dilepton events ($e\tau, \mu\tau$) is the same as for the sum of $ee, \mu\mu$, and $e\mu$ dilepton events.

1.5 Overview of the CDF detector

The data used in this analysis were collected during CDF's third (Run Ia) and fourth (Run Ib) major physics runs. In Run Ia, which took place in 1992-1993, 19.6 pb^{-1} of data were collected. During the 1993 summer shut down the Fermilab Linac system was upgraded. The resulting lower emittances in the transfer of protons allowed the instantaneous luminosity to be increased substantially and CDF was able to collect about 90 pb^{-1} of data during the Run Ib period 1994-1995.

Detailed descriptions of the CDF detector can be found in various places. The best source of information for most of the detector hardware except for the silicon vertex detectors is a series of NIM articles collected in the CDF 'Blue Book' [29]. The original silicon vertex detector was replaced after Run Ia with a radiation-hard version. These detectors are described in Refs. [30, 31]. Instead of repeating this descriptive information, we describe the detector only briefly and focus on some aspects of the detector performance in Run I.

Figure 1.4 schematically depicts a quadrant of the central detector with the components most relevant to the dilepton analysis. These are (i) a 4-layer barrel silicon microstrip detector (SVX), located immediately outside the beampipe, providing precise track reconstruction to identify secondary vertices from b and c quark decays, (ii) a central drift chamber (CTC), immersed in

Figure 1.4: Schematic drawing of one quadrant of the CDF central detector. The projective tower geometry of the calorimeters is indicated. Note that the forward calorimeters are actually located further upstream and downstream than shown here. CES stands for Central Electromagnetic Shower-maximum detector and CPR for Central Pre-Radiator.

a 1.4 T solenoidal magnetic field, used for tracking charged particles in the pseudorapidity [32] range $|\eta| < 1.1$, (iii) electromagnetic (CEM, PEM, FEM) and hadronic calorimeters (CHA, WHA, PHA, FHA) covering the range $|\eta| < 4.2$ and arranged in a projective tower geometry for identifying electrons and jets, (iv) strip chambers (CES) embedded in the electromagnetic calorimeter at approximately shower maximum for detailed shower sampling, and (v) drift

chambers (CMU, CMP, CMX) outside the calorimeters in the region $|\eta| < 1.0$ for muon identification. The calorimeters also measure the missing transverse energy $\not\!\!E_T$, which can indicate the presence of undetected energetic neutrinos. A three-level trigger selects the inclusive electron and muon events used in the dilepton analysis.

1.6 Calorimetry

1.6.1 Fiducial CEM coverage

The electromagnetic (CEM) and hadronic (CHA, WHA) calorimeters in the central region cover the pseudorapidity range $-1.1 < \eta_{det} < 1.1$, corresponding to the polar angle range $143^\circ < \theta < 37^\circ$. The central calorimeter consists of 2 barrels (one for the positive and one for negative η range) with 24 wedges each, so that one wedge covers 15° in azimuthal angle ϕ. Each CEM wedge consists of 10 projective towers (numbered 0-9 with increasing $|\eta|$). Due to its geometry, CEM tower 9 is not a full size tower and is not used for electrons in the dilepton analysis, which reduces the fiducial η range for electrons to $|\eta_{det}| < 1.0$. The determination if an electron is fiducial is based on the shower position in the CEM as measured by the CES chambers. These proportional chambers have wires parallel to the z-axis providing a ϕ sampling of an electromagnetic shower. The strips perpendicular to the wires sample the shower along the z-axis.

Figures 1.5 and 1.6 show the position measured in the CES for all fiducial central electron candidates in the inclusive electron sample that pass the tight selection cuts (see section 2.1.2) for Run Ia and Run Ib. The fiducial coverage of every single wedge can be seen clearly. The region $-0.05 < \eta < 0.05$,

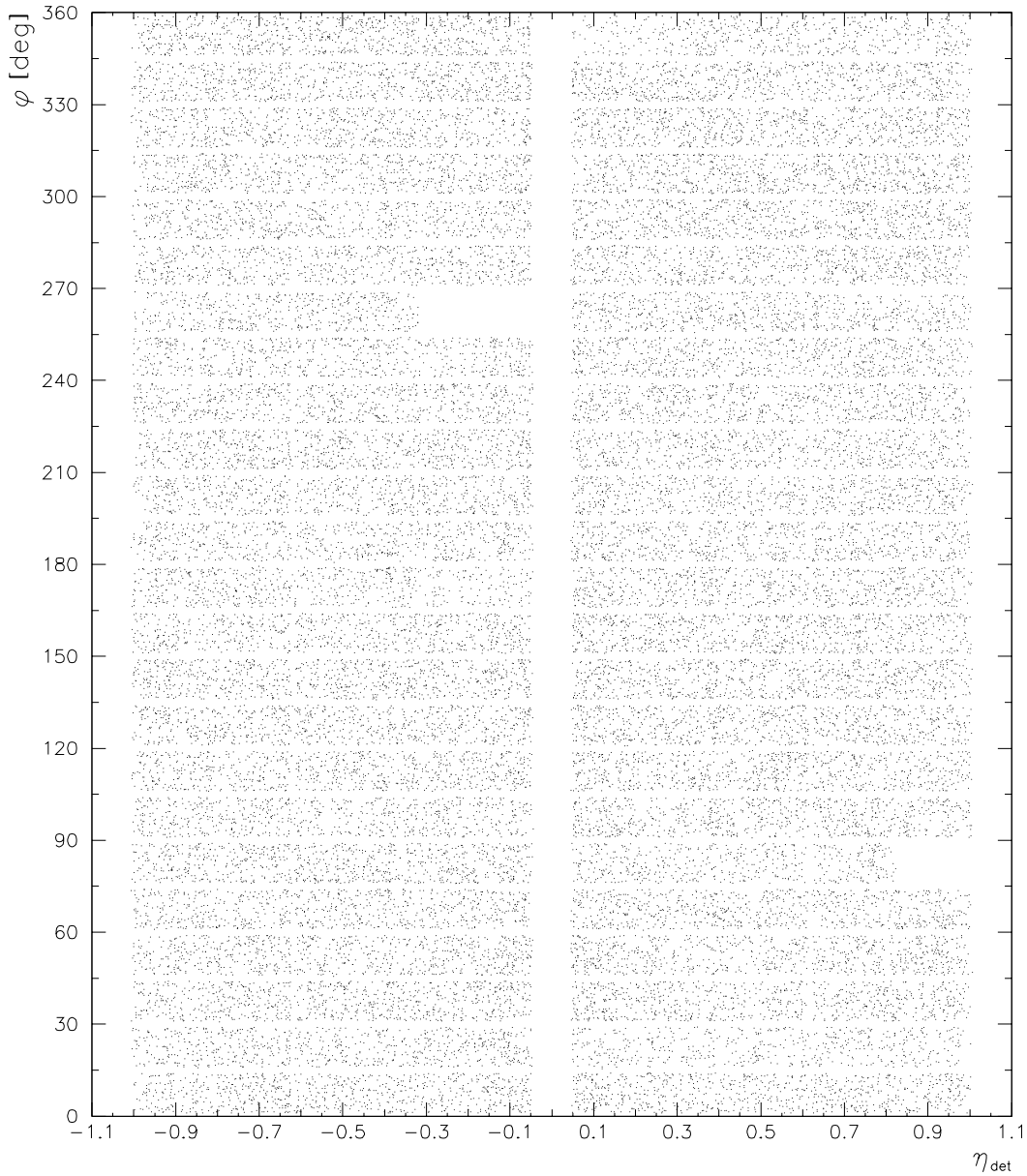

Figure 1.5: Position of fiducial tight central electrons in the Run Ia inclusive central electron sample as measured by the CES.

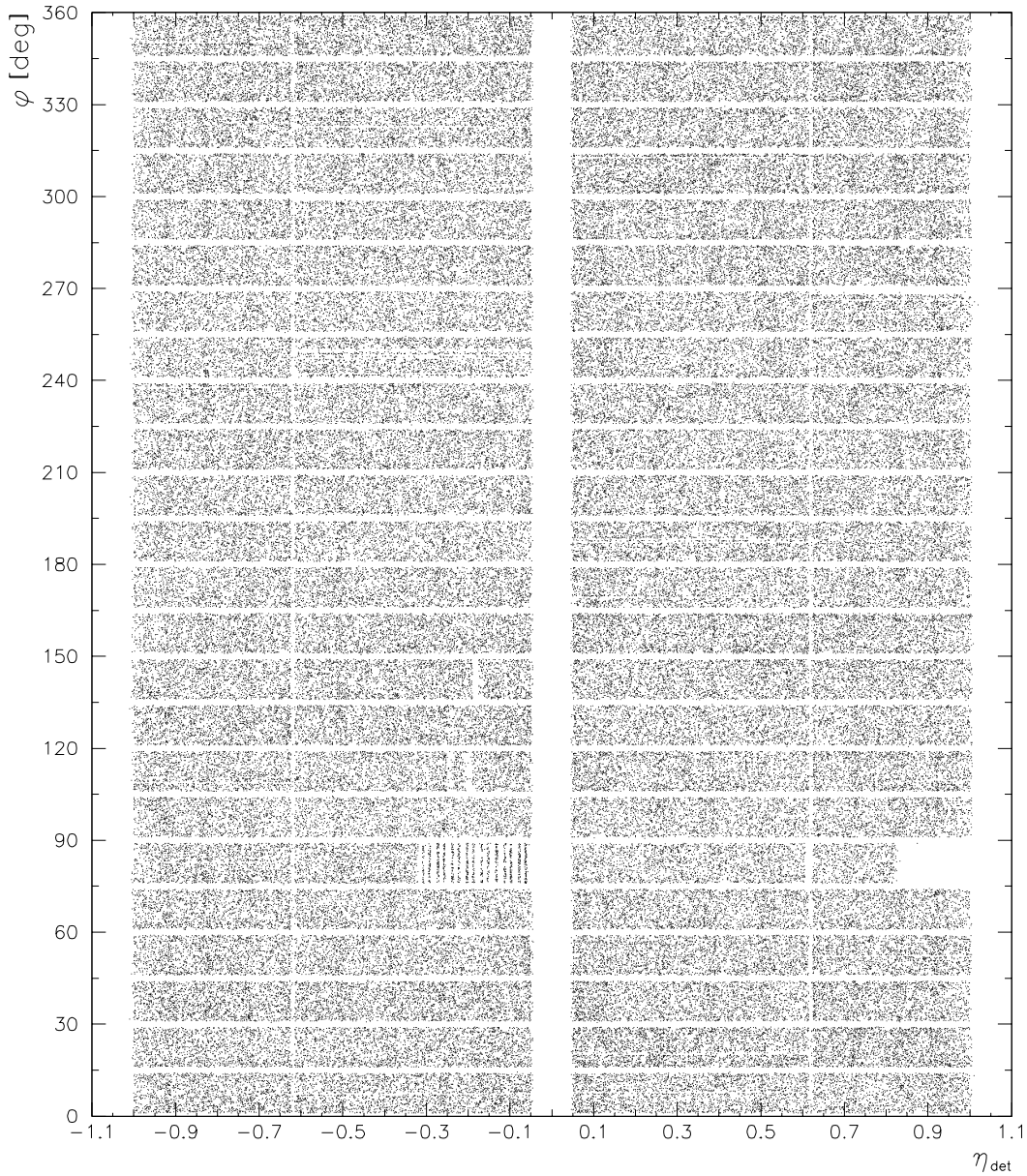

Figure 1.6: Position of fiducial tight central electrons in the Run Ib inclusive central electron sample as measured by the CES.

i.e. 5% of the total coverage, near the 90° crack where the detector halves meet, is explicitly cut out as the chambers are not fully efficient near the edge. For the same reason showers with a distance $< 1°$ from the nominal ϕ boundary between wedges are explicitly removed. This is done by requiring that the CES wire cluster closest to the extrapolated electron track be located < 21 cm from the center of the strip chamber in the $r - \phi$ plane [33]. The resulting loss in acceptance is $24 \cdot 2°/360° = 13.3\%$. The region $0.82 < \eta < 1.0$, $75° < \phi < 90°$ is explicitly excluded as it is uninstrumented. This is the access port ('chimney') for the cryogenic supply of the superconduction coil. The loss in acceptance here is 0.4%. The total acceptance loss due to explicit fiducial requirements is 18.7% of the purely geometric acceptance.

In general, the detector coverage appears quite uniform. However, various detector inefficiencies can be seen in Figures 1.5 and 1.6. The wires are split in a wedge at $\eta = \pm 0.62$ which gives rise to a small region of ≈ 0.01 units in η without gas gain, corresponding to a 1% acceptance loss. In Run Ia the strip chamber region $-0.275 < \eta < 0$, $255° < \phi < 270°$ had a readout problem; likewise the chamber at $-0.325 < \eta < 0$, $75° < \phi < 90°$ during Run Ib. We estimate the acceptance loss due to these effects to be on the order of 0.7%. Furthermore, there are several very small regions visible with single wire or strip inefficiencies.

1.6.2 CEM energy resolution

The energy resolution of the CEM for the high-p_T electrons used in the top analysis can be measured from $Z \to ee$ decays. LEP has measured the decay width of the Z to be 2.490 ± 0.007 GeV [4]. Figure 1.7 shows the invariant mass of central-central dielectrons in the mass range 50 – 120

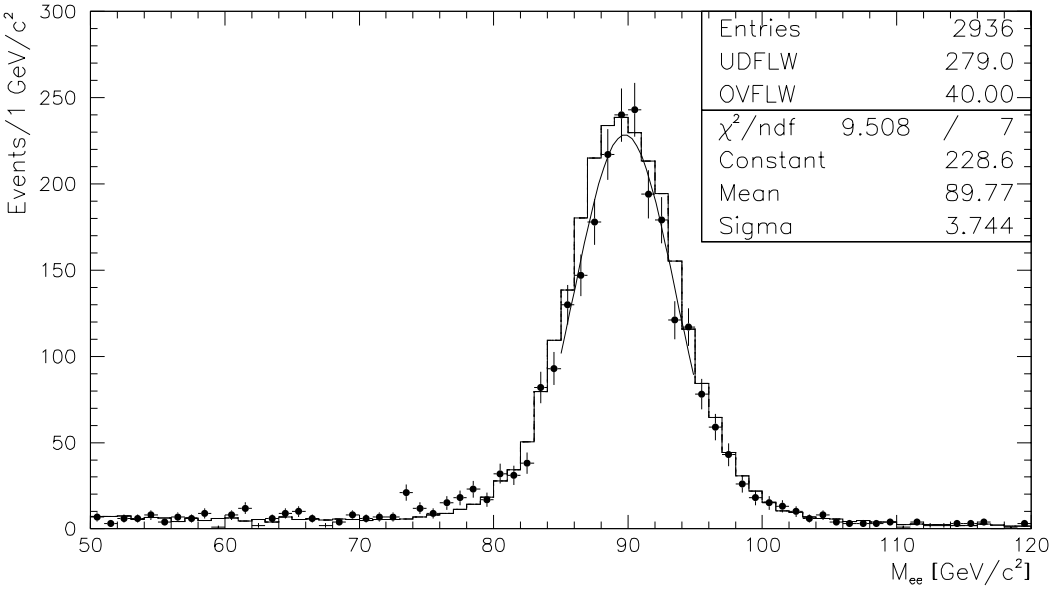

Figure 1.7: Dielectron mass of $Z/\gamma \rightarrow ee$ events. For the data (points) masses are calculated using *raw* electron energies, i.e. the calibration to flatten out the CEM response is *not* applied. This is compared with a Monte Carlo template (histogram) generated using a CEM resolution $\Delta E/E = 13.5\%/\sqrt{E[\mathrm{GeV}]} \oplus 5.0\%$. Also shown is a Gaussian fit to the data.

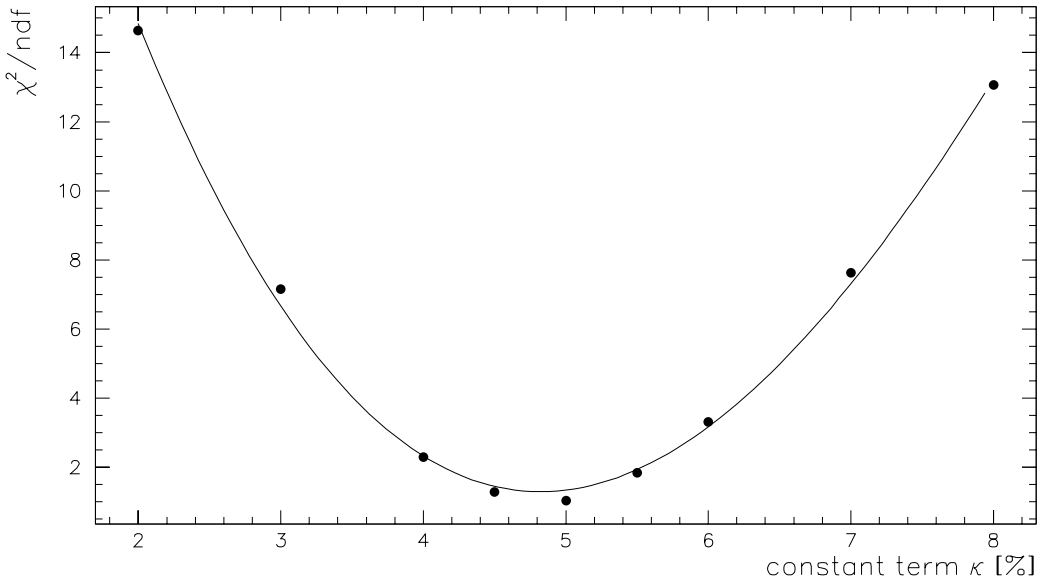

Figure 1.8: Cubic fit of the χ^2 obtained from comparing $Z/\gamma \rightarrow ee$ data using *uncorrected* electron energies in the peak region 80-100 GeV/c^2 to Monte Carlo templates with different constant terms κ for the energy resolution $\Delta E/E = 13.5\%/\sqrt{E[\mathrm{GeV}]} \oplus \kappa$ %. The fit returns $\kappa = (4.8 \pm 0.9)\%$.

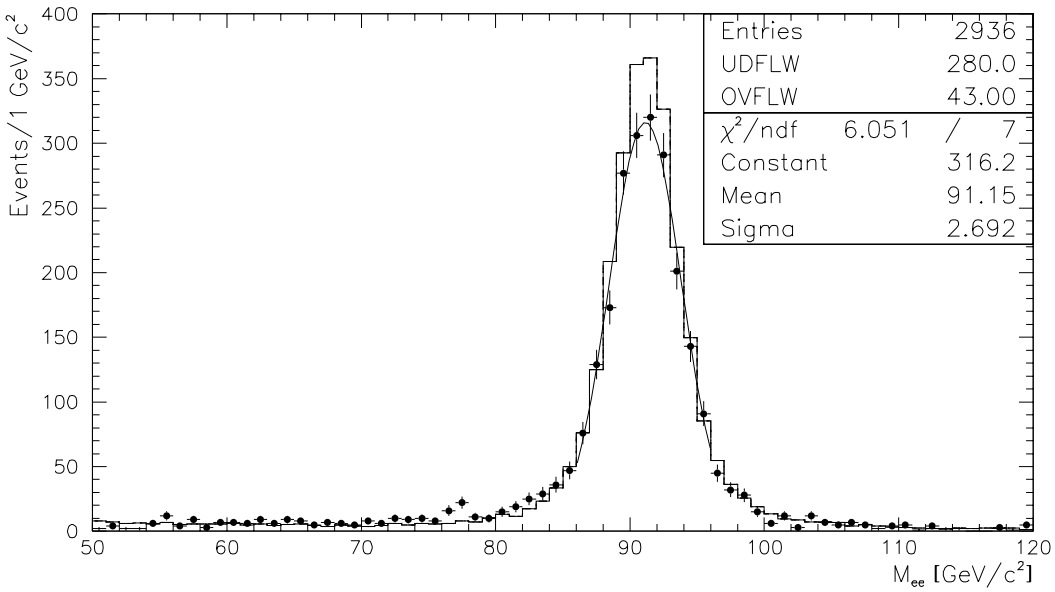

Figure 1.9: Dielectron mass of $Z/\gamma \rightarrow ee$ events. For the data (points) masses are calculated using *corrected* electron energies, i.e. the calibration to flatten out the CEM response is applied. This is compared with a Monte Carlo template (histogram) generated using a CEM resolution $\Delta E/E = 13.5\%/\sqrt{E[\mathrm{GeV}]} \oplus 2.0\%$. Also shown is a Gaussian fit to the data.

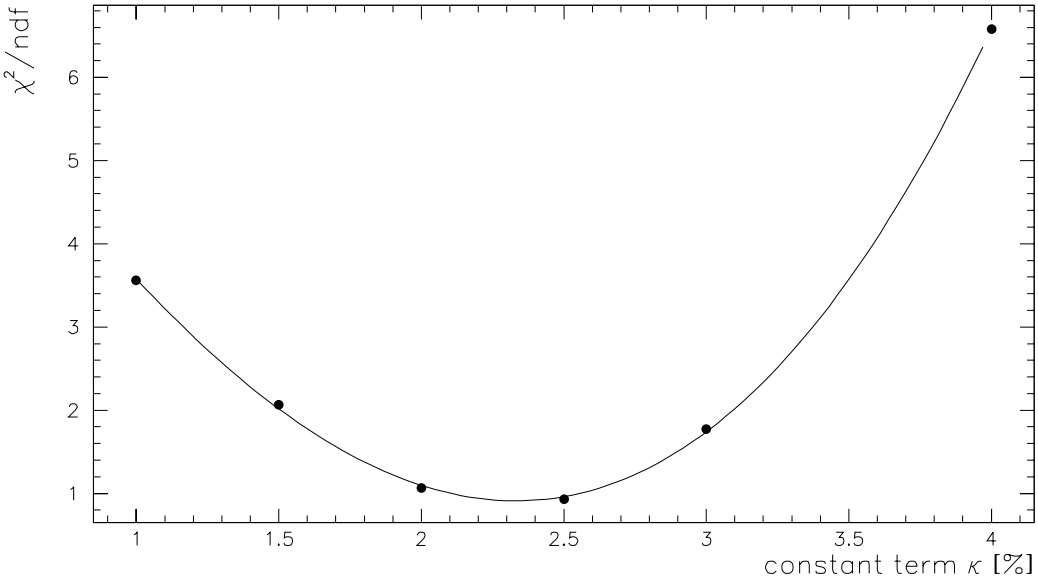

Figure 1.10: Cubic fit of the χ^2 obtained from comparing $Z/\gamma \rightarrow ee$ data using *corrected* electron energies in the peak region 80-100 GeV/c^2 to Monte Carlo templates with different constant terms κ for the energy resolution $\Delta E/E = 13.5\%/\sqrt{E[\mathrm{GeV}]} \oplus \kappa\ \%$. The fit returns $\kappa = (2.3 \pm 0.8)\%$.

GeV/c^2. Here both electrons are required to be fiducial and pass the tight electron identification cuts (see section 2.1.2) of the top dilepton analysis. The mass is calculated from the raw electron energies which are used in the dilepton analysis for the cut on electron E_T. No calibration is done to increase the uniformity of the calorimeter response. The peak width is larger than 2.5 GeV due to radiative decays $Z \to ee\gamma$ and, more importantly, the finite energy resolution of the calorimeter. This measured width provides a measure of the resolution.

From test beam measurements the irreducible statistical resolution due to sampling fluctuations in this lead–scintillator sandwich calorimeter is known to behave as $(\Delta E/E)_{stat} = 13.5\%/\sqrt{E[\mathrm{GeV}]}$ [34]. Non-uniformities make energy-independent contributions that are parameterized by a constant term κ added in quadrature to the statistical term. The total resolution is given by

$$\Delta E/E = 13.5\%/\sqrt{E[\mathrm{GeV}]} \oplus \kappa\%. \tag{1.5}$$

To measure the constant term we compare the data to Monte Carlo templates made with different values of resolution. We have generated $Z/\gamma \to ee$ decays with the PYTHIA [35] Monte Carlo, smeared the resulting electron energies according to the resolution, and calculated the dielectron mass. Templates with various constant terms κ are compared to the data by calculating the χ^2's in the peak region 80-100 GeV/c^2. In Figure 1.8 we plot the reduced χ^2 as a function of κ. Using a third-order polynomial, we find that the χ^2 is minimized for $\kappa = 4.8 \pm 0.9$. The uncertainty is calculated from the value for κ where the reduced χ^2 increases by one unit.

The constant term can be reduced by calibrating the CEM. The calibration comprises corrections as a function of the shower position in local

System	η range	Energy resolution
CHA	$\lvert\eta\rvert < 0.9$	$50\%/\sqrt{E} \oplus 3\%$
WHA	$0.7 < \lvert\eta\rvert < 1.3$	$75\%/\sqrt{E} \oplus 4\%$
PHA	$1.3 < \lvert\eta\rvert < 2.4$	$106\%/\sqrt{E} \oplus 6\%$
FHA	$2.4 < \lvert\eta\rvert < 4.2$	$137\%/\sqrt{E} \oplus 3\%$

Table 1.2: Coverage and energy resolution of hadronic calorimeters from test-beam measurements for incident isolated pions[16].

tower coordinates, corrections to account for tower-to-tower variations and time-dependence, and global energy scale corrections [36]. As Figure 1.9 shows the Z peak is significantly sharper after the calibrations are applied. Using the same fitting method as above we now find for the constant term $\kappa = 2.3 \pm 0.8\%$.

1.6.3 Jets

The hadronic calorimeters of CDF measure energies of jets up to a pseudorapidity $\eta = \pm 4.2$. The resolution for incident pions was measured in test beams after construction; the results are shown in Table 1.2. The top dilepton analysis uses only jets in the more central region $|\eta| < 2.0$.

The energy resolution also has been measured for jets *in situ* by balancing dijet events. The total transverse momentum of the initial $p\overline{p}$ system is zero. An imbalance in E_T between two jets in a dijet event can be due to two effects: One effect is recoil against initial state radiation which will give the dijet system transverse momentum. The recoil jet might actually be lost giving rise to missing transverse energy. The other effect is the finite resolution in the E_T measurement of the two jets. The jet energy resolution can be measured in dijets from the projection of the missing transverse energy along the direction of the jet to be tested. This method takes radiation effects and unclustered energy outside of jets into account [37]. At least one of the jets must be in the

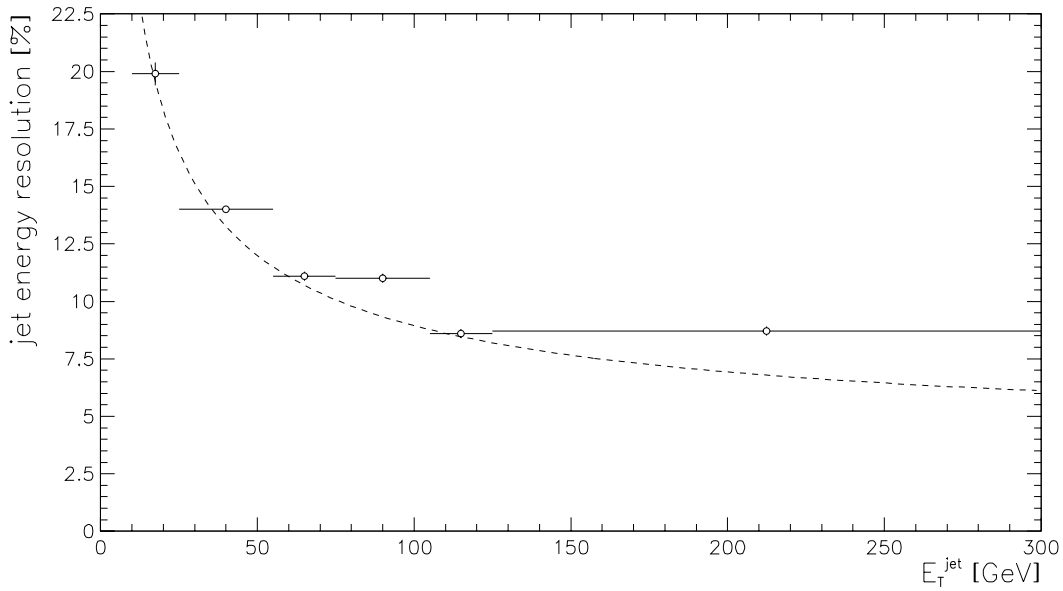

Figure 1.11: Jet energy resolution as a function of jet E_T for central jets with $0.2 < |\eta_{jet}| < 0.8$ measured from dijet balancing. For comparison a parameterization of the CHA resolution $\Delta E_T^{jet}/E_T^{jet} = 80\%/(E_T[GeV])^{1/2} \oplus 4\%$ is shown. Note that this is not a fit.

region $0.2 < |\eta_{jet}| < 0.8$. These central jets are well away from the boundaries between different calorimeters components and thus provide the best energy measurement for jets available at CDF.

The result of this measurement for central jets with $0.2 < |\eta_{jet}| < 0.8$ is shown in Figure 1.11. As expected the resolution for jets is not as good as for isolated pions. A reasonable parameterization of the CHA for jets with $E_T < 125$ GeV is given by $\Delta E_T^{jet}/E_T^{jet} = 80\%/\sqrt{E_T[\mathrm{GeV}]} \oplus 4\%$.

At the boundary between the two detector halves, $-0.1 < \eta < 0.1$, and at the boundary between central and plug detector, $0.95 < |\eta| < 1.25$, where particles get lost in the gaps, the resolution for jets above 25 GeV is found to be $(15 \pm 2)\%$, independent of E_T .

1.6.4 Missing transverse energy

The missing transverse energy $\not\!\!E_T$ is useful for inferring the presence of particles that escape direct detection, such as neutrinos. It is defined as the negative of the vector sum of transverse energy in all calorimeter towers with $|\eta| < 3.6$ [32]. The η range is restricted because the final focusing magnets of the Tevatron obscure part of the forward hadron calorimeter. To be included in the sum, the individual tower energies E (not E_T) must exceed thresholds of 100 MeV in the CEM, CHA, and WHA, 300 MeV in the PEM, 500 MeV in the PHA and FEM, and 800 MeV in the FHA.

Ideally, the measured transverse momentum would exactly balance in events where all particles produced are detected and absorbed in the calorimeters, and $\not\!\!E_T$ would vanish. Due to energy flow through gaps in the detector, limited η coverage of the calorimeter, and finite resolution of the energy measurement, there is also a finite resolution on the $\not\!\!E_T$ measurement. We can measure this resolution for dilepton events using $Z \rightarrow ee$ and $Z \rightarrow \mu\mu$ events. The leptons are required to pass the identification cuts used in this analysis and to form a mass 75 GeV/c^2 $< M_{\ell\ell} <$ 105 GeV/c^2. Events containing jets with $E_T > 10$ GeV are excluded and all hadronic energy deposition is required to be in time with the hard scattering ($E_T^{out-of-time} = 0$). For $Z \rightarrow \mu\mu$ events the vector sum of the calorimeter E_T is corrected by vectorially subtracting the energy deposited by the muon and adding the p_T of the muon as measured by the CTC. In Figure 1.12 we plot the x- and y components of $\not\!\!E_T$ in the selected events. The data fit well to Gaussians centered at zero with widths $\sigma \approx 5$ GeV, which is a measure of the average $\not\!\!E_T$ resolution.

Figure 1.13 shows that the $\not\!\!E_T$ resolution degrades as the scalar sum of transverse tower energies, $\sum E_T$, increases. For $Z \rightarrow ee$ events the E_T's

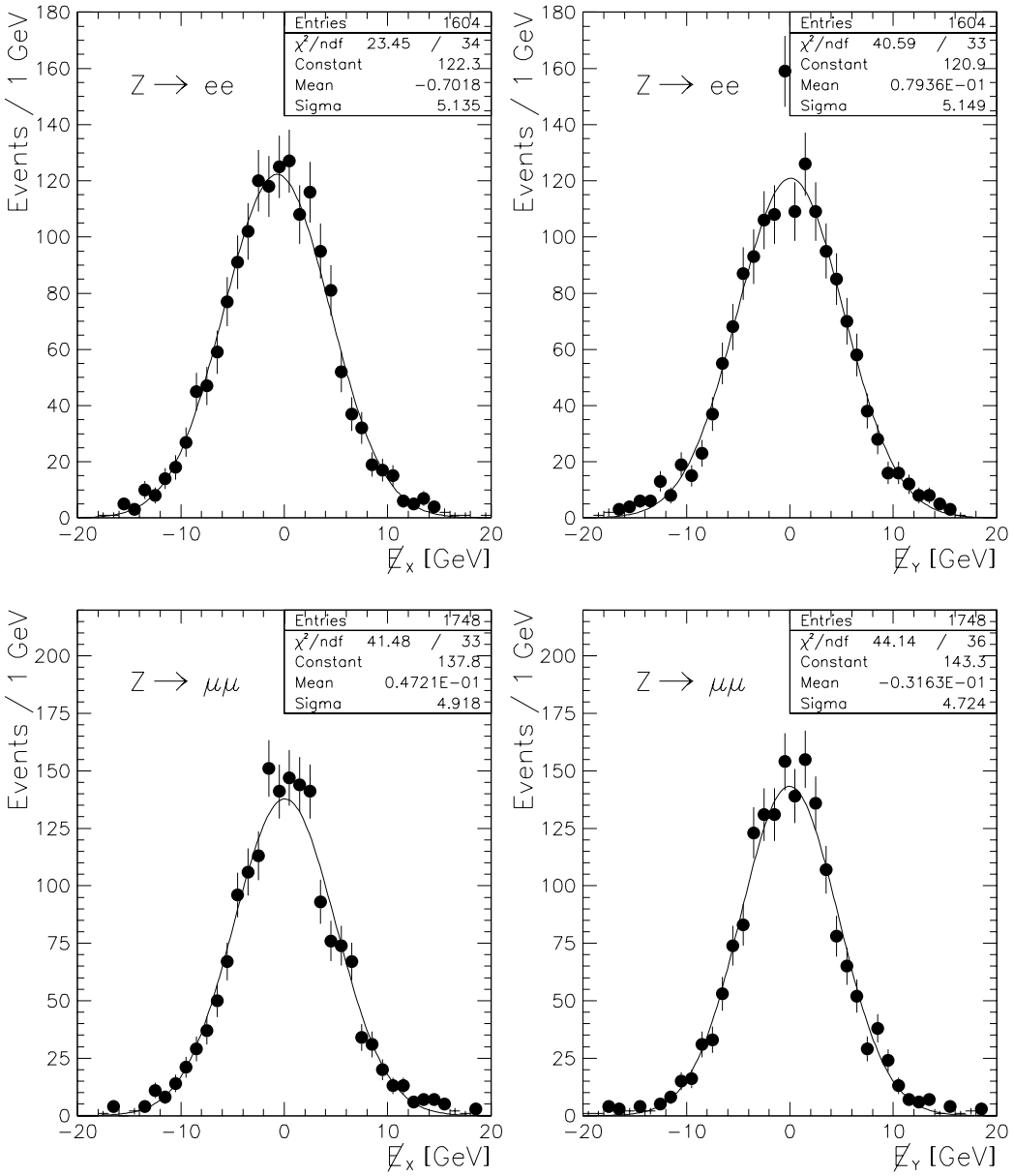

Figure 1.12: Components of $\not\!\!E_T$ in $Z \to ee$ and $Z \to \mu\mu$ events.

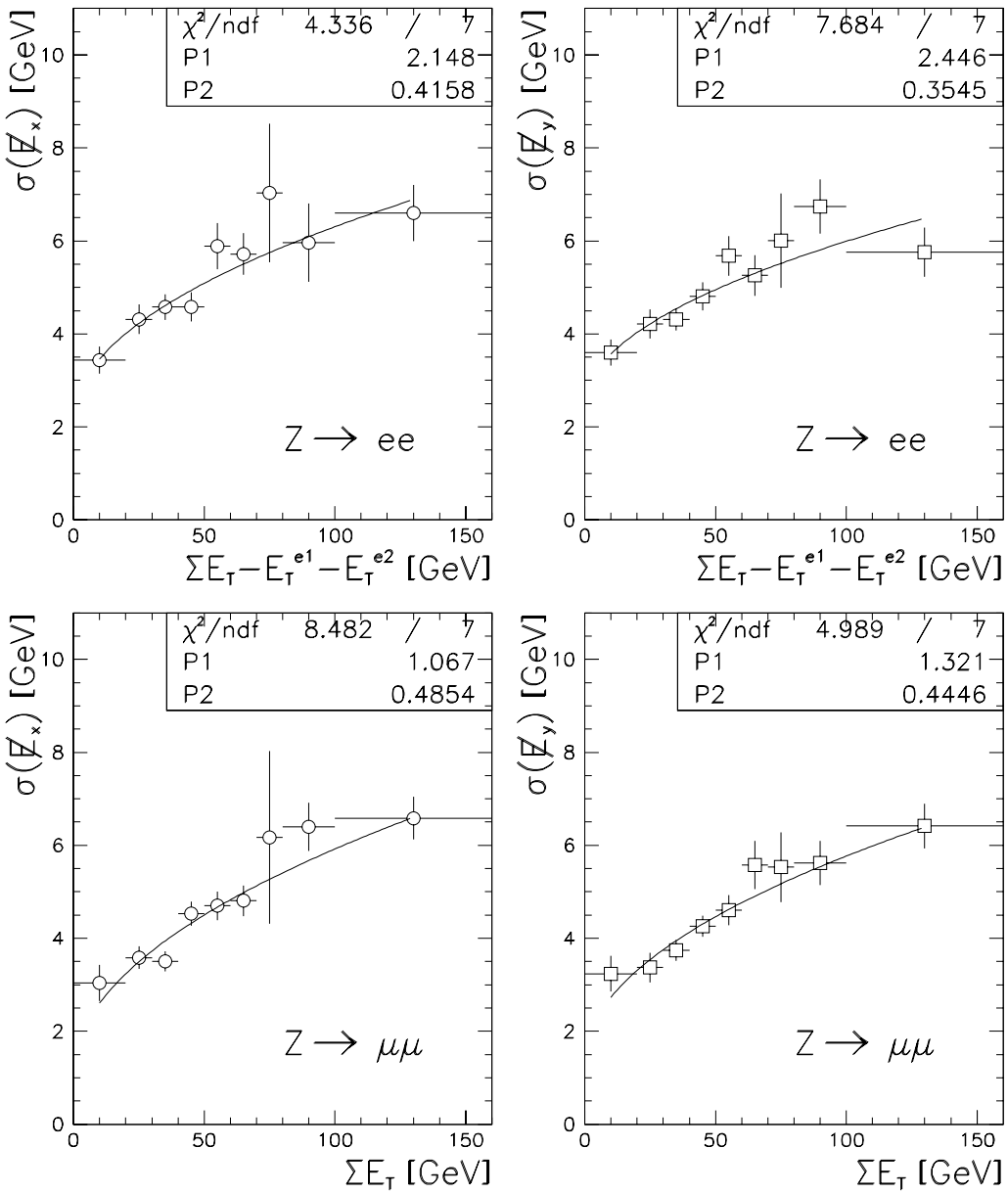

Figure 1.13: Resolution of $\not{E}_T$ components vs $\sum E_T$ for $Z \to ee$ and $Z \to \mu\mu$ events. The $\not{E}_T$ data are placed in bins of $\sum E_T$; $\not{E}_T^x$ and $\not{E}_T^y$ are fitted to Gaussians for each bin and the resulting σ's plotted vs $\sum E_T$. The curves are fits to the functional form $\sigma = P_1 + P_2 \cdot \sqrt{\sum E_T}$.

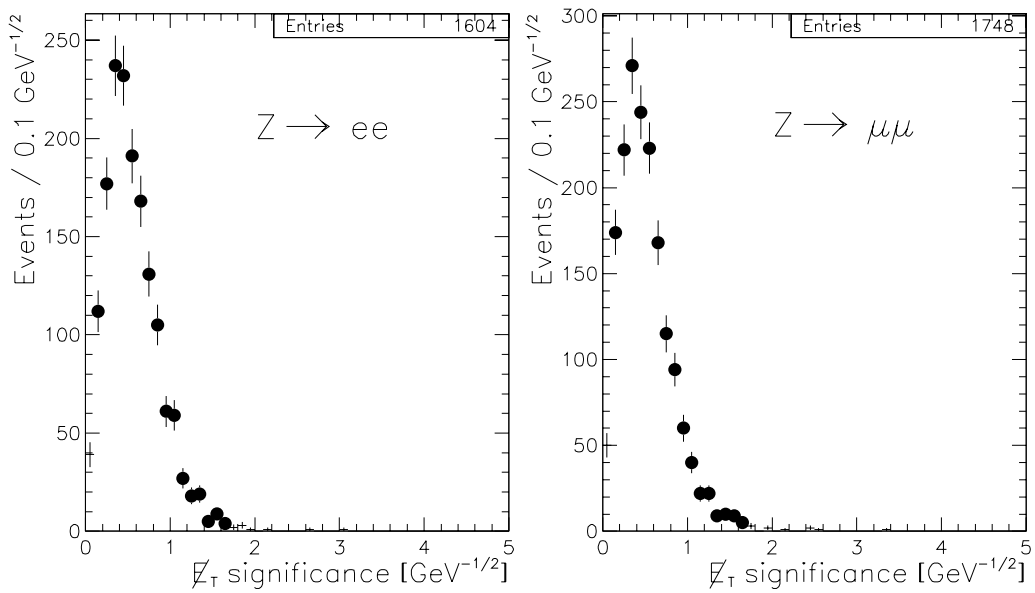

Figure 1.14: The $\not{E}_T$ significance $S_{\not{E}_T}$, as defined in the tau dilepton analysis (chapter 3), for Z events.

of the two electrons have been subtracted from $\sum E_T$. The increase can be described by a square root function, which indicates that the $\not{E}_T$ is due to statistical fluctuations in the overall energy measurement. Consequently, a figure of merit for the momentum imbalance in an event is the '$\not{E}_T$ signifcance' $S_{\not{E}_T} \equiv \not{E}_T/\sqrt{\sum E_T}$. It roughly gives the number of standard deviations that the $\not{E}_T$ is away from zero. Figure 1.14 shows $S_{\not{E}_T}$ for Z events as defined in the tau dilepton analysis. Here the full $\sqrt{\sum E_T}$ is used for $Z \to ee$ events; for $Z \to \mu\mu$ events the p_T of each of the two muons have been added to the $\sum E_T$ for consistency with the electron case. There are only 2 out of 3350 Z events with $S_{\not{E}_T} > 3$ GeV$^{1/2}$.

1.7 B-tagging

Figure 1.15 shows the impact parameter d with respect to the primary vertex of the interaction for electron tracks in the SVX in $Z \to ee$ events.

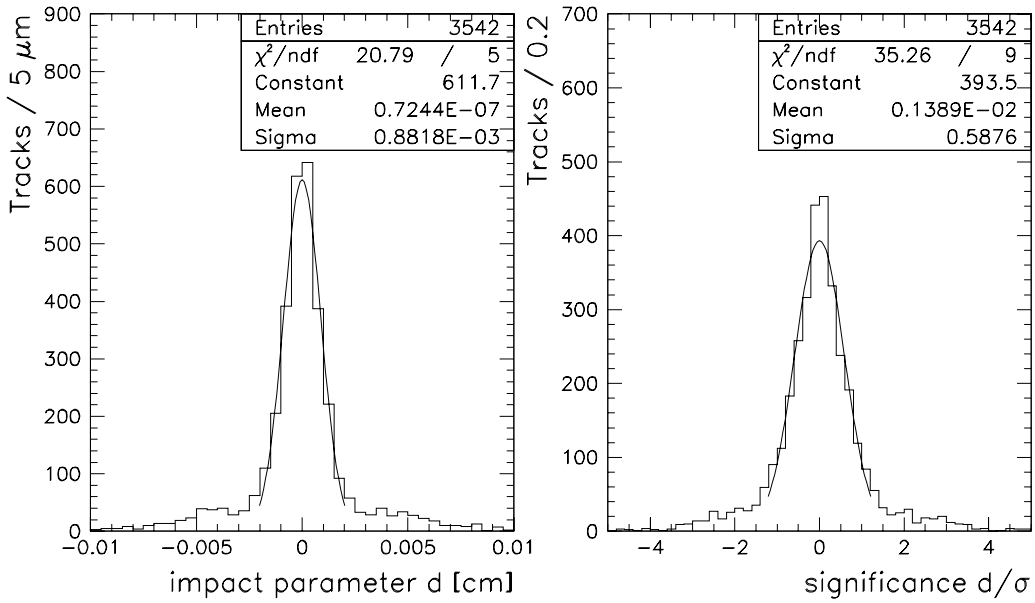

Figure 1.15: Impact parameter with respect to the primary interaction vertex and the impact parameter significance for electron tracks in the SVX using $Z \rightarrow ee$ events.

At the CDF interaction region, primary vertices have a Gaussian distribution along the beam direction with $\sigma \approx 30$ cm and transverse to the beam axis with a $\sigma \approx 40$ μm. The primary vertex is found for each event by a weighted fit of the SVX tracks and the VTX z-vertex position of the event, with appropriate corrections for detector offset and slope. The sign of d is given by the location of the beam in the transverse plane relative to the circle that describes the track trajectory in the transverse plane. For positively charged tracks, the CDF convention is to assign a negative sign to d when the location of the beam lies outside of the circle, and a positive sign when it is outside. This convention is reversed for negatively charged tracks. Also shown in the figure is the significance of the impact parameter d/σ_d. The uncertainty σ_d on d is computed for each track from the measured momentum and multiple scattering based on the traversed material. The core of the d distribution can be fitted to a Gaussian giving an average resolution of $\approx 9\mu m$. The core of the d/σ_d

distribution can be described by a Gaussian with width $\sigma = 0.6$. This is to be compared with Monte Carlo simulations which show that $\approx 30\%$ of tracks from b decays in $t\bar{t}$ events have $d/\sigma_d > 3$ [16].

The acceptance and efficiency for tagging b quark decays in $t\bar{t}$ events have been studied extensively for the top discovery [16, 17, 38]. A Monte Carlo study of $t\bar{t}$ events ($m_{top} = 170$ GeV/c^2) using a detailed simulation of the SVX detector gives the following results: A b-jet that falls within the SVX fiducial volume and passes the track requirements for the SVX tagging algorithm ('SECVTX') is called a 'taggable' jet. The algorithm searches for either three SVX tracks passing loose requirements or for two SVX tracks passing more stringent requirements. Of all $t\bar{t}$ events that pass the lepton + jets selection (≥ 3 jets with $E_T > 15$ GeV and $|\eta| < 2.0$) $30.2 \pm 0.7\%$ have exactly one taggable b-jet, while $34.1 \pm 0.7\%$ have two taggable b-jets [38]. Consequently, $64.3 \pm 1.0\%$ of all such events have at least one taggable b-jet. The efficiency of the SVX tagging algorithm for successfully tagging a taggable jet is $55 \pm 4\%$. Combining this efficiency with the acceptance gives a total efficiency of $43 \pm 4\%$ for tagging at least one b-jet in a $t\bar{t}$ event.

1.8 Muon Chambers

1.8.1 Detector Coverage

The central muon system consists of three separate sets of muon chambers. Located behind every one of the 48 wedges of the central barrel calorimeter is a four-layer Central Muon (CMU) drift chamber, covering the region $|\eta| < 0.6$. These chambers detect particles emerging from the CHA.

The Central Muon Upgrade (CMP) system consists of four layers of

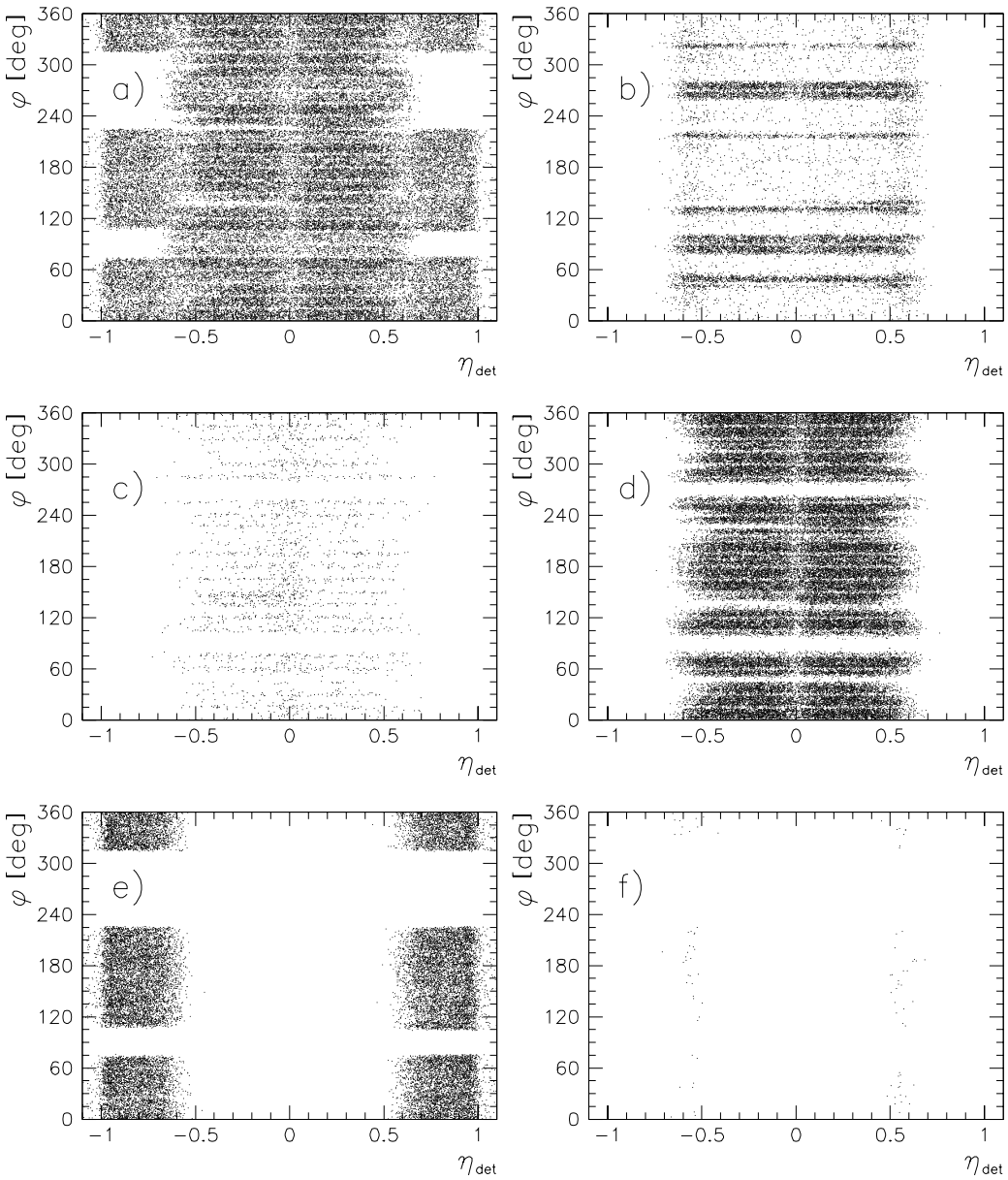

Figure 1.16: Position of isolated, tight central muons in the Run Ib inclusive central muon sample as measured from the muon track. a) All muons, b) CMU only, c) CMP only, d) CMU-CMP, e) CMX only, f) CMU-CMX.

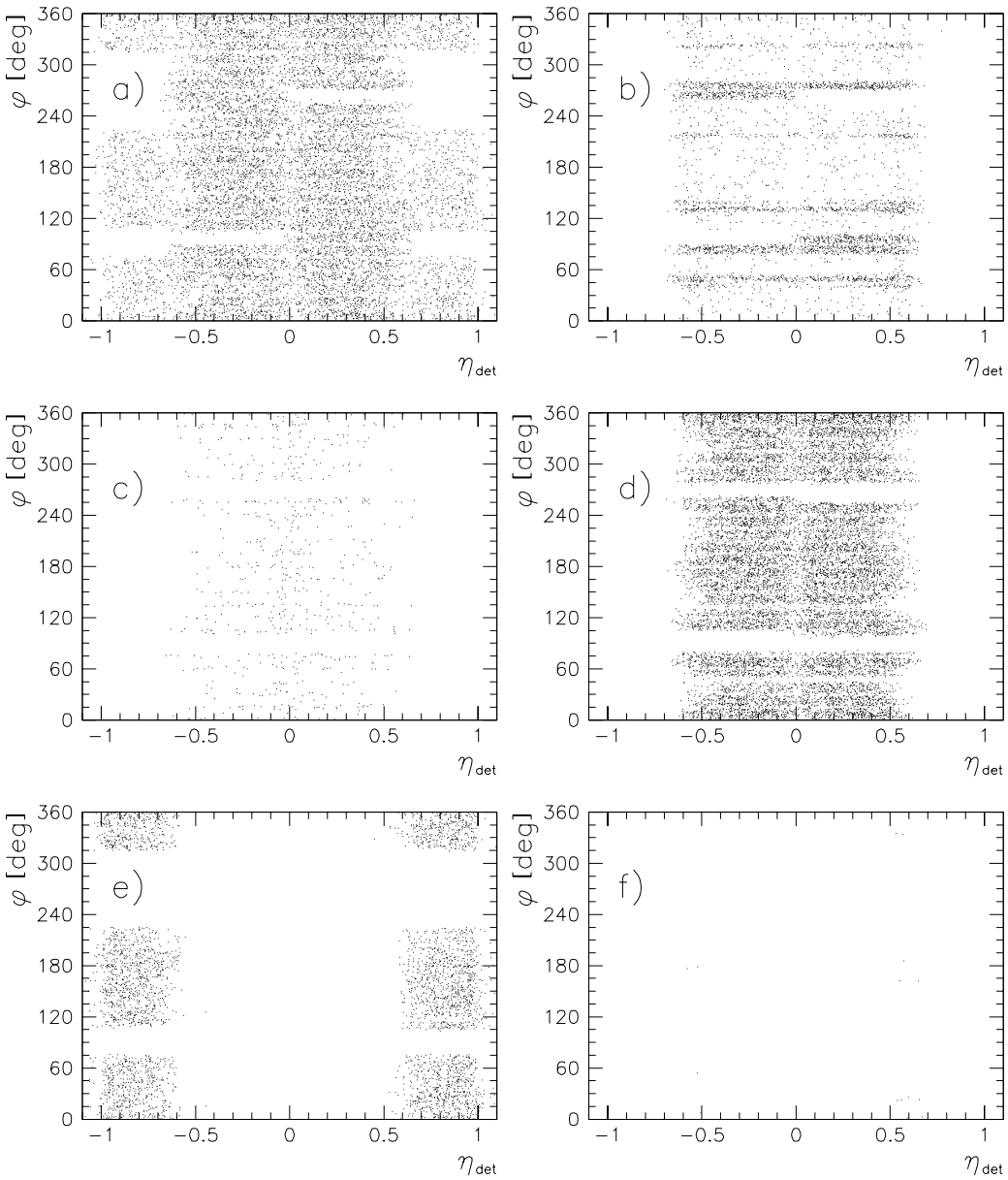

Figure 1.17: Position of isolated, tight central muons in the Run Ia inclusive central muon sample as measured from the muon track. a) All muons, b) CMU only, c) CMP only, d) CMU-CMP, e) CMX only, f) CMU-CMX.

drift chambers that are placed behind the yoke or walls of 0.6 m of uninstrumented steel shielding in the region $|\eta| < 0.6$. The areas above (near 90°) and below (near 270°) the detector are not completely covered due to space limitations.

The Central Muon Extension (CMX) system extends the central muon coverage to the region $0.6 < |\eta| < 1.0$ for azimuthal angles satisfying $315 < \phi < 75$ and $105 < \phi < 225$. It also consists of four layers of drift chambers.

Figure 1.16a shows the position in $\eta - \phi$ space of all isolated central muon candidates in the Run Ib inclusive muon sample that pass the CMUO identification cuts (see section 2.1.2) for the top dilepton analysis. There are about 54,000 events in this sample. The ϕ and η are determined from the muon track. We observe a reasonably uniform coverage of the central region for muons.

Figures 1.16b-f give a breakdown by muon detector system. The dense bands in the plot of 'CMU only' muons (Fig. 1.16b) indicate the gaps in the coverage of the CMP at the top and bottom of the detector and also at the corners where the yoke and shielding walls meet. Likewise the bands in the 'CMP only' plot (Fig. 1.16c) are due to the gaps between calorimeter wedges. About 82% of the muon candidates in the region $|\eta| < 0.6$, or 60% of all muon candidates, are 'CMU-CMP' muons, i.e. they are detected by two independent muon systems (Fig. 1.16d). The shape of the edge near $\eta = \pm 0.6$ in the $\eta - \phi$ plot for these muon candidates is a consequence of the CMP geometry near the corners.

The CMX muons (Fig. 1.16e) account for 27% of all muon candidates. Equivalently the extension to $\eta = 1$ increases the single muon acceptance for the top dilepton analysis by 37%. Only a very small fraction of muon

candidates are CMU-CMX muons, as expected from the small geometrical overlap of the two muon systems.

Figure 1.17 is the analogous plot for Run Ia. Additional features are 2 dead CMU wedges.

1.8.2 Momentum resolution

Similarly to measuring the CEM resolution with $Z \rightarrow ee$ decays we can measure the momentum resolution of the tracking system with high-p_T muons from $Z \rightarrow \mu\mu$ decays. Figure 1.18 shows the invariant mass of central-central dimuons in the mass range 50 – 120 GeV/c^2. Both muons are required to pass the tight CMUO identification cuts (see section 2.1.2) of the top dilepton analysis. The momentum of a track is determined from its curvature obtained from a combined SVX–CTC fit. In addition there is a constraint that the track originate from the beam. With increasing momentum the tracks become straighter and the relative uncertainty on the curvature and thus on the momentum increases. The momentum resolution can therefore be parameterized as

$$\Delta p_T/p_T = [(\alpha/100) \times p_T[\mathrm{GeV}/c] \oplus 0.66]\%. \tag{1.6}$$

For high-p_T tracks the term proportional to p_T dominates over the constant term. Here we use 0.66% for the constant term due to multiple scattering as given in Ref. [16].

To measure α we have generated $Z/\gamma \rightarrow \mu\mu$ decays with the PYTHIA Monte Carlo, smeared the resulting muon momenta according to the above parameterization of the resolution, and calculated the dimuon mass. A set of templates with various α's is compared to the data by calculating the χ^2's in the peak region 80-100 GeV/c^2. In Figure 1.19 we plot the reduced χ^2 as a

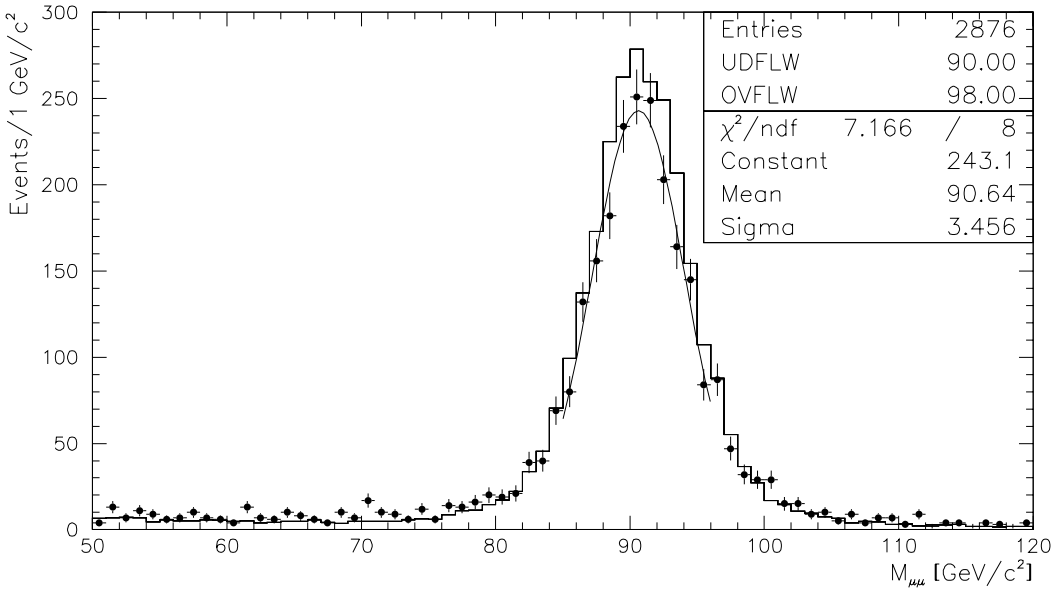

Figure 1.18: Dimuon mass of $Z/\gamma \rightarrow \mu\mu$ events. Data (points) are compared with a Monte Carlo template (histogram) generated using a tracking resolution $\Delta p_T/p_T = 0.09\% \times p_T[\mathrm{GeV}/c] \oplus 0.66\%$. Also shown is a Gaussian fit to the data in the peak region.

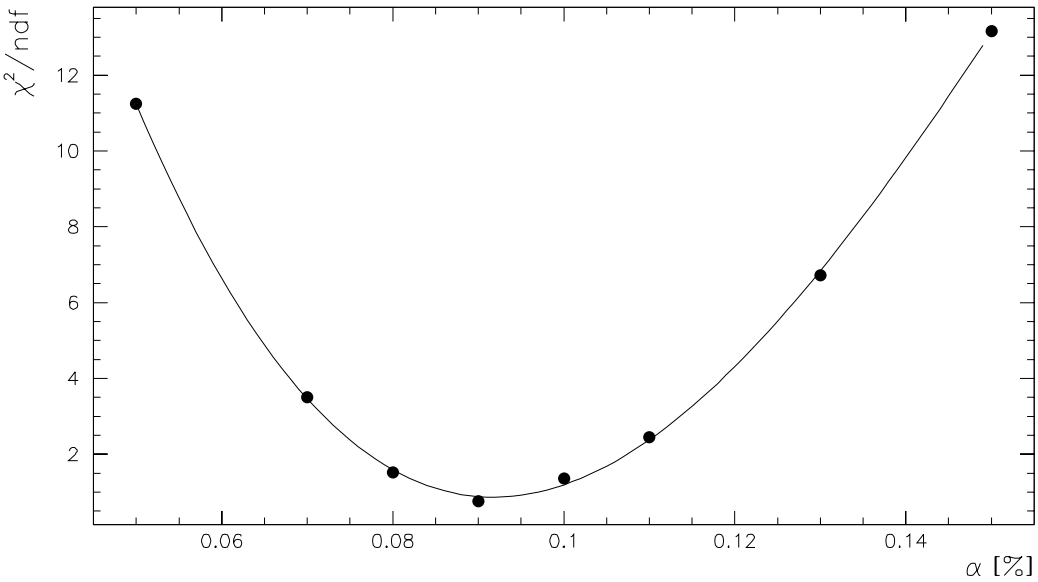

Figure 1.19: Cubic fit of the χ^2 obtained from comparing $Z \rightarrow \mu\mu$ data in the Z peak region (80-100 GeV/c^2). Monte Carlo templates are used with different parameters α for the track momentum resolution $\Delta p_T/p_T = [(\alpha/100) \times p_T[\mathrm{GeV}/c] \oplus 0.66]\%$. The fit returns $\alpha = 0.091 \pm 0.015$.

function of α. A third-order polynomial shows that the χ^2 is minimized for $\alpha = 0.091 \pm 0.015$. The uncertainty is calculated from the value for α where the reduced χ^2 increases by one unit. The result is

$$\Delta p_T/p_T = (0.091 \pm 0.015)\% \times p_T[\mathrm{GeV}/c] \oplus 0.66\%. \tag{1.7}$$

Chapter 2

DILEPTONS WITH ELECTRONS AND MUONS ONLY

Daß ich erkenne, was die Welt
Im Innersten zusammenhält.

J.W. v. Goethe, *Faust I, Nacht*

In this chapter we summarize the methods and results of the standard dilepton analysis, which uses only electron and muons. We present the event selection, acceptance and efficiencies, backgrounds and the observation in the data. The acceptance correlations between the dilepton channel and the lepton plus jets channel are investigated.

2.1 Acceptance and efficiencies

2.1.1 Geometrical and kinematical acceptance $A_{geom \cdot P_T}$

The first step in calculating the total acceptance for dileptons from $t\bar{t}$ decays is getting the combined geometrical and kinematic acceptance $A_{geom \cdot P_T}$. The geometrical acceptance is given by the (fiducial) coverage of the relevant detector components (CEM, CHA, CTC, CMU, CMP, CMX). The kinematic acceptance reflects the fraction of dilepton events for which both leptons have p_T above a certain threshold. This threshold is set at 20 GeV for both leptons, which allows the preferential selection of leptons from W decays.

For the kinematic part of $A_{geom \cdot P_T}$ we rely on the Monte Carlo generation of $t\bar{t}$ events. We assume that these correctly describe the production of the $t\bar{t}$ system and its subsequent decay into dileptons. We have generated 80,000 $t\bar{t}$ Monte Carlo events using PYTHIA 5.7[35]+CLEO+TAUOLA[39]+QFL for $m_{top} = 175$.

In the PYTHIA generation the b quark from the top decay is allowed to radiate gluons[40]. For the quark fragmentation we use a hybrid scheme with Lund string fragmentation for light quarks and 'Peterson fragmentation' for charm and heavier quarks[41]. We use PYTHIA's internal CTEQ2L parton distribution function for the generation of events.

The CLEO package is used for decaying b quarks. For τ decays we use the TAUOLA package which takes the τ polarization into account before the detector simulation is applied. The geometrical acceptance of the detector is obtained with the QFL detector simulation which gives the detector coverage and response. Figure 2.1 illustrates that the branching ratios of W's, τ's ,

and b's into electrons, muons, and hadrons are modeled properly in the Monte Carlo.

To ensure that the reconstructed electrons and muons (ELES, CMUO banks) found in the simulated event records correspond to generated particles at the generator level (listed in the GENP bank) we match them to each other. We do this by requiring that the distance $\Delta R = \sqrt{(\Delta\phi)^2 + (\Delta\eta)^2}$ in $\eta - \phi$ space between reconstructed object and generated particle be less than 0.04[1]. In Figure 2.2 we show the ΔR distributions. The electron distribution has a longer tail due to electrons radiating photons at large angles.

For the matching we first identify all e's, and μ's in the list of generated particles that have $p_T^{GENP} > 5$ GeV. We use this low threshold at the generator level because it is possible that the reconstructed p_T or E_T is significantly higher than p_T^{GENP}; this is especially important for leptons from semi-leptonic b or c decays. Then we loop over all corresponding reconstructed object banks and identify the banks that match to the generated particles.

The geometric and kinematic acceptance $A_{geom \cdot P_T}$ is simply defined as the number of reconstructed dilepton events passing the following selection criteria divided by the number of all generated $t\bar{t} \rightarrow X$ events. This definition includes the various branching ratios in $A_{geom \cdot P_T}$. Reconstructed electrons with $E_T^{rec} > 20$ GeV have to match to an electron at the generator level that is central ($|\eta| < 1.0$) and fiducial ('CE'). Electrons that are identified as due to conversions using a standard CDF conversion filter are excluded. Similarly, reconstructed central muons with stubs in a muon chamber ('MU'), or isolated minimum ionizing tracks ('MI') that do not produce track stubs in the muon chambers must match to a muon at the generator level with $P_T^{rec} > 20$ GeV.

[1] As shown in the next chapter we require $\Delta R < 0.2$ for τ 's because of the angle between the τ and its charged decay products.

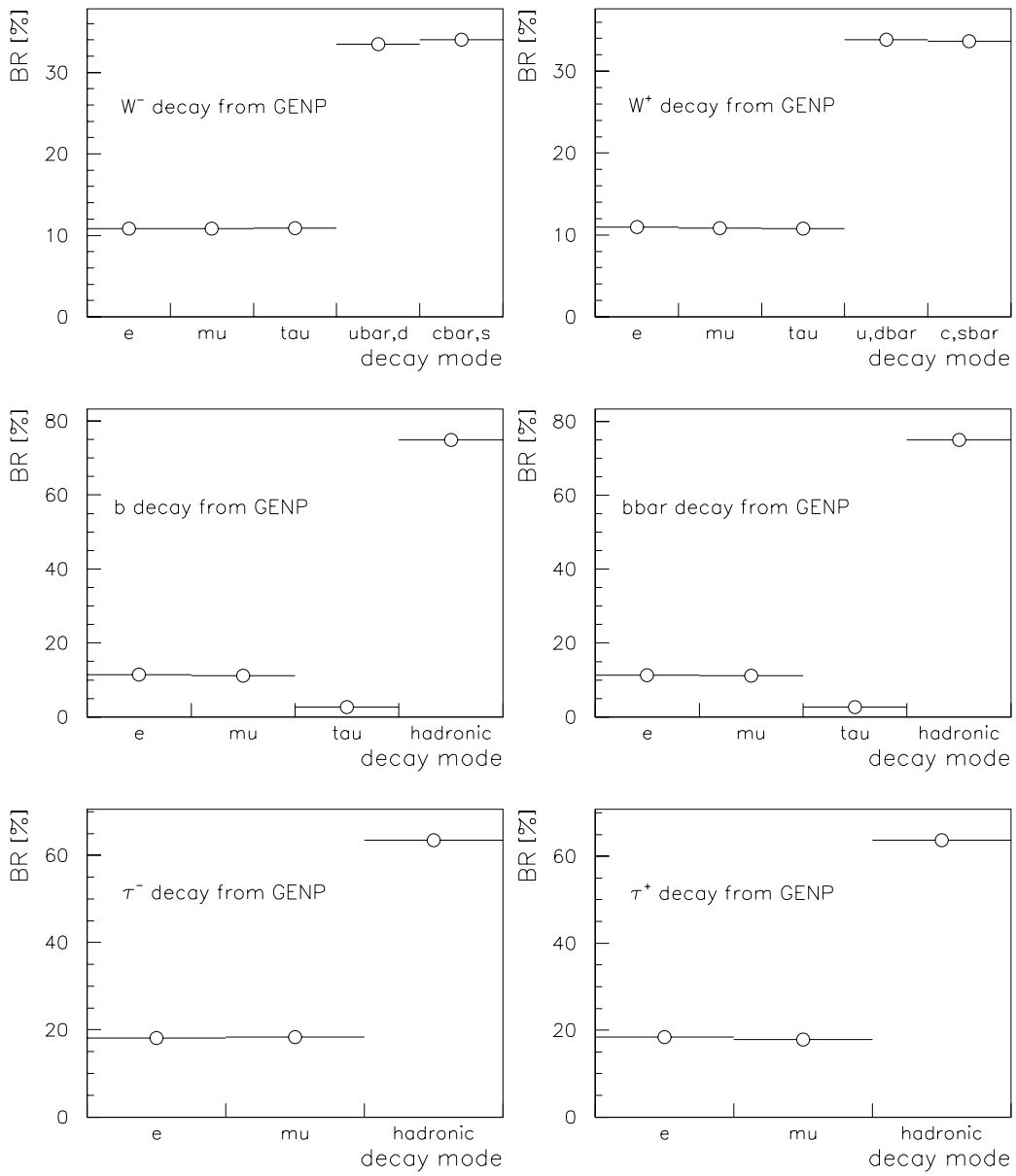

Figure 2.1: Branching ratios of W's, τ's , and b's into electrons, muons, and hadrons in the PYTHIA $t\bar{t}$ MC at the generator level.

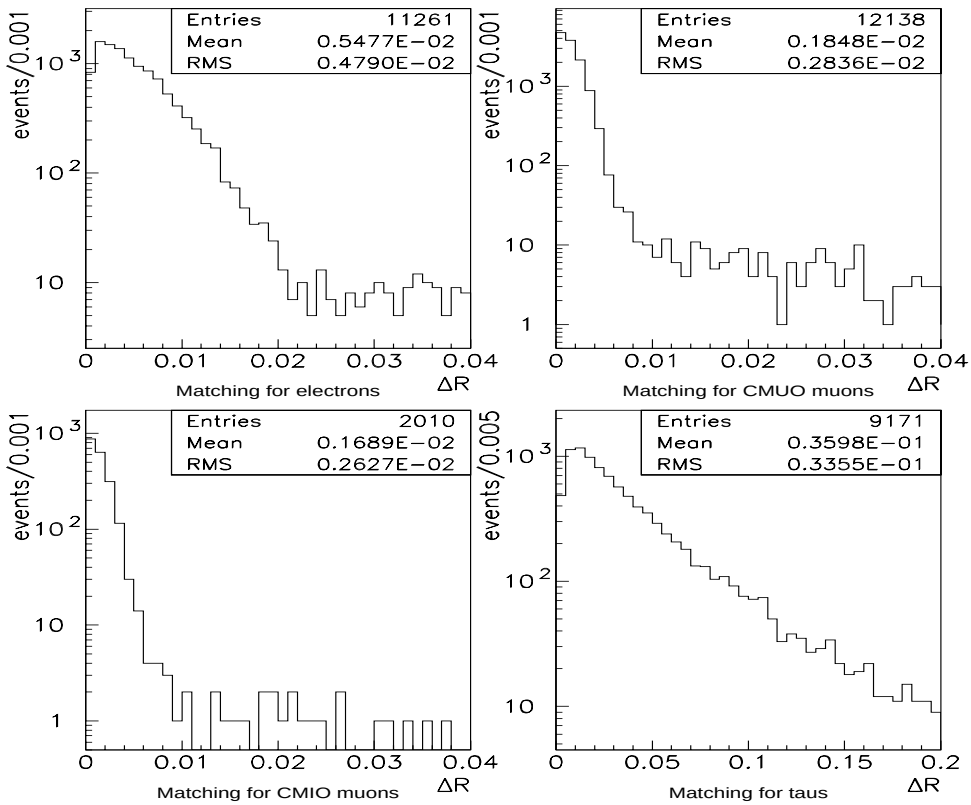

Figure 2.2: The ΔR distributions for matching of e, μ and τ at the generator level (GENP bank) to fully reconstructed e, μ and τ (ELES, CMUO, CMIO and TAUO banks).

We count events with more than one matching lepton satisfying the above cuts and categorize them. Events can only be in *one* category. We search first for events with more than 2 matching leptons ("multileptons") and then sequentially for CE–MU; CE–MI;CE–CE; MU–MU MU–MI events.

Table 2.1 shows the results from this procedure. We list the absolute dilepton acceptances $A_{geom \cdot P_T}$ as a percentage of all generated $t\bar{t} \rightarrow X$ events. For each category the acceptance is broken down by sources, i.e. the combinations of particle decays that give rise to the 2 leptons (WW,Wb, τ τ , ...). 'Charm' means that at least one lepton is from a charm decay. The

Category	Total	W, b, τ Total	WW	$W\tau$	$\tau\tau$	Wb	τb	bb	$charm$	π^0, η
CE-MU	1.42±.04	1.26±.04	0.63	0.11	0.00	0.46	0.04	0.02	0.16	0.00
CE-CMU(P)		1.01±.04	0.50	0.08	0.00	0.37	0.03	0.02	0.14	0.00
CE-CMX		0.25±.02	0.12	0.03	0.00	0.09	0.01	0.00	0.02	0.00
CE-MI	0.20±.02	0.20±.02	0.13	0.02	0.00	0.04	0.00	0.00	0.01	0.00
CE-CE	0.65±.03	0.55±.03	0.29	0.06	0.00	0.16	0.02	0.01	0.08	0.01
MU-MU	0.77±.03	0.67±.03	0.33	0.06	0.00	0.23	0.03	0.01	0.10	0.00
CMU(P)-CMU(P)		0.41±.02	0.21	0.04	0.00	0.13	0.02	0.01	0.07	0.00
CMU(P)-CMX		0.23±.02	0.11	0.02	0.00	0.09	0.01	0.00	0.02	0.00
CMX-CMX		0.03±.01	0.01	0.00	0.00	0.01	0.00	0.00	0.01	0.00
MU-MI	0.22±.02	0.21±.02	0.14	0.02	0.00	0.05	0.00	0.00	0.01	0.00
CMX-MI	0.04±.01	0.04±.01	0.03	0.01	0.00	0.01	0.00	0.00	0.00	0.00
Sum	3.26±.06	2.88±.06	1.52	0.27	0.02	0.94	0.09	0.05	0.36	0.02
Multileptons										
$ee\mu$, $e\mu\mu$, $\mu\mu\mu$	0.15±.01									
$ee\tau$, $e\mu\tau$, $\mu\mu\tau$	0.21±.02									
GRAND TOTAL	**3.62±.06**									

2.1: Absolute geometric and kinematic acceptance $A_{geom \cdot P_T}$ for dileptons using PYTHIA+TAUOLA+CLEO+QFL ($m_{top} = 175$ GeV). All numbers are in percent and include all branching ratios. Rows refer to the reconstructed dilepton type (CE: central electron, MU: central muon, CMU(P): non-CMX muon, CMX: CMX muon, MI: isolated minimum ionizing track). Columns refer to the parent particles of the 2 leptons. 'Charm' ('π^0, η') means that at least one lepton is from a charm (π^0 or η) decay.

category π^0, η likewise means that one lepton is from a π^0 or η decay. We also break down the MU category by detector into a CMX sub–category and a non-CMX sub–category 'CMU(P)' (CMU only, CMP only, CMU–CMP). For each category we give a grand total and the total of all sources not involving charm, π^0's or η's. All uncertainties are statistical only. The total geometric and kinematic acceptance is found to be

$$A_{geom \cdot P_T} = (3.62 \pm .06)\%. \tag{2.1}$$

The contribution from $W^+ \to \ell^+\nu$, $W^- \to \ell^{-\prime}\nu'$ decays to this is 1.52% (not including multilepton events), which is 30.7% relative to the full branching ratio of $4/81 = 4.94\%$ for these decay modes. Other significant contributions at this level are from events with one lepton due to W decay and the other from a semileptonic b decay (0.94%) or c decay (0.36%) or due to a leptonic τ decay (0.27%). However, the lepton selection criteria (see next section) are designed to reduce the contributions from semileptonic heavy quark decays while preserving efficiency for the decay modes $W^+ \to \ell^+\nu$, $W \to \ell^{-\prime}\nu'$ and $W \to \ell\nu$, $W \to \tau\nu_\tau \to \ell'\nu'\nu_\tau\overline{\nu}_\tau$.

2.1.2 Lepton identification

Electrons

The following variables are used to select high-p_T electrons:

- **E/p**: The ratio of the energy measured in the calorimeter and the momentum measured from the track curvature.
- $\boldsymbol{E_{had}/E_{em}}$: The ratio of hadronic and electromagnetic energy measured in the calorimeter.

ID variable	TCE	LCE
E_T	> 20 GeV	> 20 GeV
E/p	< 1.8	< 4.0
E_{had}/E_{em}	< 0.05	$< 0.055 + 0.045\ E[\text{GeV}]/100$
Lshr	< 0.2	< 0.2
χ^2_{strip}	< 10	–
$\lvert\Delta x\rvert$(track-shower)	< 1.5 cm	< 1.5 cm
$\lvert\Delta z\rvert$(track-shower)	< 3.0 cm	< 3.0 cm
$\lvert\Delta z\rvert$(vertex-track)	< 5.0 cm	–
Efficiency	0.815 ± 0.007	0.896 ± 0.005

Table 2.2: Identification cuts for tight central electrons (TCE) and loose central electrons (LCE) and their efficiencies as measured from Z events [20]. Note that the E_T cut is not considered a proper identification cut; it rather determines the kinematic acceptance of the electron selection. It is listed here for completeness.

- **Lshr**: The lateral sharing of energy between CEM towers compared to the sharing measured with electrons in a test beam – expressed in a χ^2 like variable.

- $\boldsymbol{\chi^2_{strip}}$: The χ^2 of a fit between the observed CES shower profile in the z view and the nominal shape measured with test beam electrons.

- $\boldsymbol{\Delta x}$**(track-shower)**: The distance in x between the extrapolated track and the shower position measured in the CES.

- $\boldsymbol{\Delta z}$**(track-shower)**: The distance in z between the extrapolated track and the shower position measured in the CES.

- $\boldsymbol{\Delta z}$**(vertex-track)**: The distance in z between the position where the track intercepts the beam and the closest high-quality vertex.

Figure 2.3 shows the distributions of these identification variables in $Z \rightarrow ee$ data. One "leg" of the Z is required to pass the tight electron identification cuts and be isolated (see below). If another ELES bank ("second leg") forms a mass $75 < m < 105$ with the tight electron it is very likely also an electron and can be used for getting distributions of the identification variables from data with little bias.

We define two categories of central electron candidates: tight central electrons (TCE) and loose central electrons (LCE). The cuts on the identification variables that are imposed for each category and the overall electron identification efficiencies using these cuts as measured with the second legs of $Z \rightarrow ee$ decays [20] are listed in Table 2.2.

Muons

We define two categories of muon candidates: TCM muons are those that have track stubs in the CMU, CMUP or CMX muon chambers. Tracks consistent with minimum ionizing particles that are not associated with muon chamber stubs are CMI muon candidates. The variables used to select high-p_T muons are:

- $\boldsymbol{d_0}$: The impact parameter of the track with respect to the beam in the $r\phi$ plane as measured by the CTC.
- $\boldsymbol{\Delta z}$**(vertex-track)**: The distance in z between the position where the track intercepts the beam and the closest high-quality vertex.
- $\boldsymbol{\Delta x}$**(stub-track)**: The distance in the $r\phi$ plane between the extrapolated CTC track and the track stub in the respective muon chamber.
- $\boldsymbol{N_{ASL}}$: The number of axial super layers of the CTC with track hits.

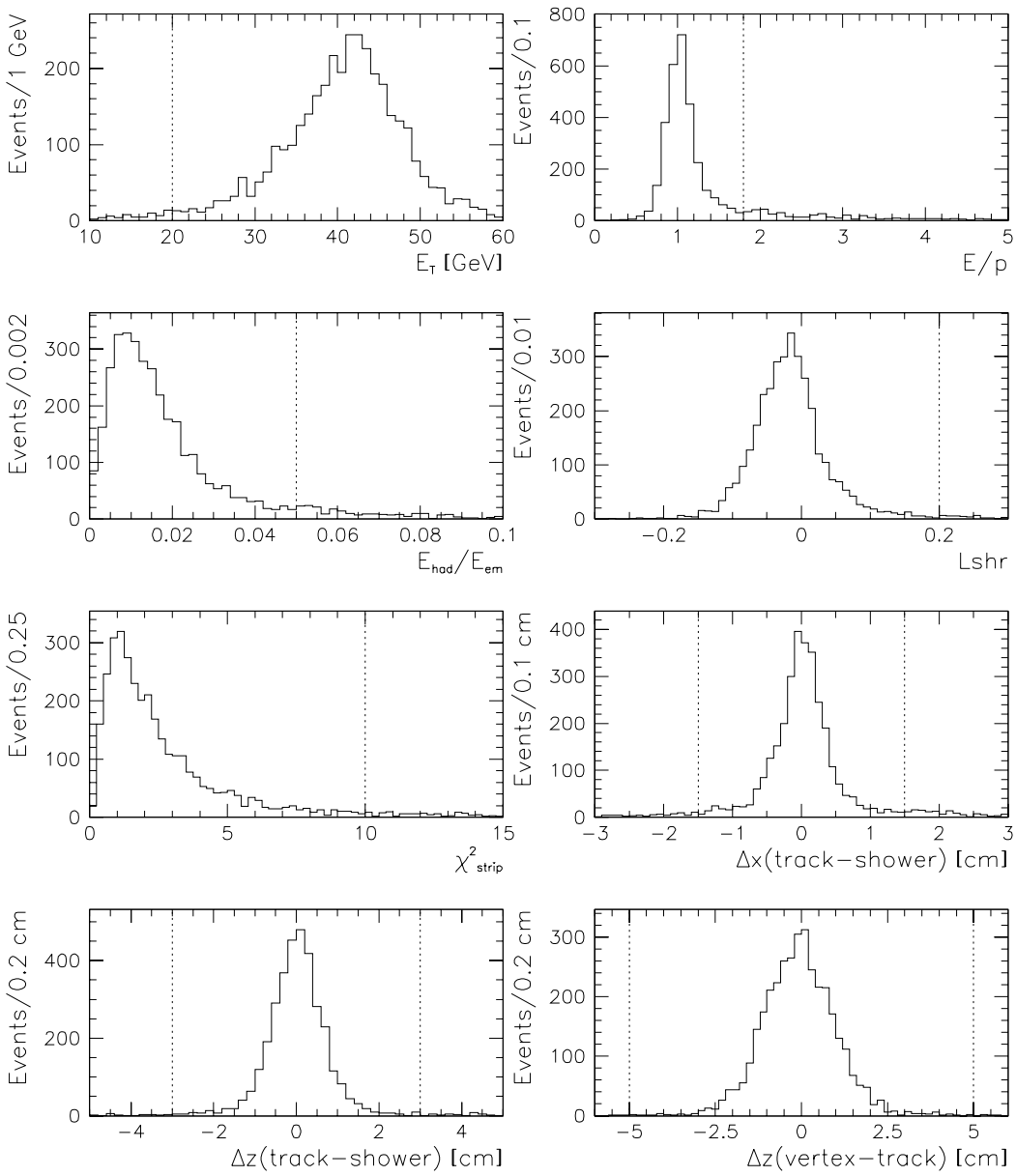

Figure 2.3: Distribution of central electron identification variables for the unbiased second leg in $Z \to ee$ decays. The first electron is required to pass tight cuts. The dotted lines indicate the cuts used for tight central electrons (TCE) in the dilepton analysis.

ID variable	TCM	CMI
p_T	$20 < p_T < 250$ GeV/c	$20 < p_T < 250$ GeV/c
$\|d_0\|$	< 0.3 cm	< 0.3 cm
$\|\Delta x_{CMU}\|$	< 2 cm	n/a
$\|\Delta x_{CMP}\|$	< 5 cm	n/a
$\|\Delta x_{CMX}\|$	< 5 cm	n/a
$\|\Delta z(\text{vertex-track})\|$	< 5.0 cm	< 5.0 cm
N_{ASL}	≥ 3	≥ 3
N_{SSL}	≥ 2	≥ 2
$N_{ASL} + N_{SSL}$	≥ 6	≥ 3
E_{em}	< 2 GeV	< 2 GeV
E_{had}	< 6 GeV	< 6 GeV
$E_{em} + E_{had}$	> 0.1 GeV	< 0.1 GeV
I_{trk}	-	< 0.1
I_{cal}	-	< 0.1
Efficiency	0.917 ± 0.007 (CMU,CMP) 0.897 ± 0.018 (CMX)	0.913 ± 0.013

Table 2.3: Identification cuts for tight central muons (TCM) and CMI muons and their efficiencies as measured from Z events [20]. For CMU-CMUP tight central muons only one $|\Delta x|$ cut needs to be satified. Note that the p_T cut is not considered a proper identification cut; it rather determines the kinematic acceptance of the muon selection. It is listed here for completeness. Note that CMI muons are by definition isolated, even though the isolation is rather a topological cut than an identification cut.

- $\boldsymbol{N_{SSL}}$: The number of stereo super layers of the CTC with track hits.
- $\boldsymbol{E_{em}}$: The energy deposition in the CEM.
- $\boldsymbol{E_{had}}$: The energy deposition in the CHA and WHA .
- $\boldsymbol{I_{trk}}$ and $\boldsymbol{I_{cal}}$: The track and calorimeter isolation as defined below (for CMI muons only).

Figure 2.4 shows the distributions of the TCM and CMX identification variables from the second leg of $Z \rightarrow \mu\mu$ decays. The cuts on the

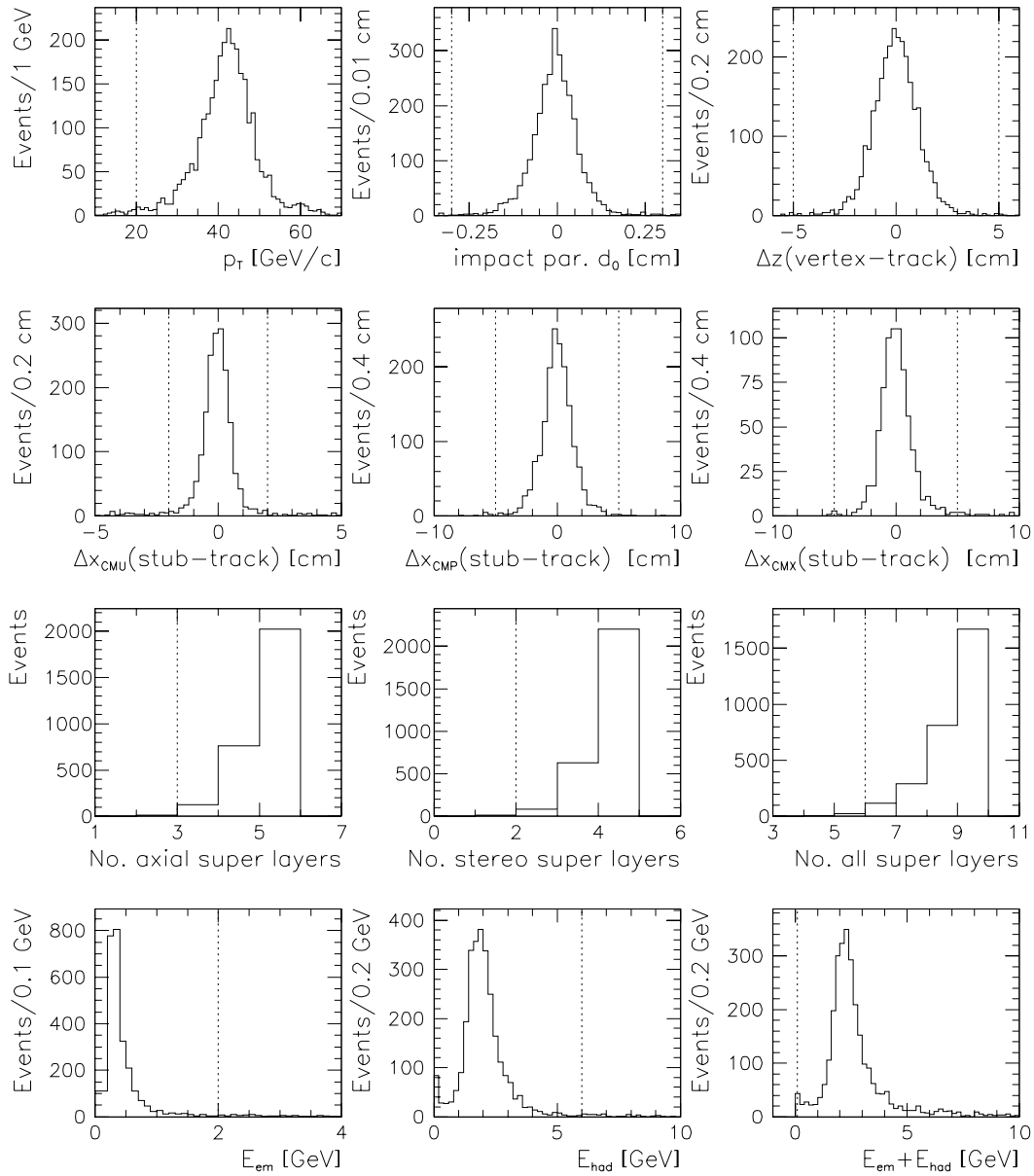

Figure 2.4: Distribution of central muon (CMUO) identification variables for the unbiased second leg in $Z \to \mu\mu$ decays. The first muon is required to pass tight cuts. The dotted lines indicate the cuts used for tight central muons (TCM) in the dilepton analysis.

identification variables that are imposed for both muon categories and the overall muon identification efficiencies using these cuts [20] are listed in Table 2.3. An upper limit of 250 GeV/c is placed on the p_T of the muons as a track quality cut. Problems with the momentum reconstruction for very straight tracks can lead to unphysically large momenta. Since we correct the $\not\!\!E_T$ for the muon momenta this in turn yields unphysically large $\not\!\!E_T$. This cut is most relevant for rejecting cosmic ray events and has a negligible effect on the top acceptance.

2.1.3 Dilepton selection

We define 7 combinations of electron and muon types as valid dilepton categories. They are shown in Table 2.4. Each category requires at least one tight lepton, TCE or TCM, which also must be isolated in the calorimeter as well as in the tracking chamber. The calorimeter isolation I_{cal} is defined as the ratio $I_{cal} = E_T^{cone}/E_T^e$ for electrons and $I_{cal} = E_T^{cone}/p_T^\mu$. E_T^{cone} is the total transverse energy measured by the calorimeter in a cone of 0.4 in $\eta - \phi$ space around the lepton excluding the energy deposit due to the lepton itself. Similarly, I_{trk} is defined as the ratio $I_{trk} = p_T^{cone}/p_T^e$ for electrons and $I_{trk} = p_T^{cone}/p_T^\mu$ for muons. Here p_T^{cone} is the sum of the transverse momenta of all tracks in a cone of 0.4 in $\eta - \phi$ space around the lepton track excluding the lepton track itself. The tight leptons are required to satify the requirements

$$I_{cal} < 0.1 \text{ and } I_{trk} < 0.1. \tag{2.2}$$

CMI muon candidates are by definition required to satisfy these isolation cuts, so that dilepton candidates involving CMI muons require both leptons to be isolated.

Dilepton type	combination
ee	TCE-TCE TCE-LCE
$\mu\mu$	TCM-TCM TCM-CMI
$e\mu$	TCE-TCM TCE-CMI TCM-LCE

Table 2.4: Valid dilepton categories.

2.1.4 Topological selection

In order to separate the top signal from backgrounds several topological cuts are applied:

- **Cosmic ray removal:** Dimuons are rejected as cosmic rays, if the muons are back-to-back:
  - $\Delta\phi > 178.5°$, $|\eta_{\mu_1} + \eta_{\mu_1}| < 0.1$, **or**
  - $\Delta\phi > 177°$, $|\eta_{\mu_1} + \eta_{\mu_1}| < 0.25$ and either at least one muon is out–of–time with the beam crossing or the muons are out of time with each other. The timing cuts are $t_\mu - t_0 > 18(22)$ ns for Run Ia(Ib), $t_\mu - t_0 < -14$ ns and $|t_{\mu 1} - t_{\mu 2}| < 14$ ns.
- Z **removal:** $Z \to ee$ and $Z \to \mu\mu$ events are a copious source of high-pt dilepton events. We remove dielectron and dimuon events where the 2 leptons form an invariant mass $75 < m_{\ell\ell} < 105$.
- **2 jet cut:** In $t\bar{t}$ events there are canonically 2 jets from the decay of the b and $\bar{b}$. At least two jets with $E_T > 10$ GeV are required. The jet energy is not corrected for detector response here.

$\epsilon_{trigger}$	0.937 ± 0.005
ϵ_{ID}	0.451 ± 0.013
ϵ_{Iso}	0.949 ± 0.006
$\epsilon_{Z-removal}$	0.874 ± 0.009
$\epsilon_{\not{E}_T}$	0.757 ± 0.013
ϵ_{2-jet}	0.844 ± 0.012
$\epsilon_{opp.-sign}$	0.976 ± 0.006

Table 2.5: Summary of efficiencies that give the total acceptance for ee, $\mu\mu$, and $e\mu$ dilepton events using 80,000 PYTHIA $t\bar{t}$ Monte Carlo events ($m_{top} = 175$ GeV/c^2). Each efficiency is calculated using only the events that pass the preceding cuts. The values for $\epsilon_{trigger}, \epsilon_{ID}$, and ϵ_{Iso} are taken from Ref. [20].

- $\not{E}_T$ **:** Due to the two high-p_T neutrinos from leptonic W decays top dilepton events are expected to exhibit substantial $\not{E}_T$. We require

  - $\not{E}_T > 25$ GeV. We correct $\not{E}_T$ for muons by adding the measured muon p_T to the transverse energy measured in the calorimeter. We also correct for jets by using the standard jet corrections [42].

  - $\Delta\phi(\not{E}_T, lj) > 20°$ if $\not{E}_T < 50$ GeV. The angle between $\not{E}_T$ and the closest jet or lepton in the $r - \phi$ plane must be greater than 20° to protect against background events with large fake $\not{E}_T$ due to mismeasurements. This cut is not made if the $\not{E}_T$ is sufficiently large ($\not{E}_T > 50$ GeV).

- **Opposite sign cut:** We require the two leptons to have opposite charge as expected for dileptons from leptonic decays of W^+W^- in $t\bar{t}$ events.

2.1.5 Total Acceptance

The efficiencies of all cuts including the topology cuts for $t\bar{t}$ events ($m_{top} = 175$ GeV/c^2) as determined from the PYTHIA Monte Carlo are listed in Table 2.5 [20]. The total acceptance A_{tot} for ee, $\mu\mu$, and $e\mu$ dilepton events is given by

$$A_{tot} = A_{geom \cdot P_T} \cdot \epsilon_{trigger} \cdot \epsilon_{ID} \cdot \epsilon_{Iso} \cdot \epsilon_{Z-removal} \cdot \epsilon_{\not{E}_T} \cdot \epsilon_{2-jet} \cdot \epsilon_{opp.-sign} \quad (2.3)$$

The final result for A_{tot} obtained by averaging the results of the PYTHIA Monte Carlo and a HERWIG Monte Carlo is [20]:

$$A_{tot} = (0.74 \pm 0.02(stat) \pm 0.07(syst))\% \quad (2.4)$$

The dominating systematic uncertainties in the calculation of A_{tot} are uncertainties in the lepton identification efficiencies (7%), Monte Carlo generation (3%), and initial and final state radiation (3%). For more details see Ref. [20].

2.1.6 Expected number of events in 109 pb^{-1}

With A_{tot} in hand we can calculate how many ee, $\mu\mu$, and $e\mu$ events from $t\bar{t}$ production and decay we expect to find in Run I. Using the theoretical estimate of the $t\bar{t}$ production cross section for $m_{top} = 175$ GeV/c^2 from Ref. [26] we find:

$$\begin{aligned} N_{exp} &= \sigma_{t\bar{t}}^{theory} \, \mathcal{L} \, A_{tot} \\ &= (4.8 \pm 0.7)pb \; (109 \pm 7(syst))pb^{-1} \\ &\quad \times (0.74 \pm 0.02(stat) \pm 0.07(syst))\% \\ &= 3.9 \pm 0.7 \text{ events}, \end{aligned} \quad (2.5)$$

where we take a 6% systematic uncertainty on the total integrated luminosity.

2.1.7 Acceptance for $t\bar{t}$ events with both W's decaying into leptons

We find that 0.74% of all produced $t\bar{t}$ events are expected to pass all cuts of the dilepton analysis. This is only 15% of the approximate branching ratio $4/81 = 4.94\%$ for 'canonical' dilepton events, where both W's decay leptonically. We investigate at which steps of the analysis canonical $t\bar{t}$ dilepton events are lost. In Table 2.6 we list the percentages of canonical dilepton events in the PYTHIA $t\bar{t}$ MC that survive the successive selection cuts. Figure 2.5 displays these percentages. The table also gives the efficiency of each cut with respect to the events passing the previous cut.

The largest loss, about 50%, is due to the restriction of the analysis to the central part of the detector. With the current configuration of the detector this is unavoidable: In case of the muons the detector is instrumented with central muon chambers only out to $\eta = \pm 1.0$. For electrons the identification requires tracking information, but the track finding efficiency of the CTC falls rapidly for $|\eta| > 1.1$, so that only a small fraction of the plug calorimeter is recoverable. This was done in the Run Ia dilepton analysis [16] and increased the acceptance by a factor of 1.04. These problems will be remedied in Run II using extended muon chamber coverage in the plug and forward region and using the new plug calorimeters together with tracking in the intermediate silicon layers [80].

As already mentioned in the discussion of the calorimeter in Chapter 1, the fiducial cuts on the electron are responsible for another significant acceptance loss of about 40%. All other cuts give rise to losses on the order of 15-25%.

$e\ e$			
Cut	# events passing	relative fraction [%]	efficiency wrt previous cut [%]
$W^+ \to e^+\nu, W^- \to e^-\nu$	1003	100	-
Both $\lvert\eta^e_{det}\rvert < 1.0$	479	47.8 ± 1.6	47.8 ± 1.6
Both leptons $p_T > 20$	405	40.4 ± 1.5	84.6 ± 1.7
leptons reconstructable & fiducial	247	24.6 ± 1.4	61.0 ± 2.4
ID and Isolation	193	19.2 ± 1.2	78.1 ± 2.6
Z removal	145	14.5 ± 1.1	75.1 ± 3.1
$\not\!\!E_T > 25$	127	12.7 ± 1.1	87.6 ± 2.7
$\Delta\phi > 20$ or $\not\!\!E_T > 50$	117	11.7 ± 1.0	92.1 ± 2.4
$N_{jet} \geq 2$	93	9.3 ± 0.9	79.5 ± 3.7
$\mu\ \mu$			
Cut	# events passing	relative fraction [%]	efficiency wrt previous cut [%]
$W^+ \to \mu^+\nu, W^- \to \mu^-\nu$	961	100	-
Both $\lvert\eta^\mu_{det}\rvert < 1.2$	580	60.4 ± 1.6	60.4 ± 1.6
Both leptons $p_T > 20$	499	51.9 ± 1.6	86.0 ± 1.4
leptons reconstructable	397	41.3 ± 1.6	79.6 ± 1.8
ID and Isolation	319	33.2 ± 1.5	80.4 ± 2.0
cosmic ray removal	319	33.2 ± 1.5	100.0 ± 0.3
Z removal	245	25.5 ± 1.4	76.8 ± 2.4
$\not\!\!E_T > 25$	214	22.3 ± 1.3	87.3 ± 2.1
$\Delta\phi > 20$ or $\not\!\!E_T > 50$	189	19.7 ± 1.3	88.3 ± 2.2
$N_{jet} \geq 2$	157	16.3 ± 1.2	83.1 ± 2.7
$e\ \mu$			
Cut	# events passing	relative fraction [%]	efficiency wrt previous cut [%]
$W^\pm \to e^\pm\nu, W^\mp \to \mu^\mp\nu$	1899	100	-
$\lvert\eta^e_{det}\rvert < 1.0,\ \lvert\eta^\mu_{det}\rvert < 1.2$	1047	55.1 ± 1.1	55.1 ± 1.1
Both lepton $p_T > 20$	883	46.5 ± 1.1	84.3 ± 1.1
leptons reconstructable & fiducial	641	33.8 ± 1.1	72.6 ± 1.5
ID and Isolation	521	27.4 ± 1.0	81.3 ± 1.5
$\not\!\!E_T > 25$	455	24.0 ± 1.0	87.3 ± 1.5
$\Delta\phi > 20$ or $\not\!\!E_T > 50$	393	20.7 ± 0.9	86.4 ± 1.6
$N_{jet} \geq 2$	339	17.9 ± 0.9	86.3 ± 1.7

Table 2.6: Percentages of canonical dilepton events in the PYTHIA $t\bar{t}$ MC that survive the successive selection cuts. The last column lists the efficiency of each cut with respect to the events passing the previous cut. The lepton p_T and η information are evaluated at the generator level.

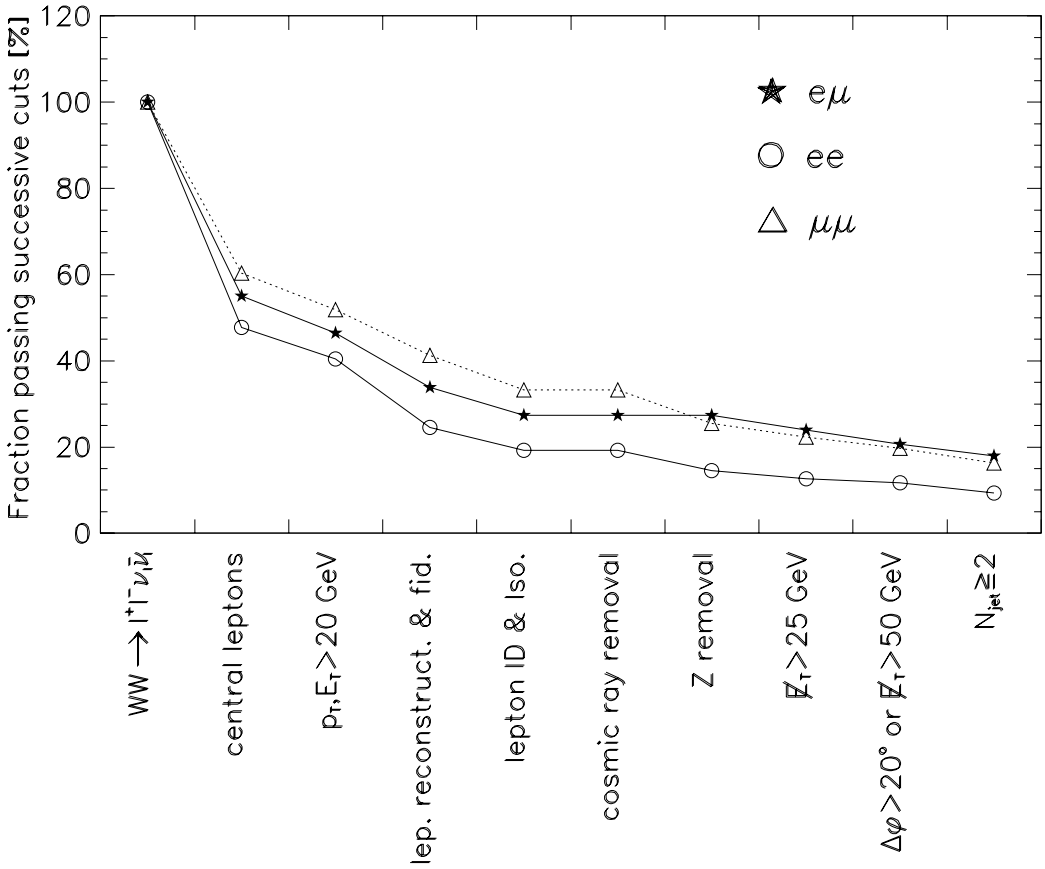

Figure 2.5: Percentages of dilepton events in the $t\bar{t}$ MC with both W's decaying leptonically that survive the successive selection cuts. The lepton p_T and η information are evaluated at the generator level.

2.1.8 Origin and relative fraction of ee, $\mu\mu$, and $e\mu$ events

We study the expected relative fraction of the three individual channels, ee, $\mu\mu$, and $e\mu$ in the Monte Carlo. After reconstruction and all cuts we are left with 727 identified ee, $\mu\mu$ or $e\mu$ candidate events in the PYTHIA $t\bar{t}$ Monte Carlo simulation (80,000 events generated). In Fig. 2.6 we plot the W^+ decay mode vs the W^- decay mode at the generator level for these events.

We evaluate the various decay modes of the W's that contribute to the dilepton channel. The results are listed in Table 2.7 and graphically displayed in Figure 2.7. For 612 of the 727 events identified as ee, eμ, or $\mu\mu$

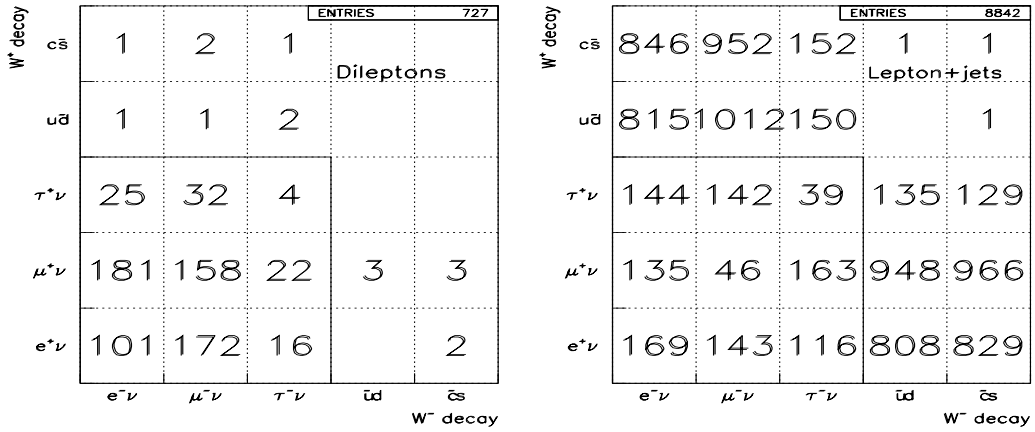

Figure 2.6: W^+ decay mode vs W^- decay mode as obtained at the generator level for 80,000 generated $t\bar{t}$ MC events. A total of 9569 events pass the dilepton selection or the lepton + jets selection. Dilepton events are shown on the left; lepton + jets events on the right. The numbers indicate the number of events found for each combination.

ee, $e\mu$, $\mu\mu$	84.2	$\pm$	1.4 %
$e\tau$, $\mu\tau$	13.1	$\pm$	1.3 %
$\tau\tau$	0.6	$\pm$	0.3 %
e, μ + jets	1.8	$\pm$	0.5 %
τ + jets	0.4	$\pm$	0.2 %
all hadronic	0.0	$\pm$	0.1 %

Table 2.7: Contribution of various W^+W^- decay modes to events identified as dilepton events in the $t\bar{t}$ Monte Carlo (statistical uncertainties only).

dileptons both W's decayed into e's or μ's (84.2$\pm$1.4)%. The relative fraction of the three W^+W^- decay modes for these 612 events is $e\mu$ (57.7$\pm$2.0)%, $\mu\mu$ (25.8$\pm$1.8)% and ee (16.5$\pm$1.5)%. If we ask instead how each of the total 727 events was *reconstructed*, we find very similar numbers for the distribution among the three categories: $e\mu$ (56.5$\pm$1.8)%, $\mu\mu$ (26.8$\pm$1.6)% and ee (16.6$\pm$1.4)%.

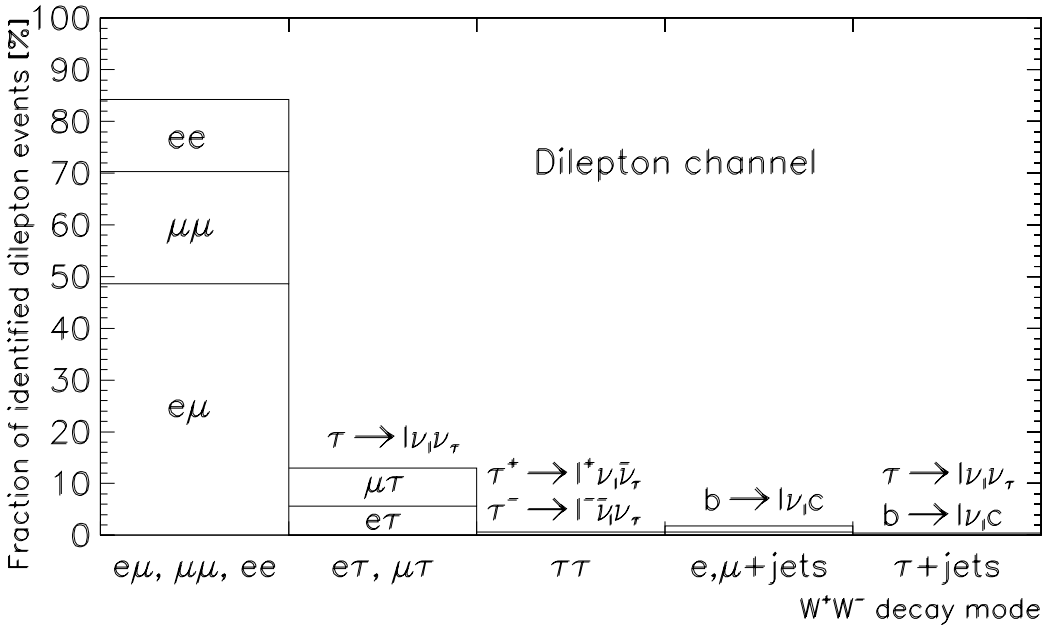

Figure 2.7: Contribution of various W^+W^- decay modes to events identified as dilepton events in the $t\bar{t}$ Monte Carlo. For the cases where not both leptons are from W decays the origin of the lepton that is not from a W is indicated.

Another 95 events originate from $W^\pm \to e^\pm(\mu^\pm)\ W^\mp \to \tau^\mp\nu$ decays, which represent a fraction of $(13.1 \pm 1.3)\%$ of all reconstructed ee, eμ or $\mu\mu$ dilepton events. We find that $(99\pm1.0)\%$ of these events contain a leptonically decaying τ, as expected. Four events, corresponding to a fraction of $(0.6\pm0.3)\%$, are due to $W^+ \to \tau^+\nu, W^- \to \tau^-\nu$ decays. All τ's in the four events are found to decay leptonically.

The contribution to the dilepton channel from decay modes with hadronic decays of one W, leptonic decay of the other W and a semi-leptonic b decay is 16 events $[(2.2\pm0.5)\%]$. Lastly, we have 3 events $[(0.4\pm0.2)\%]$ with a hadronic W decay, at least one semi-leptonic b decay and a $W \to \tau\nu \to l\nu\nu\nu$ decay. No events with all–hadronic W decays are found to contribute to the dilepton channel.

2.2 Correlation with lepton + jets channel

We investigate the correlation of the dilepton channel with the lepton + jets channel [17, 38]. In principle, we expect that in the lepton + jets channel one W decays leptonically into e or μ and the other W decays hadronically. However, as in the dilepton channel, it is possible for events with W decay modes other than these 'nominal' ones to get accepted as candidates. Contributing to this effect are semi-leptonic b decays, fake leptons from jets, lost leptons and τ decays. The event selection in the lepton + jets channel is as follows:

- **Lepton identification:** Require one tight central electron or muon (TCE, TCM) using the same definitions as in the dilepton channel.
- **Isolation:** Require $I_{cal} < 0.1$ on the lepton as in the dilepton channel. The cut on the track isolation I_{trk} is not applied.
- $\not\!\!E_T$ **:** Require $\not\!\!E_T > 20$ GeV. We correct $\not\!\!E_T$ for muons by adding the measured muon p_T to the transverse energy measured in the calorimeter. The $\not\!\!E_T$ is not corrected for jets.
- **Jets:** Top events in this channel canonically have 4 jets from the decays of b, $\bar{b}$ and a W. To increase the acceptance at least three jets with $E_T > 15$ GeV are required. The jet energy is not corrected for detector response.

After all cuts we find 8842 lepton + jets events in the 80,000 event sample from the PYTHIA $t\bar{t}$ MC. Here we have required that there be only one high-p_T lepton found. Specifically, we remove any events with two or more leptons passing the dilepton identification and isolation cuts, regardless of missing E_T

	require ≥ 3 jets	require 4th jet
e + jets, μ + jets	81.2 $\pm$ 0.4 %	86.5 $\pm$ 0.4 %
all other top sources	18.8 $\pm$ 0.4 %	13.5 $\pm$ 0.4 %
ee, eμ, $\mu\mu$	5.6 $\pm$ 0.2 %	2.9 $\pm$ 0.2 %
all τ's	13.2 $\pm$ 0.4 %	10.6 $\pm$ 0.4 %
$e\tau$, $\mu\tau$, $\tau\tau$	6.8 $\pm$ 0.3 %	4.0 $\pm$ 0.2 %
τ + jets	6.4 $\pm$ 0.3 %	6.7 $\pm$ 0.3 %
all hadronic	$< 0.1\%$	$< 0.1\%$

Table 2.8: Contribution of various W^+W^- decay modes to lepton + jets events (statistical uncertainties only). The column on the right gives the contributions if a fourth jet with $|\eta_{det}| < 2.4$ and $E_T > 8$ GeV is required as in the top mass analysis.

and jet multiplicity. Fig. 2.6 shows the W^+ decay mode vs the W^- decay mode for these events.

For 81.2$\pm$0.4% of the lepton + jets candidates one W decays leptonically and the other W decays hadronically. However, other top decay modes contribute the remaining 18.8$\pm$0.4% of the candidate events. The various contributions are listed in Table 2.8 and plotted in Figure 2.8. The dominant contribution is due to τ decays, either in the form of $e\tau$ or $\mu\tau$ dilepton events or τ + jets events. The majority (76.1$\pm$1.8%) of τ's in $e\tau$ or $\mu\tau$ events decay hadronically. This explains the 'misidentification' of this event type as lepton + jets events, because the τ produces a third jet in addition to the 2 b jets. For the τ + jets events we find that all of the τ's decay leptonically, so in this case the e or μ stem from the τ and the jets are from b's and a W decay. Another significant contribution is from ee, $e\mu$, or $\mu\mu$ dileptons that do not pass all cuts to make it as dilepton candidates. Contributions from purely hadronic W decays are small.

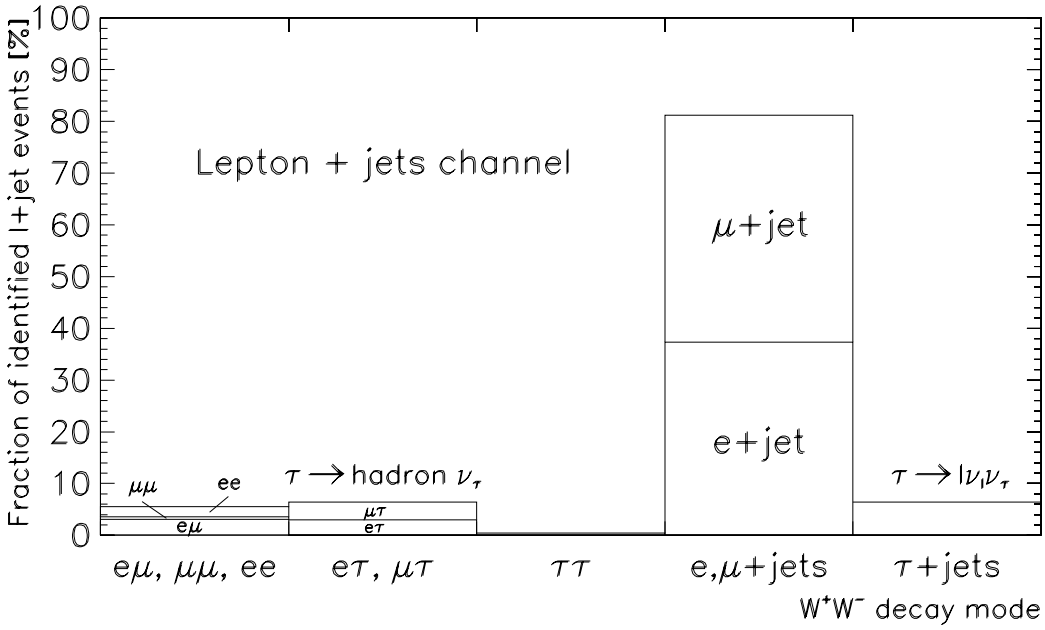

Figure 2.8: Contribution of various W^+W^- decay modes to events identified as lepton +jet events in the $t\bar{t}$ Monte Carlo. For the cases where τ's are involved the decay mode of the τ is indicated.

The problem of misidentification improves somewhat if we require a fourth jet with $E_T > 8$ GeV and $|\eta| < 2.4$ as is done in the top mass analysis [17]. The relative contributions for this case are also shown in Table 2.8.

We compare the total acceptances of events where both W's decay leptonically into e or μ for the dilepton analysis and the lepton + jets analysis. In the 80,000 generated $t\bar{t}$ MC event we find 3863 events of that type ($\frac{3.9\pm0.1}{81}$ of all events). In the dilepton analysis 612 events get accepted, corresponding to a total acceptance for the 'canonical' dilepton events of

$$A_{tot}^{dil} = (15.8 \pm 0.6)\%. \tag{2.6}$$

For the lepton + jets analysis we find 493 events, which corresponds to a total acceptance of

$$A_{tot}^{l+j} = (12.8 \pm 0.5)\%, \tag{2.7}$$

WW decay mode	Dilepton analysis	Lepton + jets analysis
eμ	9.1 $\pm$ 0.5 %	7.2 $\pm$ 0.4 %
ee	2.6 $\pm$ 0.3 %	4.4 $\pm$ 0.3 %
$\mu\mu$	4.1 $\pm$ 0.3 %	1.2 $\pm$ 0.2 %

Table 2.9: Percentages of $t\bar{t}$ MC events with both W's decaying into $e\nu$ or $\mu\nu$ ($W^+ \rightarrow \ell^+\nu$, $W^- \rightarrow \ell^{-\prime}\nu'$ $\ell = e, \mu$ $\ell' = e, \mu$) that get accepted by the dilepton analysis and the lepton + jets analysis. Events are counted either in the dilepton channel or in the lepton + jets channel, but not in both, i.e. the percentages are exclusive.

i.e. the acceptance in the lepton + jets channel for these events is almost as large as in the dilepton channel.

In Table 2.9 and Figure 2.9 the acceptances are broken up into the three categories. We find that the acceptances for $e\mu$ events are similar. As noted above, in this simulation we accept about 50% more $\mu\mu$ events than ee events in the dilepton analysis. The ratio is reversed in the lepton + jets analysis: We accept about three times as many ee events as $\mu\mu$ events. This increased acceptance for ee events is due to the fact that if one electron falls outside of the central detector or fails just one cut, e.g. the fiducial cut, it gets counted as a jet in addition to the 2 b jets, so that the events then can get accepted as a lepton + ≥ 3 jets event. For $\mu\mu$ events this is not likely to happen because the muons do not deposit enough energy in the calorimeters.

We note that there is a large potential for future improvement in the ee channel here. If the handling of electrons could be improved so that electrons are not mistakenly labelled as jets, the acceptance in the ee channel could be improved significantly. If it were possible to pull all the ee events out of the lepton + jets channel and identify them as dilepton events the ee acceptance would increase by a factor $\frac{4.4\%+2.6\%}{2.6\%} = 2.7$! In reality it will not

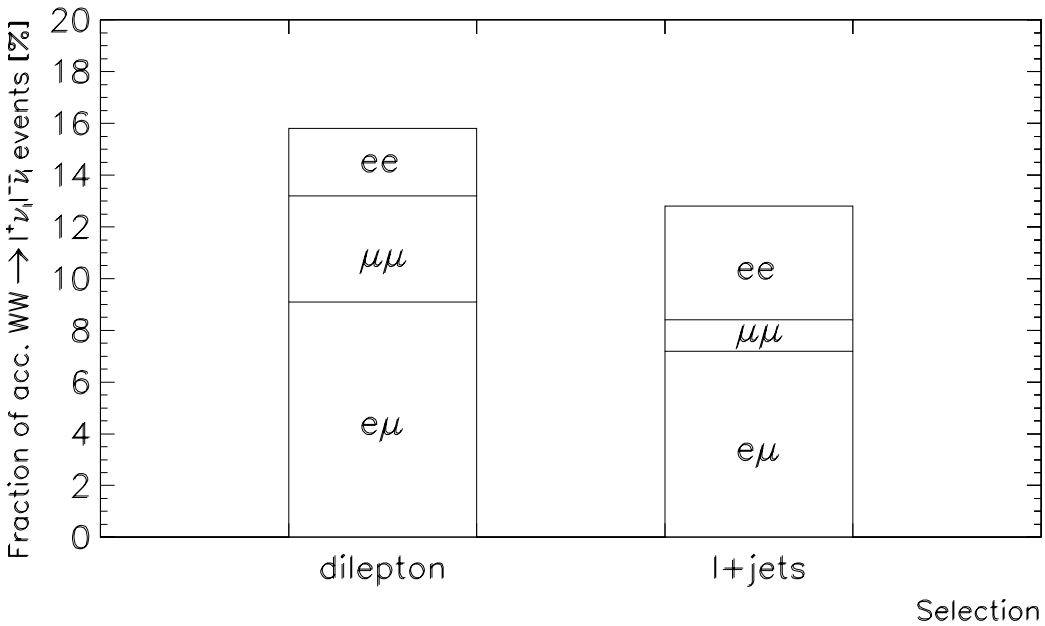

Figure 2.9: Percentages of $t\bar{t}$ MC events with both W's decaying into $e\nu$ or $\mu\nu$ ($W^+ \to \ell^+\nu$, $W^- \to \ell^{-\prime}\nu'$ $\ell = e, \mu$ $\ell' = e, \mu$) that get accepted by the dilepton analysis and the lepton + jets analysis. Events are counted either in the dilepton channel or in the lepton + jets channel, but not in both, i.e. the percentages are exclusive.

be possible to get the full factor, but with the new plug calorimeter and some rethinking on the handling of electrons a factor two might be achievable in Run II.

2.3 Backgrounds

We summarize the background contributions in Table 2.10. The total expected background is [20]

$$B = 2.1 \pm 0.4 \text{ events.} \tag{2.8}$$

Background process	$e\mu$	$ee + \mu\mu$	determined from
Drell–Yan	0.00 ± 0.00	0.61 ± 0.30	Data, MC
$Z \to \tau\tau$	0.38 ± 0.11	0.21 ± 0.08	MC
WW	0.20 ± 0.09	0.16 ± 0.07	MC
Fake	0.16 ± 0.16	0.21 ± 0.17	Data
$b\bar{b}$	0.02 ± 0.02	0.03 ± 0.02	MC
Subtotal	0.76 ± 0.21	1.22 ± 0.36	
$ee + \mu\mu + e\mu$ subtotal		2.0 ± 0.4	
other $(WZ, ZZ, Wb\bar{b})$		0.1	MC
TOTAL		2.1 ± 0.4	

Table 2.10: Summary of backgrounds in the ee, $\mu\mu$, and $e\mu$ analysis after all cuts [20].

2.4 Observation in the data

In the following we discuss the selection of data samples used for the analysis. The results of the final $ee, \mu\mu$, and $e\mu$ event selection are presented.

2.4.1 Data samples

The data collected in Run I represents $109 \pm 7\ pb^{-1}$. In order to handle this large amount of data three steps in data reduction are employed. We begin with events that pass a predefined set of mostly unprescaled triggers (so-called "STREAM 2" in Run Ia, "STREAM A" in Run Ib) including the high-p_T lepton triggers. Inclusive lepton samples are created by selecting events that pass offline high-p_T lepton cuts. Out of these samples events with at least one lepton passing tight identification cuts and an additional lepton passing very loose cuts are collected in dilepton samples. The final event selections are then applied to the dilepton data sets.

central electron (ELES)
$E_T > 18$ GeV
$p_T > 13$ GeV/c
$E_{had}/E_{em} < 0.125$
$Lshr < 0.2$
$\|\Delta x(track - shower)\| < 3$ cm
$\|\Delta z(track - shower)\| < 5$ cm
$\chi^2_{strip} < 10$

Table 2.11: Cuts for selecting the inclusive electron data sample. All values are taken from the ELES bank.

Inclusive lepton sample

The inclusive lepton samples are made by selecting events with leptons that pass loose identification cuts. For Run Ia this was done for electrons by David Saltzberg and for muons by Mark Krasberg [43]. In the case of Run Ib ($\approx 90\ pb^{-1}$) this was done for electrons and muons at the University of Chicago [44], independent from the efforts at Fermilab. The Run Ib input consists of 131 8mm data tapes from STREAM A with approximately 4 million events. The cuts used to select the inclusive lepton sets are listed in Tables 2.11 and 2.12. They were chosen to have little sensitivity to the changing CDF data base (tracking, alignment, calibration) to provide stability. There is no explicit trigger requirement in the offline selection, i.e. events containing leptons that did not come in on a lepton trigger ("volunteers") are accepted. The data set was checked extensively to validate it for analyses that use high-p_T leptons. Also a cross–check with the 'official' data set at Fermilab [45] was performed.

central muon (CMUO)
$p_T > 15$ GeV/c
$E_{had} < 6$ GeV
$\lvert\Delta x_{CMU}\rvert < 10$ cm
$\lvert\Delta x_{CMP}\rvert < 20$ cm
$\lvert\Delta x_{CMX}\rvert < 20$ cm

Table 2.12: Cuts for selecting the inclusive muon sample. All values are taken from the CMUO bank.

Dilepton sample

From the inclusive lepton samples a dilepton subsample was made using the following selection:

- We require at least one isolated, tight central electron or muon as the *primary* lepton. For electrons the only difference from the final TCE selection is that the electron is not required to be fiducial to make it into the data set; for muons the selection is identical with the TCM selection.
- For the second lepton we require that the event contain
  - a central electromagnetic cluster (ELES bank) with $E_T > 10$ GeV or
  - a track stub in a muon chamber that is associated with a CTC track (CMUO bank) with $p_T > 10$ GeV/c or
  - an isolated ($I_{cal} < 0.1$ and $I_{trk} < 0.1$) track (CMIO bank[2]) with $p_T > 10$ GeV/c or

[2]Tracks that are associated with muon stubs are associated only with CMUO banks, and not with CMIO banks, so that there is no double-counting between CMIO and CMUO banks.

	CMU Ia	CMU Ib	ICE Ia	ICE Ib
# of events in incl. sample	83051	313961	133805	474912
second lepton ELES	1386	1943	1593	7099
second lepton CMUO	766	3894	183	1052
second lepton CMIO	738	2001	343	1504
second lepton TAUO	744	2742	749	3273

Table 2.13: Breakdown of events in the dilepton sample, (CMU=incl. central muon sample, ICE=incl. central electron sample).

- a narrow calorimeter cluster (TAUO bank) with $|\eta_{det}| < 1.2$ and $\sigma_{cl} < 0.13$ (see next chapter).

Whereas the cuts on the primary lepton are very tight to achieve significant data reduction, the cuts on the second lepton are as loose as possible. The number of events in each category are listed in Table 2.13. Certain events, such as $e\mu$ events, can be found in the inclusive muons as well as the inclusive electron samples, so we remove duplicate events throughout the sample.

2.4.2 Final dilepton selection

In Table 2.14 we list the number of observed dilepton events in each category when successively applying the topology cuts of section 2.1.4. We find 10 events that pass all cuts, 1 ee event, 2 $\mu\mu$ events, and 7 $e\mu$ events. These events are the top dilepton candidates for the $ee, \mu\mu$ and $e\mu$ channels. Schematic displays of the 10 candidate events are shown in Figures 2.10 and Figures 2.11.

	Dilepton category									
Cut	TCE TCE	TCE LCE	ee	TCM TCM	TCM CMI	$\mu\mu$	TCE TCM	TCE CMI	TCM LCE	$e\mu$
Dilepton	2331	418	2749	2683	873	3556	36	11	4	51
Cosmic ray	2331	418	2749	2506	860	3366	36	11	4	51
Z removal	252	129	381	288	164	452	36	11	4	51
$\not\!\!E_T > 25\,\mathrm{GeV}$	7	2	9	15	6	21	15	2	2	19
$\Delta\phi > 20^\circ$ or $\not\!\!E_T > 50\,\mathrm{GeV}$	3	2	5	7	1	8	15	0	2	17
0 jets	0	1	1	0	0	0	3	0	0	3
1 jet	2	1	3	5	1	6	4	0	1	5
≥ 2 jets	1	0	1	2	0	2	8	0	1	9
same sign	0	0	0	0	0	0	2	0	0	2
opposite sign	1	0	**1**	2	0	**2**	6	0	1	**7**

Table 2.14: The number of events observed in the data after successive cuts for the different dilepton categories. To qualify as a dilepton at least one tight lepton (TCE or TCM) must be isolated.

Significance

From a Poisson distribution we calculate the probability for 2.1 ± 0.4 background events to have fluctuated to ≥ 9 events. One of the 10 final events (Run 58281/Event 44805) is very likely a radiative Z decay, as one of the jets is photonlike and forms an invariant mass of 87 GeV/c^2 with the two muons (see Ref. [20]). More details on the event are given below in section 4.3.3. We remove this event by hand for calculating the significance. Taking the uncertainty of 0.4 on the number of background events into account we find a probability $\mathcal{P} = 0.062\%$ for such a fluctuation. This corresponds to about 3.2 σ for a Gaussian distribution. If the background uncertainty is not taken into account the probability is $\mathcal{P} = 0.033\%$.

As shown above we expect 3.9 ± 0.7 events from $t\bar{t}$ decays assuming

the theoretical $t\bar{t}$ production cross section, for a total expected number of events of 6.0 ± 0.8 events from $t\bar{t}$ + background. The probability for this to fluctuate to ≥ 9 events is $\mathcal{P} = 16.4\%$, which corresponds to about 1.5 σ on a Gaussian. Here the uncertainty of 0.8 events is also taken into account. Taking the ratios of the probabilities we find that the '$t\bar{t}$ + background' hypothesis is about 265 times more likely than the 'background only' hypothesis.

We consider the fact that we observe more events than expected from $t\bar{t}$ + background. Suppose there is an additional process due to new physics not described by the Standard Model that produces dilepton events. If the mean expected number of events from this process '$p\bar{p} \rightarrow X \rightarrow$ dileptons' is 3 events so that the mean expected number of $t\bar{t}$ + background + X equals the observed number of events, then the probability to observe ≥ 9 events will be 54%. This is only about 3 times more likely than $t\bar{t}$ + background[3].

Based on the counting experiment only we conclude that we have a clear signal for $t\bar{t}$ production in this channel, but no significant evidence for other processes due to new physics.

Cross section

The $t\bar{t}$ production cross section

$$\sigma_{t\bar{t}} = \frac{N - B}{\mathcal{L}\ A_{tot}}, \tag{2.9}$$

is calculated using $B = 2.1 \pm 0.4$ for the expected background (see section 2.3), $\mathcal{L} = 109 \pm 7\ pb^{-1}$ for the total integrated luminosity in Run I, and $A_{tot} = (0.74 \pm 0.02(stat) \pm 0.07(syst))\%$ for the total acceptance times

[3]If there is new physics with a mean expected number of events greater than 3 then we have to ask for the probability for the total number of events to have fluctuated *down* to ≤ 9 events, which is less than 54%. Consequently, this is the probability in the most favorable case.

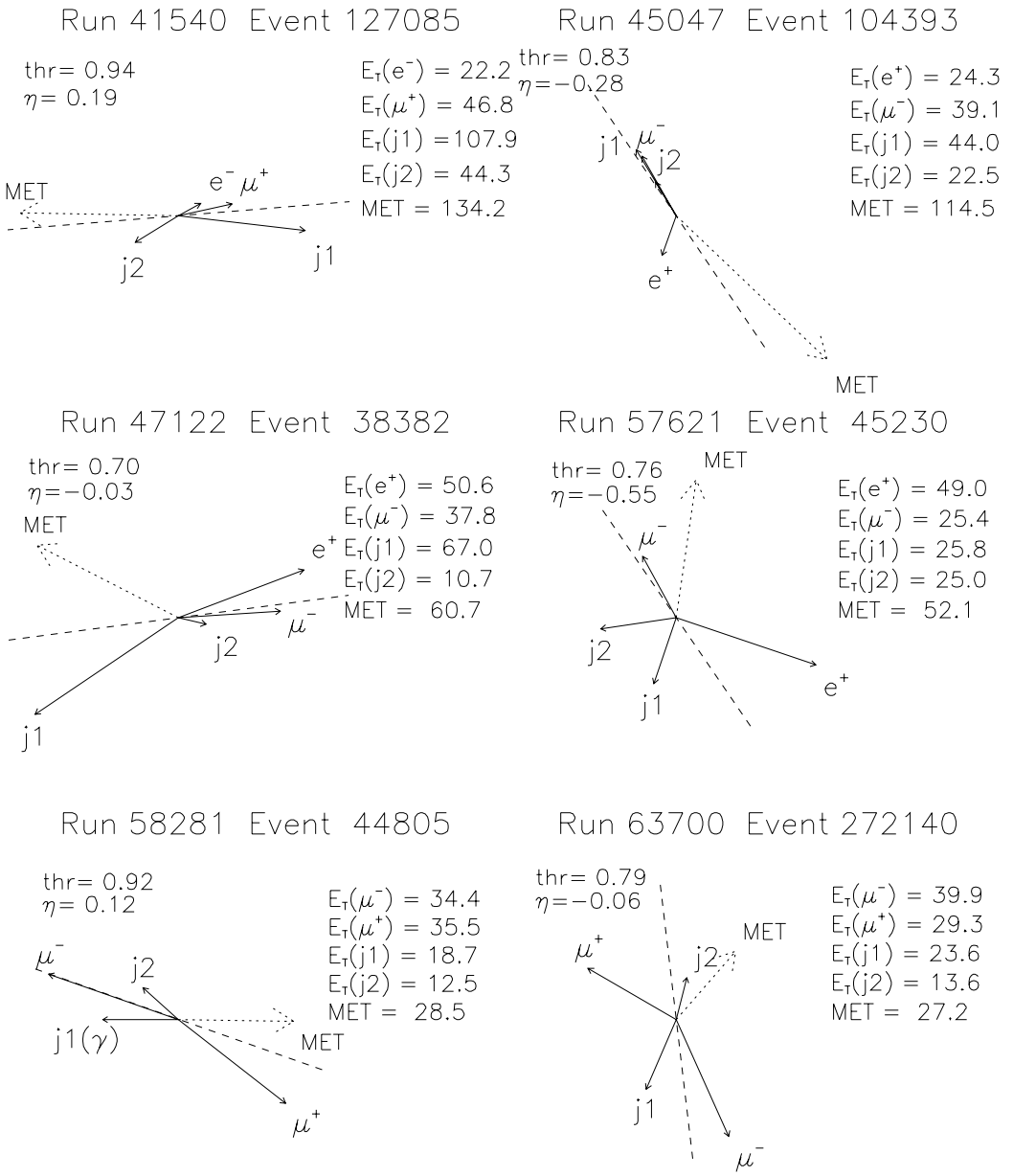

Figure 2.10: Schematic (r, ϕ) display of ee, $\mu\mu$, and $e\mu$ top dilepton candidates. The vector lengths represent the transverse momenta of the objects. Note that we plot quantities as used for the dilepton selection; i.e. electron and jet energies are not corrected, but $\not\!\!E_T$ is corrected for muons and jets. The dashed lines represent the thrust axes of the events (see Chapter 4).

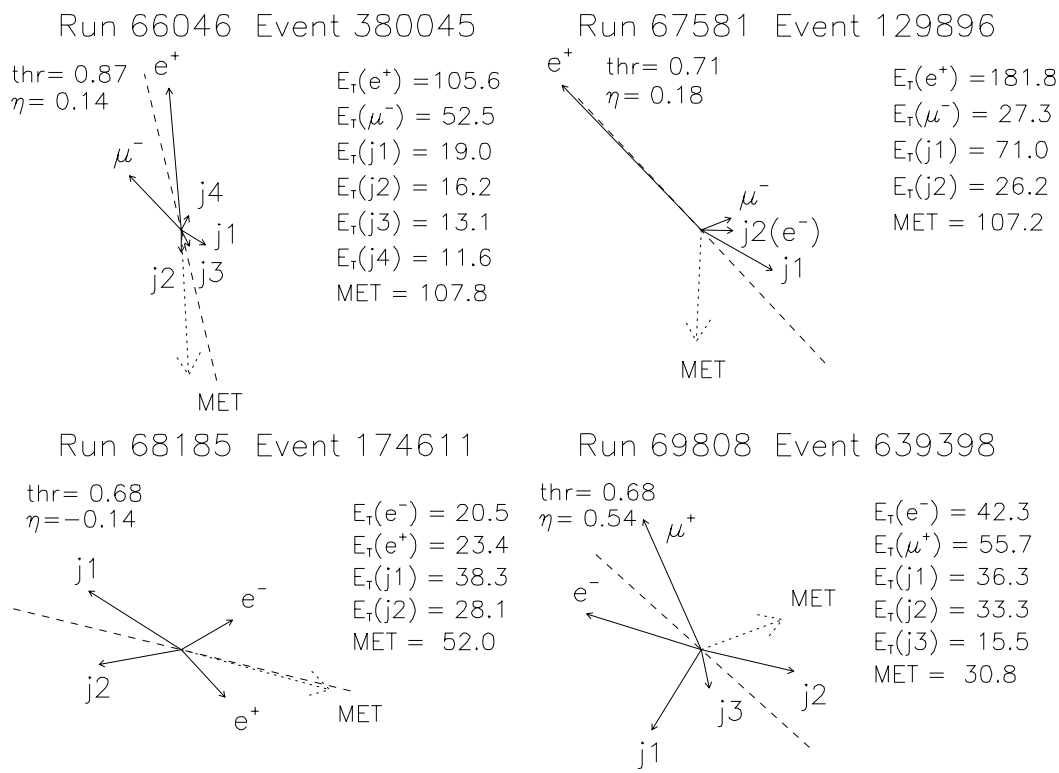

Figure 2.11: Schematic (r, ϕ) display of ee, $\mu\mu$, and $e\mu$ top dilepton candidates. The vector lengths represent the transverse momenta of the objects. Note that we plot quantities as used for the dilepton selection; i.e. electron and jet energies are not corrected, but $\not\!\!E_T$ is corrected for muons and jets. The dashed lines represent the thrust axes of the events (see Chapter 4).

Run/Event	SLT tag			SVX tag	
	type		jet tagged	vertex type	jet tagged
41540/127085	μ	$p_t = 8.7$ GeV/c	j1	2–track	j1
57621/45230	μ	$p_t = 21$ GeV/c	j1	4–track	j1
63700/272140	μ	$p_t = 3.7$ GeV/c	j2	-	-
69808/639398	-	-	-	5–track	j2

Table 2.15: Top dilepton candidates with b-tags. Jets are ordered by E_T, i.e. 'j1' is the jet with the highest E_T , 'j2' is the jet with the second–highest E_T, etc.

efficiency. We again remove the event that is likely to be a radiative Z decay by hand for the cross section calculation, so that the number of observed events is $N = 9$. The result is

$$\sigma_{t\bar{t}} = 8.5^{+4.1}_{-3.3}(stat)^{+1.6}_{-0.8}(syst)\ pb. \tag{2.10}$$

B–tagging

We use the presence of a soft lepton from semileptonic b decays (SLT tag) [46] or of a secondary vertex in the silicon vertex detector (SVX tag) as identified by the SECVTX tagging algorithm [38] to identify jets from b quarks. We find that four of the ten events are tagged. Three events have SLT tags and three events have SVX tags. Two events have a jet that is tagged by both SVX and SLT. The tagging information is summarized in Table 2.15.

Chapter 3

TAU DILEPTONS

Er scheint mir, mit Verlaub von euer Gnaden,
Wie eine der langbeinigen Zikaden,
Die immer fliegt und fliegend springt
Und gleich im Gras ihr altes Liedchen singt;
Und läg er nur noch immer in dem Grase!
In jeden *Quark* begräbt er seine Nase.

J.W. v. Goethe, *Faust I, Prolog im Himmel*

In this chapter we present a search for dileptons from $t\bar{t}$ decays with one electron or muon and one *hadronically* decaying tau lepton:

$$t\bar{t} \to W^+W^-b\bar{b} \to (\ell\nu_\ell)(\tau\nu_\tau)\, b\bar{b} \qquad (\ell = e \text{ or } \mu)$$
$$\hookrightarrow hadrons + \nu_\tau.$$

The first algorithm to identify hadronically decaying τ's with CDF was developed to study lepton universality in $W \to \tau\nu$ decays [48]. Top dileptons with hadronic τ's were previously searched for by [49]. The starting point for this analysis was the work described in Ref. [50].

In the following sections we will discuss in detail all the steps of the analysis: τ decays, clustering algorithm in the calorimeter for τ's, kinematical and geometrical acceptance, τ identification variables, identification cuts and

their efficiencies, Z removal, topological cuts, total acceptance $\times$ efficiency and expected number of events from top, backgrounds, observation in the data, and cross section.

3.1 Starting the τ search

3.1.1 τ decays

In Table 3.1 we list the dominant decay modes of the τ lepton and their branching ratios. The PDG [52] gives a total branching ratio for decays into one charged hadron ("one-prongs") of (49.83$\pm$0.35)% and (14.38$\pm$0.24%) for decays into three charged hadrons ("three-prongs"), for a total of 64.21%. The vast majority of the charged hadrons in the final state are pions; decays into charged kaons occur only at the couple–of–percent level.

We note that about 73% of all one-prong and 41% of all three-prong decays are associated with at least one π^0. This analysis uses the method developed in Ref. [50] to identify π^0's by searching for the photons from the decay $\pi^0 \rightarrow \gamma\gamma$ in the CES. By incorporating π^0's we are able to increase the acceptance for hadronic τ decays.

3.1.2 Finding τ clusters in the calorimeter

Based on the above observations and taking into account the low τ mass one expects an hadronically decaying τ lepton to appear in the detector as a narrowly collimated jet with low track multiplicity and possibly an electromagnetic component due to a π^0. A τ–searching algorithm can therefore start in two ways: One can either look for isolated tracks pointing at hadronic energy in the calorimeter or search for narrow clusters in the calorimeter. The

Decay Mode	Branching Ratio
"Leptonic Decay Modes"	
$\tau^- \to e\bar{\nu}_e\nu_\tau$	(18.01 ± 0.18) %
$\tau^- \to \mu\bar{\nu}_\mu\nu_\tau$	(17.65 ± 0.24) %
"One Prong Hadronic Decay Modes"	
0 neutrals:	
$\tau^- \to \pi^-\nu_\tau$	(11.7 ± 0.4) %
$\tau^- \to K^-\nu_\tau$	(0.67 ± 0.23) %
$\tau^- \to K^*(892)^-\nu_\tau$	(1.45 ± 0.18) %
Sum:	(13.82 ± 0.50) %
≥ 1 neutrals:	
$\tau^- \to \rho\nu_\tau \to \pi^-\pi^0\nu_\tau$	(25.2 ± 0.4) %
$\tau^- \to K^-\pi^0\nu_\tau$	(1.2 ± 0.5) %
$\tau^- \to a_1\nu_\tau \to \pi^-2\pi^0\nu_\tau$	(9.6 ± 0.4) %
$\tau^- \to \pi^-3\pi^0\nu_\tau$	(1.28 ± 0.24) %
Sum:	(37.28 ± 0.79) %
"Three Prong Hadronic Decay Modes"	
0 neutrals:	
$\tau^- \to a_1\nu_\tau \to \pi^-\pi^-\pi^+\nu_\tau$	(8.42 ± 0.31) %
≥ 1 neutrals:	
$\tau^- \to ... \to \pi^-\pi^-\pi^+ \geq 1\pi^0\nu_\tau$	(5.63 ± 0.22) %
$\tau^- \to (a_1\pi)^-\nu_\tau$	
$\tau^- \to \rho^0\pi^-\pi^0\nu_\tau$	
$\tau^- \to \rho^-\pi^-\pi^+\nu_\tau$	
$\tau^- \to \rho^+\pi^-\pi^-\nu_\tau$	
$\tau^- \to \omega\pi^-\nu_\tau$	(1.6 ± 0.4) %

Table 3.1: Current world averages for the branching ratios of dominant decay modes of the τ^- lepton [52].

analysis presented here starts from calorimeter clusters; a track–based analysis is presented in Ref. [53].

The tau clustering algorithm [54] begins by checking the E_T of the tower with the highest E_T in a standard CDF jet cluster[1]. If the E_T of this tower is larger than 4 GeV, it is defined as the 'seed tower' for a tau cluster.

[1]We use jets that are clustered using a cone of radius 0.4 in η–ϕ space for this.

At least one calorimeter seed tower with $E_T > 4$ GeV
≤ 6 towers with $E_T > 1$ GeV in a cluster
Seed track with $p_T > 4.5$ GeV within $\Delta R < 0.4$ of cluster center

Table 3.2: Loose requirements for creating a tau cluster.

The calorimeter towers form a grid in η–ϕ space. All of the eight towers surrounding the seed tower that have $E_T > 1$ GeV become part of the tau cluster. The algorithm then selects *narrow* calorimeter clusters by requiring that there be fewer than 6 towers in a cluster. Clusters with more towers are dropped.

Next, the highest-p_T track with $p_T > 4.5$ GeV/c pointing within a cone of radius 0.4 in η–ϕ space from the cluster center becomes the 'seed track'. If there is no such track found the tau cluster is dropped. If there is a primary z-vertex as measured by the vertex chamber (VTX) within 5 cm of the z of the track this becomes the z-vertex of the τ jet, otherwise the z of the seed track is used. The calorimeter quantities (E_T, η) of the cluster are recalculated using this z. Tracks with $p_T > 1$ GeV/c and a z within 10 cm of the z-vertex of the τ jet, that also extrapolate to a tower in the cluster, are defined as 'shoulder tracks'. The track multiplicity of the τ jet is then defined as the number of tracks (seed and shoulder) within a 10° cone of the cluster center. Table 3.2 summarizes the cuts imposed at the tau cluster level.

3.1.3 Identification of π^0's in the CES

Here we describe the identification of π^0's in the strip chamber (CES) as developed in Ref. [50]. In the rest frame of the π^0 the 2 photons from the decay $\pi^0 \rightarrow \gamma\gamma$ have an energy $m_{\pi^0}/2 = 67.5\ MeV$. The maximum separation of the 2 photons in the CES is $\delta = R \times \frac{67.5}{E_{\pi^0}(MeV)}$, where R is the distance of

the photon shower in the CES from the interaction point (the radial distance of the center of the CES is about 184 cm). For a π^0 with an energy of several GeV the separation is on the order of only a couple of cm. Therefore, the algorithm takes the possibility into account that the two photon showers have a significant overlap.

We start by extrapolating the tracks in the 10° cone associated with the tau cluster to the plane of the CES inside the CEM. The average response of the CEM [48, 50] to charged hadrons as a function of their p_T is subtracted from the E_T in the CEM tower to which the track extrapolates. In the following we consider only towers that are left with $E_T^{EM} > 0.1$ GeV. For each such tower we search the corresponding section of the CES for narrow strip clusters(5 channels) and wire clusters (7 channels). We accept strip clusters that have $E > 0.5$ GeV and $\chi^2_{str} < 20$. Clusters with $E > 20$ GeV are accepted regardless of the χ^2_{str} in order to account for overlapping photon showers. Wire clusters are accepted if $E > 0.5$ GeV (no χ^2_{wire} cut). The cluster energies are then corrected for local variations of the CES response. (for details see appendix of Ref. [50]).

Next, we search for strip and wire clusters with matching energies. We allow for 2 cases: 1) one wire cluster and one strip cluster match in energy within 1 GeV. If both have $E > 10$ GeV they are only required to match within 5 GeV. 2) the energy of one wire cluster matches the energy sum of two strip clusters (to allow for photons overlapping in the z-view). The energy matching requirement is the same as in case 1 except that if the wire cluster energy as well as the energy sum of the strips are above 20 GeV they are only required to match within 50 GeV. If we find a match we define the matching strip and wire cluster as a π^0 candidate. Its energy is given by the CEM energy of the tower (after the subtraction of any energy due to a track pointing at

the same tower as described above) and its position in the CES is given by the wire and strip cluster(s). From this we can calculate E_T, ϕ and η for the π^0 candidate.

If we do not find a match we consider a strip cluster with $E > 1$ GeV a π^0 candidate in order to maintain efficiency. In that case we measure only the z-position from the strip cluster. We use the center of the tower as the best guess for the local x-position in the chamber when calculating the ϕ of the π^0 candidate.

It is possible that more than one π^0 candidate is found for a tau cluster. Using the information of all π^0 candidates associated with a tau cluster we define the p_T of the τ as the scalar sum of the p_T of the tracks in the 10° cone and the E_T^{EM} of the π^0 candidates as measured in the CEM:

$$p_T^{\tau} = p_T^{trk+\pi^0} \equiv \sum_{trk} p_T^{trk} + \sum_{\pi^0} E_T^{EM} \tag{3.1}$$

3.2 Geometrical and kinematical acceptance

We use the PYTHIA $t\bar{t}$ Monte Carlo and the matching method from section 2.1.1 to calculate the geometrical and kinematical acceptance, $A_{geom \cdot P_T}$, for tau dileptons. Because of the angle between the τ and its charged decay products we require that the distance $\Delta R = \sqrt{(\Delta\phi)^2 + (\Delta\eta)^2}$ in $\eta - \phi$ space between the generated tau and the tau cluster in the calorimeter be less than 0.2, whereas $\Delta R < 0.04$ is required for electrons and muons. Figure 2.2 shows the ΔR distribution for τ's.

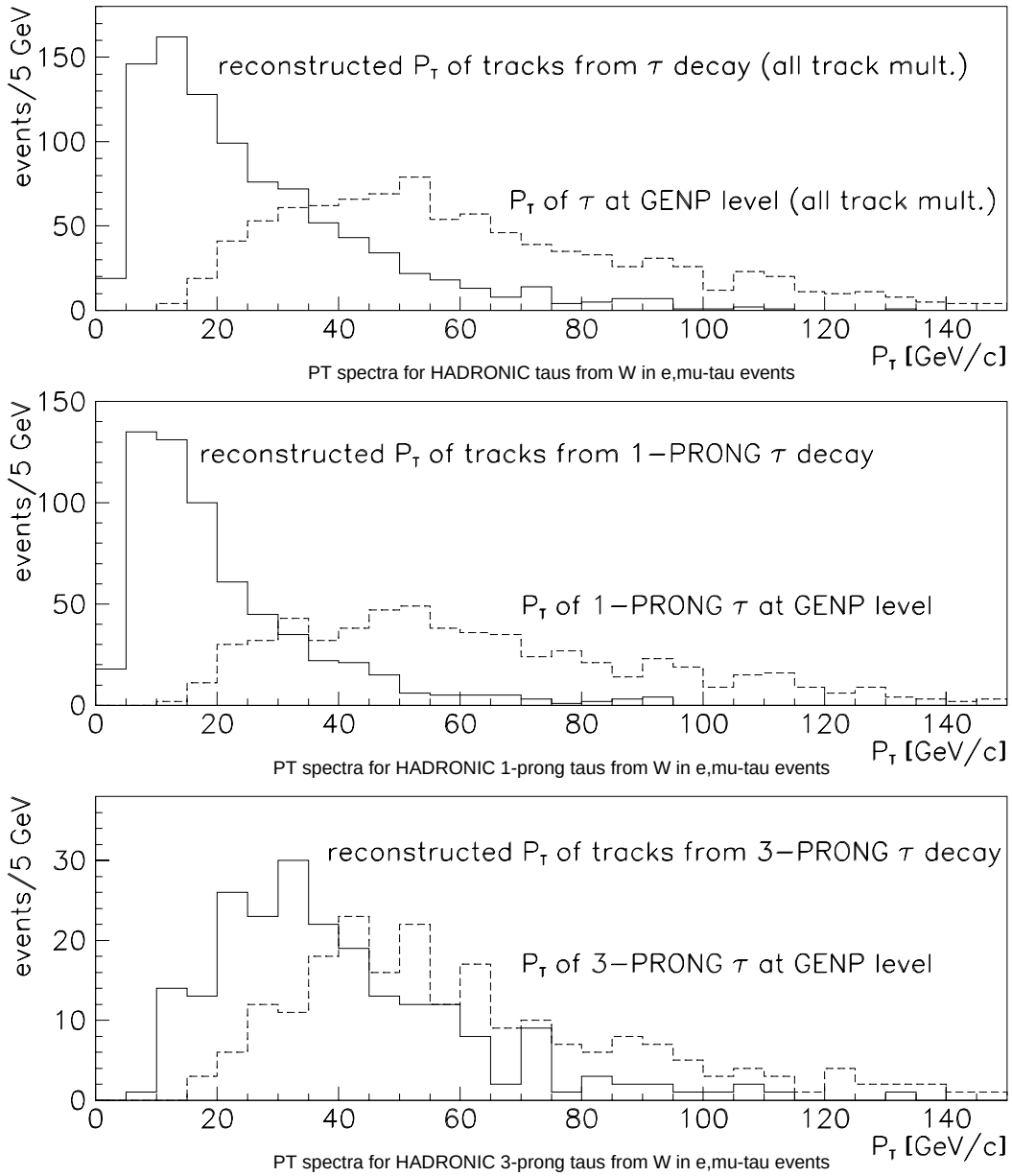

Figure 3.1: Top: The p_T spectra of τ's at the generator level (GENP) and of their reconstructed charged decay products in $e\tau$ and $\mu\tau$ $t\bar{t}$ MC events (m_{top} = 175). Center: One-prong τ decays only. Bottom: Three-prong τ decays only.

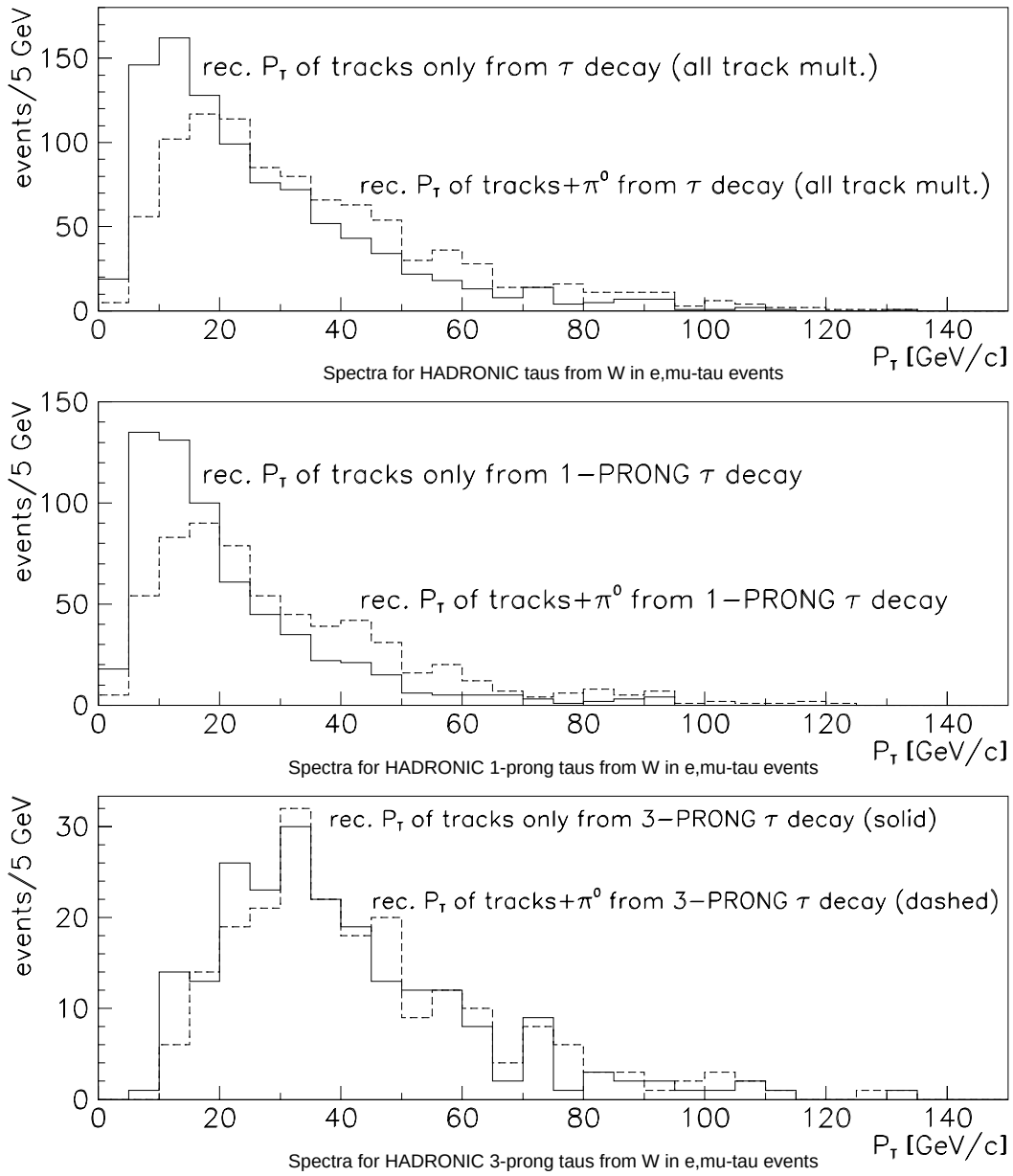

Figure 3.2: Comparison of reconstructed p_T spectra of tracks only and tracks + π^0's for τ decays in $e\tau$ and $\mu\tau$ $t\bar{t}$ MC events ($m_{top} = 175$).

3.2.1 p_T spectra

In Figure 3.1 we compare the p_T of τ's at the generator level with the reconstructed $\sum_{trk} p_T^{trk}$ of the tracks associated with the tau clusters that matches to the generated τ's. The τ's are selected from $e\tau$ and $\mu\tau$ events in the PYTHIA $t\bar{t}$ Monte Carlo. As expected from the presence of the τ neutrino in the τ decay the reconstructed p_T–spectrum is much softer. This results in a reduced kinematical acceptance for τ leptons compared with electrons and muons. In addition, due to the large fraction of one-prong decays accompanied by π^0's the effect is even stronger for one-prong decays compared with three-prong decays. As mentioned above, the identification of π^0's helps to gain some of the lost acceptance back. In Figure 3.2 we illustrate this point by plotting p_T^{trk} and $p_T^{trk+\pi^0}$ for one-prongs and three-prongs. For a cut at 15 GeV we find an increase in acceptance of 22% if all track multiplicities are combined. The increase is 37% for one-prongs; for three-prongs it is 5%.

3.2.2 Calculation of $A_{geom \cdot P_T}$

For the $e\tau$ and $\mu\tau$ channel we use the same definitions of primary tight electrons and muons as in Chapter 2. Due to the softer p_T spectrum for τ's we increase the acceptance for hadronic taus by using $p_T^{trk+\pi^0}$ and lowering the cut to 15 GeV compared with 20 GeV used for electrons and muons. We choose not to cut on the E_T of the τ jet because of potential problems with the detector simulation [55].

Table 3.3 gives a detailed break down of the results we obtain for $A_{geom \cdot P_T}$. We list $e\tau$ and $\mu\tau$ events separately, distinguish one-prongs and three-prongs, and separate the events by the lepton origins, i.e. by the particle decays that produced the leptons. All numbers in the table are in percent. We

find a non-negligble contribution from b decays at this level. However, since we later impose isolation cuts for both leptons (see below) there is basically no efficiency for identifying τ's in these types of events (see also Table 3.7). Consequently, the only two classes of events that we are *efficient* for are those with both leptons coming from W's and events where the e or μ comes from a leptonic τ decay and the hadronically decaying τ comes from a W decay. Therefore, we calculate the total *acceptance* $A_{geom \cdot P_T}$ based only on these two classes. The result is

$$A_{geom \cdot P_T} = (0.65 \pm 0.03)\% \tag{3.2}$$

with 0.32% for $e\tau$ events and 0.33% for $\mu\tau$ events. For one-prongs (three-prongs) we get 0.39% (0.18%), and for other track multiplicities we find 0.08%.

In Table 3.4 we list the corresponding numbers if we do not use π^0's and cut on $p_T^{trk} > 15$ GeV instead of $p_T^{trk+\pi^0} > 15$ GeV. In this case we find a smaller acceptance $A_{geom \cdot P_T} = (0.52 \pm 0.02)\%$.

3.3 τ lepton identification

3.3.1 Identification variables

In Table 3.5 we list the set of cuts we place on various variables for identifying hadronically decaying τ's. These cuts were chosen to be simple and efficient for τ's . At the same time they are intended to be effective in reducing the misidentification of QCD jets as τ's . As we show below, the identification variables for τ's are reasonably well modeled by the simulation. We therefore use simulated τ decays from $t\bar{t}$ pairs to set cuts and to calculate their efficiency. Since the efficiency of the isolation cut depends on the topology of the event, we choose the $t\bar{t}$ MC over a $W \to \tau\nu$ MC. In Figure 3.3 we show distributions

τ from	W	W	W	W	b	b	b	From	Grand
ℓ from	W	b	c	τ	W	τ	b	$W \to \tau$	total
$e\tau$(tot.)	0.32	0.11	0.03	0.00	0.09	0.00	0.01	0.46±.02	0.59±.03
1-prong	0.20	0.08	0.02	0.00	0.00	0.00	0.00	0.29±.02	0.30±.02
3-prong	0.09	0.02	0.01	0.00	0.02	0.00	0.00	0.12±.01	0.14±.01
other	0.04	0.01	0.00	0.00	0.07	0.00	0.01	0.05±.01	0.15±.01
$\mu\tau$(tot.)	0.31	0.14	0.03	0.02	0.09	0.01	0.02	0.50±.03	0.63±.03
1-prong	0.18	0.09	0.02	0.01	0.00	0.00	0.00	0.30±.02	0.30±.02
3-prong	0.09	0.04	0.01	0.00	0.01	0.00	0.00	0.14±.01	0.16±.01
other	0.03	0.01	0.00	0.01	0.08	0.01	0.01	0.06±.01	0.17±.01
$e\tau + \mu\tau$	0.63	0.25	0.07	0.02	0.18	0.01	0.02	0.96±.03	1.22±.04

Table 3.3: The geometrical and kinematic acceptance $A_{geom \cdot P_T}$ for tau dilepton events with $|\eta^{\tau}_{det}| < 1.2$ and $p_T^{trk+\pi^0} > 15$ GeV calculated from the PYTHIA $t\bar{t}$ Monte Carlo. All numbers are given *in percent*. They are relative to all 80,000 generated $t\bar{t}$ events, i.e. all branching ratios are included in these numbers. Here ℓ stands for e or μ only. The acceptance is broken down by track multiplicity of the τ's (rows) and by the parent particles of the leptons (columns).

of the identification variables for these MC τ's together with distributions for QCD jets from unbiased dijet samples (JET20 and JET70 samples, see section 3.8.1) to illustrate how we can separate hadronically decaying τ's from QCD jet background. In the following we discuss each of the identification cuts:

1. Track multiplicity:

   Since τ's decay hadronically into one-prongs and three-prongs we require that a reconstructed τ have a track multiplicity of either one or three in a 10° cone around the tau cluster center. Two-prongs stem either from a one-prong with an extra track in the cone or a three-prong where one track misses the cone. However, Figure 3.3 shows that the ratio of signal

τ from	W	W	W	W	b	b	b	From	Grand
ℓ from	W	b	c	τ	W	τ	b	$W \to \tau$	total
$e\tau$(tot.)	0.25	0.08	0.03	0.00	0.08	0.00	0.01	0.36±.02	0.47±.02
1-prong	0.14	0.05	0.02	0.00	0.00	0.00	0.00	0.21±.02	0.21±.02
3-prong	0.08	0.02	0.01	0.00	0.01	0.00	0.00	0.11±.01	0.13±.01
other	0.03	0.01	0.00	0.00	0.07	0.00	0.01	0.04±.01	0.14±.01
$\mu\tau$(tot.)	0.24	0.11	0.03	0.02	0.08	0.00	0.01	0.40±.02	0.51±.03
1-prong	0.12	0.07	0.02	0.01	0.00	0.00	0.00	0.21±.02	0.21±.02
3-prong	0.09	0.04	0.01	0.00	0.01	0.00	0.00	0.14±.01	0.15±.01
other	0.03	0.01	0.00	0.01	0.07	0.00	0.01	0.05±.01	0.15±.01
$e\tau + \mu\tau$	0.50	0.19	0.06	0.02	0.16	0.00	0.02	0.76±.03	0.98±.04

Table 3.4: Same as Table 3.3, except using $p_T^{trk} > 15$ GeV instead of $p_T^{trk+\pi^0} > 15$ GeV. All numbers are given *in percent*. They are relative to all 80,000 generated $t\bar{t}$ events, i.e. all branching ratios are included in these numbers. Here ℓ stands for e or μ only. The acceptance is broken down by track multiplicity of the τ's (rows) and by the parent particles of the leptons (columns).

to background for two-prongs is low, and so we do not use them. The loss in acceptance is about 10%.

2. E/p:

   Here we incorporate π^0's by defining E/p as $E_T/p_T^{trk+\pi^0}$. Figure 3.4 shows how this reduces the tail of the distribution on the high side. Because one-prongs have a larger high tail than three-prongs we make different cuts on the high side for one-prongs ($E/p < 2.0$) and three-prongs ($E/p < 1.5$) to get similar efficiencies. This cut is mostly useful for rejecting fake three-prongs and fake high-p_T one-prongs (see Figure 3.3).

3. RMS cluster width σ_{cl}:

   The RMS width σ_{cl} of a cluster is defined as the second moment of the

Track multiplicity in 10° cone:
use 1-prongs and 3-prongs only

E/p cut:
$0.5 < \frac{E_T}{p_T^{trk+\pi^0}} < 2.0$ (1-prongs)
$0.5 < \frac{E_T}{p_T^{trk+\pi^0}} < 1.5$ (3-prongs)

Sliding RMS cluster width cut:
$\sigma_{cl} < 0.11 - 0.025 \times E_T/100$ (1-prongs)
$\sigma_{cl} < 0.13 - 0.034 \times E_T/100$ (3-prongs)

Mass cut:
$m_{trk+\pi^0} < 1.8$ GeV

of π^0 candidates:
$\#\pi^0 < 3$

Isolation:
$I^{\tau}_{trk} < 1$ GeV$/c$

Electron removal:
Reject 1-prongs with $E/p < 4, \mathrm{EMFrac} > 0.9$ or
clusters with EMFrac > 0.95 as electrons

Muon removal:
Reject clusters with $E_T < 8$ GeV, $0.05 < E_{EM} < 2$ GeV,
$0.5 < E_{Had} < 5$ GeV or with a muon stub with $|\phi_\tau - \phi_{stub}| < 15^o$
as muons

Table 3.5: Summary of τ identification variables and cuts.

E_T distribution among the towers in the cluster:

$$\sigma_{cl} \equiv \sqrt{\sigma_\phi^2 + \sigma_\eta^2}\ , \tag{3.3}$$

where $\sigma_\phi = \sqrt{<(\phi_i - <\phi>)^2>}$, and $\sigma_\eta = \sqrt{<(\eta_i - <\eta>)^2>}$, with ϕ_i and η_i being the coordinates of the i-th tower in the tau cluster.

We use the center of gravity of the energy detected by the 2 photomultiplier tubes for calculating ϕ_i in each tower to get the best possible ϕ resolution from the calorimeter. In the η direction the center of the tower is used. Figure 3.3 shows how we can capitalize on the fact that τ clusters are narrower than clusters from QCD jets.

In Figure 3.5 we plot the mean RMS vs the E_T of the jet for τ's as well as for QCD jets. We see that the shower becomes more collimated with increasing E_T and the cluster width decreases. We take this effect into account by making a sliding cluster width cut. We select the parameters for the cut by using use the slope of the linear fit and setting the offset such that the cut is about 90% efficient for τ's . Since we find different behavior for one-prongs and three-prongs we use different parameters for the two cases.

4. Mass:

   We reconstruct the invariant mass of a τ from the tracks in the 10° cone and the π^0's associated with a tau cluster. We use the position information from the CES for the π^0's as described in section 3.1.3. For one-prongs without any identified π^0's we set the mass equal to the π mass (140 MeV). We find that a physically well motivated cut near the actual τ mass (1.78 GeV) has good efficiency for τ's and good rejection power against QCD jets, especially high-p_T jets.

5. Number of π^0's:

   Table 3.1 shows that τ decays basically do not involve more than 2 π^0's, so we require that we reconstruct fewer than 3 π^0 candidates in a tau cluster, as defined in section 3.1.3. This cut is very efficient for τ's after all other cuts have been applied and gives an additional 10% rejection of QCD jets (see Table 3.6).

6. Tracking Isolation:

   For τ's we define the tracking isolation I^{τ}_{trk} as the sum of the transverse momenta of all tracks in a cone with radius 0.4 in $\eta - \phi$ space around the tau cluster center and with $\Delta z = z_{trk} - z_{\tau} < 20$ cm. The tracks that define the track multiplicity associated with the tau cluster, i.e. the seed track and the shoulder tracks, are exluded from the sum. Consequently, only tracks that point near the tau cluster but that do not point directly at towers in the cluster are used to form the τ isolation variable. This definition is different from that for electrons and muons because it is not relative to the p_T of the lepton itself. We place a tight cut on the tracking isolation by requiring $I^{\tau}_{trk} < 1$ GeV/c.

7. Electron Removal:

   Electrons produce very narrow clusters with one track pointing at them and can therefore be mistaken as one-prong τ's. We rely on the high electromagnetic fraction in electron clusters to reject them. Note that we cut on the usual E/p ($= E_T/p_T$) here because the EM energy of an electron gets 'interpreted' by the algorithm as a π^0, so that the E/p value used for the τ algorithm (item 2) comes out wrong for electrons. The removal is very efficient for keeping real τ's (see the EM fraction for τ's in Figure 3.3).

8. Muon Removal:

   Muons are minimum ionizing particles and deposit typically about 300 MeV in the electromagnetic compartment and about 2 GeV in the hadronic compartment of the calorimeter towers that they hit. However, as the seed tower E_T requirement for a tau cluster is only 4 GeV it is not unlikely that a tau cluster is created due to a muon. Tau clusters are rejected either if there is a track stub in a muon chamber within 15° of the tau cluster or if the energy depositions in the CEM and the CHA are consistent with that of a minimum ionizing particle.

3.3.2 τ identification efficiency for $t\bar{t}$ events

We list the efficiency of all cuts and the total τ identification efficiency ϵ^{τ}_{ID} that we find for hadronic τ decays using the PYTHIA $t\bar{t}$ Monte Carlo in Table 3.6. We use two ways for calculating the single cut efficiency. First we divide the number of dilepton events with an accepted tau cluster that matches to a generated τ from a W decay and passes the cut in question by the number of accepted and matching events (869 events). The results from this calculation are listed in the column 'Cut in question only'. For the second calculation we divide the number of accepted and matching events that pass all identification cuts by the number of accepted and matching events that survive all identification cuts *except* the one cut in question. The results are listed in the column 'All other cuts applied'. The second calculation is intended to reveal correlations among the cuts. For example, cutting on the number of π^0's for all accepted events is only 92.9% efficient. However, if this cut is applied after all other cuts have already been applied we only lose an additional 2.2%. In the third column we list the efficiency for cumulative cuts.

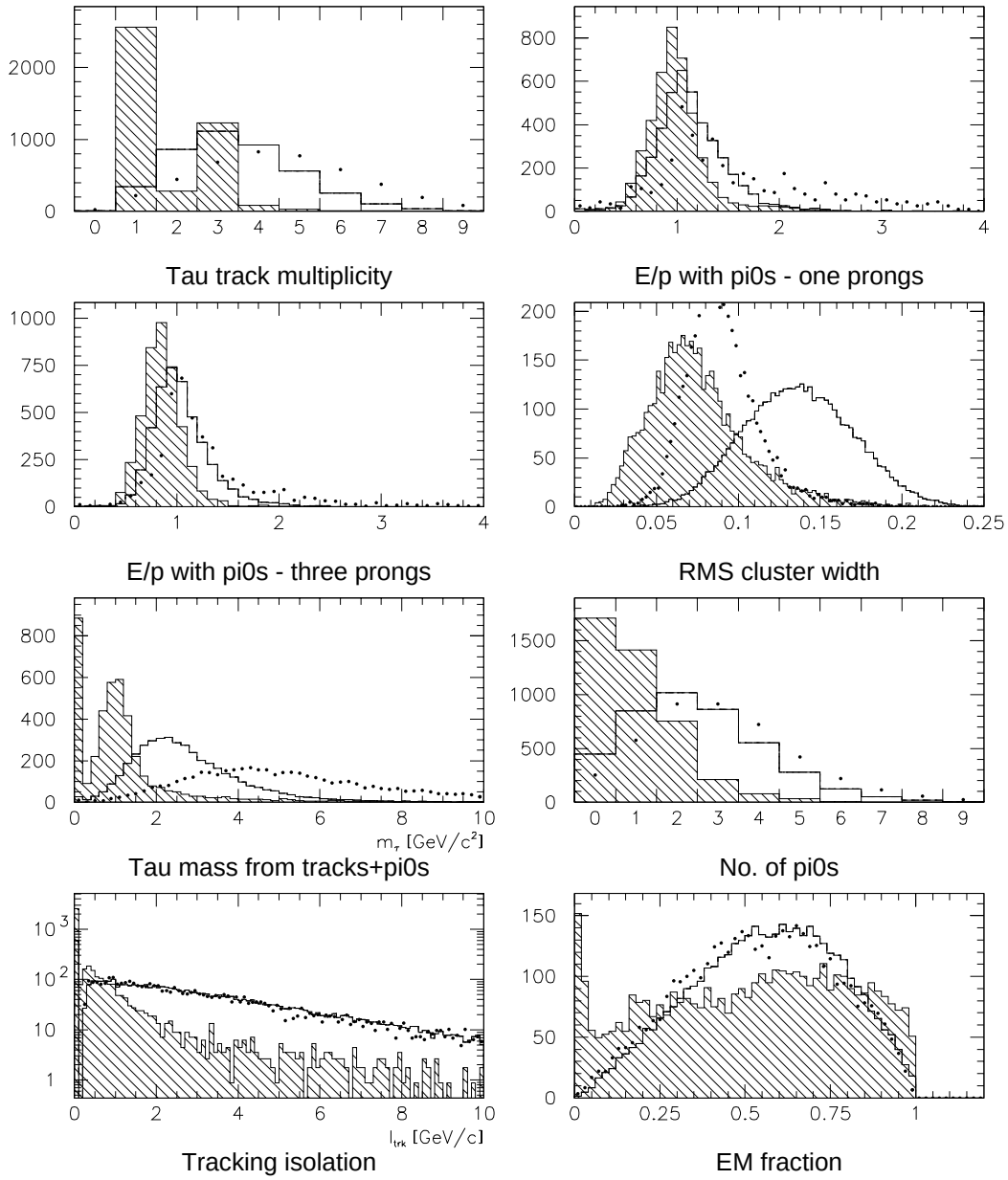

Figure 3.3: Comparison of τ identification variables in the $t\bar{t}$ MC (hatched) and for QCD jets from the unbiased JET20(solid histogram) and JET70(dots) samples. All three histograms for a particular variable are normalized to equal area.

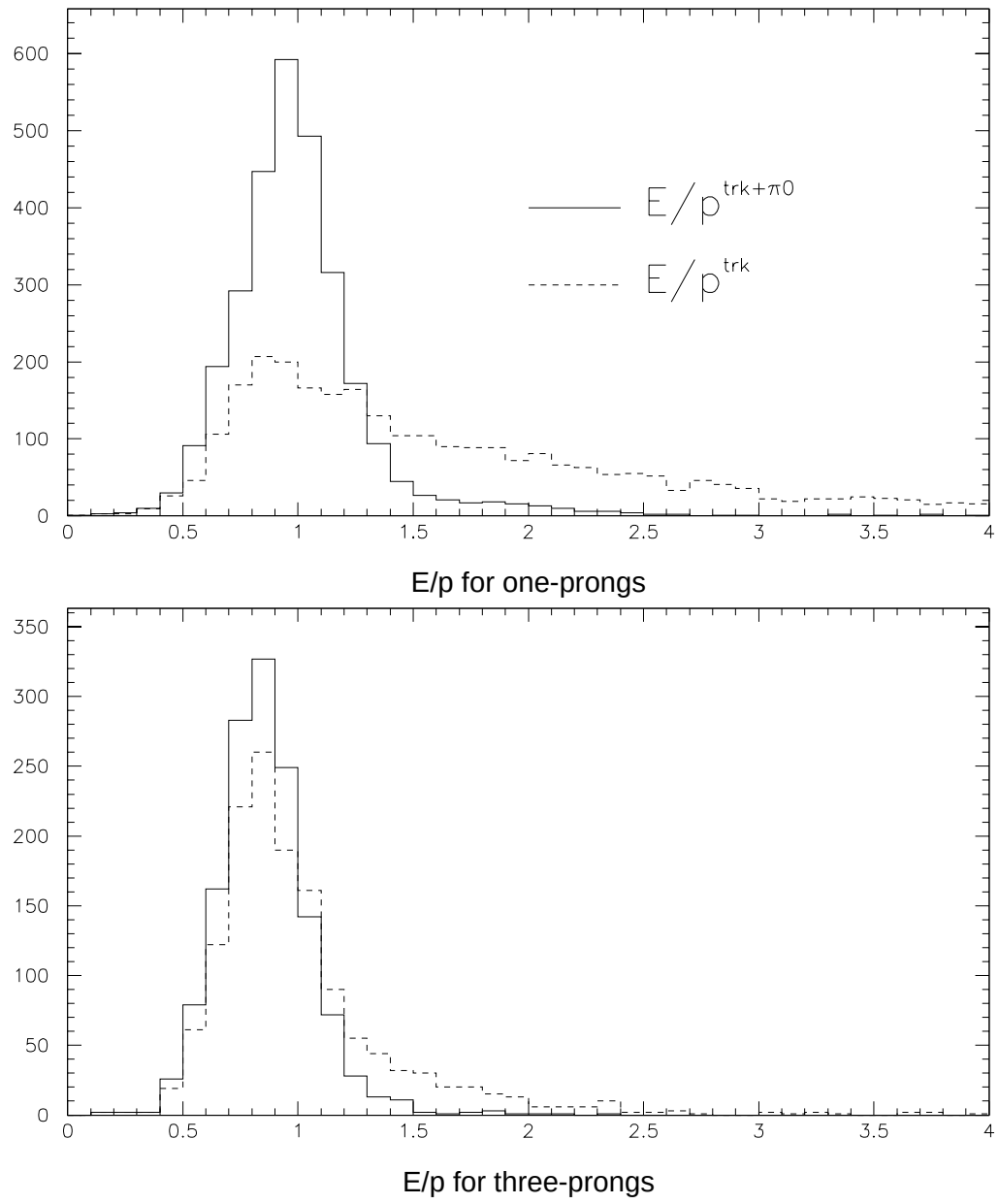

Figure 3.4: The distribution of E/p using p_T^{trk} and $p_T^{trk+\pi^0}$ for one-prong and three-prong τ decays in the PYTHIA $t\bar{t}$ MC.

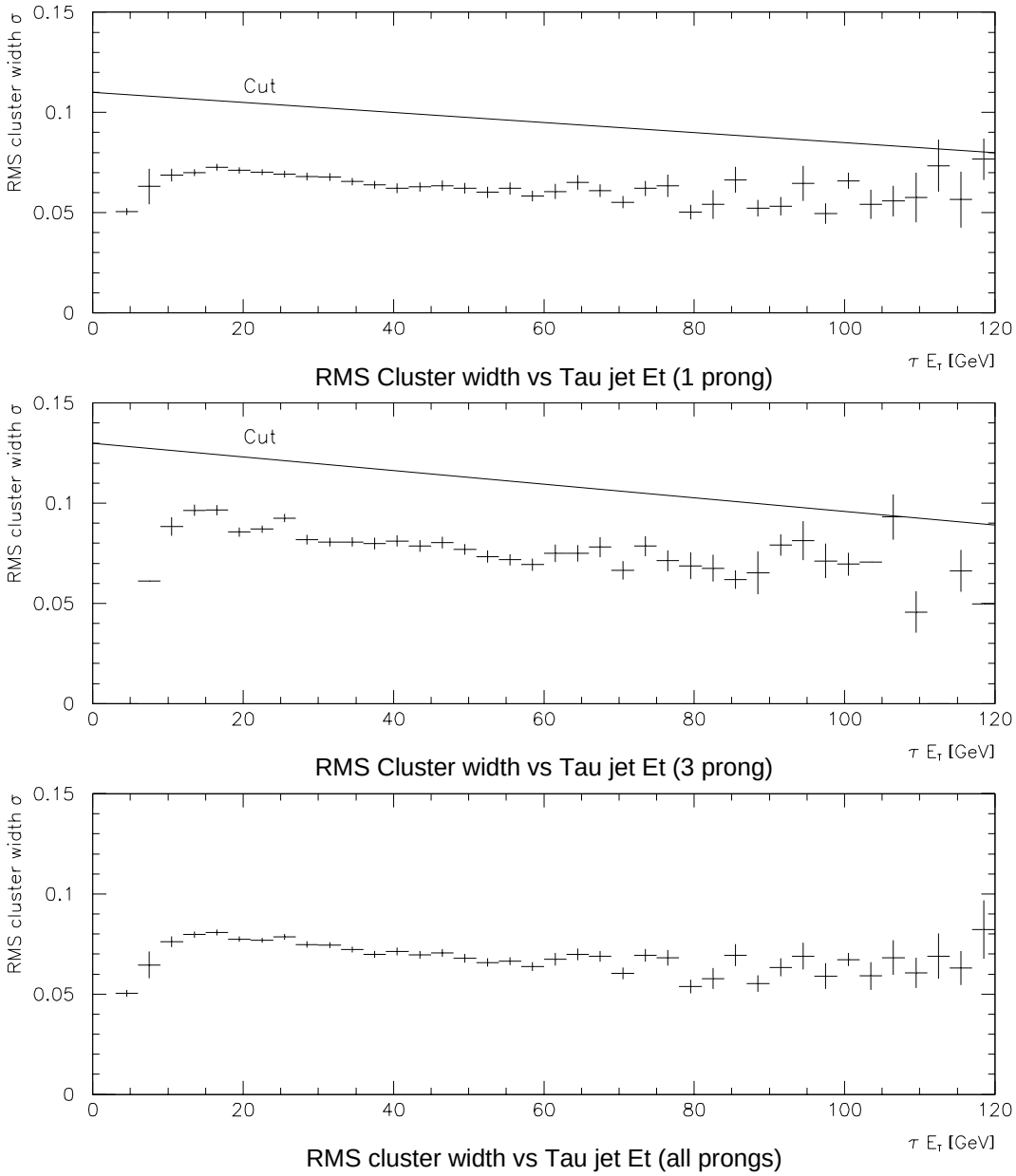

Figure 3.5: The RMS cluster width σ_{cl} vs E_T of the τ jet for matched, hadronically decaying (as determined at the generator level) τ's from $W's$ in the PYTHIA $t\bar{t}$ MC. Top: 1-prongs, Center: 3-prongs, Bottom: all track multiplicities.

For calculating the total efficiency we simply apply all cuts. The ratio between the events that pass all identification cuts (numerator) and all matched and accepted events (denominator) gives the total identification efficiency of

$$\epsilon_{ID}^{\tau} = (56.5 \pm 1.7(stat))\%. \tag{3.4}$$

In Figure 3.6 we plot ϵ_{ID}^{τ} versus $p_T^{trk+\pi^0}$ separately for one-prongs, three-prongs and both combined. Note that the plotted efficiency is higher than 56.5% because to make the plot the track multiplicity cut has been moved from the numerator into the denominator. We find that the efficiency is basically flat as a function of $p_T^{trk+\pi^0}$ out to around 100 GeV/c. However, we observe a slight turn-on for three-prongs. The τ selection for three-prongs becomes fully efficient at about $p_T^{trk+\pi^0} = 25$ GeV/c. After the three-prong efficiency plateaus it is basically the same as for one-prongs.

In Table 3.7 we list the τ identification efficiency for τ's from b quarks. We find a negligible efficiency of $(0.5 \pm 0.3)\%$. As expected, most of these τ's are rejected by the mass cut, the track multiplicity cut and the isolation cut.

3.4 Check of τ identification efficiency with $W \to \tau\nu$ data

Since the τ identification efficiencies are determined from a $t\bar{t}$ Monte Carlo simulation we need to check these efficiencies with an appropriate τ *data* set. Specifically, we are interested in checking if there are any systematic discrepancies in the distributions of the τ identification variables between data and Monte Carlo, and if the identification cut efficiencies are sensitive to these.

The process $W \to \tau\nu$ is an obvious source of high-p_T τ's with hadronic decays. The challenge here is to create a data sample with reasonably high

	Cut in question	All other cuts applied	Cumulative cuts
Track multiplicity 1 or 3	88.6%	93.5%	88.6%
E/p with π^0	96.2%	96.5%	85.3%
slid. RMS Cluster width cut	88.1%	93.9%	77.1%
$m_{trk+\pi^0} < 1.8$ GeV	83.8%	91.8%	68.4%
Number of $\pi^0 < 3$	92.9%	97.8%	66.4%
$I^{\tau}_{trk} < 1$ GeV/c	85.7%	93.2%	61.9%
Electron removal	95.1%	94.8%	58.6%
Muon removal	96.1%	96.5%	56.5%
TOTAL efficiency	(56.5±1.7)%		

Table 3.6: Efficiency of τ identification cuts in MC top dilepton events for τ's from W's.

	Cut in question	All other cuts applied	Cumulative cuts
Track multiplicity 1 or 3	17.4%	100.0%	17.4%
E/p with π^0	97.4%	100.0%	16.3%
slid. RMS Cluster width cut	43.9%	57.1%	7.9%
$m_{trk+\pi^0} < 1.8$ GeV	9.7%	57.1%	2.4%
Number of $\pi^0 < 3$	67.0%	100.0%	2.4%
$I^{\tau}_{trk} < 1$ GeV/c	27.9%	22.2%	0.5%
Electron removal	99.5%	100.0%	0.5%
Muon removal	88.7%	100.0%	0.5%
TOTAL efficiency	(0.5±0.3)%		

Table 3.7: Efficiency of τ identification cuts in MC top events for τ's from b's.

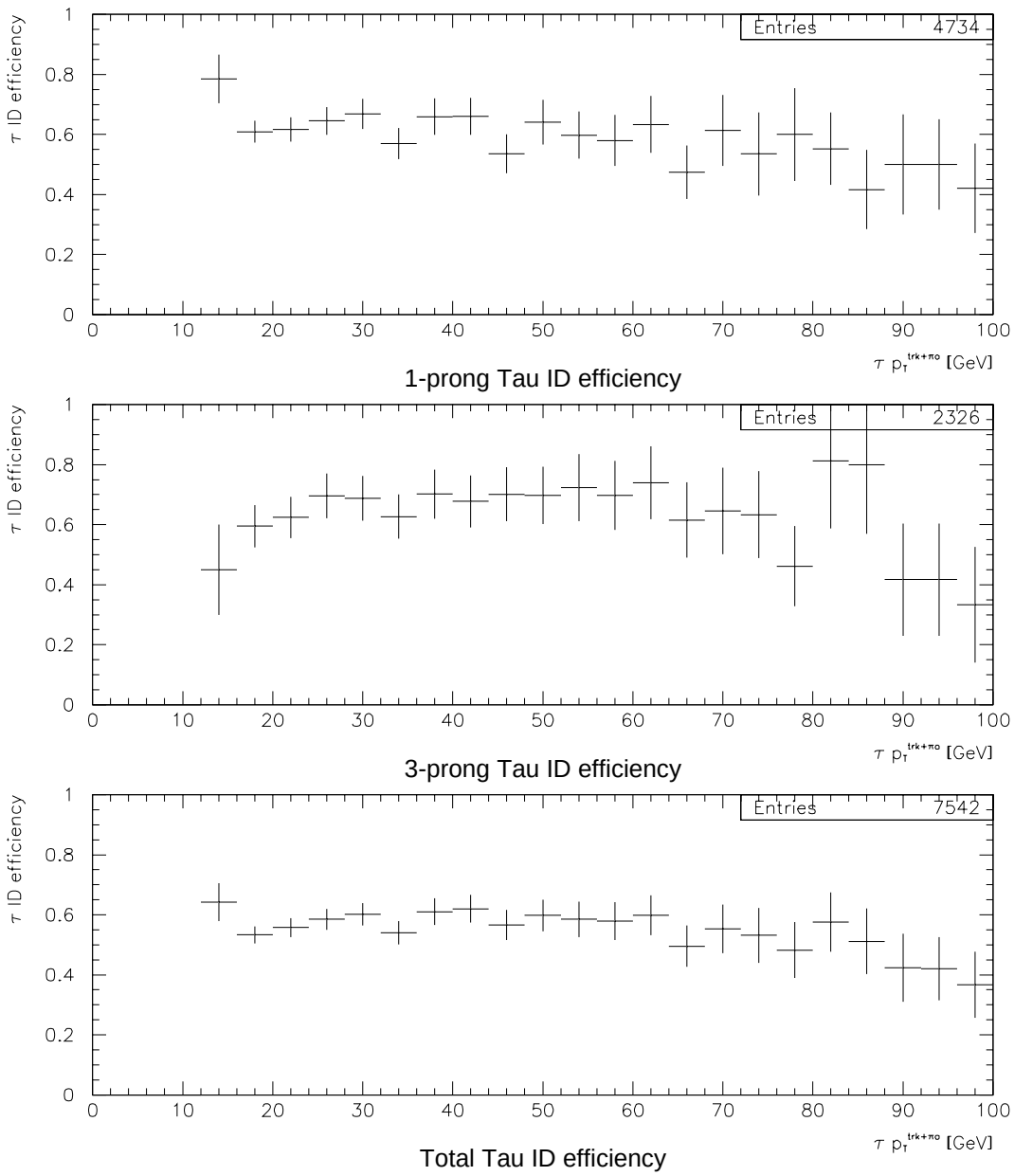

Figure 3.6: Efficiency of τ identification cuts as a function of $p_T^{trk+\pi^0}$. Top: One-prongs only. Center: Three-prongs only. Bottom: Both combined.

$W \to \tau\nu$ content without applying any tau selection (neither offline nor in the trigger) as this would bias the distribution of the τ identification variables. Typically, a $W \to \tau\nu \to hadrons$ decay has one jet from the τ, in addition to missing transverse energy, $\not\!\!E_T$, due to the neutrinos. These events consequently appear as 'monojet' events. Selecting the sample solely based on $\not\!\!E_T$ minimizes the bias as far as the properties of the (τ) jet are concerned.

3.4.1 Data samples

The $\not\!\!E_T$ sample

We start with the $\not\!\!E_T$ sample created by the Rutgers group from the Exotic Streams XOXB_5P (XOX1_3P in Run Ia), which is fed by the Level 3 triggers EXOB(1)_MET_30_TRK_3 and EXOB(1)_MET_30_COSFLT. The selection and cleanup are described in great detail in Ref. [56]. The selection cuts are:

- 1 jet with $E_T > 15$ GeV, $|\eta| < 1.0$, with ≥ 1 associated tracks
- no other jet with $E_T > 10$ GeV
- no other jet with $E_T > 5$ GeV and a 3D angle to monojet of $> 160^o$ ("dijet veto")
- $\not\!\!E_T > 20$ GeV
- Missing E_T significance $S_{\not\!\!E_T} \equiv \frac{\not\!\!E_T}{\sqrt{\Sigma E_T}} > 2.4$.

Events that pass only the following two cuts are also accepted:

- ≥ 1 tau cluster (TAUO bank) with $E_T > 10$ GeV
- $\not\!\!E_T > 30$ GeV

The sample contains about 760k events on 8 tapes.

The monojet sample

To isolate monojet events in this sample we apply additional cuts. Note that the first two cuts are necessary as the $\not\!\!E_T$ sample also contains multijet events (see the last 2 items in the previous list):

- exactly 1 jet with $E_T > 15$ GeV, $|\eta| < 2.0$
- no other jet with $E_T > 7$ GeV, $|\eta| < 4.0$
- the jet makes a tau cluster
- electron and muon removal
- $\Sigma E_T < 100$ GeV
- No energy deposition in the hadron calorimeters that is out of time with the $p\overline{p}$ collision. ($E_T^{out-of-time} = 0.0$ GeV)
- no spurious muon stubs (helps to reject cosmic rays)
- no track with $p_T > 5.0$ GeV within 35° of the $\not\!\!E_T$ direction. This cut helps to protect against jets lost in calorimeter cracks creating false $\not\!\!E_T$.
- no hits in any layer of the muon chambers behind the tau cluster

Next, we make some kinematic requirements to isolate $W \rightarrow \tau\nu$ events: Figure 3.7 shows the $\not\!\!E_T$ distribution for a $W \rightarrow \tau\nu$ Monte Carlo. We expect very few $W \rightarrow \tau\nu$ events with $\not\!\!E_T > 40$ GeV and place a cut accordingly. As a comparison, the $\not\!\!E_T$ distribution for a $W \rightarrow e\nu$ Monte Carlo is also shown. The selection criteria are:

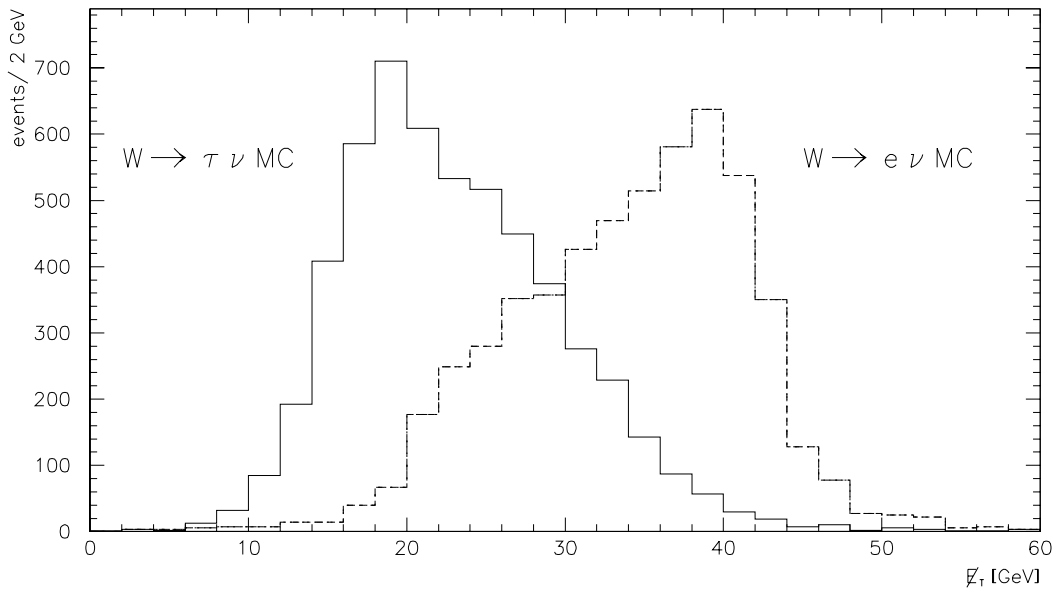

Figure 3.7: The $\not{E}_T$ distribution in simulated central $W \rightarrow \tau\nu$ and $W \rightarrow e\nu$ events.

- $20 < \not{E}_T < 40$
- 15 GeV $< E_T^{\tau-jet} <$ 40 GeV
- $|\eta_{det}^{\tau}| < 1.2$

In order to ensure that the τ candidates are associated with a good vertex we impose some stringent vertex cuts. Tracks associated with a (τ) jet are required to point back to a good vertex:

- ≥ 1 good beam–beam vertex [57] as measured by the VTX detector
- $|z_{vertex} - \overline{z}_{\tau-track}| < 5$ cm
- $|z_{vertex}| < 80$ cm for vertex closest to τ tracks

Finally, we require that the $\not\!\!E_T$ measured by the Level 2 trigger be larger than 35 GeV and that the leading Level 2 calorimeter cluster be in the central calorimeter [58]. This requirement is necessary in order to have an unbiased selection because the Level 2 trigger in Run I was configured in such a way that the majority of events in the monojet sample turn out to be triggered by clustered CEM energy. This biases the sample toward one-prong τ decays because these have a higher fraction of associated π^0's, and also possibly towards electrons faking τ's . After this selection process we are left with 423 events.

3.4.2 $W \to \tau\nu$ cross section

As the final number of events in the monojet sample is rather small compared with the initial $\not\!\!E_T$ sample and also compared with the size of the CDF $W \to e\nu$ and $W \to \mu\nu$ samples (about 50,000 events), we have checked the cross section $\times$ branching ratio $\sigma \cdot BR$ for $W \to \tau\nu$ production and decay as obtained from this sample. The calculation requires an understanding of the various trigger efficiencies involved, which are discussed in Ref. [59]. We find

$$\sigma \cdot BR(W \to \tau\nu) = 2400 \pm 300(stat) \pm 1300(syst)\ pb \tag{3.5}$$

The large systematic error is due to difficulties in measuring the trigger efficiencies at Levels 1, 2, and 3. This result for $\sigma \cdot BR$ agrees with the CDF measurement in the $W \to e\nu$ channel, $\sigma \cdot BR(W \to e\nu) = 2490 \pm 120\ pb$ [60]. We conclude that we have a reasonable $W \to \tau\nu$ sample for studying the τ identification variables.

3.4.3 Comparison of τ identification variables

In Figures 3.9 – 3.16 we plot the distributions of all τ identification variables used for the tau dilepton analysis. In all figures the distribution of a specific identification variable for the full monojet sample of 423 events is plotted at the top. At the bottom we plot the same distribution for all events where the jet passes all *other* τ identification cuts except the one plotted, which reduces the background significantly.

Figure 3.8 illustrates that requiring $\not{E}_T > 35$ GeV at the trigger level forces the E_T of the tau jet to be large (> 30 GeV) because the $\not{E}_T$ is basically determined by the monojet plus some smearing effect due to the underlying event. This can bias some of the identification variables such as the cluster width (higher E_T jets are more collimated) or the E/p. In the following we take this effect into account by comparing the monojet data to $W \to \tau\nu$ Monte Carlo and dijet data that have E_T spectra similar to the monojet data.

Track multiplicity and background normalization

Figure 3.9 shows the track multiplicity in the monojet sample. There is a clear excess in the one-prong and three-prong bins as expected for a sample with a significant τ fraction. In order to determine this fraction we also plot the track multiplicity for a sample of QCD jets (JET20) from the unbiased dijet sample (see section 3.8.1). Because only 5% of the events in the $W \to \tau\nu$ Monte Carlo have a track multiplicity of ≥ 4 we normalize the distribution for QCD jets to the monojet sample using the bins with ≥ 4 tracks.

From this procedure we estimate the background in the monojet sample to be $234 \pm 22(stat)$ events and the number of $W \to \tau\nu$ events to be 189 ± 21 ($45 \pm 5\%$). Note that the calculation of the statistical uncertainties takes into

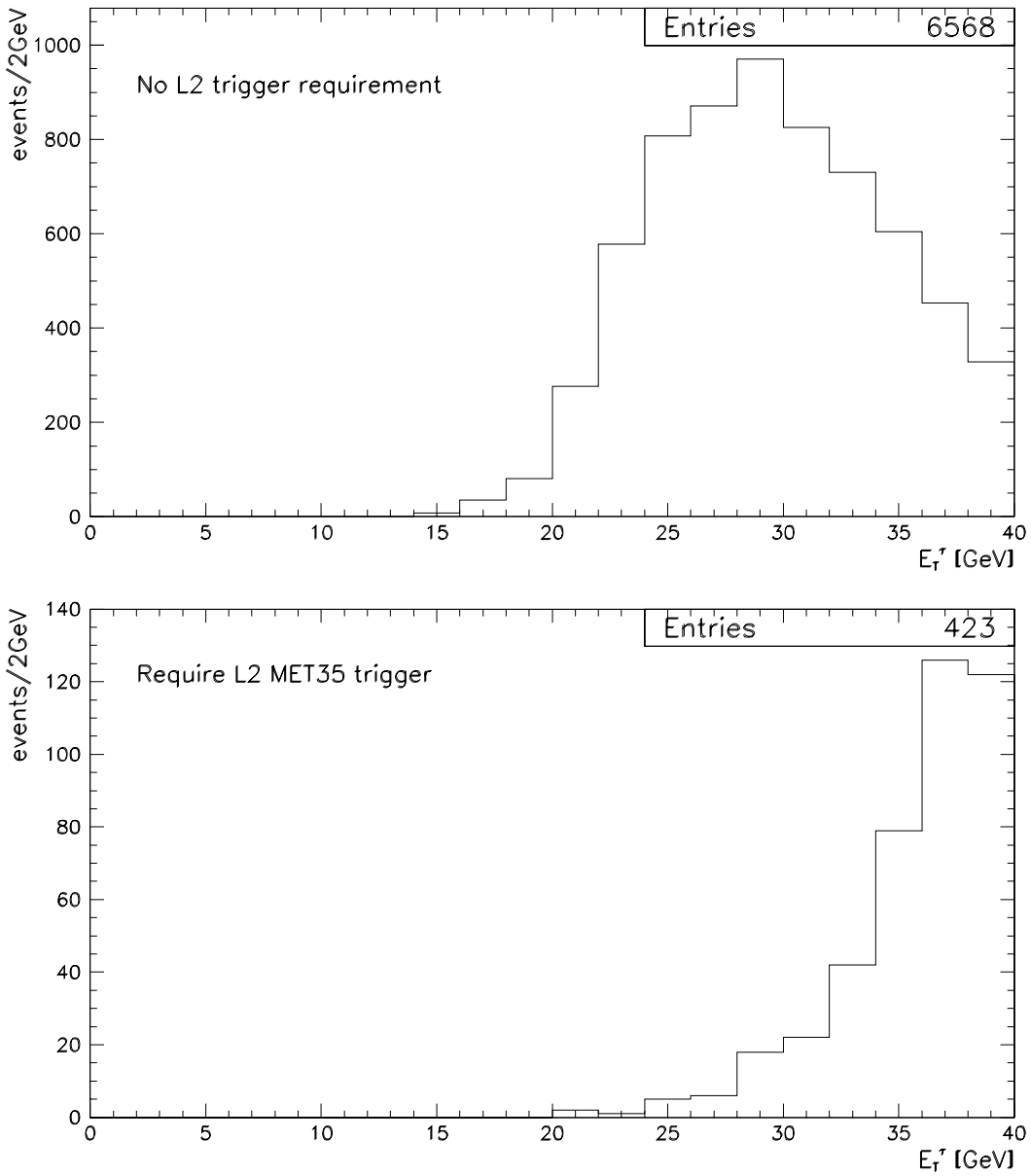

Figure 3.8: The E_T spectrum in the monojet sample before (top) and after (bottom) requiring the Level 2 MET35 trigger.

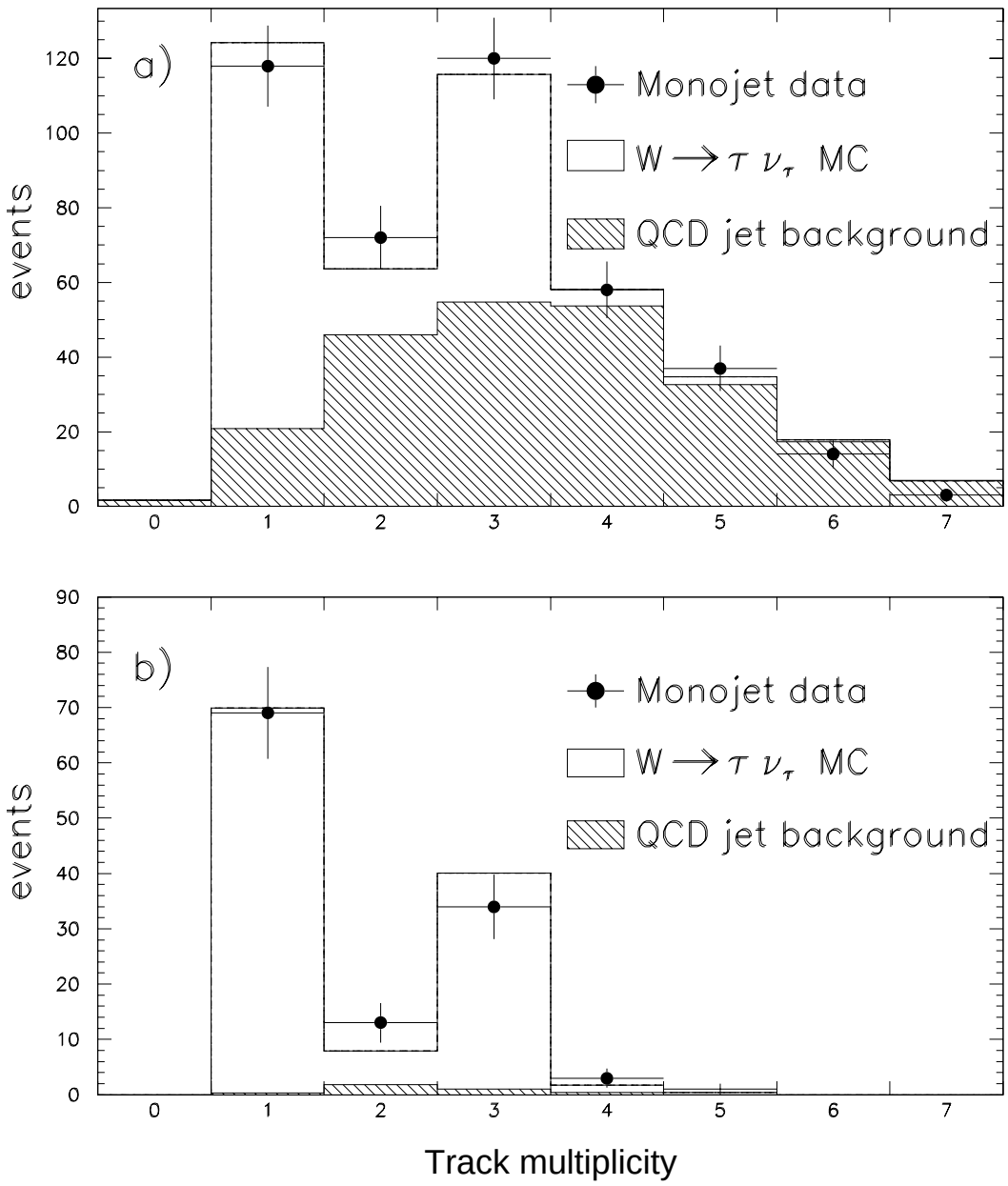

Figure 3.9: Track multiplicity in the monojet data sample. a) No τ identification cuts applied. b) After applying all τ identification cuts except track multiplicity.

account the uncertainty on the number of monojet events with ≥ 4 tracks (113 events) as the normalization is based on that.

We normalize the track multiplicity distribution obtained from the $W \rightarrow \tau\nu$ Monte Carlo (unhatched histogram) to 189 events and add it to the distribution for the QCD jet background. The resulting summed distribution is consistent within statistical uncertainties with the monojet data in the one-prong, two-prong and three-prong bins. If we apply all other identification cuts we also find agreement between the monojet data and the $W \rightarrow \tau\nu$ Monte Carlo in all bins. This gives us confidence that we actually observe $W \rightarrow \tau\nu$ candidates in the monojet sample and that the Monte Carlo simulation is reasonable with respect to the track multiplicity. Note that we use the same background fraction as obtained from the track multiplicity also for comparing all other τ identification variables.

Cluster width

Figures 3.10 and 3.11 display the RMS width σ_{cl} of the calorimeter cluster for one-prongs and three-prongs, respectively. For the comparison with the QCD jets from the JET20 sample we select the QCD jets in such a way that the E_T spectrum matches that of the monojet sample. This is necessary as the cluster width decreases systematically with increasing E_T due to the increasing boost of the particles in the jet. As expected for a sample with significant $W \rightarrow \tau\nu$ content, we observe a clear excess of events with small cluster width over the jet background for both one-prongs and three-prongs. Within statistics we find agreement between data and Monte Carlo.

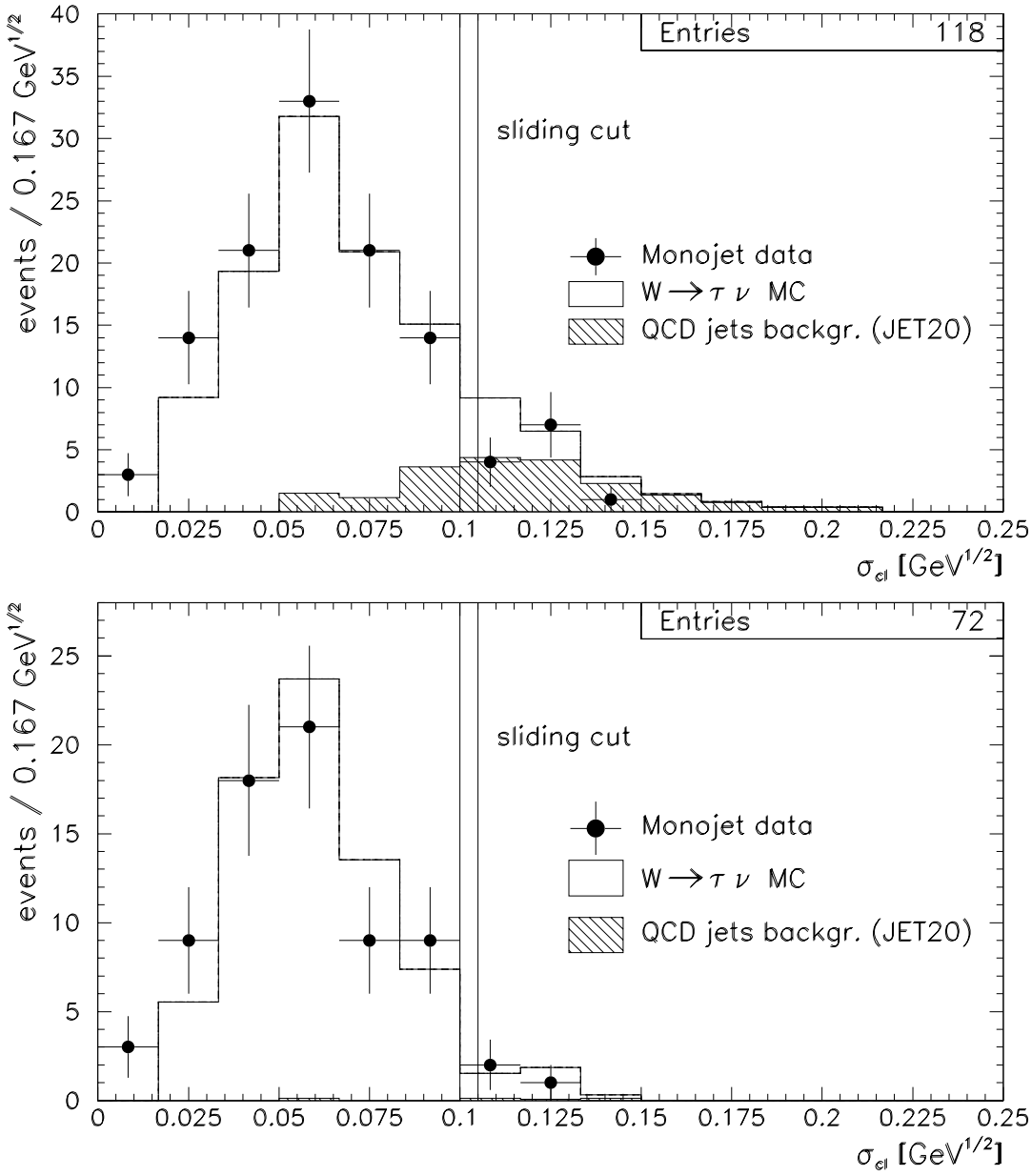

Figure 3.10: Calorimeter RMS cluster width in the monojet sample for *one-prongs*. Top: No τ identification cuts applied. Bottom: After applying all τ identification cuts except for the cluster width cut. The numbers of entries refer to the monojet data. The maximum and minimum of the sliding cut for the E_T range $20 < E_T < 40$ GeV are indicated by the 2 vertical lines.

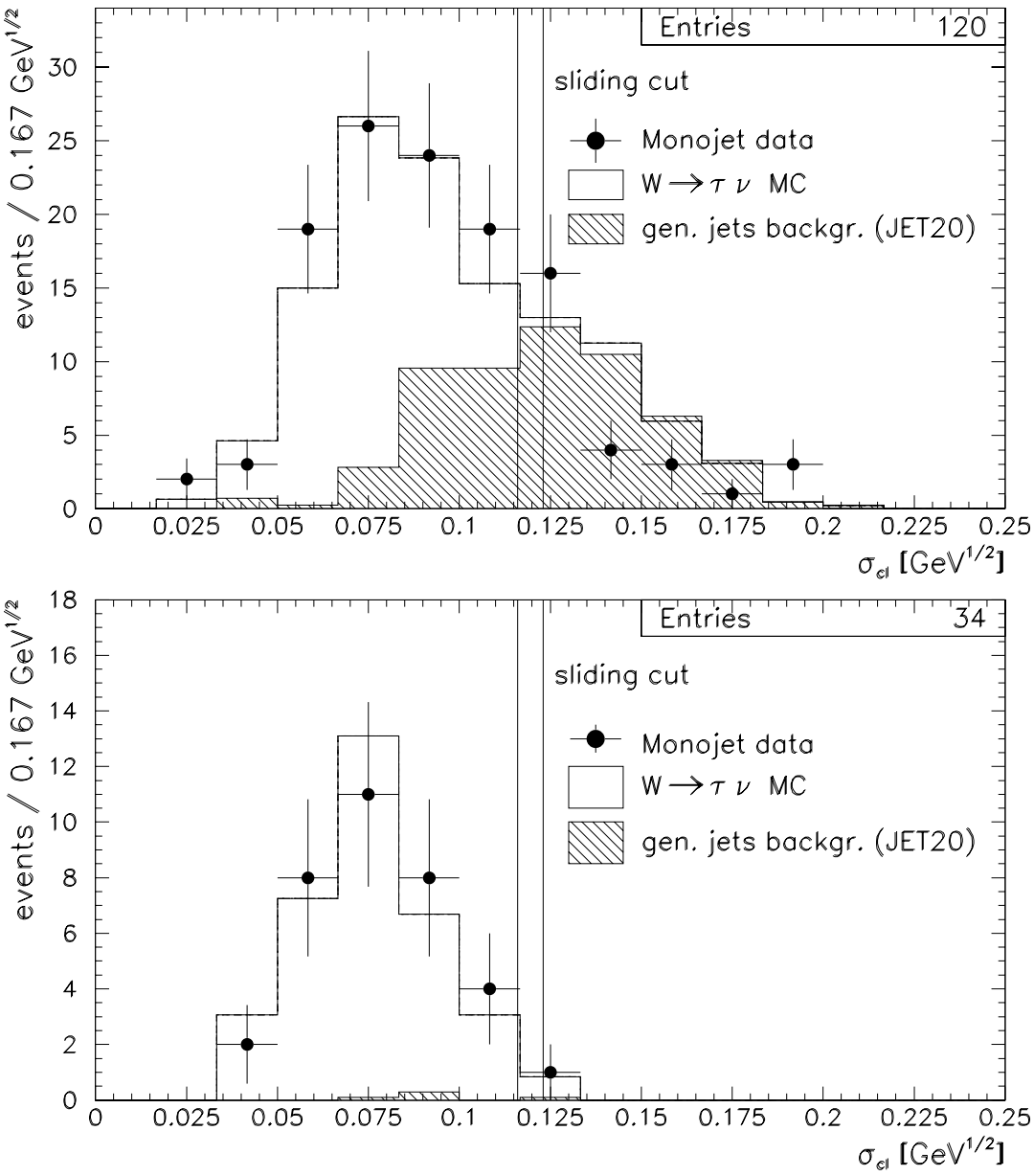

Figure 3.11: Calorimeter RMS cluster width in the monojet sample for *three-prongs*. Top: No τ identification cuts applied. Bottom: After applying all τ identification cuts except for the cluster width cut. The numbers of entries refer to the monojet data. The maximum and minimum of the sliding cut for the E_T range $20 < E_T < 40$ GeV are indicated by the 2 vertical lines.

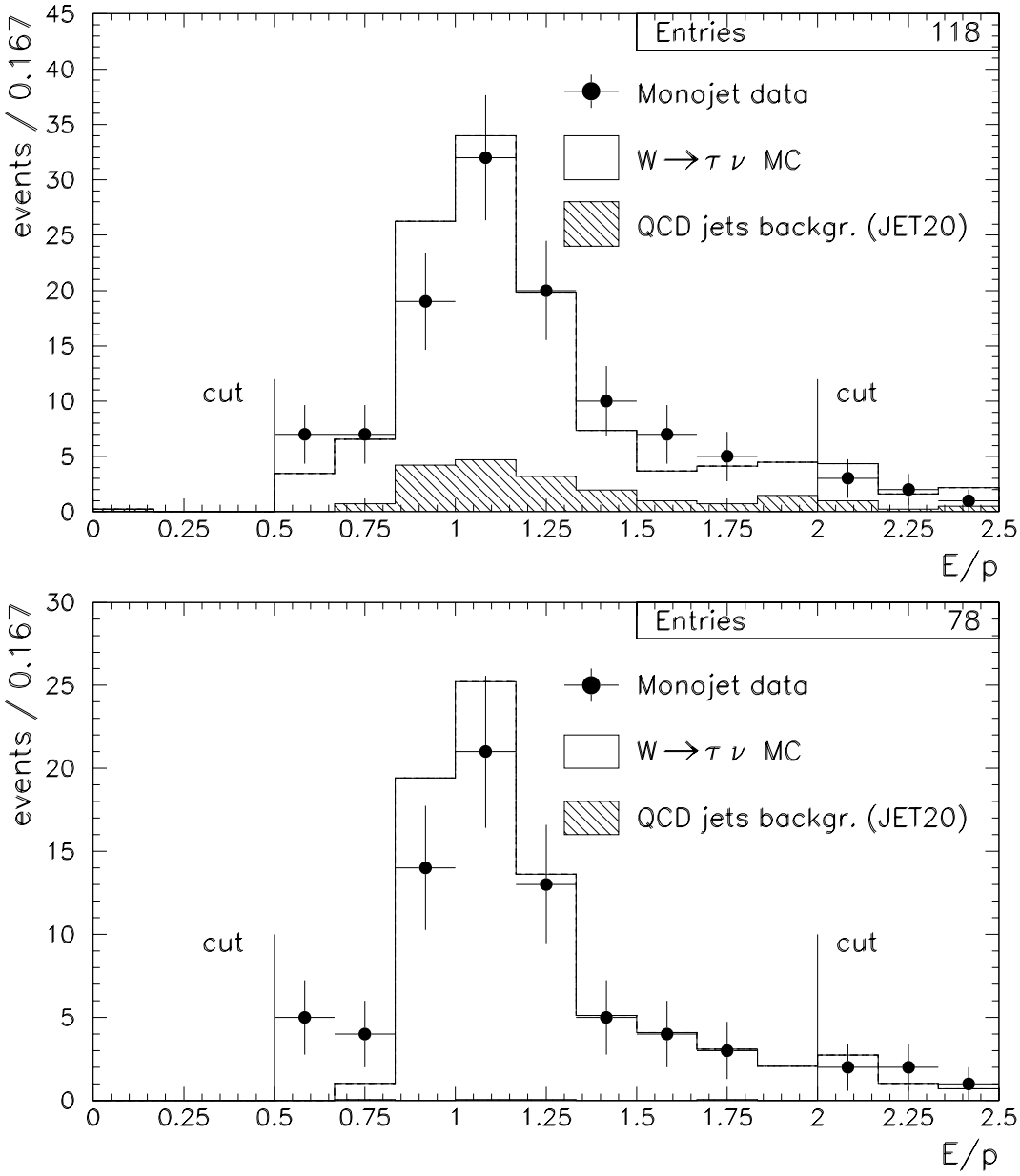

Figure 3.12: The E/p distribution in the monojet sample for *one-prongs*. Top: No τ identification cuts applied. Bottom: After applying all τ identification cuts except for the E/p cut. The numbers of entries refer to the monojet data.

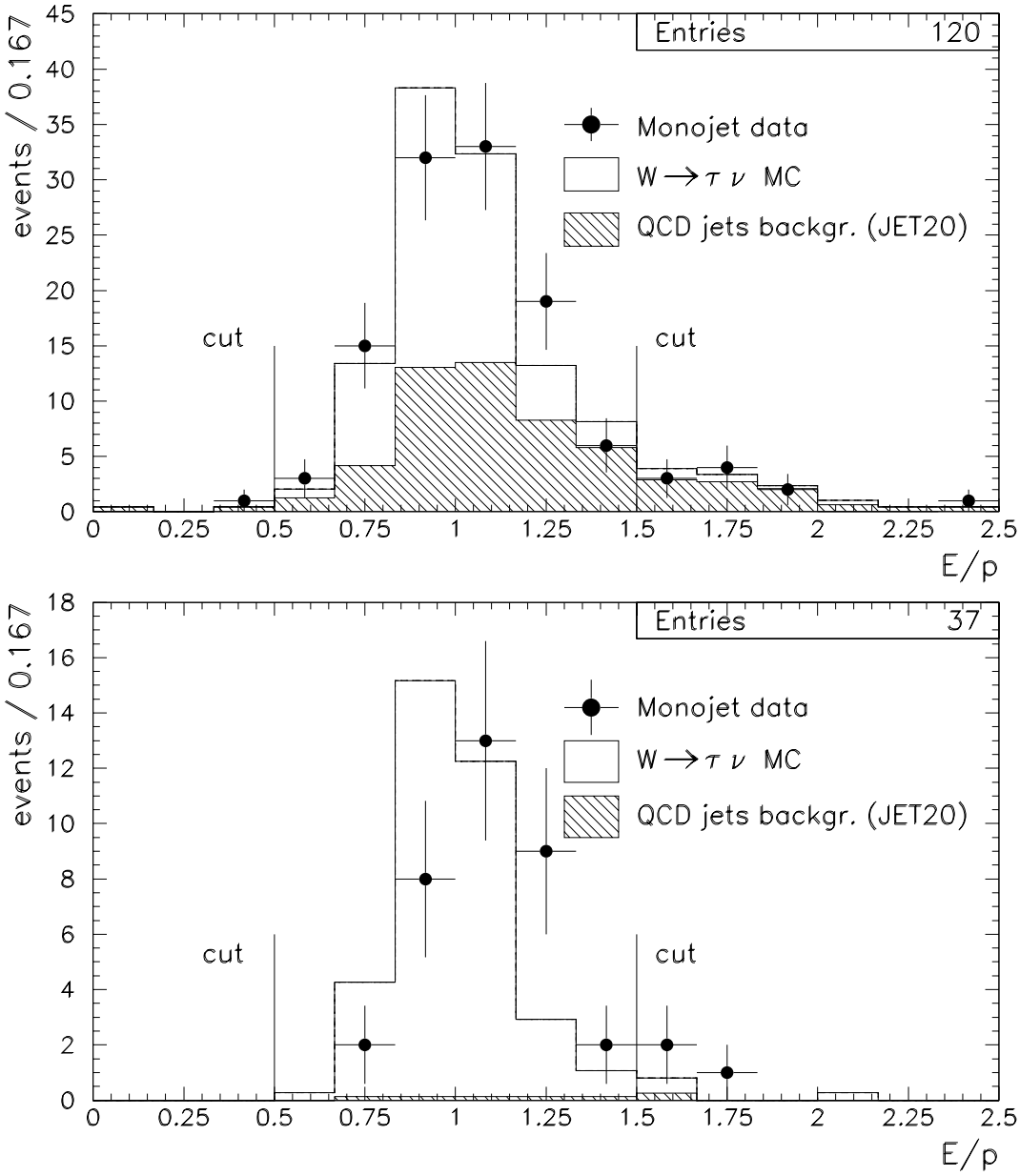

Figure 3.13: The E/p distribution in the monojet sample for *three-prongs*. Top: No τ identification cuts applied. Bottom: After applying all τ identification cuts except for the E/p cut. The numbers of entries refer to the monojet data.

E/p

The distribution for E/p, which is defined as $\frac{E_T}{p_T^{trk+\pi^0}}$ in the tau dilepton analysis, is shown in Figure 3.12 for one-prongs and in Figure 3.13 for three-prongs. For the three-prongs we find a slight shift of the mean by 0.15 towards higher E/p in the monojet data compared with the Monte Carlo. However, the placement of the cuts does not appear to be sensitive to this shift.

Number of π^0's

Figure 3.14 shows an excess of events with ≤ 2 π^0's over the jet background as expected for a sample containing $W \rightarrow \tau\nu$ events. In the data we find more events with one or two π^0's than expected from $W \rightarrow \tau\nu$ Monte Carlo and fewer with zero π^0's. This might be due to extra strip chamber hits in the data from soft multiple interactions that are not simulated in the Monte Carlo. On the other hand, the cut (≤ 2 π^0's) is not sensitive as to how the events are distributed among the first three bins (0, 1, or 2 π^0 candidates).

τ mass

Figure 3.15 shows the τ mass as reconstructed from tracks and π^0's. Again, as expected for a sample with a significant τ fraction, we find an excess of events with low masses over the jet background. The Monte Carlo predicts more events in the first bin, i.e. one-prong events without π^0's, than are found in the data. Again, the cut at 1.8 GeV is not sensitive to this.

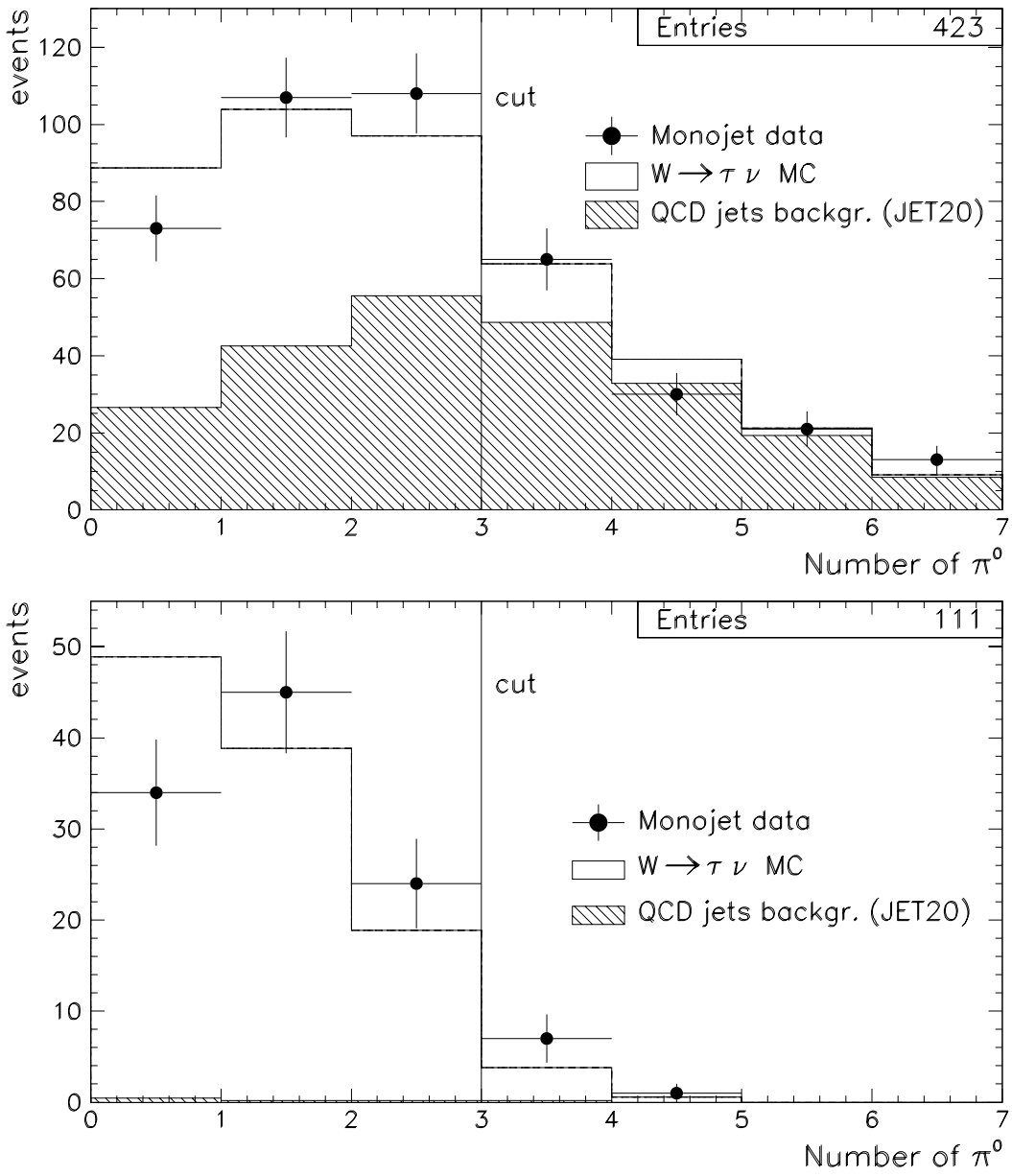

Figure 3.14: Number of π^0's in the monojet sample. Top: No τ identification cuts applied. Bottom: After applying all τ identification cuts except for the cut on the number of π^0's. The numbers of entries refer to the monojet data.

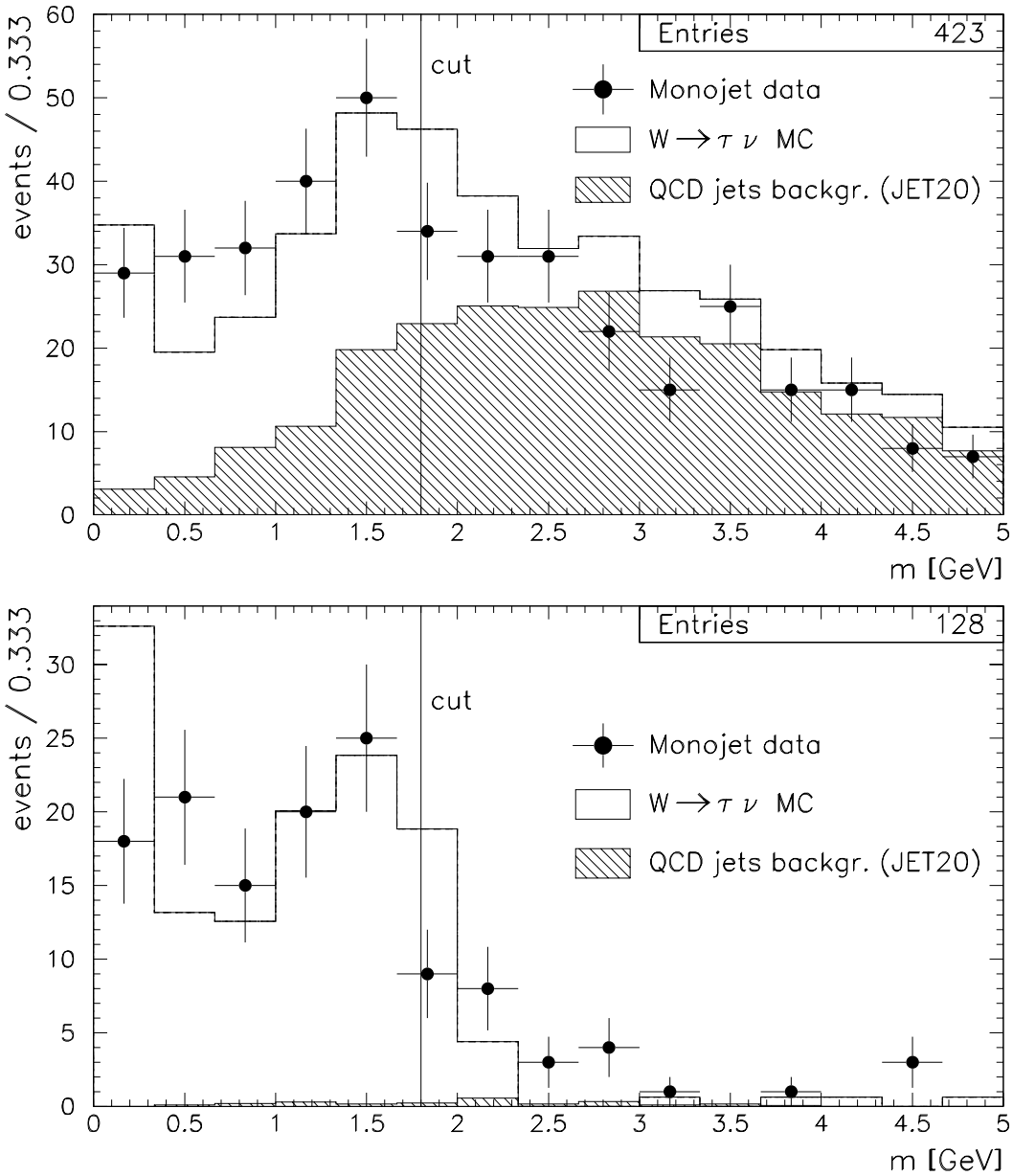

Figure 3.15: The τ mass distribution in the monojet sample. Top: No τ identification cuts applied. Bottom: After applying all τ identification cuts except for the τ mass cut. The numbers of entries refer to the monojet data.

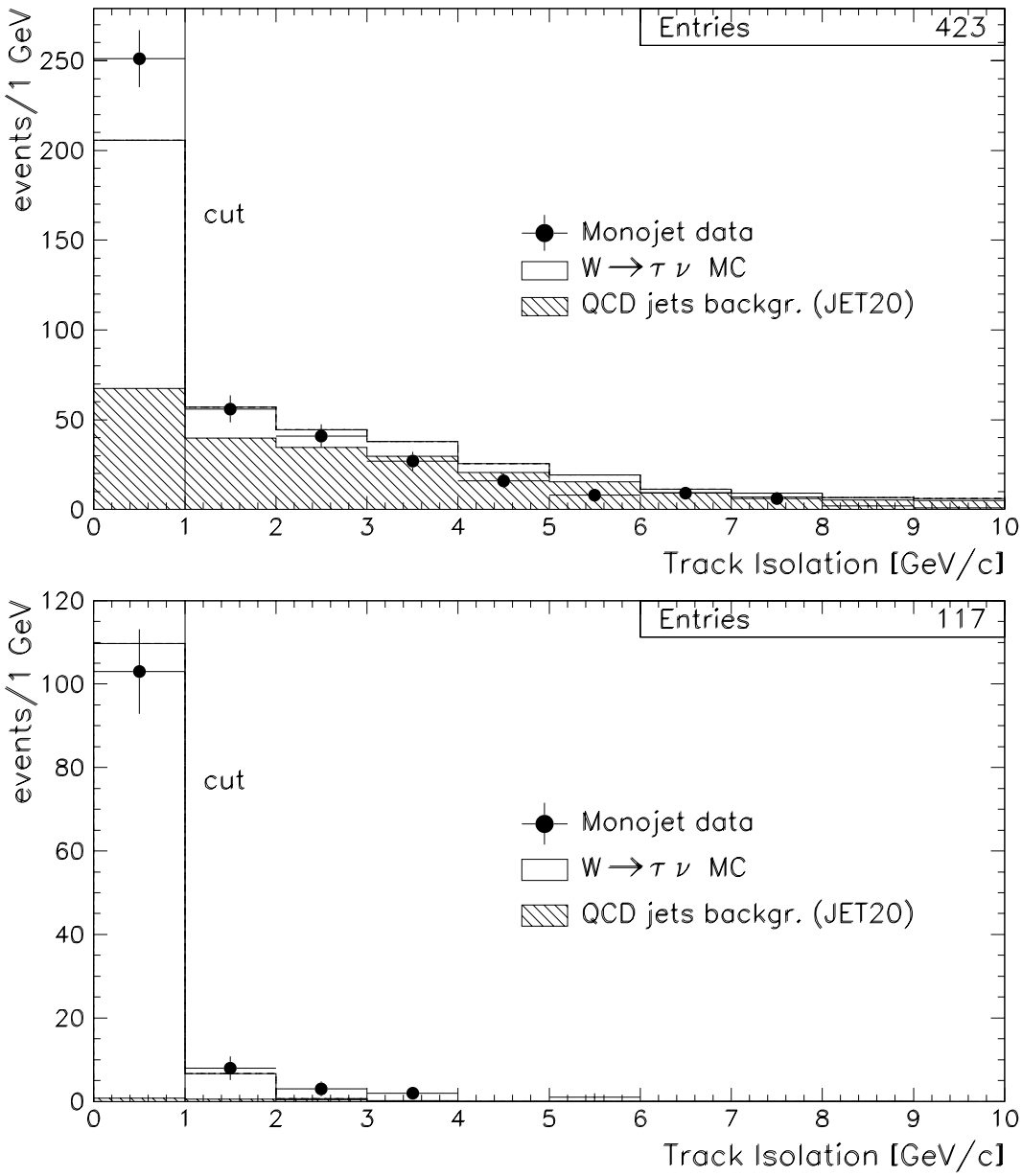

Figure 3.16: Track isolation in the monojet sample. Top: No τ identification cuts applied. Bottom: After applying all τ identification cuts except for the track isolation cut. The numbers of entries refer to the monojet data.

Track isolation

There is an excess over background of highly isolated ($I^{\tau}_{trk} < 1$ GeV) events in the monojet sample as shown in Figure 3.16. Monojet data and $W \to \tau\nu$ Monte Carlo prediction agree well.

3.4.4 Uncertainty on the τ identification efficiency

We now turn to measuring the efficiency of the τ identification cuts. Out of the 423 events in the monojet sample 103 pass all τ identification cuts. Having estimated the $W \to \tau\nu$ content of the sample to be 189 ± 21 events we calculate

$$\epsilon^{ID}_{data} = \frac{103}{189} = (54.5 \pm 6.3(stat))\%. \tag{3.6}$$

In calculating the statistical uncertainty we take the uncertainty on the $W \to \tau\nu$ content and the binomial uncertainty on the ratio ϵ^{ID}_{data} into account. The background due to fake τ's is expected to be less than one event and can be neglected in this calculation. The result agrees with the efficiency found from the $W \to \tau\nu$ Monte Carlo: $\epsilon^{ID}_{MC} = (56 \pm 1(stat))\%$. Since the statistical uncertainty of 6% in the monojet measurement limits the knowledge of the systematic uncertainty we cannot simply take the difference of the results from data and Monte Carlo as the systematic uncertainty. However, we can use this uncertainty of 6.3% from the monojet study as the *total* systematic uncertainty. This means that we have measured the τ identification efficiency in the data with $6.3/54.5 = 12\%$ relative systematic uncertainty.

3.5 Z^0 removal

As mentioned above electrons can fake τ's . This means that $Z^0 \rightarrow ee +$ jets events are a potentially large background for $e\tau$ top dilepton events. Instead of tightening the electron removal cuts and losing acceptance for real τ's, we impose a Z removal cut to reduce this specific source of fake $e\tau$ events. Following Ref. [50] we use a track–based Z removal in addition to a calorimeter–based Z^0 removal in order to remove such (slightly pathological) events [61]. This Z removal for $e\tau$ events is more stringent than the cut that we apply for ee events in Chapter 2.

If an event contains a tight central electron, the algorithm searches for an additional electron cluster in the central, plug or forward calorimeter that passes the cuts listed in Table 3.8. If the invariant mass formed by the primary electron and the cluster is between 66 and 116 GeV, the event is rejected as a Z^0 event. Likewise, if there is an isolated track with a nearby calorimeter cluster that satisfies the cuts listed in Table 3.9 and the invariant mass of tight electron and track is between 60 and 110 GeV, we also reject the event.

The calorimeter cuts remove 83.7% of central-central Z^0 events from a VECBOS $Z \rightarrow ee + 2$ jets Monte Carlo while retaining 100% of top $e\tau$ events in the PYTHIA $t\bar{t}$ Monte Carlo. With the track–based cuts 80.8% of central-central Z^0 events are removed and 98.7% of $e\tau$ events are kept. Both cuts applied together remove 86.7% Z^0 events and retain 98.7% of $e\tau$ events. All percentages are obtained after lepton identification only, but before topology cuts. As shown below the remaining necessary rejection of Z^0 events is achieved by topological cuts.

Central	Plug	Forward
$E_T > 15$	$E_T > 15$	$E_T > 10$
$E_{had}/E_{em} < 0.1$	$E_{had}/E_{em} < 0.1$	$E_{had}/E_{em} < 0.1$
$I_{cal} < 0.1$	$I_{cal} < 0.1$	$I_{cal} < 0.1$
$E/p < 2$	$\chi^2_{3\times3} < 3$	
opp. sign to primary TCE		
$66 < m_{ee} < 116$ GeV/c^2		

Table 3.8: Cuts on calorimeter clusters for calorimeter-based $Z^0 \rightarrow e^+e^-$ removal from the $e\tau$ search.

$p_T^{trk} > 10$ GeV/c in CTC
$I_{trk} \leq 0.05$
Cluster w/ $E_T > 7$ GeV + EMFrac > 0.7 within cone of 0.4 from track
track has opposite sign to primary TCE
$\lvert Z_0^{electron} - Z_0^{track}\rvert \leq 8$ cm
$60 < M_{e+trk} < 110$ GeV/c^2

Table 3.9: Cuts on tracks for track-based $Z^0 \rightarrow e^+e^-$ removal from the $e\tau$ search.

3.6 Topology cuts

3.6.1 z–vertex

In order to ensure that both leptons originate from the same hard–scattering process, we require that the z-intercepts for the tracks of the primary lepton and the tau candidate be within 5 cm of each other. For three-prong events we use the average z-intercept from all three tracks:

$$|\overline{z}_\tau^{track} - z_{e,\mu}^{track}| < 5 \text{ cm} \tag{3.7}$$

Recall that the identification cuts for the primary leptons e and μ already include the requirement that there be a beam–beam vertex in the VTX within 5 cm of the z-intercept for the primary lepton track: $|z^{vertex} - z_{e,\mu}^{track}| < 5$ cm and that this vertex be within 60 cm of the detector center: $|z^{vertex}| < 60$ cm.

3.6.2 Jets

For the b jets expected in top dilepton events we use the same jet cut as for the ee, $\mu\mu$, $e\mu$ dilepton analysis:

$$\geq 2 \text{ jets with } E_T^{uncorr.} > 10 \text{ GeV and } |\eta| < 2.0 \tag{3.8}$$

In Figure 3.17 we plot the jet E_T spectrum and the jet multiplicity for jets with $E_T^{uncorr.} > 10$ GeV and $|\eta| < 2.0$ for $t\bar{t}$ Monte Carlo events with a reconstructed isolated primary lepton that matches to a lepton at the generator level and an opposite–sign tau cluster that matches to a hadronically decaying τ from a W decay at the generator level. The identification cuts for both primary lepton and tau are applied. The jet cut is (83.1±2.3(stat))% efficient[2].

3.6.3 H_T

It has been shown that a cut on the H_T variable [62, 63] can be quite effective in reducing background in the top analysis while retaining high efficiency for the top signal. Therefore, we apply an H_T cut using the following definition of H_T for τ dileptons:

$$H_T \equiv E_T^{el} + p_T^{trk+\pi^0} + \not{E}_T + \sum_{jets} E_T^{uncorr.} > 180 \text{ GeV} \quad \text{for } e\tau \text{ events} \tag{3.9}$$

$$H_T \equiv p_T^{\mu} + p_T^{trk+\pi^0} + \not{E}_T + \sum_{jets} E_T^{uncorr.} > 180 \text{ GeV} \quad \text{for } \mu\tau \text{ events} \tag{3.10}$$

Here we sum over all jets in the event, not just over the two jets with the highest E_T. In Figure 3.18 we plot H_T for τ dilepton events in the $t\bar{t}$ MC that pass the jet cut. The H_T cut is (91.7±1.9(stat))% efficient on the $t\bar{t}$ MC sample.

[2] We use binomial statistics for calculating the uncertainties on all efficiencies.

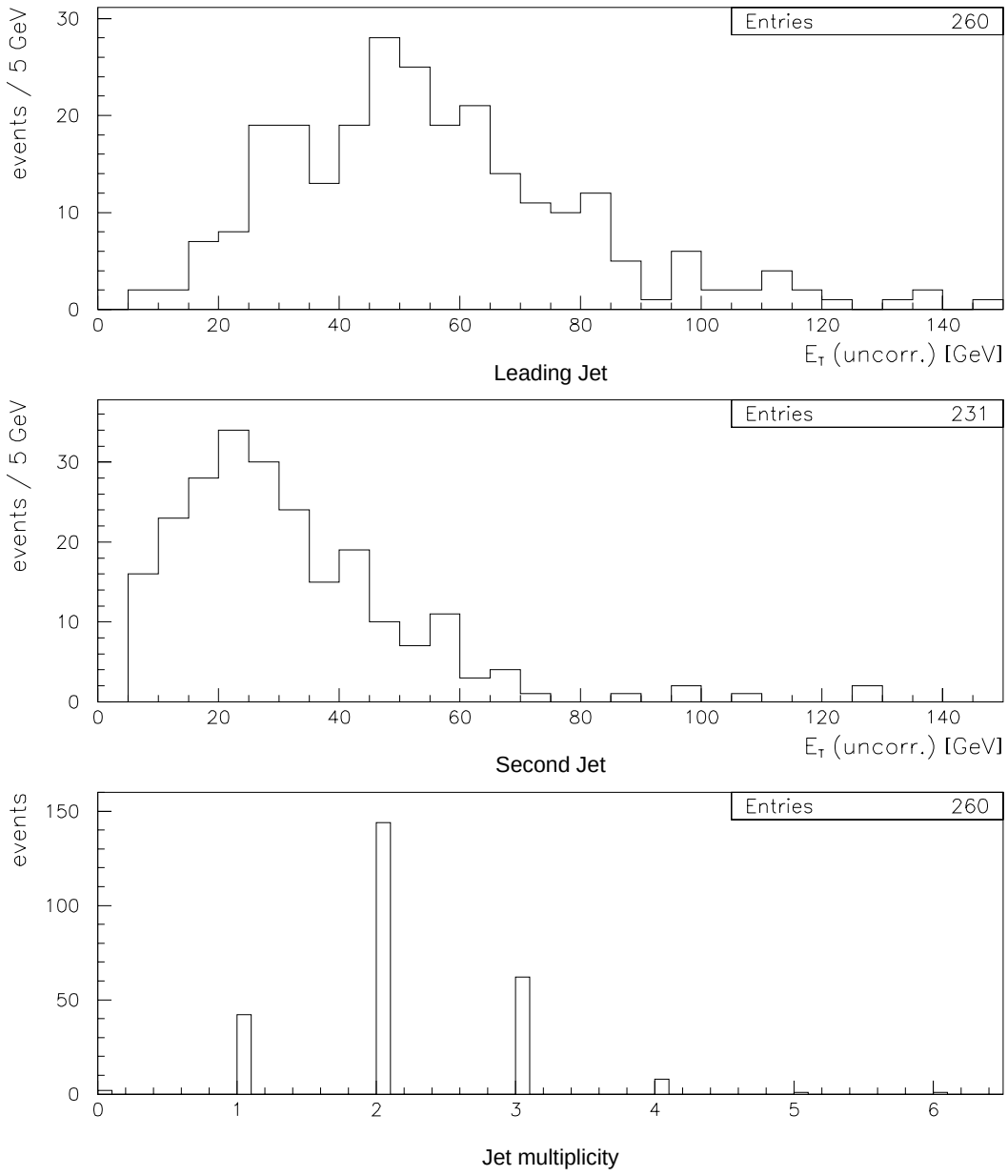

Figure 3.17: The E_T spectrum of the leading and the second jet and jet multiplicity for PYTHIA $e\tau$ and $\mu\tau$ $t\bar{t}$ MC events ($m_{top} = 175$ GeV).

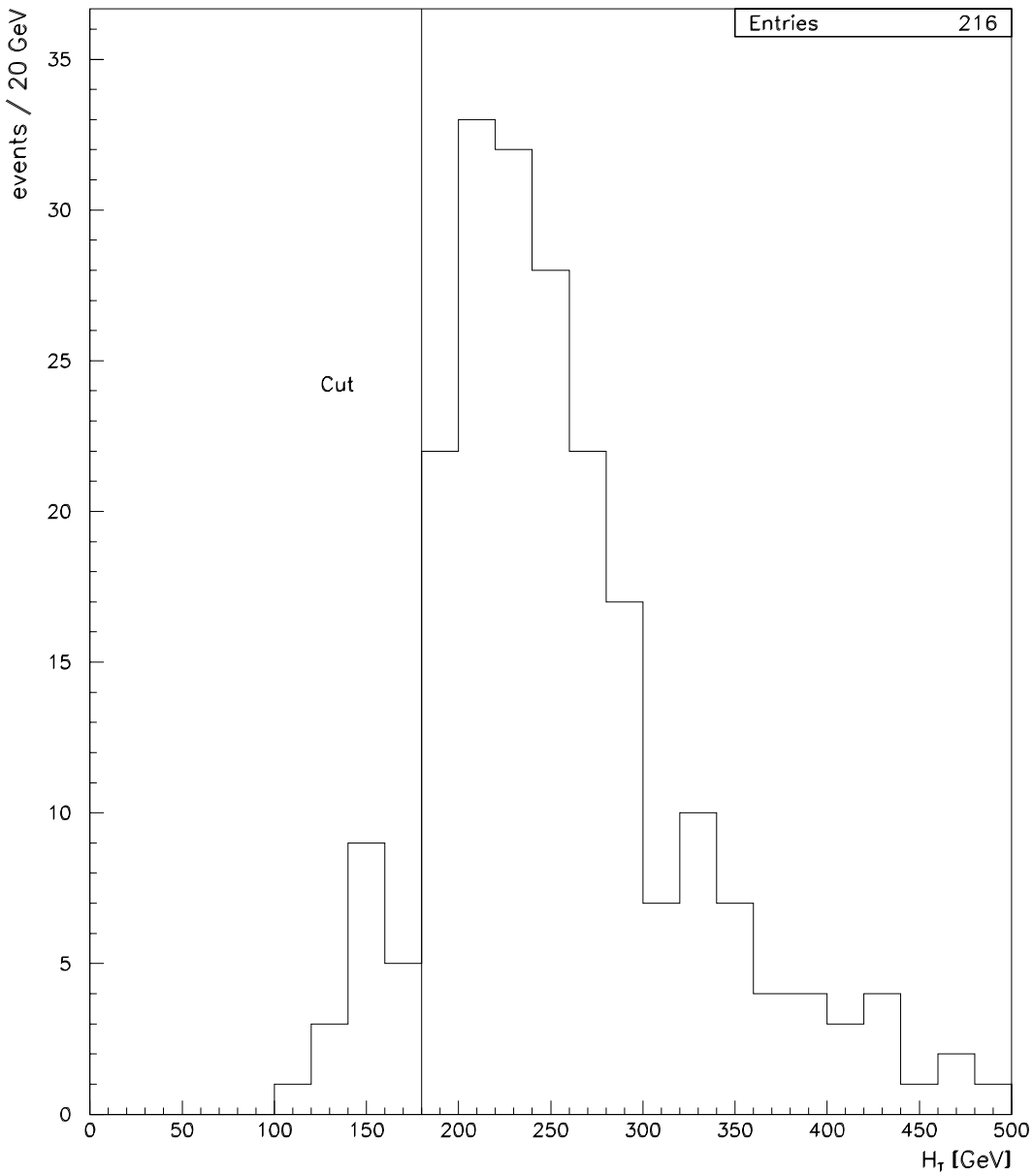

Figure 3.18: The distribution of the H_T variable for PYTHIA $e\tau$ and $\mu\tau$ $t\bar{t}$ MC events passing the jet cut.

3.6.4 $\not{E}_t$, $S_{\not{E}_T}$ and $\Delta\phi(\not{E}_t, jl)$

We correct the missing transverse energy $\not{E}_T$ for muons and jets (but not the tau jet) in the same way as for the ee, $\mu\mu$, $e\mu$ dilepton analysis. We define the $\not{E}_T$–significance $S_{\not{E}_T}$ as

$$S_{\not{E}_T} \equiv \frac{\not{E}_T}{\sqrt{\Sigma E_T}} \qquad \text{for } e\tau \tag{3.11}$$

$$\equiv \frac{\not{E}_T}{\sqrt{\Sigma E_T + p_T^{\mu}}} \qquad \text{for } \mu\tau \tag{3.12}$$

so that $e\tau$ and $\mu\tau$ events enter on the same footing. We do not bother correcting the $\not{E}_T$ and $S_{\not{E}_T}$ in $\mu\tau$ events for the E_T deposited by the muon, as it is small.

The top row of Figure 3.19 shows the standard plot of $\Delta\phi\,(\not{E}_T, jl)$, the angle between $\not{E}_T$ and the closest lepton (e, μ, or τ) or jet, versus $\not{E}_T$ and in the bottom row we plot $S_{\not{E}_T}$ vs $\not{E}_T$ for $e\tau$ and $\mu\tau$ events in the $t\bar{t}$ MC passing the jet cut and the H_T cut. Using the same topology cuts as for $ee, \mu\mu$, and $e\mu$ dileptons, $\not{E}_T > 25$ GeV and $\Delta\phi\,(\not{E}_T, jl) < 20^0$, if $\not{E}_T < 50$ GeV, we find an efficiency of (76.3±3.0(stat))%. An alternative cut on $S_{\not{E}_T}$:

$$S_{\not{E}_T} > 3 \text{ GeV}^{1/2} \tag{3.13}$$

is (66.7±3.4(stat))% efficient. The $S_{\not{E}_T}$ cut is slightly less efficient than the topology cut used for $ee, \mu\mu$, and $e\mu$ dileptons. However, cutting on the *significance* of $\not{E}_T$ instead of using the absolute value of $\not{E}_T$ takes the fact into account that large jets can yield large fluctuations and therefore large fake $\not{E}_T$. Therefore, we use the $S_{\not{E}_T}$ cut in the $e\tau$ and $\mu\tau$ event selection.

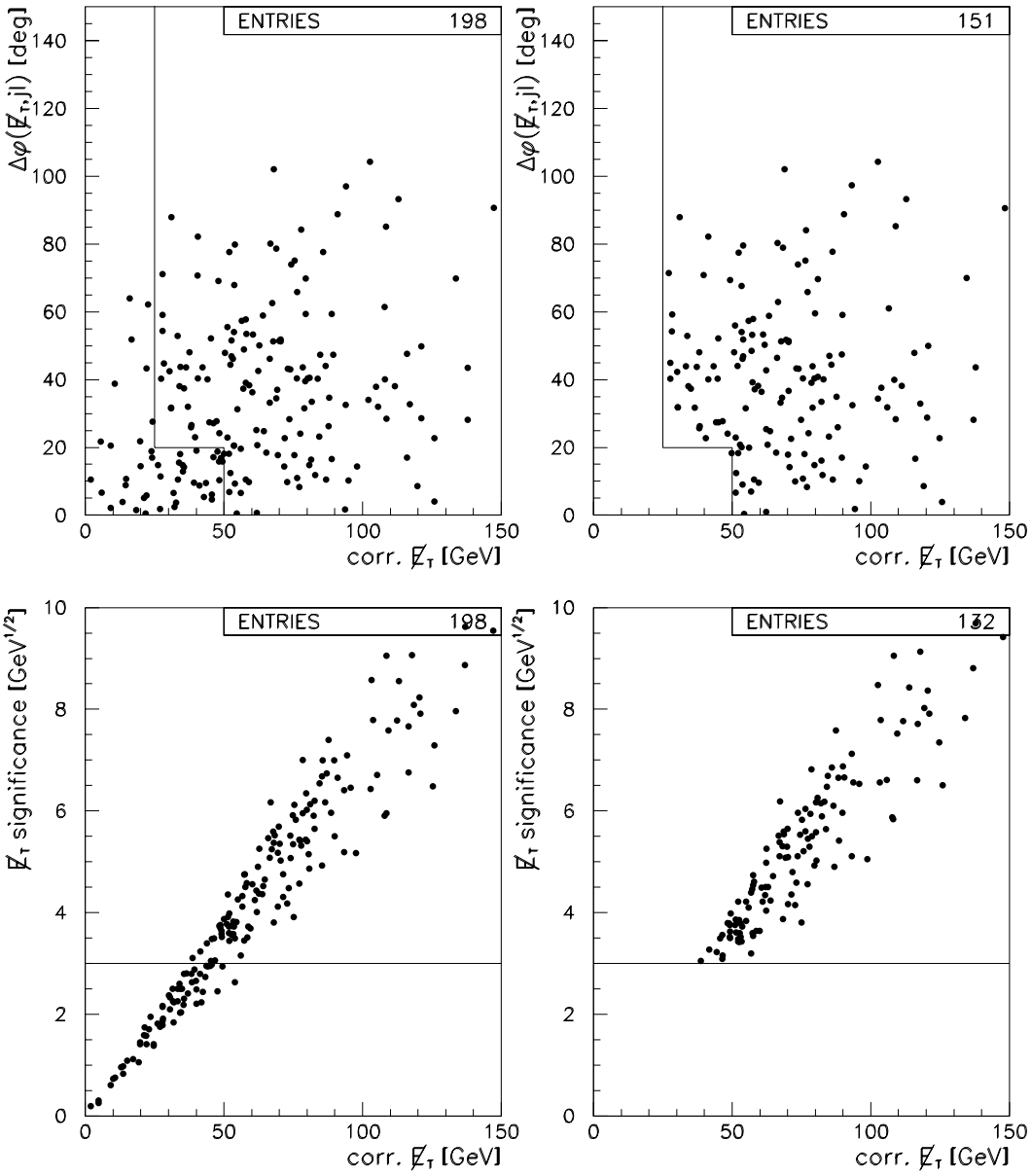

Figure 3.19: Topology cuts for PYTHIA $e\tau$ and $\mu\tau$ $t\bar{t}$ MC events. Top: $\Delta\phi\,(\not{E}_T, jl)$ vs $\not{E}_T$. Bottom: $S_{\not{E}_T}$ vs $\not{E}_T$. In the plots on the right hand side the topology cuts are imposed.

3.7 Total Acceptance × Efficiency

3.7.1 Calculating A_{tot}

The total acceptance × efficiency A_{tot} for top dilepton events involving hadronic τ's is given by:

$$A_{tot} = A_{geom \cdot P_T} \times \epsilon^{e,\mu}_{Iso} \times \epsilon^{e,\mu}_{ID} \times \epsilon^{\tau}_{ID} \times \epsilon_{opp.sign} \times \epsilon^{e,\mu}_{trigger} \times \epsilon_{Zremoval} \times \epsilon_{jets} \times \epsilon_{H_T} \times \epsilon_{topology} \tag{3.14}$$

In the following we discuss the efficiencies that were not covered in the previous sections:

- $\epsilon_{opp.sign}$:

  From the PYTHIA $t\bar{t}$ MC we find $\epsilon_{opp.sign} = (99.5 \pm 0.5(stat))\%$.

- $\epsilon_{trigger}$:

  We do not specify a trigger path for the dilepton analysis. The combination of the Level 2 track triggers and 'W–no–track' triggers for electrons is expected to be close to 100% efficient [64]. The muon trigger efficiency is determined by running the muon trigger simulation [65] on the PYTHIA $t\bar{t}$ MC. The result is $\epsilon^{\mu}_{trigger} = (87.1 \pm 2.8(stat))\%$.

In Table 3.10 we collect all the acceptances and efficencies for $e\tau$ and $\mu\tau$ events. Putting everything together we find:

$$A_{tot} = (0.065 \pm 0.006(stat))\% \quad \text{for } e\tau \tag{3.15}$$

$$A_{tot} = (0.069 \pm 0.007(stat))\% \quad \text{for } \mu\tau \tag{3.16}$$

$$A_{tot} = (0.134 \pm 0.013(stat))\% \quad \text{total} \tag{3.17}$$

	$e\tau$	$\mu\tau$
$A_{geom \cdot P_T}$	0.0032±0.0002	0.0033±0.0002
$\epsilon_{Iso}^{e,\mu}$	0.880±0.020	0.904±0.017
$\epsilon_{ID}^{e,\mu}$	0.814±0.008	0.933±0.006
ϵ_{ID}^{τ}	0.565±0.017	
$\epsilon_{opp.sign}$	0.995±0.005	
$\epsilon_{trigger}^{e,\mu}$	1.0	0.871±0.028
$\epsilon_{Zremoval}$	0.987±0.012	1.0
ϵ_{jets}	0.831±0.023	
ϵ_{H_T}	0.917±0.019	
$\epsilon_{topology}$	0.667±0.034	

Table 3.10: Summary of efficiencies needed for calculating A_{tot} . Note that $A_{geom \cdot P_T}$ includes all branching ratios.

3.7.2 Systematic uncertainty on A_{tot}

In this section we consider effects that result in systematic uncertainties in the calculation of the total acceptance for tau dileptons. Below we list the effects that we take into account. The effects that produce the largest uncertainties are listed first:

1. Top mass uncertainty
2. Hadronic energy scale
3. Uncertainties in primary lepton identification and isolation
4. Multiple vertices
5. Underlying event
6. Difference between MC generators
7. Initial and final state radiation
8. Parton distribution functions

9. CEM energy scale

10. p_T scale

Uncertainty on A_{tot} due to uncertainty on m_{top}

The uncertainty on the top mass results in a systematic uncertainty on the kinematics of the top decay products. It enters in the kinematic acceptance $A_{geom \cdot P_T}$ via the lepton energies and momenta, and in the jet efficiency ϵ_{jets} because jet energies depend on m_{top}. Both also affect the efficiency of the H_T cut ϵ_{H_T}. To study this effect we have generated nine PYTHIA $t\bar{t}$ Monte Carlo sets with top masses in the range 135 – 215 GeV/c^2. In Figure 3.20 we plot $A_{geom \cdot P_T}$, ϵ_{jets} and ϵ_{H_T} as a function of top mass, with fits to straight lines or parabolas. In all cases the efficiencies increase monotonically with m_{top}. We also check the efficiency of the topological cut on $S_{\not{E}_T}$ and find that its efficiency is very nearly flat over the considered top mass range.

To calculate the overall uncertainty we plot A_{tot} vs m_{top} in Figure 3.21. The total acceptance increases by about a factor of two over the considered range of top masses. This behavior is similar to what is found for the ee, $\mu\mu$, $e\mu$ dileptons [20]. From a straight line fit we find a slope of $dA_{tot}/dm_{top} = 0.0013$ %/GeV/c^2. Multiplying the combined current statistical and systematic uncertainty of 6.5 GeV/c^2 on the CDF top mass measurement ($m_{top} = 176.8 \pm 4.4(stat) \pm 4.8(syst)$ [68]), we find $\Delta A_{tot} = 8.5 \times 10^{-5}$. This corresponds to a relative systematic uncertainty of $\Delta A_{tot}/A_{tot} = 8.5 \times 10^{-5}/0.00134 = 6\%$ due to the uncertainty in the top mass.

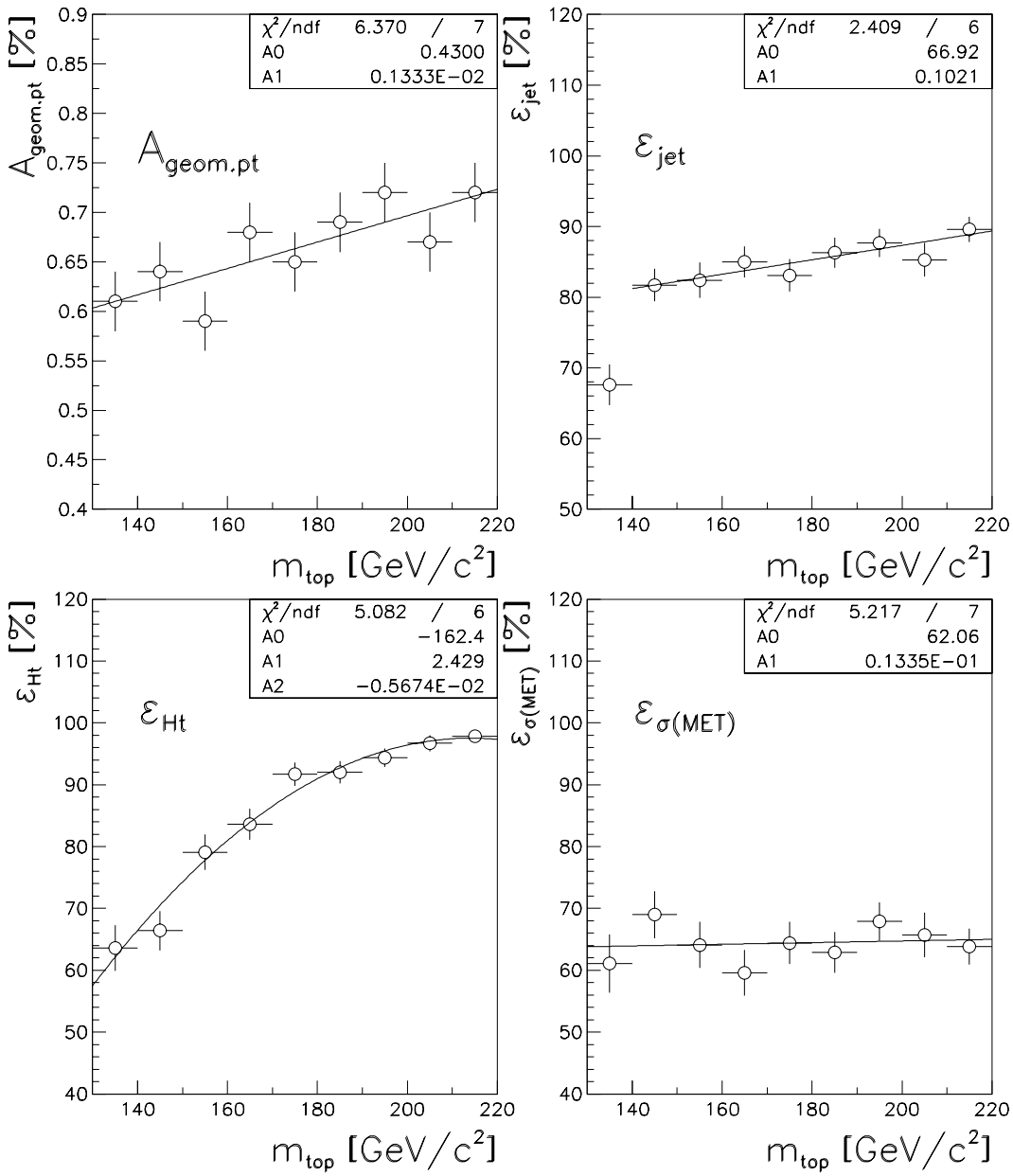

Figure 3.20: Acceptance $A_{geom \cdot P_T}$ and efficiencies ϵ_{jets}, ϵ_{H_T}, and $\epsilon_{topology}$ versus top mass from PYTHIA $t\bar{t}$ Monte Carlo.

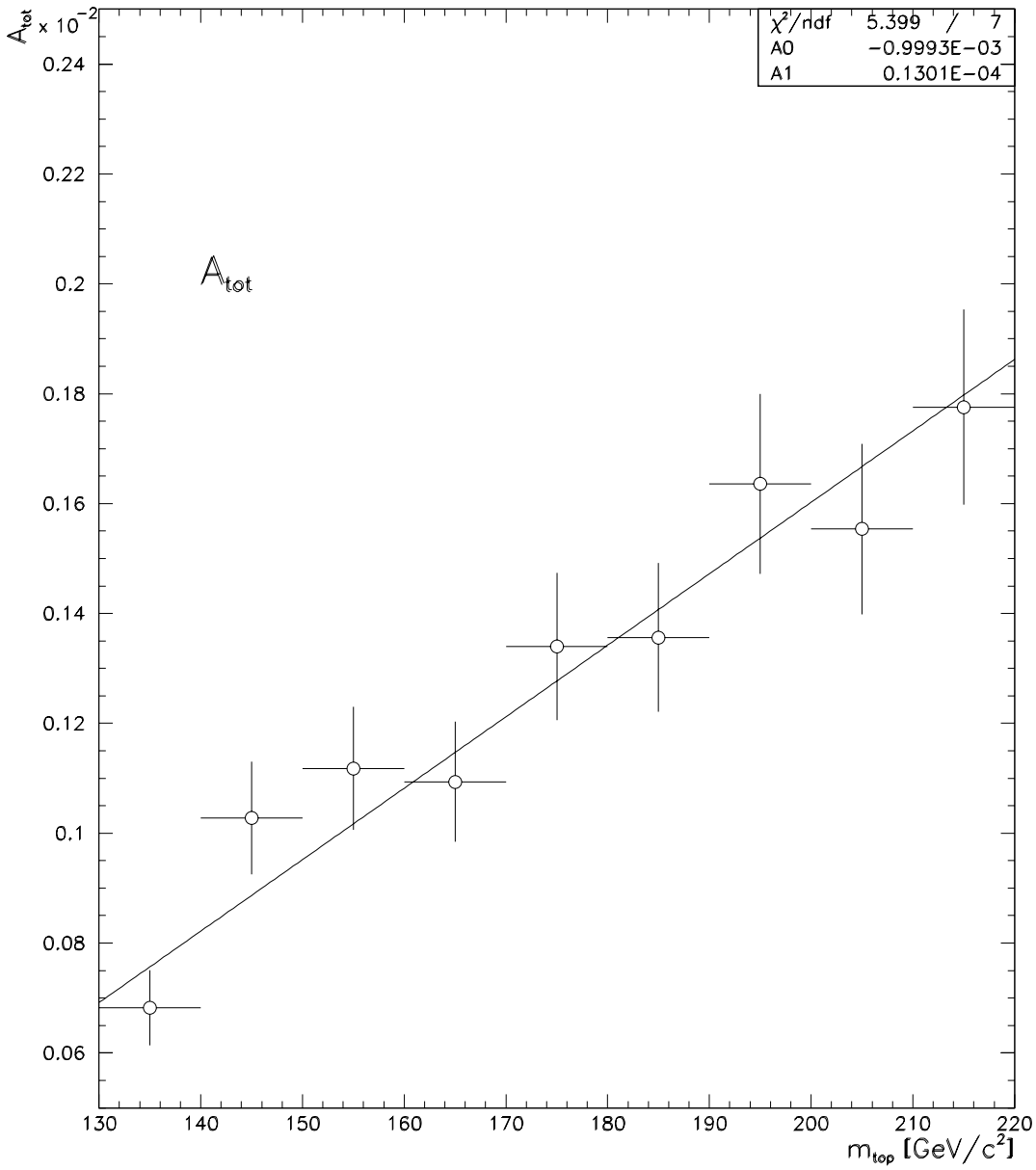

Figure 3.21: Total Acceptance A_{tot} versus top mass using $t\bar{t}$ MC sets.

Uncertainty on τ lepton identification ϵ^{τ}_{ID}

The following effects can introduce systematic uncertainties on the τ identification efficiency:

- **Hadronic energy scale:**

  This uncertainty enters only where the E_T of the τ measured in the calorimeter is used in the tau identification. This occurs directly for the cut on $E/P = E_T/p_T^{trk+\pi^0}$, and, with less sensitivity, in the cut on the sliding RMS cluster width: $\sigma_{cl} < 0.11 - 0.025 \times E_T/100$ (1-prongs); $\sigma_{cl} < 0.13 - 0.034 \times E_T/100$ (3-prongs).

  The uncertainty of the hadronic energy scale in CDF is estimated to be approximately 10% [66]. To estimate the systematic uncertainty we calculate ϵ^{τ}_{ID} by increasing or decreasing the tau jet E_T by 10%:

  $$\epsilon^{\tau}_{ID} = (56.5 \pm 1.7(stat))\% \qquad \text{for } E_T \rightarrow E_T + 10\% \tag{3.18}$$

  $$\epsilon^{\tau}_{ID} = (56.0 \pm 1.7(stat))\% \qquad \text{for } E_T \rightarrow E_T - 10\%. \tag{3.19}$$

  Comparing this with the standard result $\epsilon^{\tau}_{ID} = (56.5 \pm 1.7)\%$ we find a relative systematic uncertainty $\Delta\epsilon/\epsilon = \pm 1\%$. Note that the statistical uncertainties in the $E_T \rightarrow E_T + 10\%$ sample and $E_T \rightarrow E_T - 10\%$ are highly correlated because we use the same events. This allows us to estimate systematic effects that are smaller than the overall statistical uncertainty on ϵ^{τ}_{ID}.

- **Multiple vertices:**

  An important part of the τ identificaton and rejection of jet fakes is the tight cut on the track isolation: $I^{\tau}_{trk} < 1$ GeV/c. This is sensitive to the presence of tracks from additional minimum bias events in the data. We

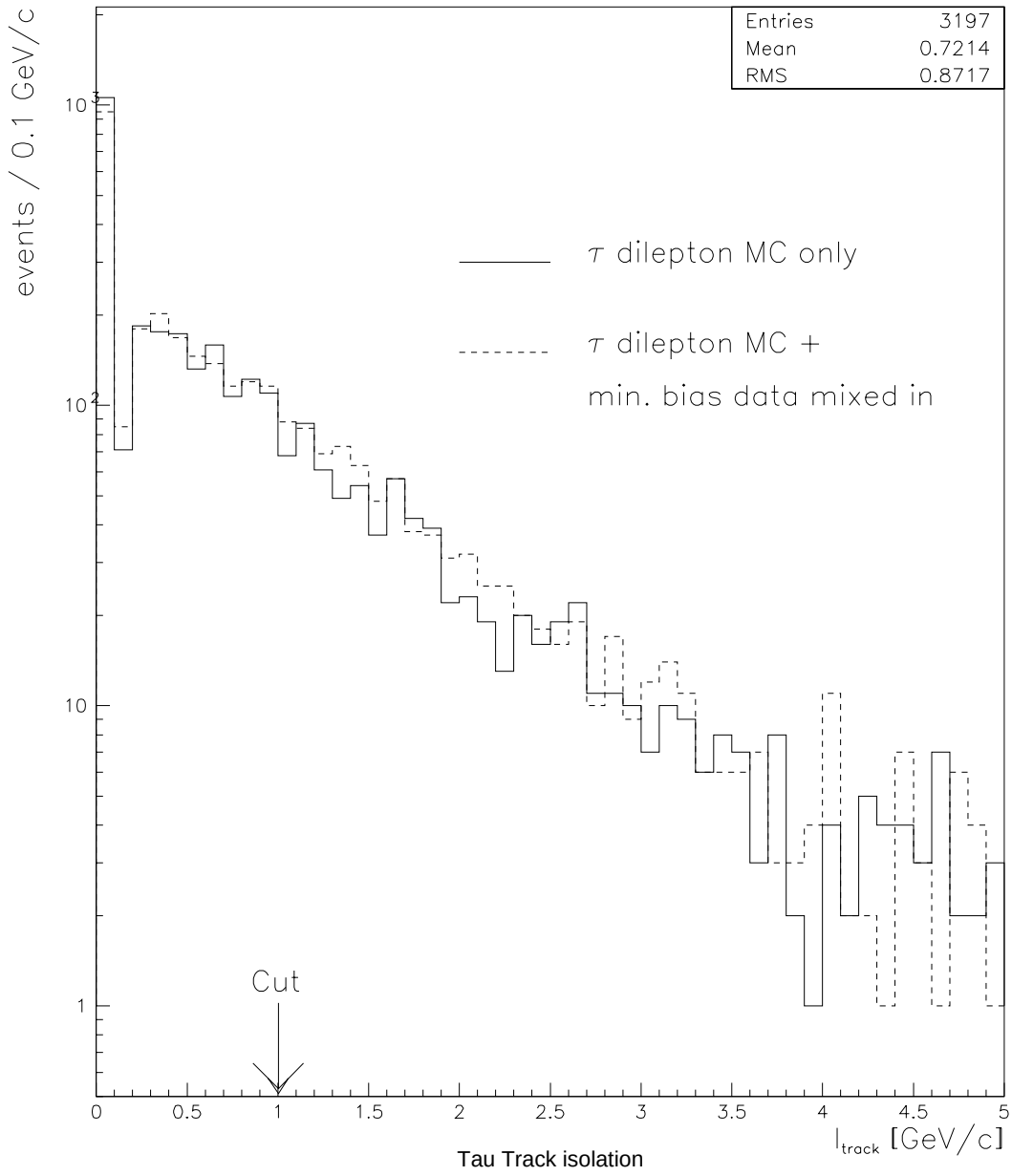

Figure 3.22: Track isolation for tau candidates in pure ISAJET Monte Carlo and in ISAJET Monte Carlo with additional minimum bias data mixed in.

compare ϵ^{τ}_{ID} for two ISAJET $t\bar{t}$ Monte Carlo sets ($m_{top} = 175$ GeV/c^2). In the first set minimum bias events from CDF data have been mixed into the Monte Carlo events with a distribution that compares to that expected in our data [67]. The second set is pure $t\bar{t}$ Monte Carlo. As expected, the cut that is most affected by the presence of minimum bias events is the track isolation cut. Its efficiency is decreased from 79.5% in the pure Monte Carlo sample to 77.3% in the sample with minimum bias events mixed in. In Figure 3.22 we compare the distributions of the track isolation variable between the two samples. The spectrum is shifted slightly towards higher values in the presence of additional tracks from minimum bias events. The shift in the mean is 0.06 ± 0.02 GeV/c.

We find that the overall τ identification efficiency is reduced from $(44.4 \pm 0.9)\%$ to $(42.3 \pm 0.9)\%$. We estimate the systematic uncertainty due to multiple vertices from the relative difference in the two ISAJET samples to be $\Delta\epsilon/\epsilon = \pm 5\%$.

- **Underlying event model:**

  We note that the τ identification efficiency in the ISAJET sample $(44.4 \pm 0.9)\%$ is smaller than the τ identification efficiency $\epsilon^{\tau}_{ID} = (56.5 \pm 1.7)\%$ found with the PYTHIA $t\bar{t}$ Monte Carlo sample. The dominant difference is due to the modelling of the track isolation in the ISAJET sample versus the PYTHIA sample. In Figure 3.23 we compare the distributions for the track isolation for τ's . The τ's are clearly less isolated in the ISAJET sample. However, Figure 3.24 shows that this effect is not τ–specific; it also occurs for tight electrons. For muons we find a similar effect. This points to a difference in the modelling of soft tracks from the underlying event in the two Monte Carlos.

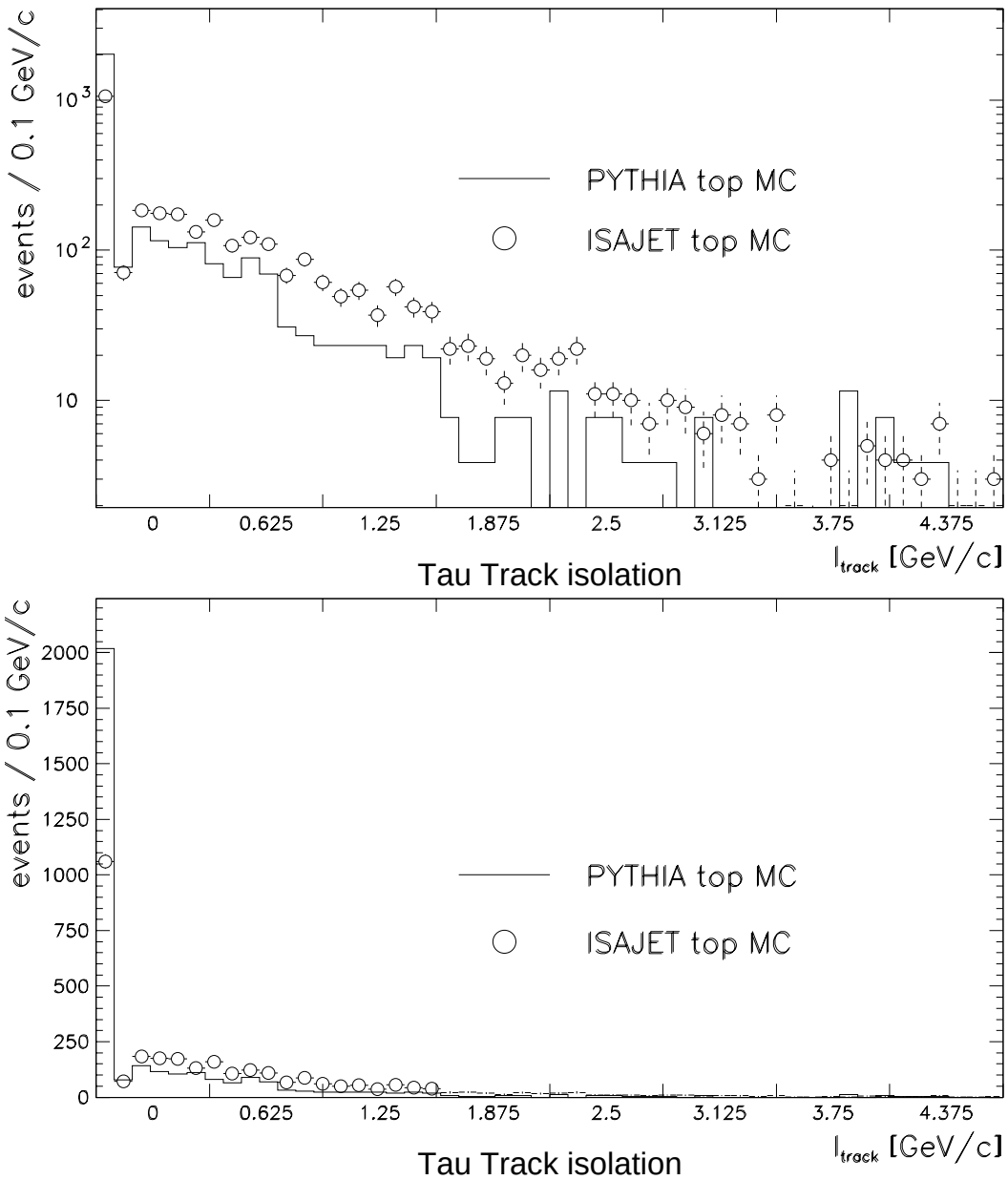

Figure 3.23: Track isolation for tau candidates in $t\bar{t}$ ISAJET Monte Carlo and in PYTHIA Monte Carlo. Top: Logarithmic scale, Bottom: Linear scale.

We check which Monte Carlo models the data better by comparing a PYTHIA central–central $Z \rightarrow ee$ sample to data in Figure 3.25. We find good agreement between PYTHIA and the data and therefore use PYTHIA for calculating the τ identification efficiency. The efficiency of the track isolation cut ($I^{\tau}_{trk} < 1$ GeV/c) for this PYTHIA Z–sample is $(92.1 \pm 0.9)\%$. For the data it is $(88.8 \pm 0.7)\%$. We take the relative difference of 3.6% as an uncertainty in the τ identification efficiency due to the modeling of the underlying event in PYTHIA.

Uncertainty on 2–jet–cut efficiency ϵ_{jets}

The systematic uncertainty on the jet energy scale (hadronic energy scale) of 10% results in a systematic uncertainty on the 2–jet–cut efficiency ϵ_{jets}. We estimate this effect by recalculating ϵ_{jets} in the standard PYTHIA $t\bar{t}$ MC for $m_{top} = 175$ GeV, where the jet energies have been increased and decreased by 10%. The result is:

$$\epsilon_{jets} = (79.2 \pm 2.5(stat))\% \qquad \text{for } E_T^j \rightarrow E_T^j + 10\% \tag{3.20}$$

$$\epsilon_{jets} = (85.4 \pm 2.2(stat))\% \qquad \text{for } E_T^j \rightarrow E_T^j - 10\%. \tag{3.21}$$

Comparing with the standard result $\epsilon_{jets} = (83.1 \pm 2.3(stat))\%$ we find a relative systematic uncertainty $\Delta\epsilon/\epsilon = \pm 4\%$. This uncertainty agrees with the uncertainty found for the ee, $\mu\mu$, $e\mu$ dilepton analysis [20]. This is expected as the jet energy spectra should be independent of the decay mode of the W in dilepton events.

Uncertainty on H_T cut efficiency ϵ_{H_T}

The systematic uncertainty on the jet energy scale (hadronic energy scale) also results in a systematic uncertainty on the efficiency of the H_T cut.

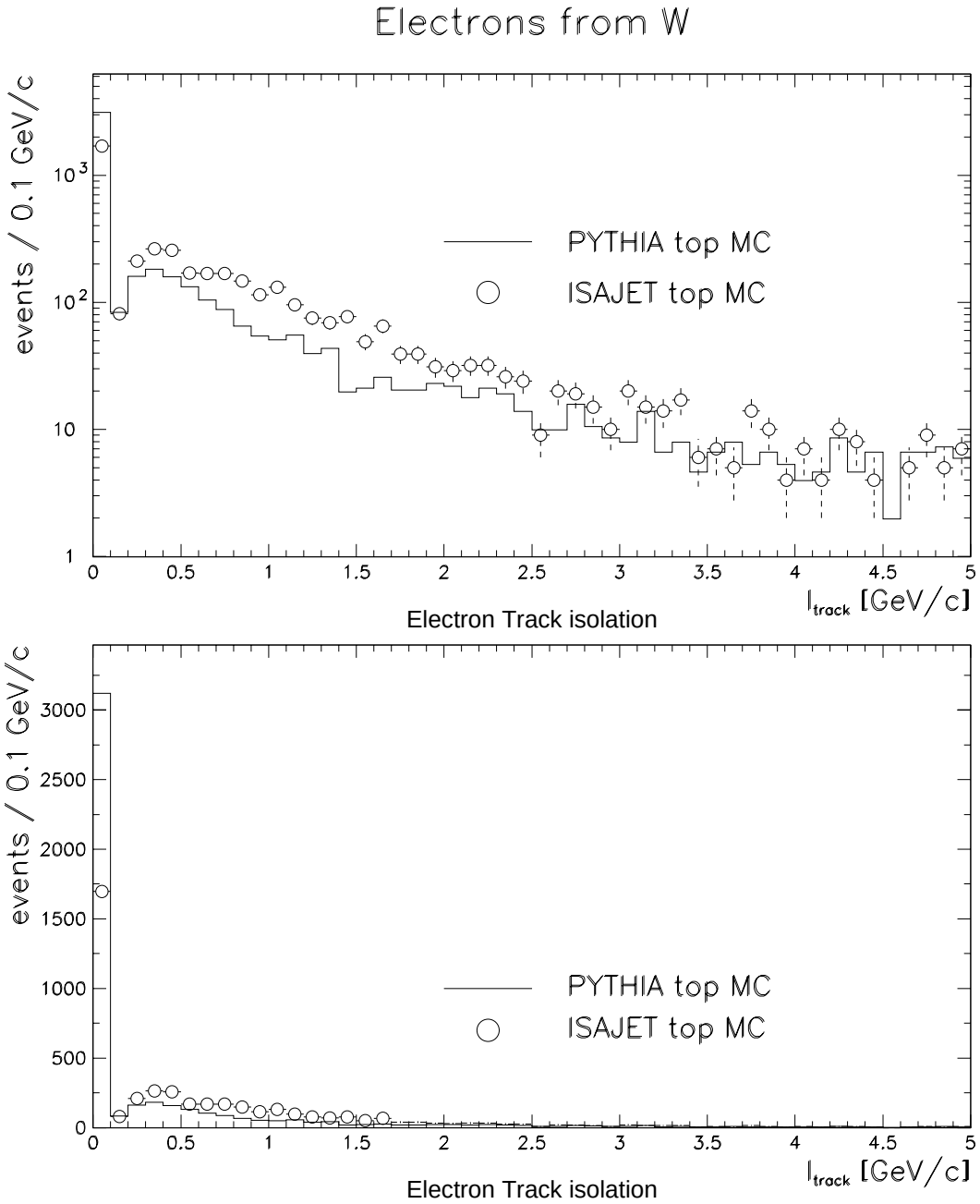

Figure 3.24: Track isolation for central electrons in $t\bar{t}$ ISAJET Monte Carlo and in PYTHIA Monte Carlo. Top: Logarithmic scale, Bottom: Linear scale.

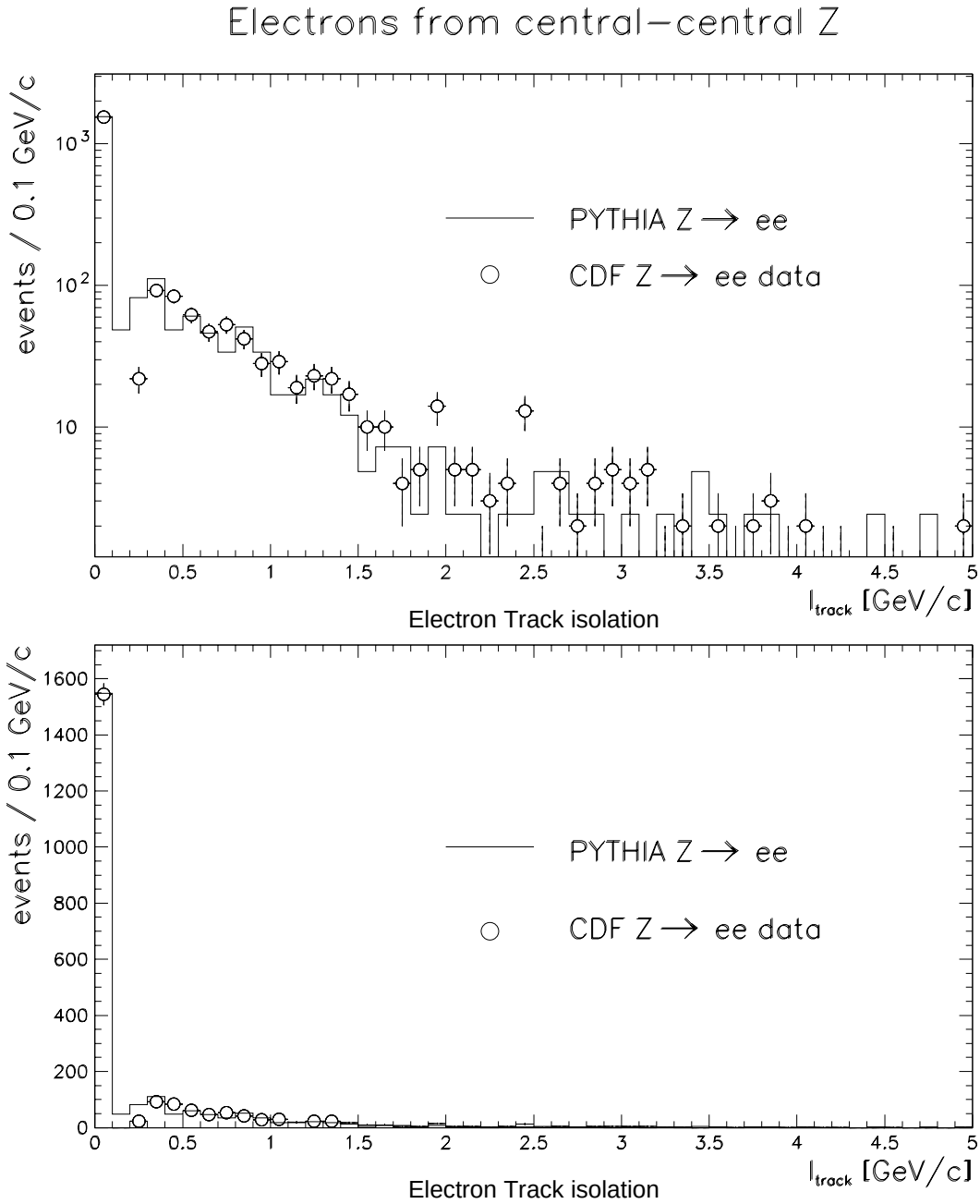

Figure 3.25: Track isolation for electrons from central-central Z's in data and in PYTHIA Monte Carlo. Top: Logarithmic scale, Bottom: Linear scale.

We use the same method as for the 2–jet–cut efficiency and find:

$$\epsilon_{H_T} = (92.1 \pm 1.8(stat))\% \qquad \text{for } E_T^j \rightarrow E_T^j + 10\% \tag{3.22}$$

$$\epsilon_{H_T} = (89.4 \pm 2.1(stat))\% \qquad \text{for } E_T^j \rightarrow E_T^j - 10\%. \tag{3.23}$$

Compared with the central value $\epsilon_{H_T} = (91.7 \pm 1.9(stat))\%$ we find a relative systematic uncertainty $\Delta\epsilon/\epsilon = \pm 3\%$.

Uncertainties in common with $ee, \mu\mu, e\mu$ dilepton analysis

We consider the systematic effects related to the primary electrons and muons in a tau dilepton event to be similar to those found for the $ee, \mu\mu$, and $e\mu$ dilepton analysis because they are unrelated to the tau lepton. We therefore adopt the following values for these systematic uncertainties from Ref. [20]:

- Primary lepton identification efficiencies $\epsilon_{ID}^{e,\mu}$: A comparison of the efficiencies for identifying electrons and muons measured in Z^0 data and Z^0 Monte Carlo yields a scale factor for converting Monte Carlo efficiencies into data efficiencies. The identification efficiencies depend on the isolation of the lepton, so that the scale factor changes as a function of the isolation. Due to the higher jet activity the isolation for a top event is considerably different from the isolation in a Z event. Consequently, it is not clear how well the scaling from Monte Carlo to data as derived from Z events works for top events. This leads to a systematic uncertainty on $\epsilon_{ID}^{e,\mu}$ for $t\bar{t}$ events.

  Recalculating the total $t\bar{t}$ dilepton acceptance using the lepton identification efficiency from Z^0 data plus or minus half the difference between data and Monte Carlo efficiencies yields a systematic uncertainty

of $\pm 7\%$ [20]. Since there is only one e or μ in a tau dilepton event we divide this result by $\sqrt{2}$ so that $\epsilon_{ID}^{e,\mu} = 5\%$ for the tau dilepton analysis.

- Primary lepton isolation efficiency $\epsilon_{Iso}^{e,\mu}$: This effect is estimated to be $\pm 2\%$ by varying the isolation cut.
- Monte Carlo generator: Comparing PYTHIA and HERWIG gives $\pm 3\%$.
- Initial and final state radiation (ISR, FSR): Turning ISR and FSR on and off in the PYTHIA $t\bar{t}$ MC makes a difference of $\pm 3\%$ on A_{tot} , which we use as the uncertainty.
- Parton distribution functions: Comparing MRS D0′ and CTEQ2pL in HERWIG gives an uncertainty of $\pm 4\%$ (using the full difference).

Uncertainty on kinematic acceptance $A_{geom \cdot P_T}$

A systematic mismeasurement of the E_T (p_T) of the primary electron (muon) or the p_T of the tau candidate will result in a systematic uncertainty on $A_{geom \cdot P_T}$. For electrons the relevant quantity is the uncertainty on the CEM energy scale; for muons it is the uncertainty in the p_T scale of the tracks. In the case of the taus we use the p_T of the tracks and the CEM energy of any π^0 candidates, so both those scale uncertainties need to be considered. Note that the total E_T of the tau jet is *not* used in the kinematic selection, so that the hadronic energy scale does not enter here.

- **p_T scale:**

  We estimate the uncertainty on the p_T scale from the $Z \rightarrow \mu\mu$ events shown in Figure 1.18. The mean of the Gaussian fit in the mass peak region $85 < m_{\mu\mu} < 95$ GeV/c^2 is 90.64 GeV/c^2. The relative difference between this fit value and the Z mass as measured by LEP (91.187$\pm$0.007 GeV/c^2) [4] is 0.6%, which we take as an estimate for the uncertainty on the p_T scale in this analysis.

- **CEM scale:**

  We estimate the CEM energy scale uncertainty from the reconstructed Z mass peak for tight–tight central dielectrons using raw electron energies. Figure 1.7 shows that the fit to the peak region of 85 – 95 GeV/c^2 gives $m_Z = 89.8 \pm 0.1$ GeV. Comparing with the PDG value $m_Z = 91.187 \pm 0.007$ GeV shows a 1.4 GeV or 1.5% shift on m_Z. From this we estimate the uncertainty on the CEM energy scale in this analysis to be 1.5%.

We recalculate $A_{geom \cdot P_T}$ with the lepton E_T's and p_T's increased and decreased according to the above uncertainties on the p_T and CEM scales. The result is a 1% change in $A_{geom \cdot P_T}$, which we take as the systematic uncertainty on $A_{geom \cdot P_T}$.

Summary of systematic uncertainties

In Table 3.11 we summarize by listing all systematic uncertainties. We consider the various sources of these systematic uncertainties as independent and add all uncertainties in quadrature. The total systematic uncertainty on the tau dilepton acceptance A_{tot} is $\pm$13%.

Source	affected quantity	systematic uncertainty
Top mass	A_{tot}	$\pm 6\%$
Hadronic energy scale	A_{tot}	$\pm 5\%$
	ϵ_{jets}	$\pm 4\%$
	ϵ_{H_T}	$\pm 3\%$
	ϵ^{τ}_{ID}	$\pm 1\%$
Primary lepton ID*	$\epsilon^{e,\mu}_{ID}$	$\pm 5\%$
Multiple vertices	ϵ^{τ}_{ID}	$\pm 5\%$
Underlying event	ϵ^{τ}_{ID}	$\pm 4\%$
MC generators*	A_{tot}	$\pm 4\%$
Radiation (ISR,FSR)*	A_{tot}	$\pm 3\%$
Primary lepton Isolation*	$\epsilon^{e,\mu}_{Iso}$	$\pm 2\%$
Parton distribution functions*	A_{tot}	$\pm 2\%$
CEM & p_T scale	$A_{geom \cdot P_T}$	$\pm 1\%$
TOTAL	A_{tot}	$\pm 13\%$

Table 3.11: Summary of all systematic uncertainties on the tau dilepton acceptance. Uncertainties marked by * have been adopted from the calculations for $ee, \mu\mu$, and $e\mu$ dileptons in Ref. [20].

Including the systematic uncertainty on A_{tot} the final result for the total acceptance is

$$A_{tot} = (0.134 \pm 0.013(stat) \pm 0.017(syst))\% \tag{3.24}$$

3.7.3 Expected number of events in 109 pb^{-1}

With A_{tot} in hand we can calculate how many dilepton events from $t\bar{t}$ production and decay we expect to find in Run I. Using the latest estimate of the top production cross section by CDF from other top decay modes (lepton+jets tagged by SVX or SLT, standard dilepton, all hadronic), $\sigma_{t\bar{t}} = 7.7^{+1.8}_{-1.5}$ [69], we find:

$$
\begin{aligned}
N_{exp}^{\tau-dilepton} &= \sigma_{t\bar{t}}\ \mathcal{L}\ A_{tot} \\
&= (7.7 \pm 2)pb\ (109 \pm 7(syst))pb^{-1} \\
&\quad \times(0.134 \pm 0.013(stat) \pm 0.017(syst))\% \\
&= 1.1 \pm 0.3(stat) \pm 0.2(syst)\ \text{events},
\end{aligned}
\tag{3.25}
$$

where we take a 6% systematic uncertainty on the total integrated luminosity. If we instead base the calculation on the theoretical $t\bar{t}$ cross section $\sigma_{t\bar{t}}^{theory} = 4.8 \pm 0.7$ pb [26] we expect $N_{exp}^{\tau-dilepton} = 0.70 \pm 0.07(stat) \pm 0.15(syst)$ events.

3.8 Backgrounds

3.8.1 Fakes

Jets from quarks and gluons (hereafter called 'QCD jets') can fake hadronic τ decays. Even though the τ identification cuts discussed above are tailored towards minimizing this background, there is always a (small) probability for a jet to fragment with low track multiplicity. With the τ identification cuts used here this process is basically indistiguishable from a τ decay and hence constitutes an irreducible background[3]. An $\ell + \not{E}_T + \geq 3\ jets$ ($\ell = e, \mu$) event where one jet is misidentified as a τ would produce a fake τ dilepton event. Sources for these events are production of $W + \geq 3\ jets$ events, and $t\bar{t}$ events that decay in the lepton + jets channel. The following sections describe how we estimate these backgrounds.

[3]In principle, cutting on SVX impact parameters and identifying SVX vertices could provide a handle here [70], but the efficiencies for real τ's are rather low, so we do not use this here.

Dijet sample

We use jets from a dijet data sample to estimate the fake rate. By using dijets we make sure that we actually pick up QCD jets and not other potential sources of background. The assumption here is that the jets in $W+ \geq 3$ *jets* events behave the same as QCD jets. The dijet sample is made from a complete set of Run Ib jet samples. The trigger thresholds on the transverse energy of jets had been set to 20 GeV, 50 GeV, and 70 GeV [71] to produce these samples. The dijet selection criteria applied to the jet samples are:

1. 2 jets with $E_T^{uncorr} > 10$ GeV, $|\eta_{det}| < 2.0$

2. $|\Delta\phi_{jj}| > 160°$ (back-to-back cut)

Jet selection with minimal bias

It was shown in Ref. [49] that naively using *all* the jets in such a sample is problematic. The Level 2 trigger is biased towards passing narrow jets with fewer tracks in the isolation cone near the trigger threshold because these jets are contained in fewer towers. Because the τ selection requires a narrow jet and tracking isolation, this leads to an overestimate of the fake rate near the trigger threshold. Conversely, non-triggering jets below the trigger threshold tend to be wider and contain more tracks in the isolation cone, leading to an underestimate of the fake rate. Using the Run Ib jet data we have reproduced this behavior and therefore we use the method of Ref. [49] to reduce the Level 2 bias in the jet selection:

1. Pick one of the 2 jets at random.

2. Match the picked jet to a cluster of energy in the calorimeter found by the Level 2 hardware trigger [71] within a cone of radius 0.4 in $\eta - \phi$ space. If there is no match, skip the event.

3. If the E_T of the matched Level 2 cluster is below the trigger threshold, skip the event.

4. If the reconstructed E_T of the other jet is below the trigger threshold, skip the event.

5. If all the above conditions are fulfilled, put the other jet into the sample.

In this way we make sure that one of the 2 jets in the η range is a Level 2 trigger jet, but we do not use it in the sample. The cut on the reconstructed E_T of the other jet ensures that in principle this jet could have passed the Level 2 trigger, but we make *no* Level 2 trigger requirement for this jet and thus minimize the Level 2 bias of the sample.

The final sample consists of 40405, 29817, and 31491 jets with $|\eta_{det}| < 1.2$ from the JET20, JET50, and JET70 samples, respectively. Figure 3.26 shows the combined jet E_T spectrum.

One problem with this algorithm is that the jets with $10 < E_T < 20$ GeV are by definition non-trigger jets. In order to get an estimate of the fake rate in this E_T range, we make a second sample from the JET20 sample, where we lower the threshold used in the algorithm from the 20 GeV trigger threshold to 10 GeV. As there are no jet triggers below 20 GeV we have to live with the remaining bias in the range $10 < E_T < 20$ GeV.

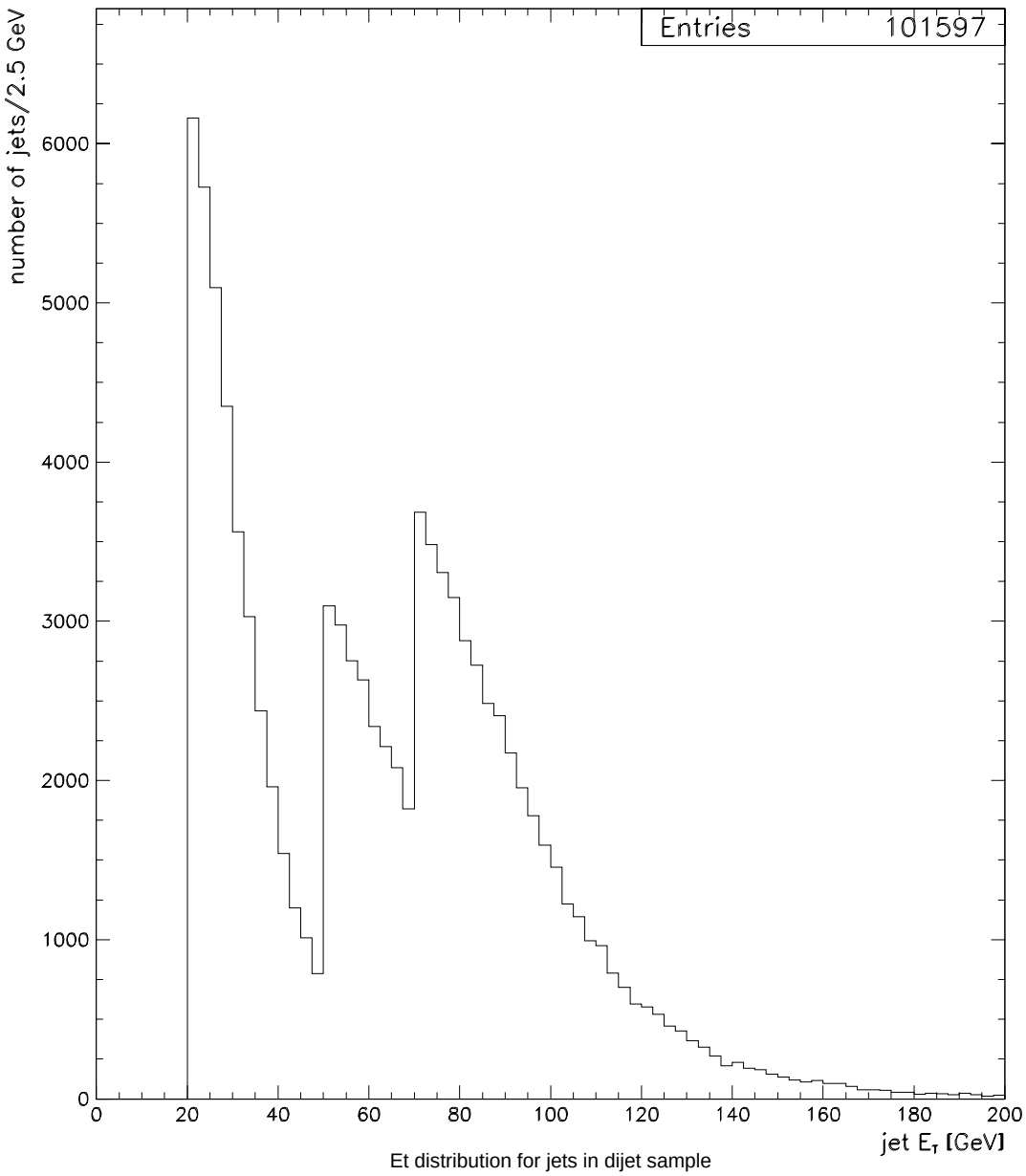

Figure 3.26: The E_T spectrum of jets in the QCD dijet sample with minimal trigger bias used for estimating the τ fake rate.

Fake rate

For one-prongs we find that 94 events out of 101713 pass the τ identification cuts for an *average* τ fake rate of $(0.09 \pm 0.01)\%$. In the case of the three-prongs 180 events pass giving an average τ fake rate of $(0.18 \pm .01)\%$. Consequently, the total average fake rate is $(0.27 \pm 0.02)\%$. All uncertainties here are statistical. To obtain the τ fake rate per jet as a function of jet E_T for QCD jets we simply apply the τ identification cuts to the jets and divide the E_T spectrum of jets passing the cuts by the spectrum of all jets. The result for one-prongs, three-prongs and both combined is shown in Figure 3.27. The fake rate drops more sharply for three-prongs than for one-prongs. We find that the total fake rate drops from 0.8% at 20 GeV to about 0.1% at 50 GeV and then stays flat at the 0.1% level out to about 100 GeV. Beyond 100 GeV we run out of statistics in the sample. In the same figure we also plot the fake rate as a function of η_{det}^{jet}. Near the crack between the plug and central calorimeter the fake rate for three-prongs is larger than in the detector center.

In analogy to Table 3.6, Table 3.12 shows the efficiency, or rather rejection power, of the τ identification cuts for jets from the JET20 sample, which is the sample with the highest fake rate.

Fake background

An $\ell + \not\!\!E_T + \geq 3\ jets$ ($\ell = e, \mu$) event where one jet is misidentified as a τ would produce a fake τ dilepton event. A jet can be misidentified as a τ, if $E_t^{jet} > 10$ GeV, $|\eta_{jet}| < 1.2$ and $|\Delta z| = |\overline{z}_{jet}^{track} - z_{e,\mu}^{track}| < 5$ cm. Such a jet is called a 'τ–taggable' jet. We calculate the expected number of background events from fakes by first multiplying the fake rate as a function of E_T bin-by-

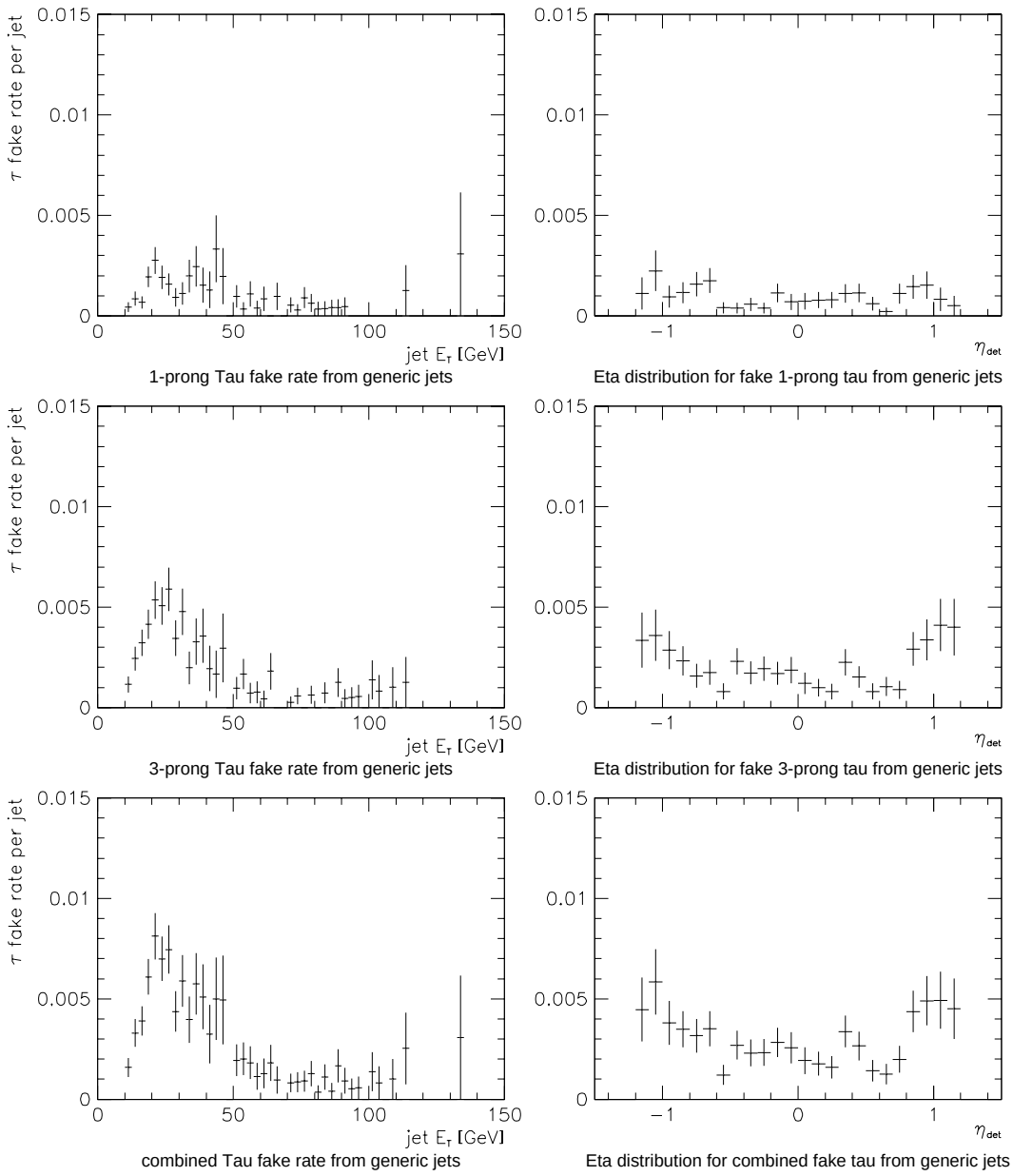

Figure 3.27: The τ fake rate per jet for QCD jets as a function of jet E_T and η_{det} as measured in the dijet sample with minimal trigger bias.

	Cut in question	All other cuts applied	Cumulative cuts
Jet makes a tau cluster	51.7%	-	51.7%
Track multiplicity 1 or 3	16.7%	52.4%	16.7%
E/p with π^0	48.3%	85.9%	15.3%
Slid. RMS Cluster width cut	14.5%	58.1%	5.0%
$m_{trk+\pi^0} < 1.8$ GeV	32.8%	55.8%	1.8%
Number of $\pi^0 < 3$	26.7%	88.9%	1.6%
$I^{\tau}_{trk} < 1$ GeV/c	13.7%	43.2%	0.69%
Electron removal	50.8%	96.3%	0.67%
Muon removal	44.7%	85.9%	0.58%
TOTAL efficiency	(0.58±.04)%		

Table 3.12: Rejection power of τ identification cuts for jets in the JET20 sample, i.e. with $E_T^{jet} > 20$. The percentages are relative to the total number of jets in the sample (101713).

bin with the E_T spectrum of all 'τ–taggable' jets, in a $\ell + \not\!\!E_T + \geq 3\ jets$ ($\ell = e, \mu$) *data* sample and then summing over all bins.

Since we need to apply the dilepton jet cuts, the Z-removal and topology cuts ($\not\!\!E_T$, $S_{\not\!\!E_T}$, H_T) to the $\ell + \not\!\!E_T + \geq 3\ jets$ sample, this sample is different from the official sample [38] used for the lepton + jets top analysis. Note that we also take the cut on $|\overline{z}^{track}_{\tau} - z^{track}_{e,\mu}|$ into account by calculating $\overline{z}^{track}_{jet}$ for central jets. We obtain this quantity by extrapolating all tracks in the event with $p_T > 1$ GeV/c to the CES chambers in the calorimeter. Using all those tracks whose extrapolated coordinates match within a cone of radius 0.4 in $\eta - \phi$ space to the jet cluster in the calorimeter, we define $\overline{z}^{track}_{jet}$ as the p_T–weighted average of the track z-intercepts.

In 109 pb^{-1} of data we find 186 $\ell + \not\!\!E_T + \geq 3\ jets$ ($\ell = e, \mu$) events with 435 τ–taggable jets. The falling jet E_T spectrum for this sample is shown in Figure 3.28. We multiply this spectrum with the fake rate shown in Figure 3.27

and sum all bins. The resulting sum is divided by 2 to take the opposite–sign cut into account as we expect the fake rate for same-sign events and opposite-sign events to be the same. From this procedure we find a background prediction for τ fakes of

one-prongs:	0.24±0.02(stat) events
three-prongs:	0.54±0.04(stat) events
total:	0.78±0.04(stat) events

To obtain the statistical uncertainties we have added the relative uncertainties of the fake rate in each bin in quadrature.

3.8.2 Physics backgrounds

$Z \rightarrow e^+e^- + jets$:

We use a $Z \rightarrow e^+e^- + 2$ *partons* VECBOS sample [73] to estimate this background. This sample was generated using $Q^2 =< p_T >^2$ and the parton distribution function MRSD0′. The preselection at the generator level on the partons is $P_T > 8$ GeV/c, $|\eta| < 3$ and $\Delta R_{jj} > 0.4$; no requirements are applied to the lepton. We start with the generator banks from this sample, resimulate the event to generate all necessary banks and apply the dilepton sample selection using the cuts described in section 2.4.1 to reduce the sample size.

We choose the VECBOS generator as it is known to model the jets in $Z + jets$ events more accurately than other generators. We test this claim by comparing the jet multiplicity and the jet E_T spectra for $Z \rightarrow e^+e^- + \geq 2\, jets$ for VECBOS and data (109 pb^{-1}) in Figure 3.29. For this purpose we require a dilepton with two tight central electrons (TCE-TCE; see section 2.1.2) of opposite sign that form an invariant mass $75 < m_Z < 105$ GeV/c^2. We use

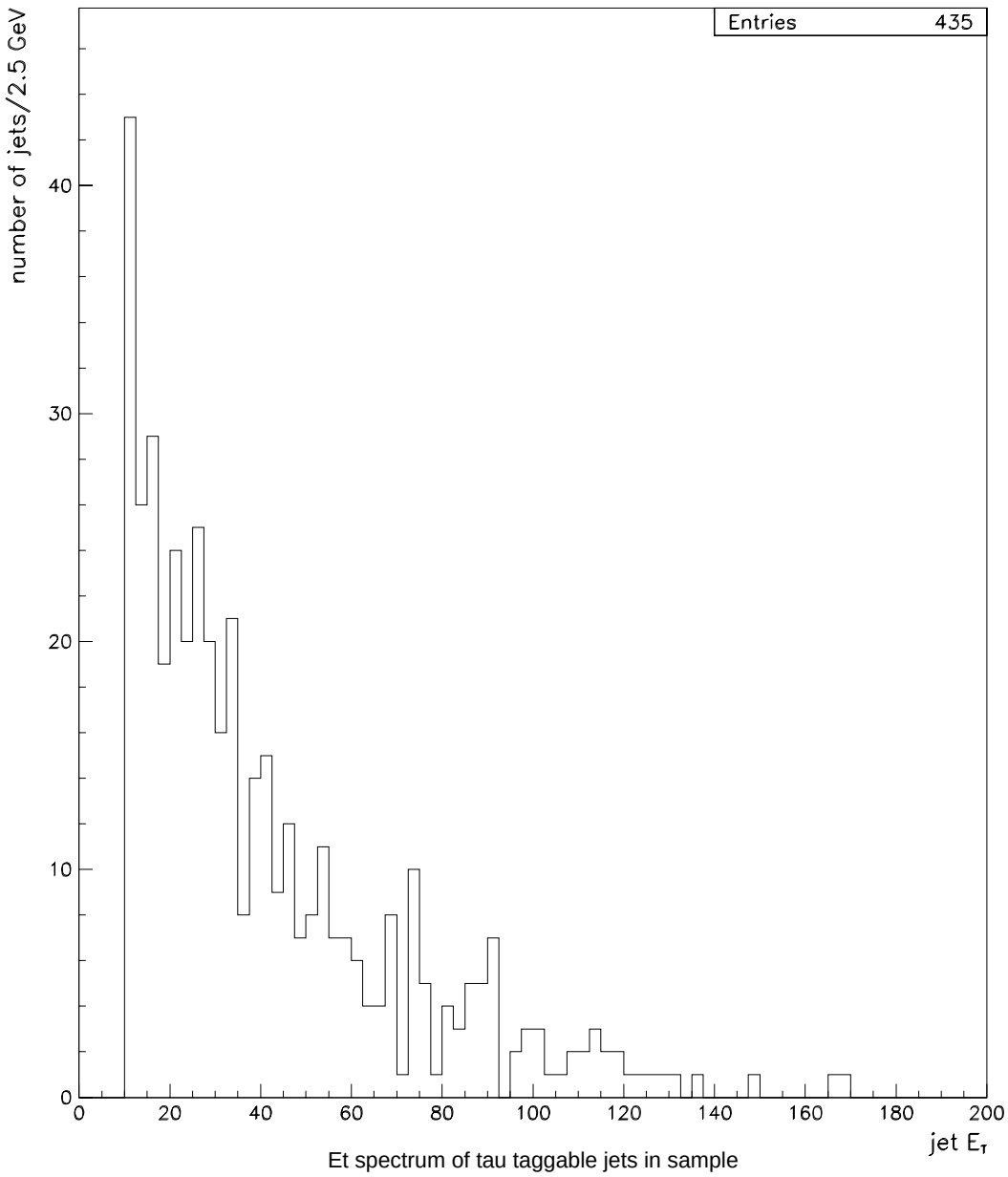

Figure 3.28: The E_T spectrum of jets in a $W+ \geq 3$ jets data sample with dilepton jet cuts and τ analysis topological cuts (109 pb^{-1}).

the standard definition of a jet from Chapter 2 ($E_T > 10$, $|\eta_{det}| < 2.0$). The VECBOS jet multiplicity is normalized to the data in the 2–jet bin (66 events) and the VECBOS jet spectra are normalized to the number of data events with ≥ 2 jets (76 events). As expected, we find that the jet multiplicity for ≥ 2 jets is in good agreement with the data. We expect to underestimate the 0 and 1 jet bin because the $Z \rightarrow e^+e^- + 0,1$ *partons* matrix elements are not incorporated here. Also, the jet spectra are well modelled within statistics.

Equally important for an accurate background estimate is the correct simulation of the high tail of the $\not\!\!E_T$ spectrum. The comparison is shown in Figure 3.30. The $Z + 0$ *jet* VECBOS spectrum is stiffer than the data spectrum. This is expected because in these events both partons are lost and hence produce additional $\not\!\!E_T$. For $Z + 1$ *jet* and $Z + 2$ *jets*, which matter most to us, we find good agreement within statistics.

These observations give us confidence that this sample will produce a reliable determination of the $Z + jets$ background. We require one tight central e or μ as the *primary* lepton and apply the τ identification cuts. In Figure 3.31 we plot $S_{\not\!\!E_T}$ versus the corrected $\not\!\!E_T$ for the events in which we have found a τ dilepton that passes all identification cuts and the opposite–sign cut. In the plot on the right hand side the $S_{\not\!\!E_T}$ cut is applied. In the same plane we plot the events that survive if we consecutively apply the other topology cuts, i.e. the 2–jet cut and H_T cut. Note that there are no overflows in the histograms. After all cuts have been applied we are left with no events.

We normalize the VECBOS sample to the data in the $Z + 2$ *jets* bin. In the data sample we find 66 events; in the VECBOS sample there are 721 events. Taking the statistical uncertainties on the number of events and an estimated 8% uncertainty on the integrated luminosity into account, we find that the VECBOS sample corresponds to an integrated luminosity of

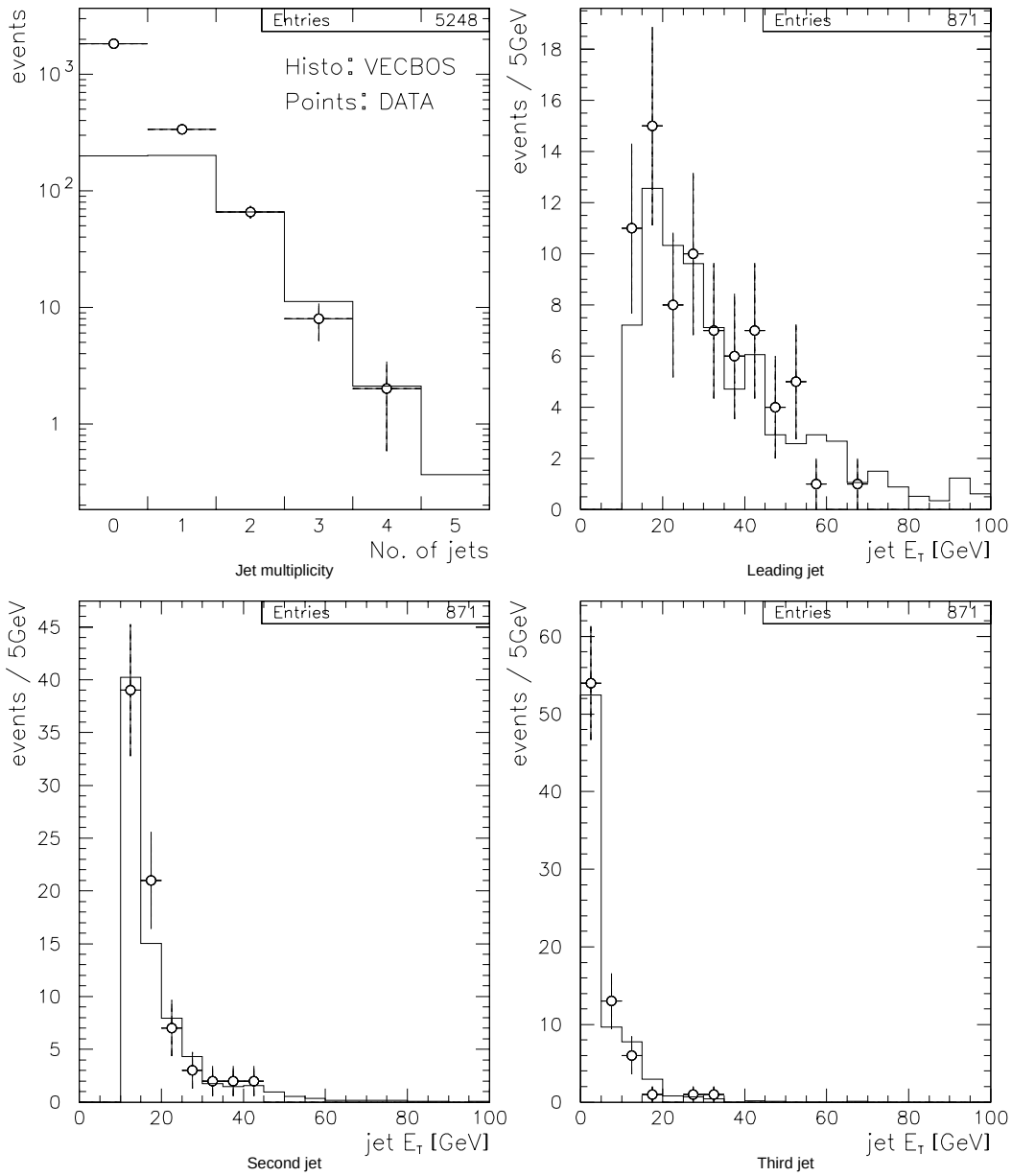

Figure 3.29: Comparison of jet multiplicity and jet E_T spectra in $Z \rightarrow e^+e^- + \geq 2jets$ events. Points are data (109 pb^{-1}); histograms are VECBOS Monte Carlo. For the jet multiplicity VECBOS is normalized to the 2 jet bin. The VECBOS Monte Carlo is expected to have fewer events than the data in the 0–jet and 1–jet bin because only $Z \rightarrow e^+e^- + 2\ partons$ were generated. For the jet E_T spectra VECBOS is normalized to 76 data events with 2 or more jets. The number of entries in all plots are for the VECBOS Monte Carlo.

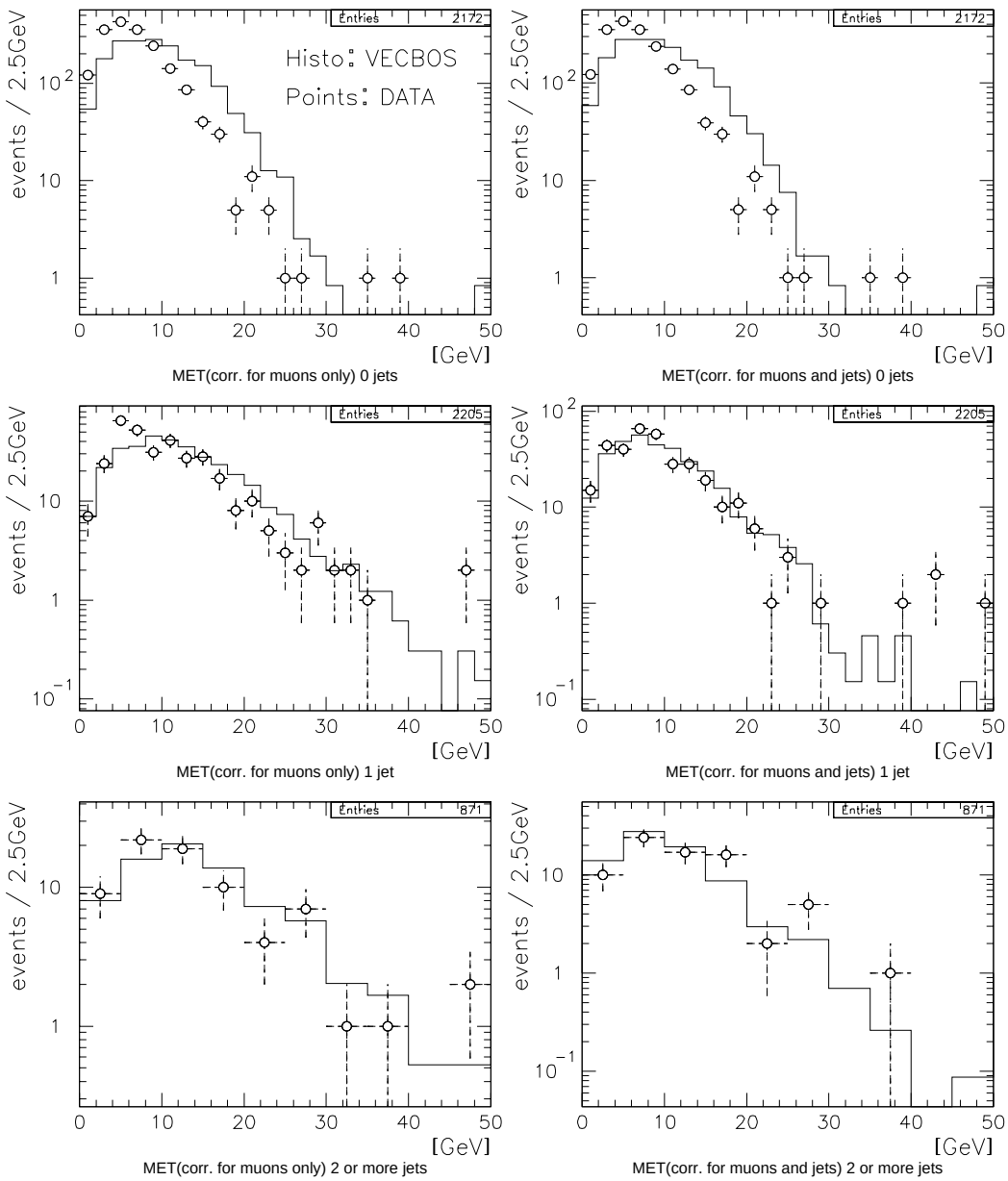

Figure 3.30: Comparison of $\not\!\!E_T$ in $Z \rightarrow e^+e^- + jets$ events. Points are data ($109\ pb^{-1}$); histograms are VECBOS Monte Carlo. VECBOS is normalized to 1822(335;76) data events with 0 (1;$\geq$ 2) jets. The number of entries are for the VECBOS Monte Carlo. The VECBOS Monte Carlo is not expected to model the data well in the 0–jet bin because only $Z \rightarrow e^+e^- + 2\ partons$ were generated.

1200 ± 195(stat) pb^{-1} . Since there are no events that survive all cuts we set an upper limit on the background from $Z \rightarrow e^+e^- + jets$. At a 1 sigma confidence level (68%) we expect < 0.09 background events.

$Z \rightarrow \tau^+\tau^- + jets$:

As we demonstrated above, the $Z \rightarrow e^+e^- + jets$ VECBOS sample models the jet activity and the $\not\!\!E_T$ well. We therefore use this sample also as the basis for estimating the background from $Z \rightarrow \tau^+\tau^- + jets$. We choose this method over the 'traditional' CDF method of starting from a $Z \rightarrow e^+e^-$ *data* sample, where the ELES banks are replaced with generated τ's and their simulated decay products [19]. In order to get sufficient statistics one $Z \rightarrow e^+e^-$ decay must be redecayed many times as a $Z \rightarrow \tau^+\tau^-$. The problem with this method is the fact that in the data some ee top signal events are expected inside the Z window [74]. These are more likely to pass the τ dilepton cuts than Z events after being turned into top $\tau\tau$ events. The resulting background estimate thus depends on the behavior of just a few events, which may in fact be due to $t\bar{t}$ decays.

Instead, we make a $Z \rightarrow \tau^+\tau^- + jets$ Monte Carlo from the $Z \rightarrow e^+e^- + jets$ VECBOS sample [72]. In the resulting sample we require one tight central e or μ as the *primary* lepton and apply the τ identification cuts. In Figure 3.32 we plot $S_{\not\!\!E_T}$ versus the corrected $\not\!\!E_T$ for the events in which we have found a τ dilepton that passes all identification cuts, the opposite–sign cut and the Z removal cuts (top). We also plot the events that survive if we consecutively apply the other topology cuts, i.e. the 2–jet cut (center) and H_T cut (bottom). There are no overflows in the histograms. We find that 15 events (8 one-prongs and 7 three-prongs) survive all cuts. Normalizing to the

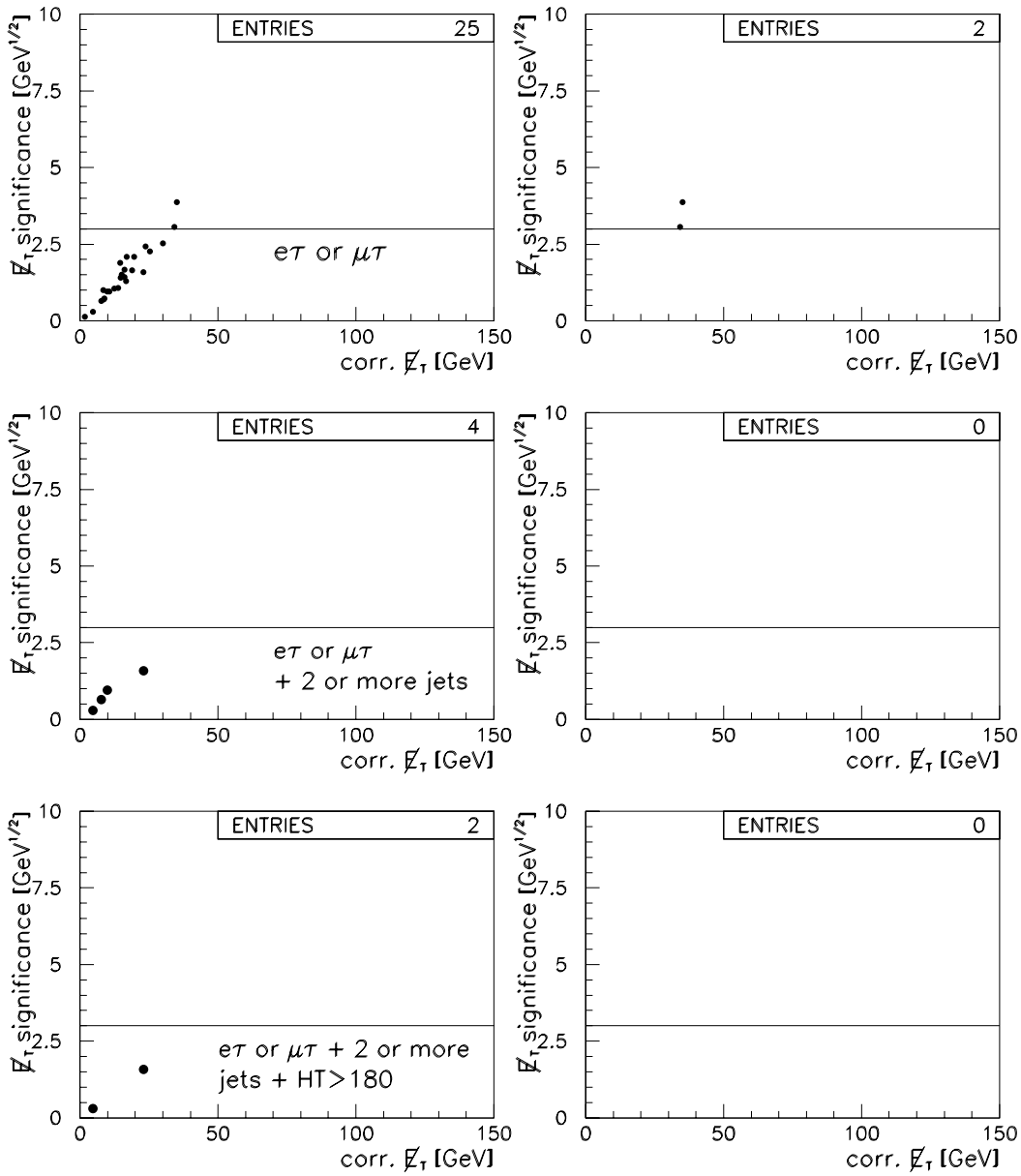

Figure 3.31: Scatterplot of $S_{\not{E}_T}$ vs $\not{E}_T$ for the Monte Carlo $Z \to e^+e^- + jets$ sample (1200 pb^{-1}). Top: after identifying a primary e or μ and a τ lepton. Center: after requiring 2 jets. Bottom: after requiring 2 jets and $H_T > 180$ GeV. Plots on the left show all events; plots on the right show only events that survive the $S_{\not{E}_T} > 3$ GeV$^{1/2}$ cut.

integrated luminosity of the sample this yields an estimate for the background from $Z \rightarrow \tau^+\tau^- + \ jets$ of:

one-prongs:	0.74±0.26(stat) events
three-prongs:	0.64±0.24(stat) events
total:	1.38±0.36(stat) events

We find that the H_T cut reduces the background by about 40%. In Figure 3.33 we present the same data in the $\Delta\phi\ (\not{E}_T, jl)$ vs $\not{E}_T$ plane used in the ee, $\mu\mu$, $e\mu$ dilepton analysis for comparison. In this case 14 events pass the $\Delta\phi\ (\not{E}_T, jl)$ vs $\not{E}_T$ cut after the 2-jet cut and the H_T cut. However, since we use the $S_{\not{E}_T}$ cut for the tau dilepton analysis, our background calculation is based on 15 events.

$Drell - Yan \rightarrow \tau^+\tau^- + jets$:

The VECBOS generator is currently not set up to produce the full Z/γ interference with a Z peak on top of the continuous Drell-Yan spectrum; it only generates the Z component. Therefore, we estimate the Drell-Yan contribution to the background with PYTHIA. We generate 2 samples: one $Z \rightarrow \tau^+\tau^- + jets$ sample (246 pb^{-1}) that only has the contribution from the Z pole and a second $Z/\gamma \rightarrow \tau^+\tau^- + jets$ sample (222 pb^{-1}) that incorporates the Drell-Yan process and the full interference between Z and γ. For the latter sample we require that the total energy $\sqrt{\hat{s}}$ in the c.m. frame of the incident partons be greater than 40 GeV to limit the total production cross section. PYTHIA returns cross sections $\times$ BR values of 285 pb for Z production alone and 1070 pb for Z/γ. In the Z/γ sample we find $(7 \pm 5)\%$ more $e\tau$ and $\mu\tau$ candidates than in the Z sample, which we attribute to the Drell-Yan process. This result is obtained before applying the jet cut, $S_{\not{E}_T}$ cut or H_T cut in order

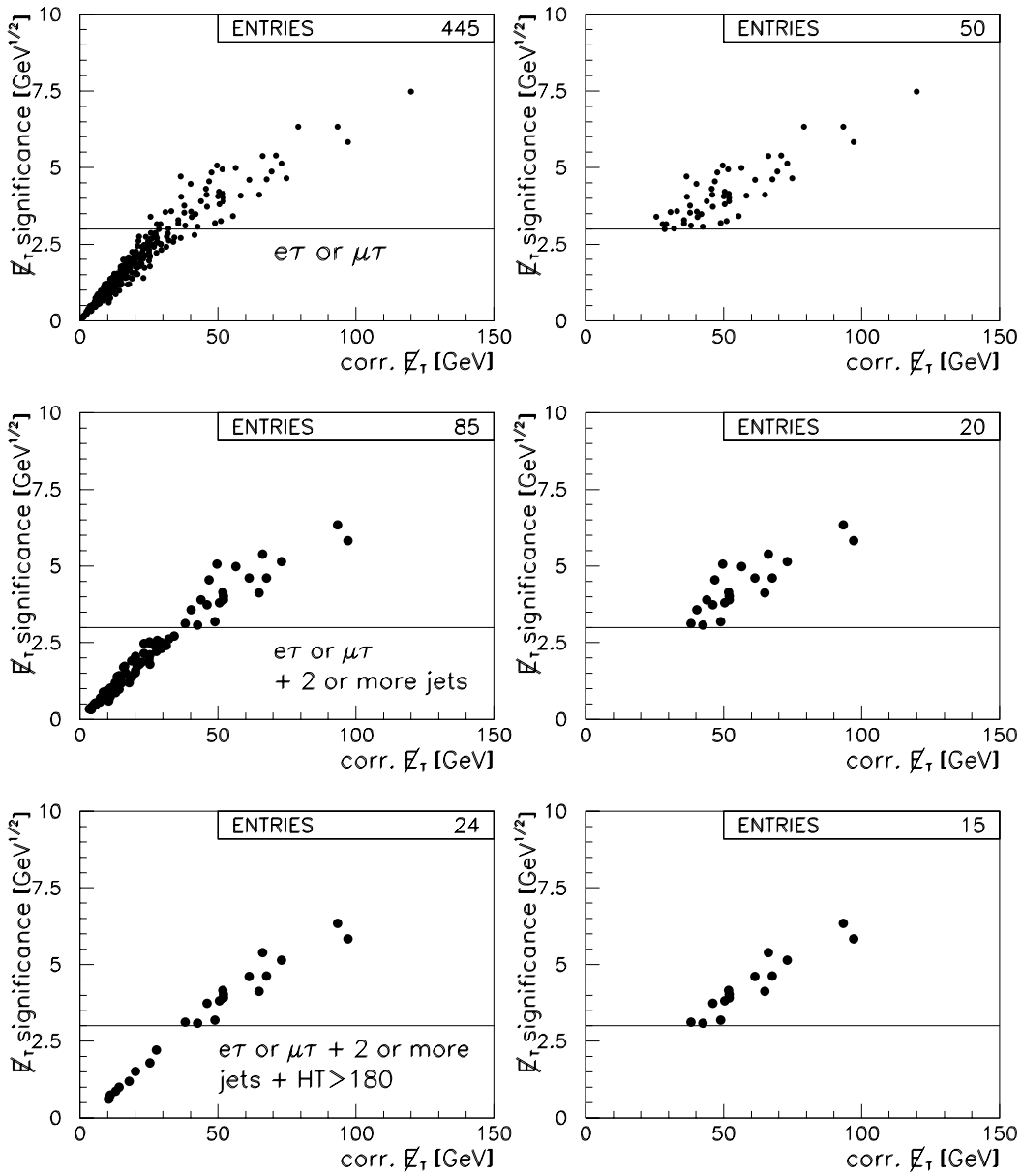

Figure 3.32: Scatterplot of $S_{\not{E}_T}$ vs $\not{E}_T$ for the Monte Carlo $Z \rightarrow \tau^+\tau^- + jets$ sample (1200 pb^{-1}). Top: after identifying a primary e or μ and a τ lepton. Center: after requiring 2 jets. Bottom: after requiring 2 jets and $H_T > 180$ GeV. Plots on the left show all events; plots on the right show only events that survive the $S_{\not{E}_T} > 3$ GeV$^{1/2}$ cut.

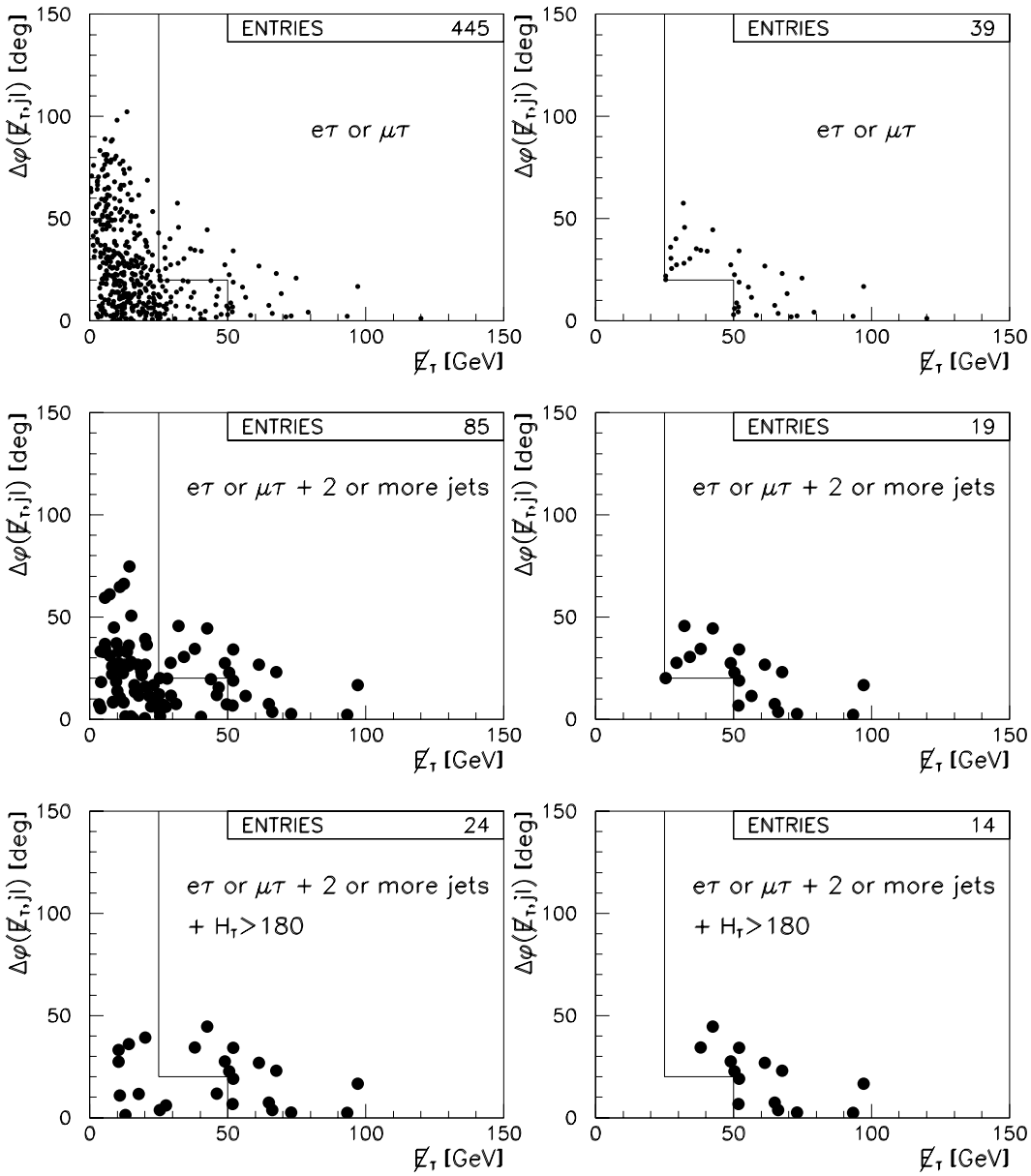

Figure 3.33: Scatterplot of $\Delta\phi\,(\not{E}_T, jl)$ vs $\not{E}_T$ for the Monte Carlo $Z \rightarrow \tau^+\tau^- + jets$ sample (1200 pb^{-1}). Top: after identifying a primary e or μ and a τ lepton. Center: after requiring 2 jets. Bottom: after requiring 2 jets and $H_T > 180$ GeV. Plots on the left show all events; plots on the right show only events that survive the topological cut indicated by the line.

to get high statistics. Note that it is assumed here that the jet production via initial state radiation in events propagated through the Z resonance is the same as for events propagated by photons. Scaling from the VECBOS result for Z's we estimate the Drell-Yan background to be 0.10 ± 0.07 events.

$Z \rightarrow \mu^+\mu^- + jets$:

By replacing e's with μ's at the generator level and resimulating we have also made a $Z \rightarrow \mu^+\mu^- + jets$ sample from the $Z \rightarrow e^+e^- + jets$ VECBOS sample. In Figure 3.34 we again plot $S_{\not{E}_T}$ versus the corrected $\not{E}_T$ for these background events. After all cuts we are left with no events and we set a limit on the background from $Z \rightarrow \mu^+\mu^- + jets$ events. At a 1 sigma confidence level (68%) we expect < 0.1 background events.

WW, WZ :

We estimate the background from dibosons using PYTHIA+TAUOLA Monte Carlo sets (20k events each). Figure 3.35 shows $S_{\not{E}_T}$ versus the corrected $\not{E}_T$ for WW. After all cuts we expect 0.18 ± 0.09 background events from WW and 0.06 ± 0.03 events from WZ.

$b\bar{b}$:

We generate 320,000 $b\bar{b}$ events using the PYTHIA+CLEO Monte Carlo requiring $\hat{p}_T(b) > 75$ GeV. Pythia calculates a cross section of 260 pb for this process; the Monte Carlo sample therefore corresponds to 1220 pb^{-1}. We find zero events passing all selection cuts and set a limit on the $b\bar{b}$ background of < 0.1 events at a 1 sigma confidence level. As expected, the most efficient cut for suppressing this type of background is the isolation cut. In 320,000 events

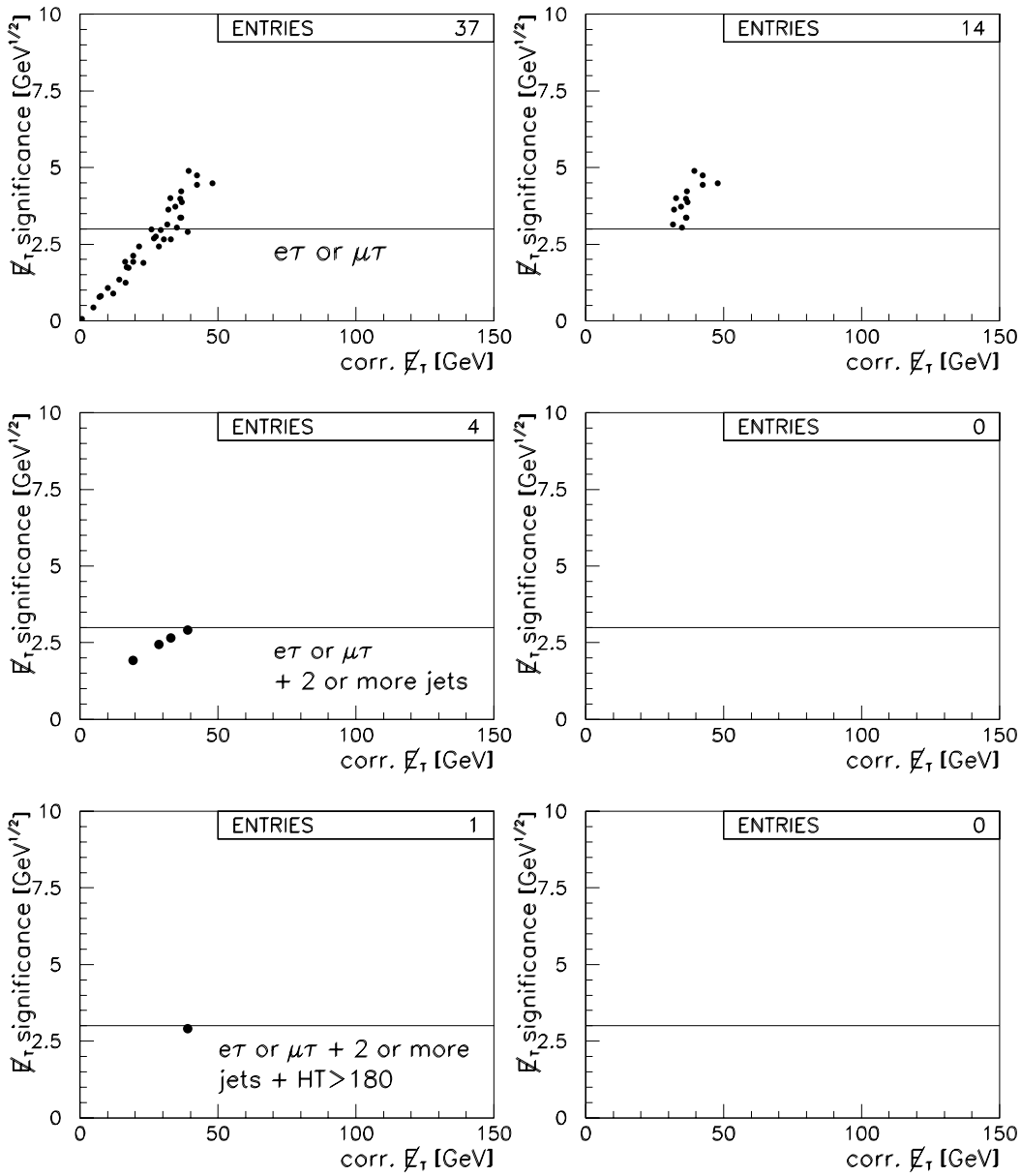

Figure 3.34: Scatterplot of $S_{\not{E}_T}$ vs $\not{E}_T$ for the VECBOS+TAUOLA+QFL $Z \rightarrow \mu^+\mu^- + jets$ sample (1200 pb^{-1}). Top: after identifying a primary e or μ and a τ lepton. Center: after requiring 2 jets. Bottom: after requiring 2 jets and $H_T > 180$ GeV. Plots on the left show all events; plots on the right show only events that survive the $S_{\not{E}_T} > 3$ GeV$^{1/2}$ cut.

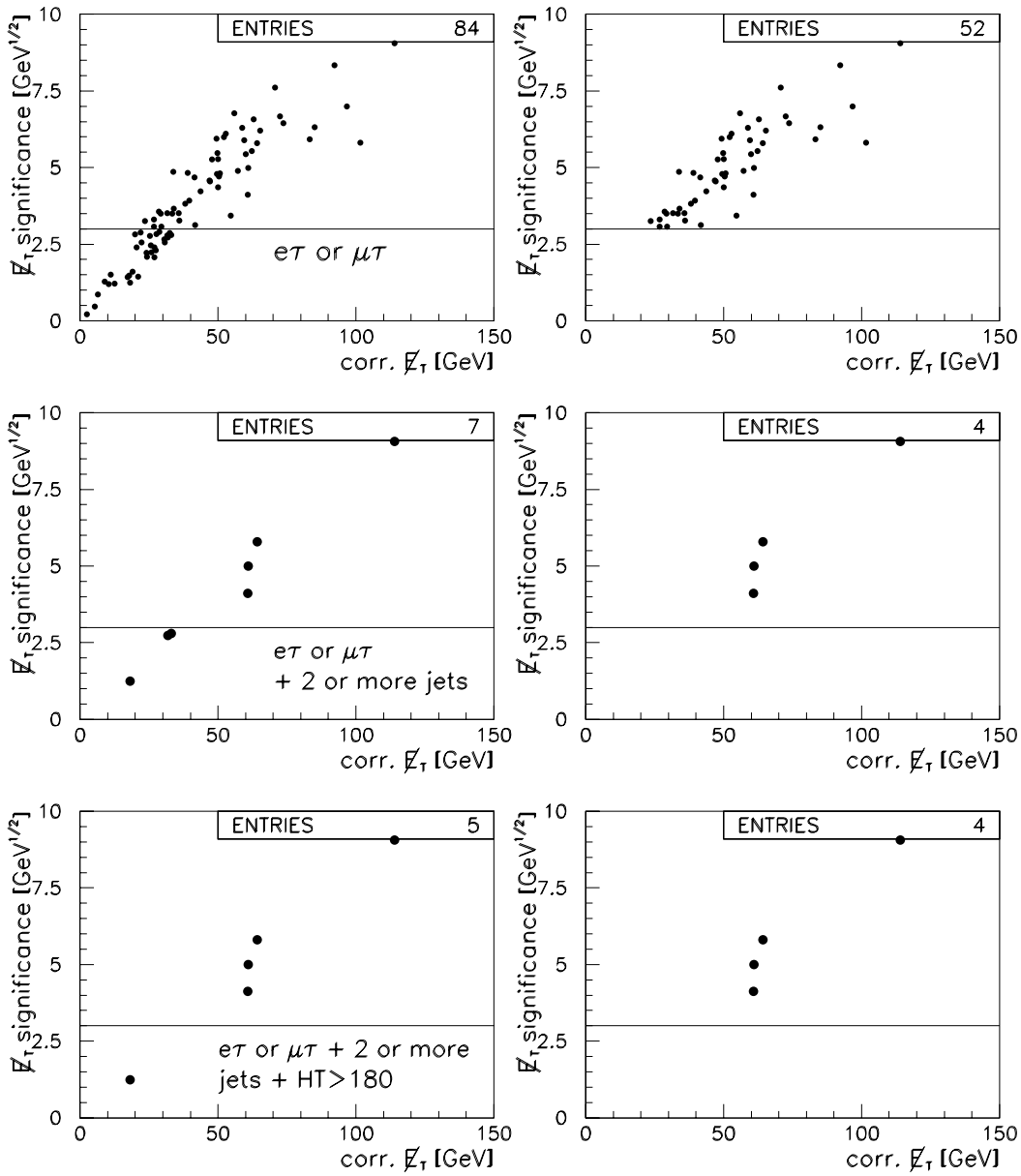

Figure 3.35: Scatterplot of $S_{\not{E}_T}$ vs $\not{E}_T$ for the PYTHIA WW sample (2500 pb^{-1}). Top: after identifying a primary e or μ and a τ lepton. Center: after requiring 2 jets. Bottom: after requiring 2 jets and $H_T > 180$ GeV. Plots on the left show all events; plots on the right show only events that survive the $S_{\not{E}_T} > 3$ GeV$^{1/2}$ cut.

we find only 7 isolated electron candidates and no isolated muon candidates. 250 τ candidates are found. There are no $e\tau$ or $\mu\tau$ candidates.

Background cross check and summary

We check if the Monte Carlo based background calculation is reasonable by relaxing the topological and kinematical cuts, recalculating the background and comparing to the data. In a first step we drop the H_T cut and in a second step we relax the $\not\!\!E_T$ requirement by requiring $\not\!\!E_T > 15$ GeV, but not cutting on $S_{\not\!\!E_T}$ at all. This is done separately for events with one jet and for events with ≥ 2 jets. For events with one jet we again derive $Z \rightarrow \mu^+\mu^-$ and $Z \rightarrow \tau^+\tau^-$ data sets from a $Z \rightarrow e^+e^- + 1$ *parton* VECBOS Monte Carlo set corresponding to (1560 ± 100) pb^{-1} [73].

The results of the background calculations and the expected number of events from top are listed in Tables 3.13 and 3.14. The section of the table for ≥ 2 jets and after all cuts summarizes the background calculation in the signal region. We find that the background calculation agrees well with the observed number of events in the data in all cases. This gives us confidence that the background estimate for the signal region is also reasonable.

3.9 Observation in the data

3.9.1 Final candidates

We apply the τ identification cuts to the events in the dilepton sample. In Figure 3.36(top) we plot the missing E_T significance ($S_{\not\!\!E_T}$) versus the corrected missing E_T ($\not\!\!E_T$) for the events in which we have found a τ candidate that passes all identification cuts, the opposite–sign cut and the Z removal

All cuts applied:

N_{jet} (10 GeV)	1	≥ 2
τ fakes	0.47±0.03	0.78±0.04
$Z \to \tau^+\tau^-$	0.50±0.16	1.38±0.37
$DY \to \tau^+\tau^-$	0.04±0.03	0.10±0.07
$Z \to e^+e^-$	< 0.16	< 0.09
$Z \to \mu^+\mu^-$	< 0.07	< 0.09
WW	0.18±0.09	0.18±0.09
WZ	0.02±0.01	0.06±0.03
$b\bar{b}$	< 0.10	< 0.10
TOTAL BACKGROUND	1.21±0.28	**2.50±0.43**
expected from top	0.13±0.03	1.1±0.4
DATA	0	4

Drop the H_T cut:

N_{jet} (10 GeV)	1	≥ 2
τ fakes	4.0±0.2	1.57±0.09
$Z \to \tau^+\tau^-$	3.2±0.5	1.84±0.41
$DY \to \tau^+\tau^-$	0.2±0.2	0.13±0.09
$Z \to e^+e^-$	0.2±0.2	< 0.09
$Z \to \mu^+\mu^-$	0.2±0.1	< 0.09
WW	0.7±0.2	0.18±0.09
WZ	< 0.1	0.07±0.03
$b\bar{b}$	< 0.1	< 0.10
TOTAL BACKGROUND	8.6±0.6	3.79±0.47
expected from top	0.14±0.03	1.3 ±0.4
DATA	9	5

Table 3.13: Comparison of the background calculation and data for relaxed topological and kinematical cuts. Note that the column in the top table for ≥ 2 jets and after all cuts summarizes the background calculation in the signal region. In those cases where no Monte Carlo events pass the cuts, an upper limit at the 1σ level is given.

Drop the H_T and $S_{\not E_T}$ cuts, but require $\not E_T > 15$ GeV:

N_{jet} (10 GeV)	1	≥ 2
τ fakes	8.3±0.5	3.6±0.2
$Z \to \tau^+\tau^-$	12.7±1.0	4.6±0.7
$DY \to \tau^+\tau^-$	0.9±0.6	0.3±0.2
$Z \to e^+e^-$	1.1±0.4	0.1±0.1
$Z \to \mu^+\mu^-$	0.2±0.1	0.4±0.2
WW	1.3±0.2	0.3±0.1
WZ	0.1±0.1	0.1±0.1
$b\bar{b}$	< 0.1	< 0.1
TOTAL BACKGROUND	24.6±1.2	9.4±0.8
expected from top	0.2±0.1	2.0±0.5
DATA	28	11

Table 3.14: Comparison of the background calculation and data for relaxed topological and kinematical cuts (continued).

cuts. In the plot on the right hand side the $S_{\not E_T}$ cut is applied. We also plot the events that survive if we consecutively apply the other topology cuts, i.e. the 2 jet cut (center) and the H_T cut (bottom). Note that there are no overflows in the histograms.

After all cuts we are left with 4 final candidate events for τ dileptons: 2 $e\tau$ and 2 $\mu\tau$ events. Note that these events are distinctly separated from the other events in the top plot. Figure 3.37 shows that the location of the 4 candidate events in the $S_{\not E_T}$ vs $\not E_T$ plane is consistent with the expectation for tau dileptons from $t\bar{t}$ decays. The event displays for the 4 candidates are shown in Figures 3.41 through 3.44. In Tables 3.15 and 3.16 we list the characteristics of the 4 candidate events.

We note that for 2 of the 4 events the tau tracks have an impact parameter d significantly different from zero. The impact parameter is given by the distance between the primary vertex of the interaction to the point of

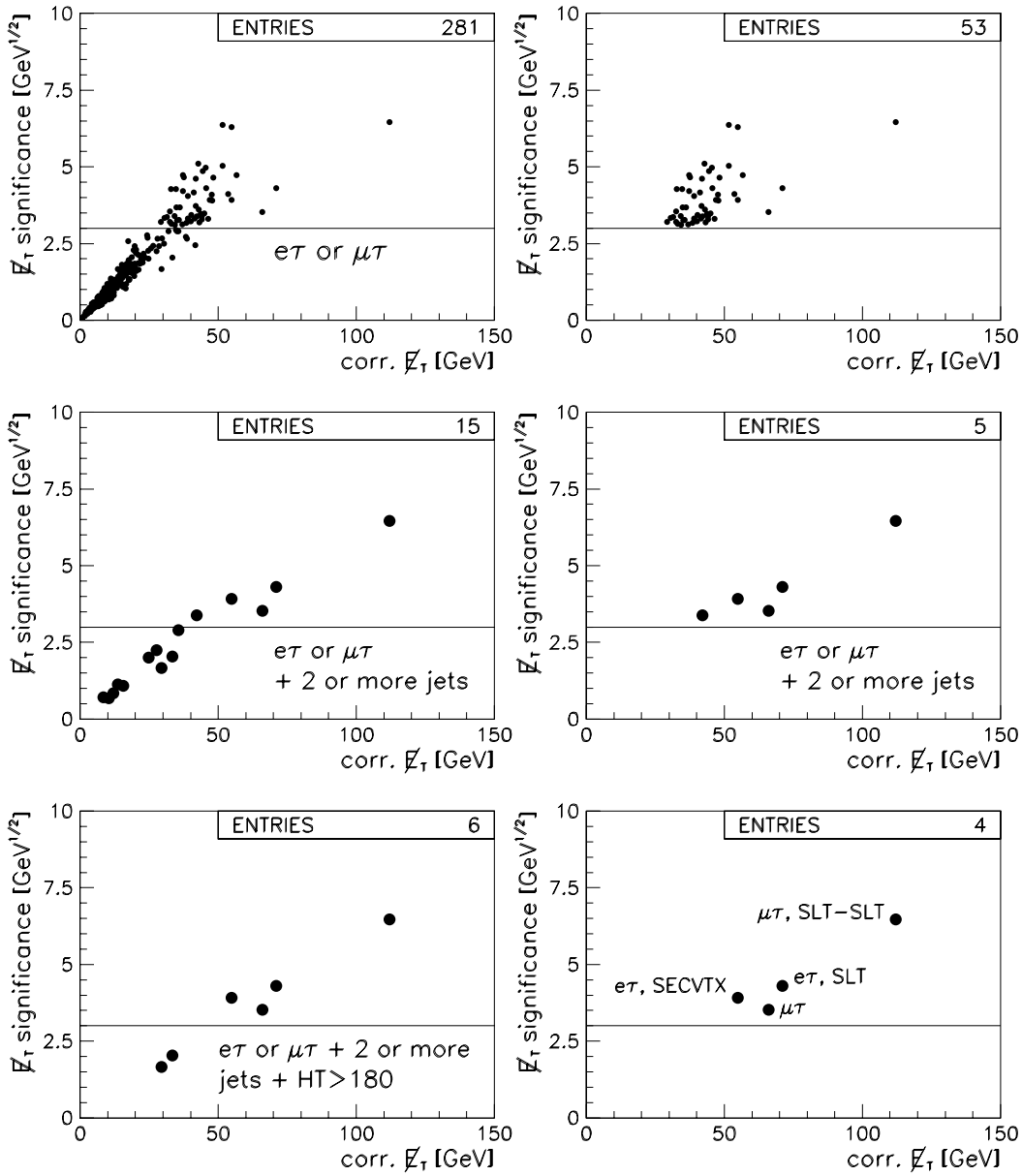

Figure 3.36: Scatterplot of $S_{\not{E}_T}$ vs $\not{E}_T$ for CDF data (109 pb^{-1}). Top: after identifying a primary e or μ and a τ lepton. Center: after requiring 2 jets. Bottom: after requiring 2 jets and $H_T > 180$ GeV. Plots on the left show all events; plots on the right show only events that survive the $S_{\not{E}_T} > 3$ GeV$^{1/2}$ cut.

Run	45880	64721	64934	65471
Event	31838	229200	416715	47719
Run	Ia	Ib	Ib	Ib
type	$e^-\tau^+$	$\mu^+\tau^-$	$e^-\tau^+$	$\mu^+\tau^-$
Primary lepton:				
E_T,p_T [GeV,GeV/c]	27.3	46.1	60.2	22.3
ϕ [deg]	255	241	66	181
η_{det}	0.07	0.26	0.20	-0.08
Tau lepton:				
$p_T^{trk+\pi^0}$ [GeV/c]	81.9	33.9	30.0	45.5
p_T^{trk} [GeV/c]	32.4	33.9	30.0	45.5
ϕ [deg]	356	70	275	81
η_{det}	-0.25	1.08	0.03	0.12
Track multiplicity	1-prong	1-prong	1-prong	1-prong
E/p (using $p_T^{trk+\pi^0}$)	1.03	1.88	0.67	1.53
σ_{cl} [GeV]	0.069	0.067	0.077	0.086
# of π^0's	1	0	0	0
$m_{trk+\pi^0}$ [GeV/c^2]	0.893	-	-	-
impact parameter d [μm]	1	-	147	93
impact parameter signif. d/σ	0.04	-	9.4	6.8
I_{trk}^{τ} [GeV/c]	0.0	0.0	0.0	0.44
$\ell\tau$ mass [GeV/c^2]	73.7	85.4	82.8	49.2
N_{jets}	3	2	2	3
(un)corr. $E_T^{j_1}$ [GeV]	61.8 (39.6)	123.6 (95.9)	59.5 (42.6)	206.0 (169.3)
(un)corr. $E_T^{j_2}$ [GeV]	32.0 (20.8)	67.8 (47.7)	26.1 (15.7)	57.8 (35.4)
(un)corr. $E_T^{j_3}$ [GeV]	24.6 (15.9)	16.8 (9.8)	-	22.3 (14.2)
corr. $\not{E}_T$ [GeV]	71.0	112.1	54.9	66.1
$S_{\not{E}_T}$ [$\sqrt{GeV}$]	4.3	6.5	3.9	3.5
ΣE_T [GeV]	271.6	254.8	197.0	328.1
$\phi(\not{E}_T^{corr})$ [deg]	125.0	232.6	191.2	79.0
$\Delta\phi$ ($\not{E}_T, jl$) [deg]	59.3	8.3	8.9	0.2
H_T [GeV]	264.9	345.5	203.3	352.8
b-tagging	SLT(e, j2)	SLT(μ, j1) SLT(e, j2)	SVX(j1)	-
in mass sample ?	yes	yes	no	no
Comments		not SVX fid.		

Table 3.15: Characteristics of the 4 tau dilepton candidate events.

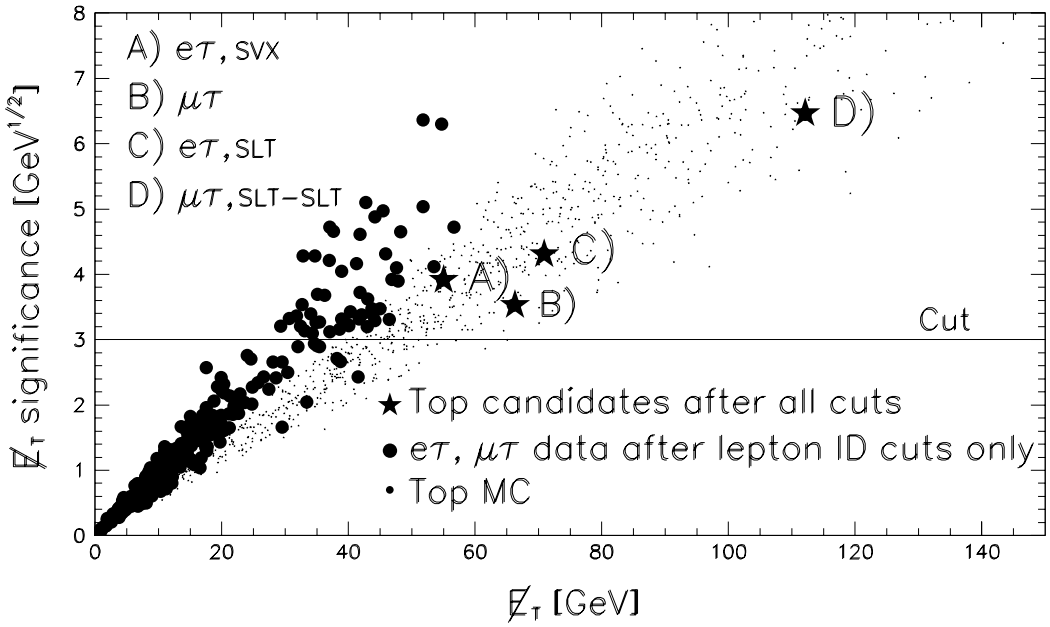

Figure 3.37: The distribution of $S_{\not{E}_T}$ vs $\not{E}_T$ for events with a primary lepton and a tau candidate in the CDF data compared with the $t\bar{t}$ Monte Carlo. Three of the four final candidate events (stars) have b-tagged jets.

closest approach of the SVX track. Its sign is defined relative to the direction of the corresponding cluster in the calorimeter. If the angle between the cluster axis and the line from the primary vertex to the point of closest approach of the SVX track is less than 90^0 the sign is defined as positive, otherwise it is negative. In Figure 3.38 we plot the expected distribution of the signed impact parameter for SVX tracks from τ's and W electrons in the $t\bar{t}$ Monte Carlo. The distribution for the electrons is basically governed by the SVX resolution. For the τ's we observe tails due to their lifetime of 296 fs, which corresponds to $c\tau = 89\mu m$. The larger tail appears on the positive side, but there is also a significant tail on the negative side because the direction of the tau cluster axis can be significantly different from the true τ direction. If the angle that

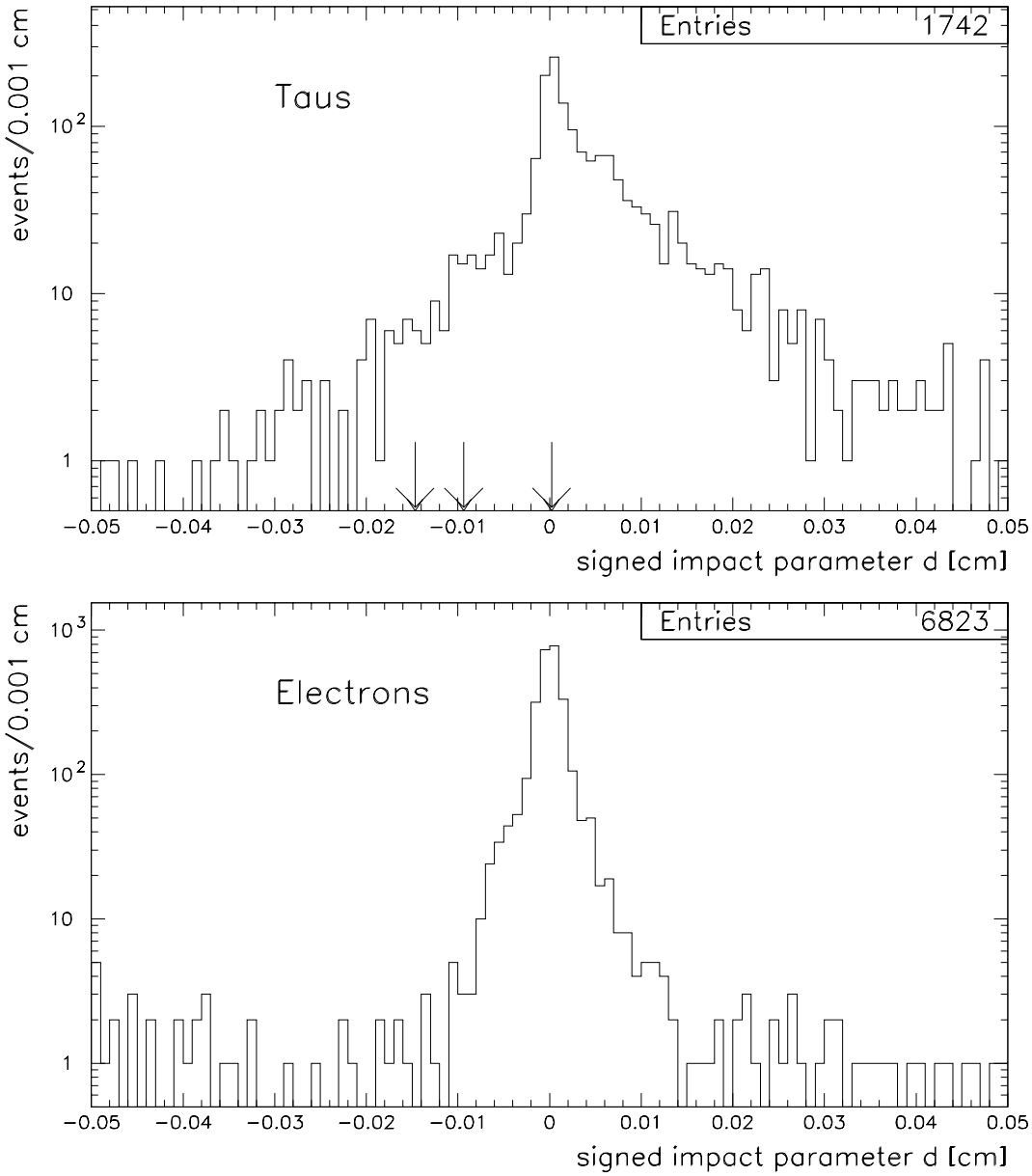

Figure 3.38: The distribution of the signed impact parameter d for SVX tracks from τ's (top) and W electrons (bottom) in the $t\bar{t}$ Monte Carlo. The arrows indicate the measured impact parameters for those τ's in the τ dilepton candidates that have tracks in the SVX.

Run/Event	E [GeV]	E_x [GeV]	E_y [GeV]	E_z [GeV]
45880/31838				
jet1	101.9	-26.1	-56.0	81.1
jet2	34.3	13.2	29.1	12.3
jet3	28.9	-20.8	-13.0	-15.3
64721/229200				
jet1	124.0	116.7	40.7	10.6
jet2	70.8	-44.3	51.4	20.1
jet3	19.0	-3.9	-16.3	8.9
64934/416715				
jet1	61.7	57.6	-15.1	-16.0
jet2	55.3	-26.1	-1.0	48.8
65471/47719				
jet1	208.2	-41.8	-201.7	-30.5
jet2	90.3	11.3	56.6	-69.4
jet3	22.7	20.0	-9.8	4.3

Table 3.16: The jet 4-vectors of the tau dilepton candidates. Standard jet corrections are applied [42].

determines the sign of the impact parameter is close to 90^0, a small change in the direction of the tau track can cause it to switch from the positive tail to the negative tail of the distribution or vice versa.

The measured impact parameters for the three tau candidates with tracks in the SVX are indicated by arrows. For both tracks on the negative tail the angles, which determine the impact parameter sign, are close to 90^0. Even though we do not cut on the impact parameter, the fact that two tracks appear on the tails gives additional support for the hypothesis that these objects are τ's.

We note that a second analysis [53] of the data that identifies hadronic one-prong decays of tau leptons using mainly tracking information finds the same four events as tau dilepton candidates.

N_{jet} (> 10 GeV)	1		≥ 2	
	expected τ fakes	obs. ss events	expected τ fakes	obs. ss events
All cuts applied	0.55±0.03	0	0.87±0.04	1
Drop the H_T cut	4.9±0.3	2	1.79±0.10	1
Drop H_T and $S_{\not{E}_T}$ cuts, require $\not{E}_T > 15$ GeV	8.8±0.5	7	3.7±0.2	3

Table 3.17: Comparison of fake background calculation and observed same-sign (ss) events in the data for relaxed topological and kinematical cuts.

In Figure 3.39 we present the same data in the $\Delta\phi\,(\not{E}_T, jl)$ vs $\not{E}_T$ plane of the ee, $\mu\mu$, $e\mu$ dilepton analysis. All 4 candidate events pass this cut as well. Two events clearly stand out from the background, the other two are closer to the cuts.

3.9.2 Same-sign events

We can cross-check the fake background estimate in the data by searching for *same-sign* events because we expect the same fake rate for same-sign as for opposite–sign events. The physics backgrounds are expected to contribute only to the opposite–sign events. In analogy to Figure 3.36 we plot $S_{\not{E}_T}$ versus the corrected $\not{E}_T$ for *same-sign* events in Figure 3.40. We find one event (Run 66347/Event 48619) that survives all cuts, which is consistent with the expectation of 0.87 events from the fake study. This event is a μ^+(CMX only, p_T = 46.9 GeV/c) τ^+($p_T^{trk+\pi^0}$ = 27.7 GeV/c) dilepton with 2 jets (no tags) and H_T = 277 GeV. The z–position of the event vertex is outside of the SVX detector so that the impact parameter of the SVX tau track cannot be determined. In Table 3.17 we compare the fake background

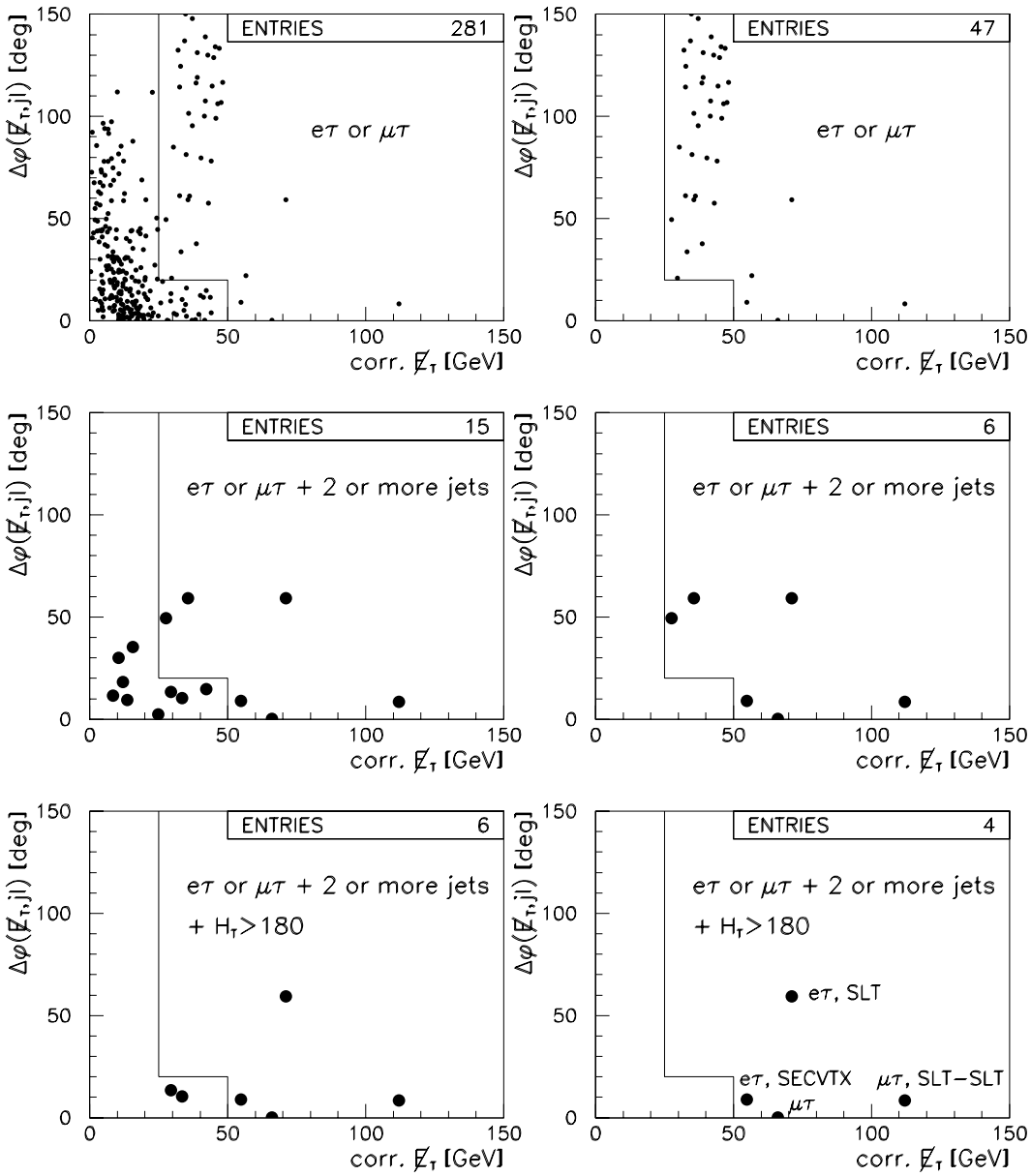

Figure 3.39: Scatterplot of $\Delta\phi\,(\not\!\!E_T, jl)$ vs $\not\!\!E_T$ for CDF data (109 pb^{-1}). Top: after identifying a primary e or μ and a τ lepton. Center: after requiring 2 jets. Bottom: after requiring 2 jets and $H_T > 180$ GeV. Plots on the left show all events; plots on the right show only events that survive the topology cut indicated by the line.

N_{jet} (15 GeV)	1	2	3	4
$Wb\bar{b}, Wc\bar{c}$	0.2%	0.8%	1.2%	1.6%

Table 3.18: Expected number of SVX-tagged events per generic W event due to heavy flavor as a function of jet multiplicity.

expected # of tagged events	SVX	SLT
from top	0.48 ± 0.12	0.24 ± 0.06
τ fakes	0.14 ± 0.01	0.12 ± 0.01
$Z \to \tau^+\tau^- + \ b\bar{b},\ c\bar{c}$	0.02 ± 0.01	0.01 ± 0.01
TOTAL	0.64 ± 0.12	0.37 ± 0.06
DATA	1	2

Table 3.19: Expected number of tagged events among the four candidate events compared to the observation in the data.

predictions for the relaxed cuts with the number of same-sign events observed in the data. Within the small statistics we find agreement in all cases.

3.10 B–tagging

Checking the b–tagging information from the SLT and SVX tagging algorithms we find that 3 of the 4 events are b–tagged. There is one event with a SVX tag, one with an SLT tag and one event with a double SLT tag.

We calculate the expected background for the 2 largest backgrounds: For τ fakes we multiply the τ fake rate with the jet E_T spectrum of *tagged* events (SLT or SVX) in the $\ell + \not{E}_T + \geq 3\ jets$ ($\ell = e, \mu$) sample after applying all other cuts. Based on 50 tagged events with 134 τ–taggable jets we find a background prediction of 0.256 ± 0.016(stat) events.

The next largest background is expected to be due to $Z \to \tau^+\tau^- +$

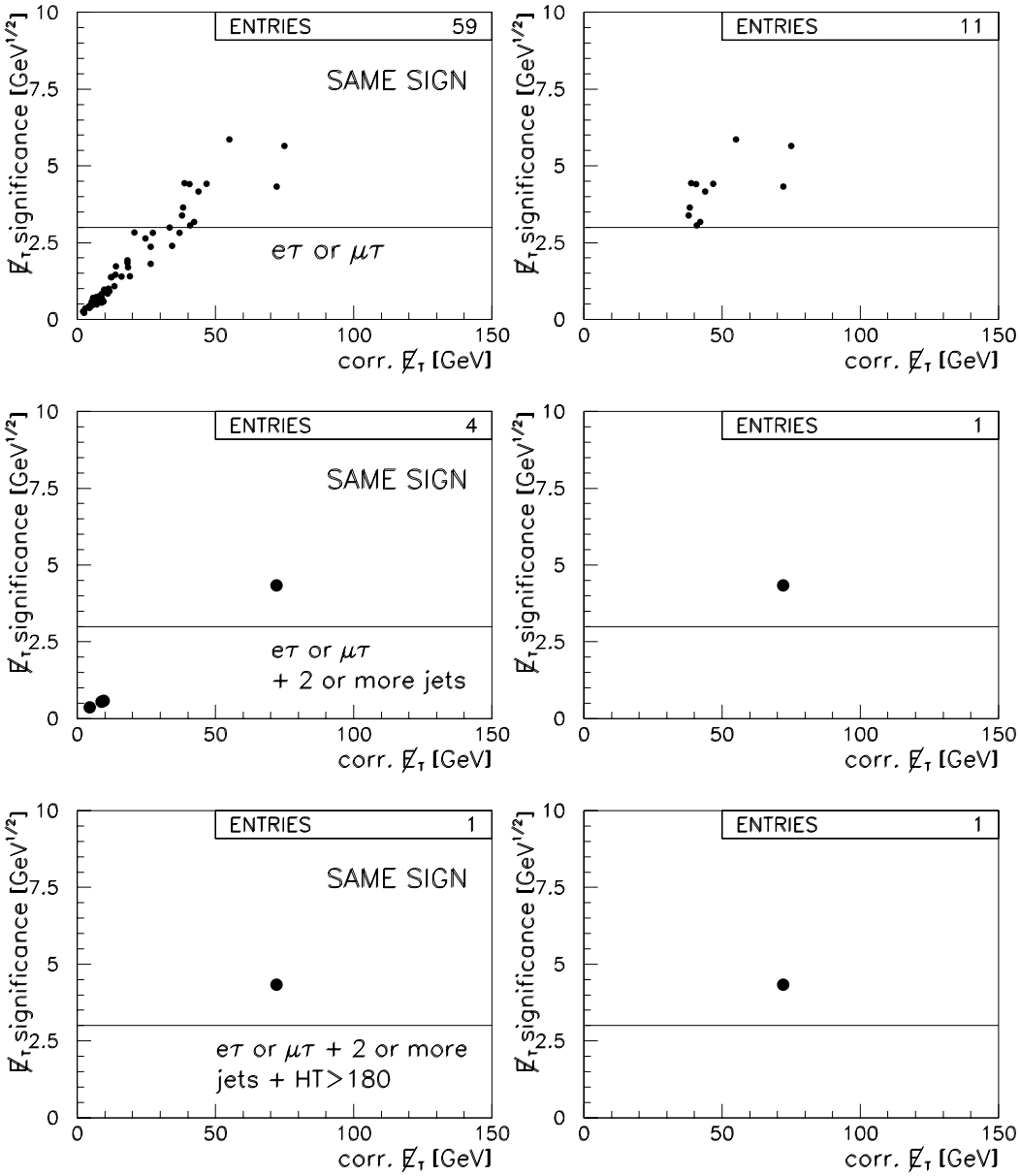

Figure 3.40: Scatterplot of $S_{\not{E}_T}$ vs $\not{E}_T$ for same-sign events in CDF data (109 pb^{-1}). Top: after identifying a primary e or μ and a τ lepton. Center: after requiring 2 jets. Bottom: after requiring 2 jets and $H_T > 180$ GeV. Plots on the left show all events, plots on the right only show events that survive the $S_{\not{E}_T} > 3$ GeV$^{1/2}$ cut. See text for details on the four event passing all cuts.

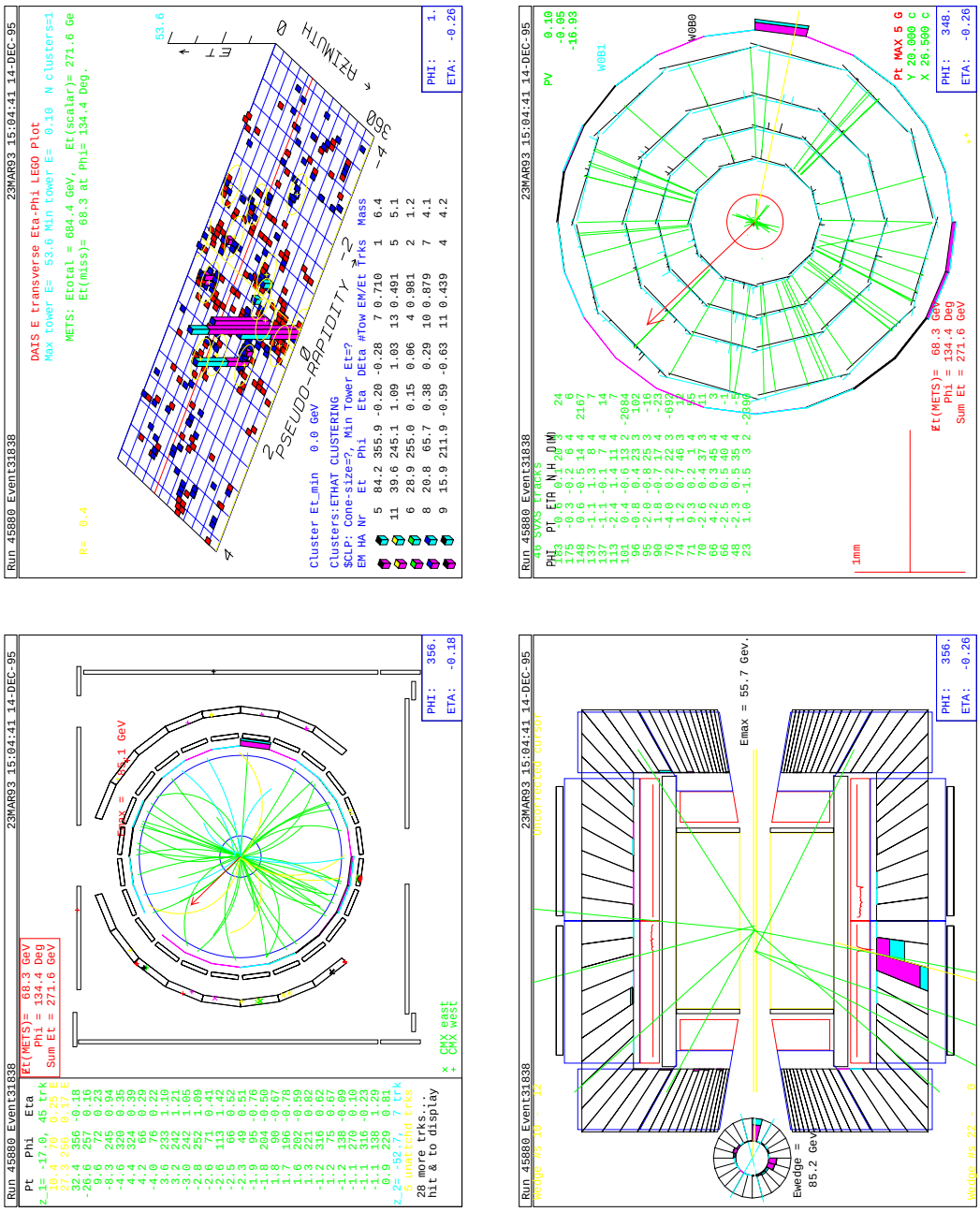

Figure 3.41: The $e^-\tau^+$ candidate 45880/31838. The hadronic τ is at $\phi = 356^o$ and $\eta_{det} = -0.25$. The jet at $\phi = 66^o$ and $\eta_{det} = -0.38$ is b–tagged by a soft electron.

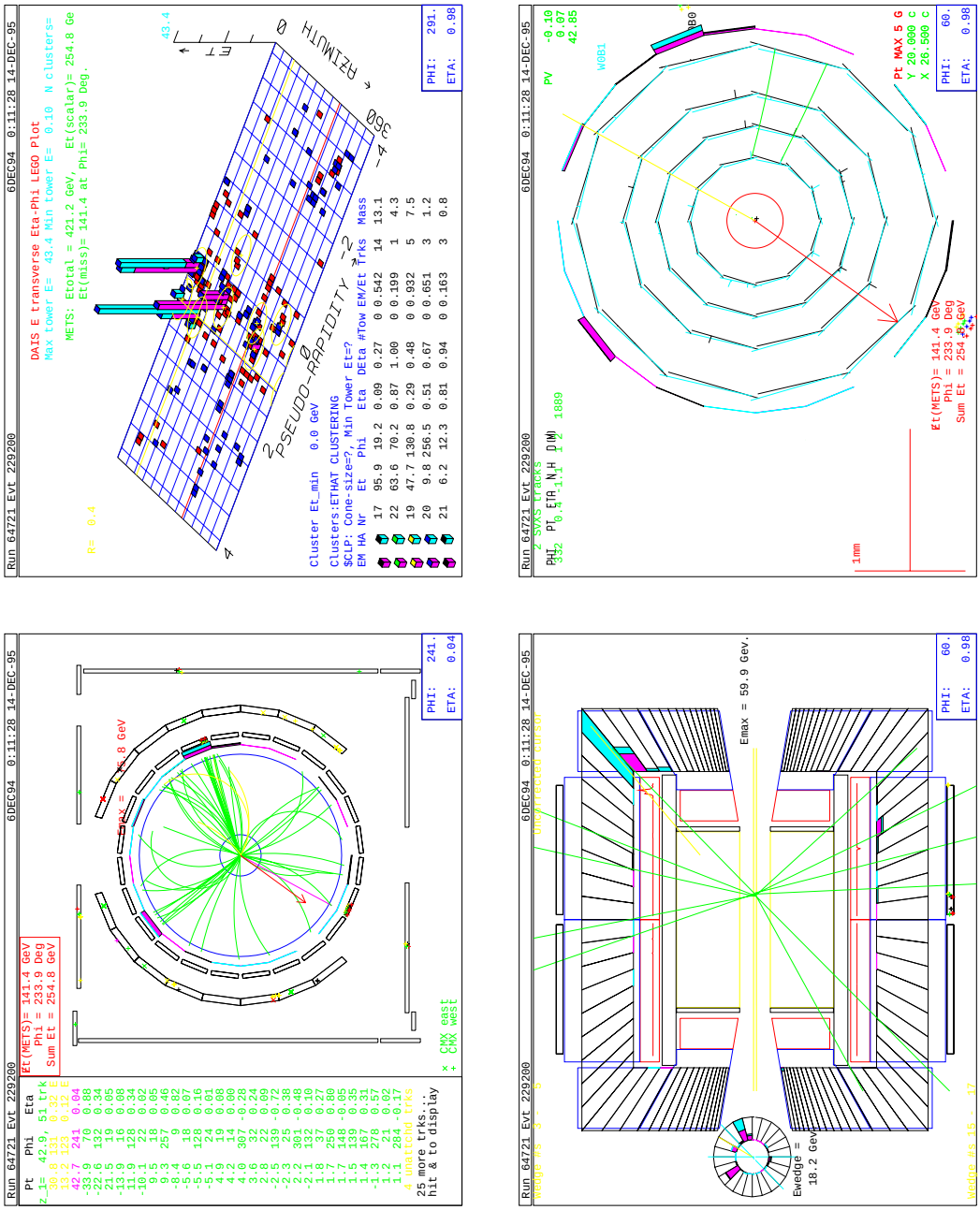

Figure 3.42: The $\mu^+\tau^-$ candidate 64721/229200. The hadronic τ is at $\phi = 70^o$ and $\eta_{det} = 1.09$. The jet at $\phi = 19^o$ and $\eta_{det} = -0.09$ is b–tagged by a soft muon and the jet at $\phi = 131^o$ and $\eta_{det} = 0.29$ is b–tagged by a soft electron.

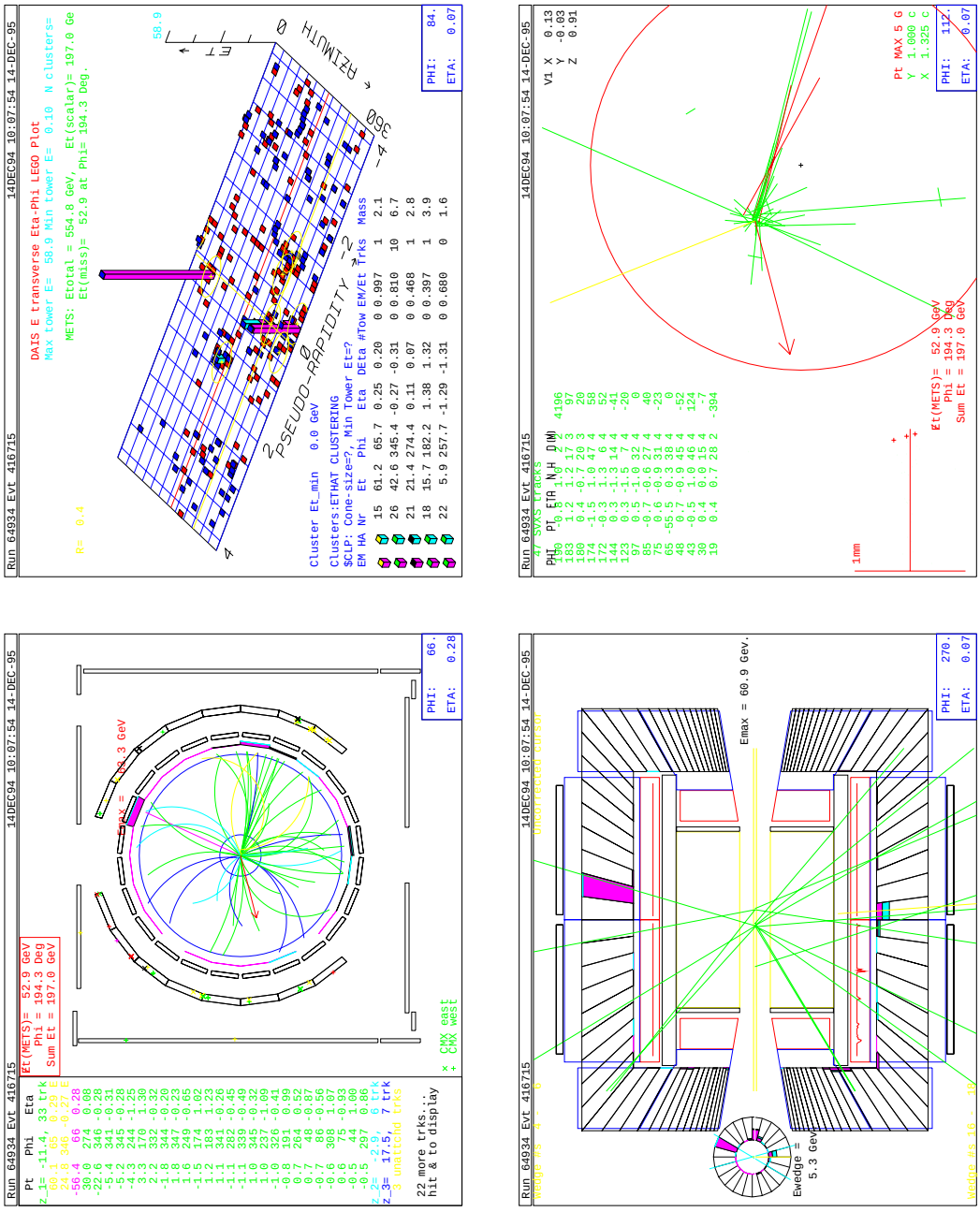

Figure 3.43: The $e^-\tau^+$ candidate 64934/416715. The hadronic τ is at $\phi = 275^o$ (behind a small cluster) and $\eta_{det} = -0.03$. The jet at $\phi = 345^o$ and $\eta_{det} = -0.27$ is b–tagged by the SVX.

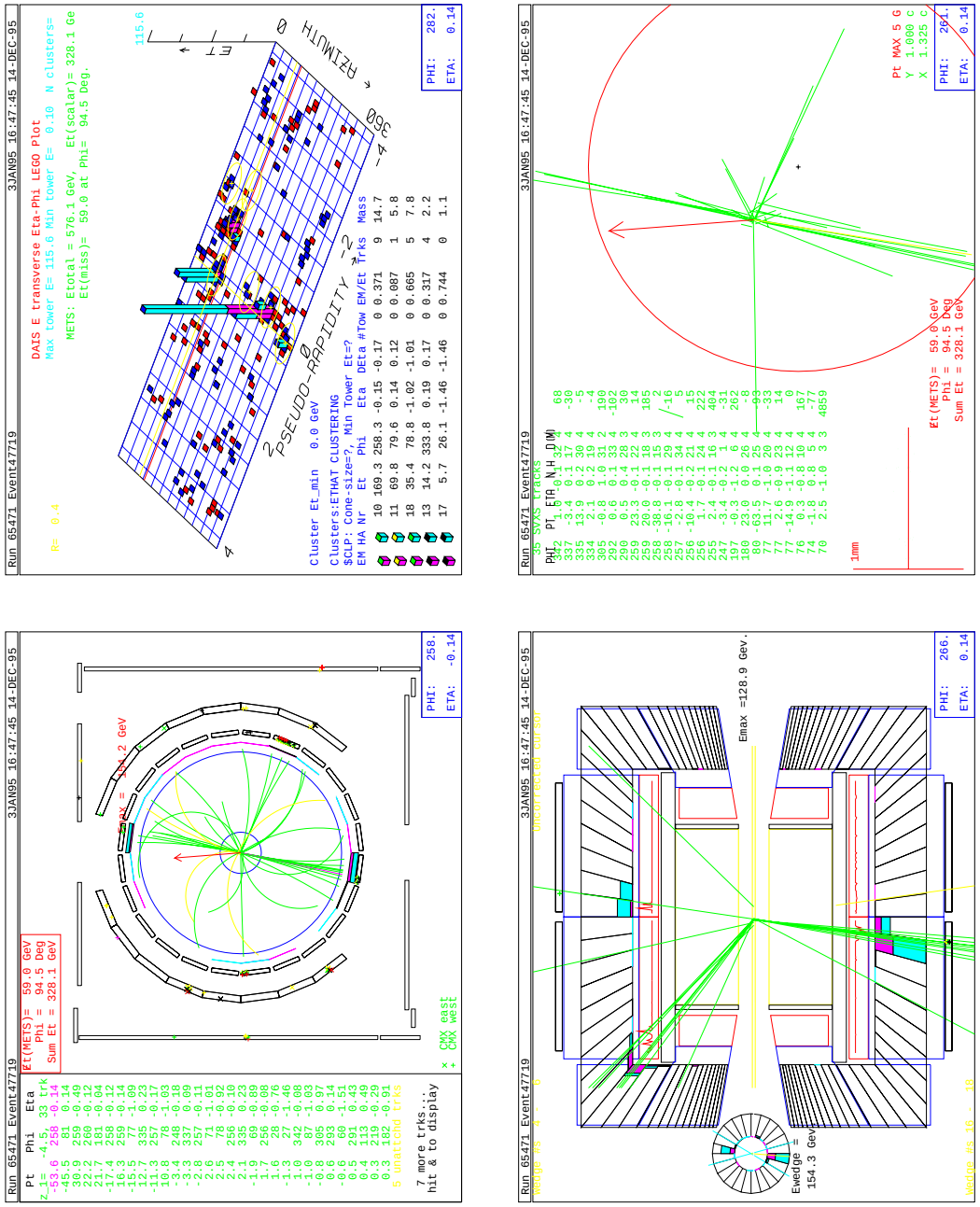

Figure 3.44: The $\mu^+\tau^-$ candidate 65471/47719. The hadronic τ is at $\phi = 81^o$ (behind a jet) and $\eta_{det} = 0.12$. There are no b–tags in this event.

$b\bar{b}$, $c\bar{c}$. We assume that the production of heavy flavors in $Z + jets$ events is very similar to that in $W + jets$ events. Therefore, we use the estimate of the number of SVX tags per generic W event from the detailed background study by Guillaume Unal for the lepton + jets analysis [75] as listed in Table 3.18. Based on the 15 events in the $Z \rightarrow \tau^+\tau^-$ Monte Carlo that pass all cuts we find the expected number of tagged events in 109 pb^{-1} to be (0.015±0.004) events. As the SLT efficiency is about half of the SVX efficiency we add another 50% to account for SLT tags and find (0.023±0.006) events.

In total we expect 0.279±0.017 events from the two dominating backgrounds. The probabilty for this to fluctuate to ≥ 3 events is 0.30%. For a Gaussian distribution this would correspond to a 3 σ excess.

As a cross-check we estimate the b-tag fake rate for the 4 τ dilepton candidates. Using the b-tag fake matrices we expect 0.31±0.03 (0.16±0.08) fake tags from SLT (SVX). The probability for 0.47±0.09 fakes to fluctuate to ≥ 4 tags is 0.16% or 2.9 σ, consistent with the result above.

We estimate the expected number of tagged $t\bar{t}$ signal events. The efficiency for tagging at least one b in a $t\bar{t}$ event with SVX (SLT) is about 40% (20%). We expect 0.48 SVX–tagged events and 0.24 SLT–tagged events from top.

Combining background and signal predictions we expect 0.6 events with SVX tags in the data while observing one event. For SLT we expect 0.4 tagged events and observe 2 events. This information is summarized in Table 3.19.

The number of SLT–taggged events in the data appears somewhat higher than what is expected from signal plus background. The probability for 0.37 expected events to fluctuate to 2 or more observed events is 6%. Since one might worry about the quality of the SLT tags in the candidate events we

Run Event	45880 31838	64721 229200	SLT cut
QTRK #	11	12	-
fiducial	y	y	required
not a conversion	y	y	required
p_T (GeV/c)	2.57	22.6	> 2.0
p (GeV/c)	2.8	24.0	-
E_{strip}/P	1.4	0.93	> 0.32 (Ia); > 0.6 (Ib)
E_{wire}/P	1.0	0.88	> 0.32 (Ia); > 0.6 (Ib)
Δx match (cm)	0.38	0.01	< 1.3 (Ia); < 0.7 (Ib)
Δz match (cm)	0.2	1.0	< 2.0
$\chi^2_{strip}/6$	1.3	1.95	< 16
$\chi^2_{wire}/6$	0.8	9.9	< 16
E/p	1.4	1.26	$0.7 < E/p < 1.5$
CPR counts	7615	25226	> 2000 (Ia) > 1357 (Ib)
CTC dE/dX	14.55	n/a f. $P > 15$	< 16
EM energy (GeV)	3.9	30.1	> 0.1
E_{had}/E_{em}	0.008	0.006	< 0.1

Table 3.20: Values of the soft electron tag variables for the two tau dilepton candidate events with soft electron tags, and the cuts.

Run / Event	64721/229200	SLT cut
stub type	CMU-CMP CMU-CMP	CMU w/ CMP confirmation
p_T (GeV/c)	5.1	> 2
# ADC hits in CMU	4	≥ 3
# TDC hits in CMU	4	≥ 3
χ^2 CTC-CMU ADC match	0.22	$0 < \chi^2 < 9$
χ^2 CTC-CMU TDC match	0.11	$\chi^2 < 9$

Table 3.21: Values of the soft muon tag variables for the tau dilepton candidate event with a soft muon tag, and the cuts.

All cuts applied:

N_{jet} (10 GeV)	1	≥ 2
DATA	0	4
# tagged events	0	3
# tags	0	4
tag types	-	1 SVX, 3 SLT

Drop the H_T cut:

N_{jet} (10 GeV)	1	≥ 2
DATA	9	5
# tagged events	3	3
# tags	3	4
tag types	3 SLT	1 SVX, 3 SLT

Drop the H_T and $S_{\not{E}_T}$ cuts, but require $\not{E}_T > 15$ GeV:

N_{jet} (10 GeV)	1	≥ 2
DATA	28	11
# tagged events	4	4
# tags	4	5
tag types	4 SLT	1 SVX, 4 SLT

Table 3.22: B-tagging results for relaxed topological and kinematical cuts. Note that the table for ≥ 2 jets and after all cuts gives the result for the signal region.

check them in detail. In Tables 3.20 and 3.21 we list the values of the SLT variables and the cuts. In general, we find that the values of the cut variables are not near the cuts. One possibly 'weaker' tag is the soft electron tag in 45880/31838 because $p_T = 2.6$ GeV/c while the cut is at $p_T = 2.0$ GeV/c. On the other hand, there is a falling p_T spectrum for the SLT tags and we do expect tags with low p_T. One of the tags is due to a muon with $p_T = 22.6$ GeV/c. The probability to find a $t\bar{t}$ event with a muon from a b or c decay with $p_T > 20$ GeV/c is $(2.9 \pm 0.1(\text{stat}))\%$.

We also check the b–tagging with relaxed topological cuts (see section 3.8.2). The results are shown in Table 3.22. Dropping the H_T cut and the $S_{\not{E}_T}$ cut (but requiring $\not{E}_T > 15$ GeV) nearly triples the number of events in the data with ≥ 2 jets but the number of tags increases by only one tag (+25%). In 28 events with 1 jet we find 4 SLT tags; i.e. in seven times the number of events as in the signal region we find the same number of tags. This supports the notion that the jets in the signal region are from b's as expected in top decays.

3.11 Significance

From a Poisson distribution we calculate the probability for the expected mean background to have fluctuated to the observed number of events before and after tagging. We also calculate the probability for the sum of expected mean background and expected mean $t\bar{t}$ signal to have produced the observed number of events. For the $t\bar{t}$ calculation we consider the theoretical cross section (4.8±0.7 pb) as well as the $t\bar{t}$ cross section from our current measurement (7.7 ± 2 pb) that combines the ee, $\mu\mu$, and $e\mu$ dilepton channel, the lepton + jets channel and the all–hadronic channel [69]. In all cases we take the uncertainties into account by a Gaussian smearing of the mean expected number of events.

The results for the $e\tau$ and $\mu\tau$ channel are listed in Table 3.23 together with the corresponding results from the ee, $\mu\mu$, and $e\mu$ channel obtained in section 2.4.2. Also listed are the results for the combination of both channels. If a b–tag is required, the probability in the $e\tau$ and $\mu\tau$ channel for the background to fluctuate to ≥ 3 events is 0.3%, which corresponds to 3.0 σ on a Gaussian distribution. The probability for background plus $t\bar{t}$ signal to have

produced ≥ 3 events is 3.2% for $\sigma^{t\bar{t}} = 4.8$ pb, and 6.7% for $\sigma^{t\bar{t}} = 7.7$ pb. Thus it is 10–20 times more likely that the 3 observed b–tagged events are due to $t\bar{t}$ production plus background than that they are due to background only.

3.12 Cross section

We calculate a $t\bar{t}$ production cross section from τ dilepton events:

$$\sigma_{t\bar{t}} = \frac{N^{observed} - N^{background}}{\mathcal{L}\ A_{tot}} \tag{3.26}$$

where $N^{observed}$ is the number of observed candidate events (4), $N^{background}$ is the estimate for the background (2.50±0.43 events), $\mathcal{L}$ is the integrated luminosity for Run Ia+Ib (109±7 pb^{-1}) and A_{tot} is the total acceptance × efficiency (0.134±0.013(stat)±0.019(syst))%. Note again that A_{tot} contains all branching ratios of the W's and τ's. Taking a Poisson uncertainty on $N^{observed}$ and propagating all uncertainties the final result is

$$\sigma_{t\bar{t}} = 10.2^{+16.3}_{-10.2}(stat) \pm 1.6(syst)\ pb \tag{3.27}$$

In Figure 3.45 we compare the cross section measurement in the τ dilepton channel with the track–based analysis [53], and with the other CDF top cross section measurements in the single lepton, ee, $\mu\mu$, $e\mu$ dilepton and all–hadronic channels as summarized in Ref. [69].

3.13 Summary and Conclusion

We have searched for dilepton events from $t\bar{t}$ decay with one high–p_T electron or muon and one hadronically decaying τ lepton. For this purpose we have developed a method to identify hadronically decaying τ's in a hadron

	N_{obs} [events]	B [events]	$\mathcal{P}(B, \geq N_{obs})$ [%]	$\sigma^{t\bar{t}} = 4.8$ pb $B+t\bar{t}$ [events]	$\mathcal{P}(B+t\bar{t}, \geq N_{obs})$ [%]	$\sigma^{t\bar{t}} = 7.7$ pb $B+t\bar{t}$ [events]	$\mathcal{P}(B+t\bar{t}, \geq N_{obs})$ [%]
$e\tau, \mu\tau$							
no tagging	4	2.5±0.4	24.4	3.2±0.5	39.6	3.6±0.5	48.1
with tagging	3	0.28±0.02	0.30	0.67±0.12	3.2	0.91±0.16	6.7
$ee, \mu\mu, e\mu$							
no tagging	9	2.1±0.4	0.062	6.0±0.8	16.4	8.4±1.3	46.0
with tagging	4	0.4±0.2	0.17	2.5±0.5	24.7	3.8±0.6	52.0
$e\tau, \mu\tau + ee, \mu\mu, e\mu$							
no tagging	13	4.6±0.6	0.16	9.2±0.9	14.8	12.0±1.4	42.4
with tagging	7	0.7±0.2	2.2×10^{-5}	3.2±0.5	5.1	4.7±0.6	20.2

3.23: The probabilities $\mathcal{P}$ in % for the expected mean background (B) and for the expected mean background plus $t\bar{t}$ signal ($B+t\bar{t}$) to have fluctuated to the number of observed events (N_{obs}) or more. For the expected $t\bar{t}$ signal we use two cross sections. One is based on the theoretical calculation (4.8±0.7 pb), the other on the combined CDF measurement (7.7±2 pb). Uncertainties are taken into account via Gaussian smearing of the mean expected numbers.

collider environment with good efficiency and small fake background from QCD jets. The method takes advantage of the fact that hadronic tau decays produce narrow clusters in the calorimeter that are associated with one or three high-p_T tracks. Applying a tight cut on the track isolation of the cluster reduces the fake background substantially. The efficiency of the tau identification method in a $t\bar{t}$ Monte Carlo simulation agrees with the efficiency measured in a $W \rightarrow \tau\nu$ data sample.

After applying cuts on the event topology to improve the ratio of signal-to-background we expect ~ 1 signal events and ~ 2 total background events in Run I (109 pb^{-1}). In the data we observe 4 tau dilepton candidate events; 2 $e\tau$ and 2 $\mu\tau$ events.

The fact that 3 out of the 4 events are b–tagged leads us to the conclusion that we have found evidence for top quark decays into τ's. If a tag is required the probability for the background to fluctuate to ≥ 3 events is 0.3%, which corresponds to a 3.0 σ (Gaussian) excess.

The measurement of the $t\bar{t}$ cross section based on the 4 events is consistent with latest measured values from other decay channels, given the large statistical uncertainty. This is an important result because effects beyond the Standard Model, e.g. the existence of a charged Higgs boson, could have significantly increased the number of tau dilepton events found in the data.

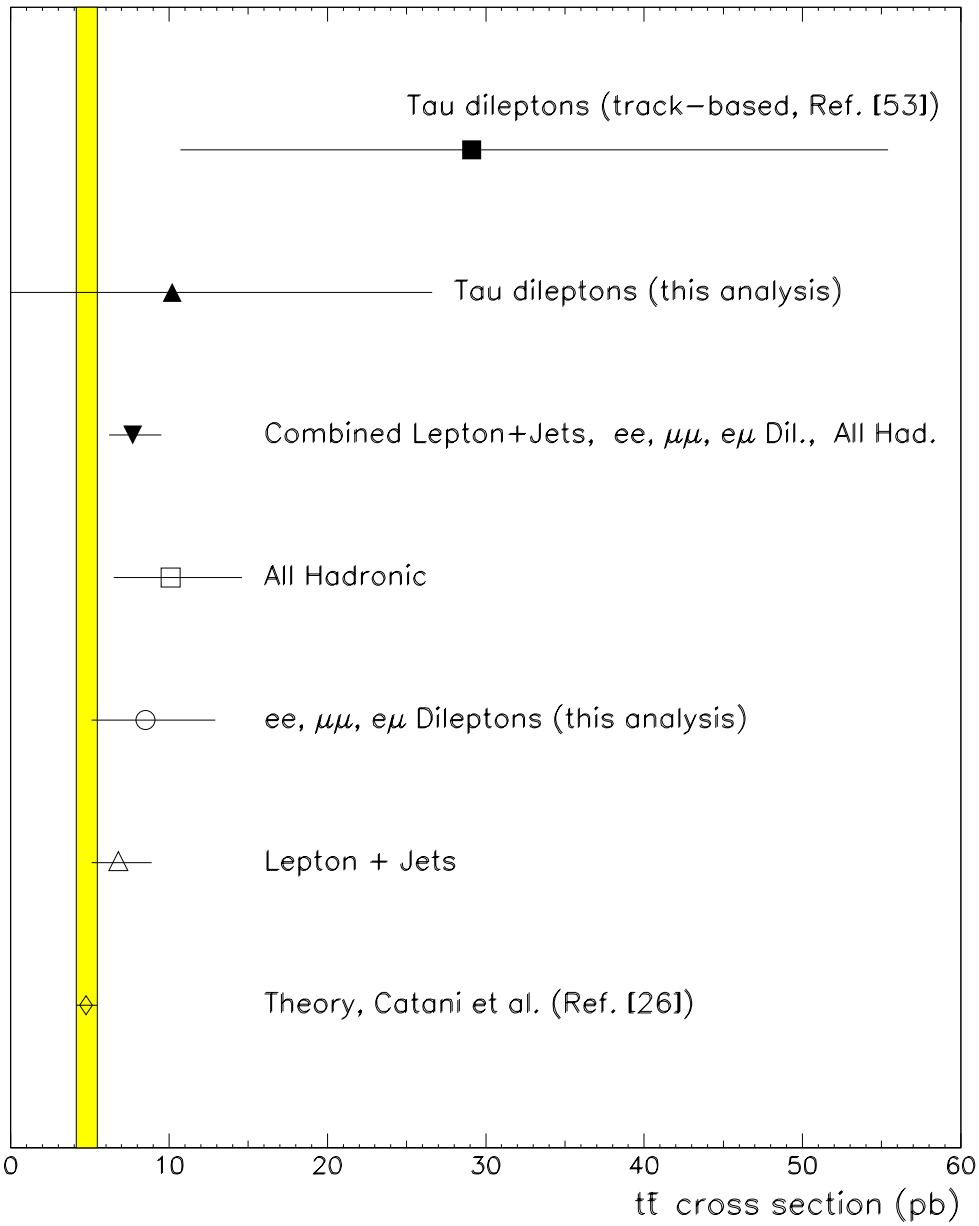

Figure 3.45: Comparison of $t\bar{t}$ cross sections measured in different channels.

Chapter 4

KINEMATICS AND TOPOLOGY OF THE CANDIDATE EVENTS

Ist es der Sinn, der alles wirkt und schafft?
Es sollte stehn: Im Anfang war die Kraft!

J.W. v. Goethe, *Faust I, Studierzimmer*

In this chapter we take a closer look at our candidate events. The purpose of this study is to see if the kinematics and topology of the events observed in the data after applying our selection are actually "top-like". This is not only an important cross check, but also offers the opportunity to look for new phenomena because there is the possibility that our selection might be sensitive to other things besides top quarks. Our motivation for looking at the data in this way is the fact that we observe 14 ee, $\mu\mu$, $e\mu$, $e\tau$, and $\mu\tau$ events, whereas the theoretical $t\bar{t}$ production cross section leads us to expect only ≈ 5 events from $t\bar{t}$ decay plus ≈ 4 background events.

The study is divided into three parts: In the first part we discuss

inclusive kinematical distributions, e.g. the lepton p_T spectrum or the E_T spectrum of the jets. The second part is a more global look at the events using variables that relate to the full events such as the event thrust. In the third part we discuss some unusual features of certain candidate events.

4.1 Kinematics of specific particles

4.1.1 Charged leptons

E_T and p_T spectra

In Figure 4.1 we plot the uncorrected E_T of the electrons and p_T of the muons in the 10 ee, $\mu\mu$, and $e\mu$ and 4 $e\tau$, $\mu\tau$ candidates as used in the lepton selection. Also plotted are the expected distributions for the two largest backgrounds and for top events. Background and top contributions have been normalized to the expected number of events and added together for a comparison with the data. All subsequent one-dimensional plots in this section are made in this manner.

The data show the expected falling spectrum. However, in the ee, $\mu\mu$, and $e\mu$ sample there are two leptons out on the tail of the distribution. Both leptons are positrons in $e^+\mu^-$ events. The raw tranverse energy of the positron in Run 66046/Event 380045 is $E_T = 105.6$ GeV; the positron in Run 67581/Event 129896 has $E_T = 181.8$ GeV. Applying the CEM corrections we find $E_T^{corr} = 109.8$ GeV and $E_T^{corr} = 197.1$ GeV, respectively. From top quark decays we expect 0.6 ± 0.1 events with $E_T^{\ell} > 105$ GeV and 0.06 ± 0.02 events with $E_T^{\ell} > 180$ GeV. The contribution of the known backgrounds in these regions is negligible compared with the top contribution. Run 67581/Event

129896 is also curious for another reason (it has a third isolated lepton) and will be discussed in more detail below.

The p_T spectra of the primary leptons in the 4 $e\tau$, $\mu\tau$ candidates agree well with the expectations. The p_T spectrum of the tau candidates is shown in Figure 4.2. The tau in Run 45880/Event 31838 with $p_T^{trk+\pi^0} = 81.9$ GeV also falls on the tail of the expected distribution.

Dilepton invariant mass

The distribution of the invariant masses formed from the two leptons are shown in Figure 4.3. The dip in the $t\bar{t}$ spectrum for ee, $\mu\mu$, and $e\mu$ events between 75 GeV/c^2 and 105 GeV/c^2 is due to the mass cut for ee and $\mu\mu$ events. The data are compatible with the expectations. The 2 $\mu\mu$ events fall in the region where the background contributions are largest.

p_T of the dilepton system

The p_T spectrum of the dilepton system $\vec{p}_T^{\,\ell\ell} = \vec{p}_T^{\,\ell_1} + \vec{p}_T^{\,\ell_2}$ is shown in Figure 4.4. Due to the large p_T of the positrons in events 66046/380045 and 67581/129896 these events appear also on the tail of the $\vec{p}_T^{\,\ell\ell}$ distribution. The dilepton systems in the 2 $\mu\mu$ events have softer p_T than in the ee and $e\mu$ events. Again, the 2 $\mu\mu$ events fall in the region where the background contributions are largest. There are no peculiarities observed in the $e\tau$ and $\mu\tau$ data.

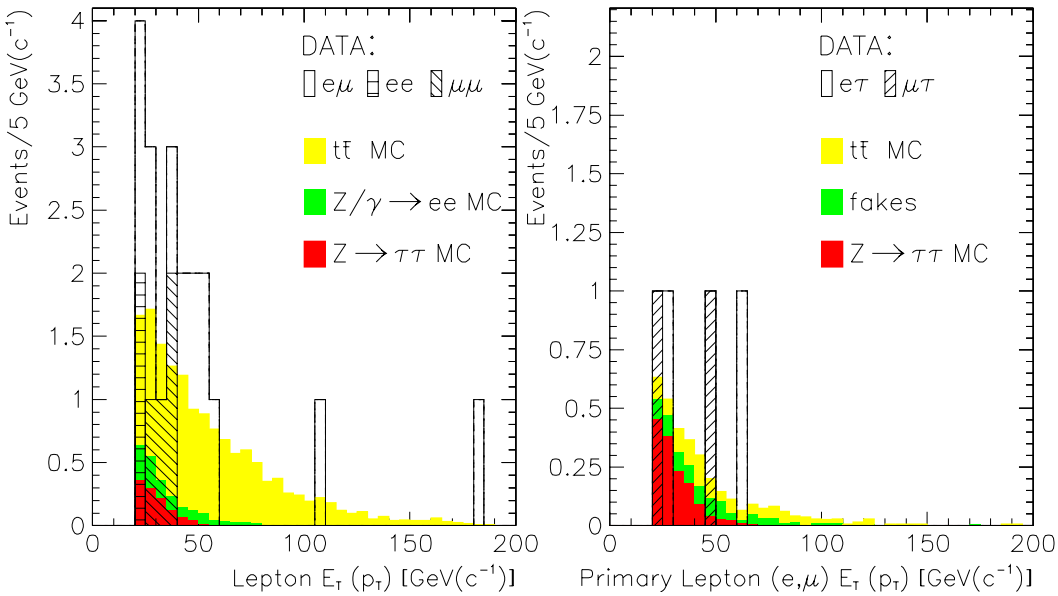

Figure 4.1: The E_T and p_T spectra of electrons and muons in the candidate events compared with the expected spectra. Electron energies are not corrected. Left: ee, $\mu\mu$, $e\mu$ candidates. There are 2 entries per event. Right: $e\tau$, $\mu\tau$ candidates. Background and top contributions have been normalized to the expected number of events.

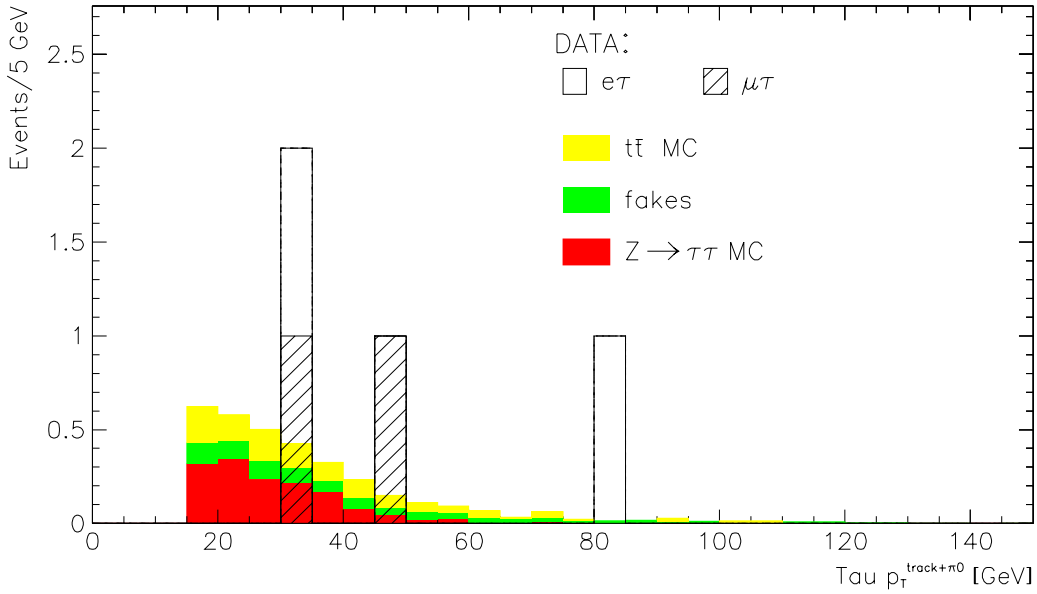

Figure 4.2: The p_T spectrum of τ's in the tau dilepton candidate events compared with the expected spectrum. Background and top contributions have been normalized to the expected number of events.

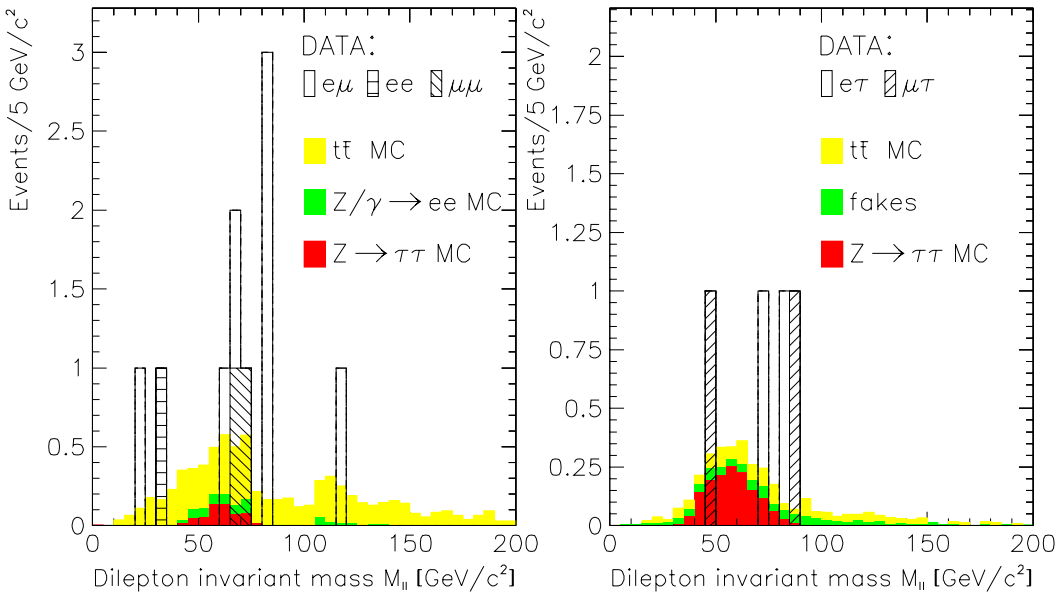

Figure 4.3: The invariant mass $m_{\ell\ell}$ formed by the leptons in the candidate events compared with the expected spectra. Left: ee, $\mu\mu$, $e\mu$ candidates. Right: $e\tau$, $\mu\tau$ candidates. Background and top contributions have been normalized to the expected number of events.

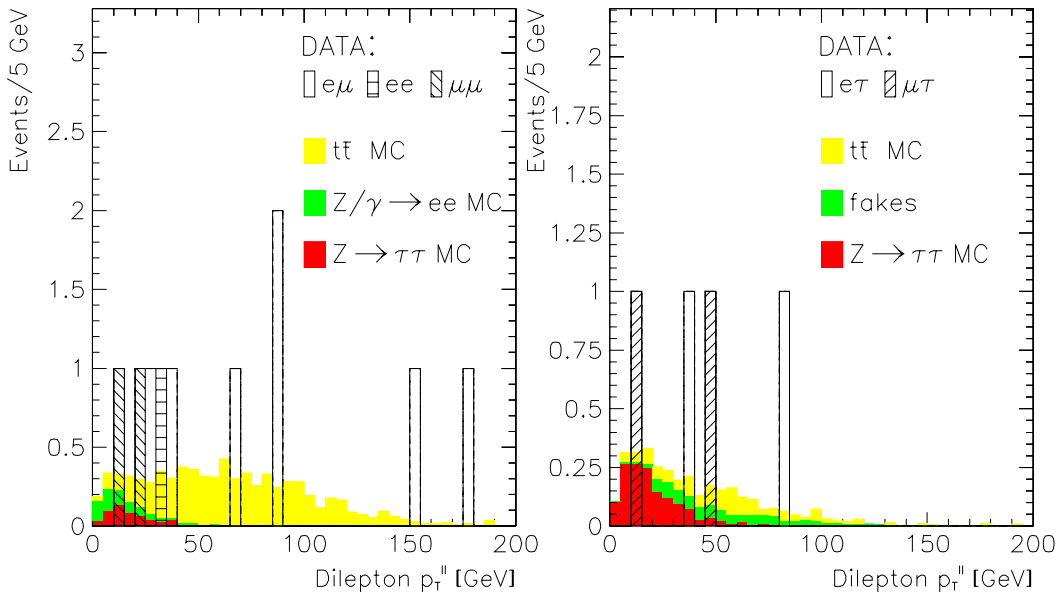

Figure 4.4: The $\vec{p}_T^{\,\ell\ell} = \vec{p}_T^{\,\ell_1} + \vec{p}_T^{\,\ell_2}$ spectrum of the dilepton system in the candidate events compared with the expected spectra. Left: ee, $\mu\mu$, $e\mu$ candidates. Right: $e\tau$, $\mu\tau$ candidates. Background and top contributions have been normalized to the expected number of events.

4.1.2 Neutrinos

Missing transverse energy $\not\!\!E_T$

Top dilepton events are expected to exhibit significant amount of $\not\!\!E_T$ due to at least 2 neutrinos that escape detection. Additional $\not\!\!E_T$ can be created by mismeasuring jets as shown in section 1.6.4 in the introduction. In Figures 4.5 and 4.6 we compare the observed $\not\!\!E_T$ in the candidate events with expectations. Figure 4.5 shows the $\not\!\!E_T$ which is not corrected for jets, whereas Figure 4.6 gives the $\not\!\!E_T$ including jet corrections as it is used in the event selection.

We find somewhat peculiar distributions because 5 of the 14 candidate events have $\not\!\!E_T{}^{corr} > 105$ GeV. Four of these are $e\mu$ events and there is also one $\mu\tau$ event. We expect 0.7 ± 0.1 ee, $\mu\mu$, and $e\mu$ top events and 0.18 ± 0.03 $e\tau$ and $\mu\tau$ events with $\not\!\!E_T{}^{corr} > 105$ GeV. Not surprisingly, we find the two events with the positrons that have very high E_T among these 4 $e\mu$ events. For Run 66046/Event 380045 the absolute value of the $\not\!\!E_T$ is very close to the E_T of the positron; the $\not\!\!E_T$ points directly opposite to the direction of the positron. The other 2 events are 2 Run Ia events: the "DPF" event[1] Run 41540/Event 127085 and Run 45047/Event 104393. Note that the topology of these events is shown schematically in Figures 2.10 and 2.11. Checking the $\mu\mu$ events we find them again in the region that has the largest expected background.

In Figure 4.7 we plot the angle $\Delta\phi(\not\!\!E_T, \ell j)$ between the corrected $\not\!\!E_T$ and the closest lepton or jet versus the corrected $\not\!\!E_T$. In order to show the expected scatter the Monte Carlo distributions for top and background are not normalized. For the ee, $\mu\mu$, and $e\mu$ events the topological cut used in the event

[1]This was the first top candidate to be presented in public at the DPF conference at Fermilab in 1992.

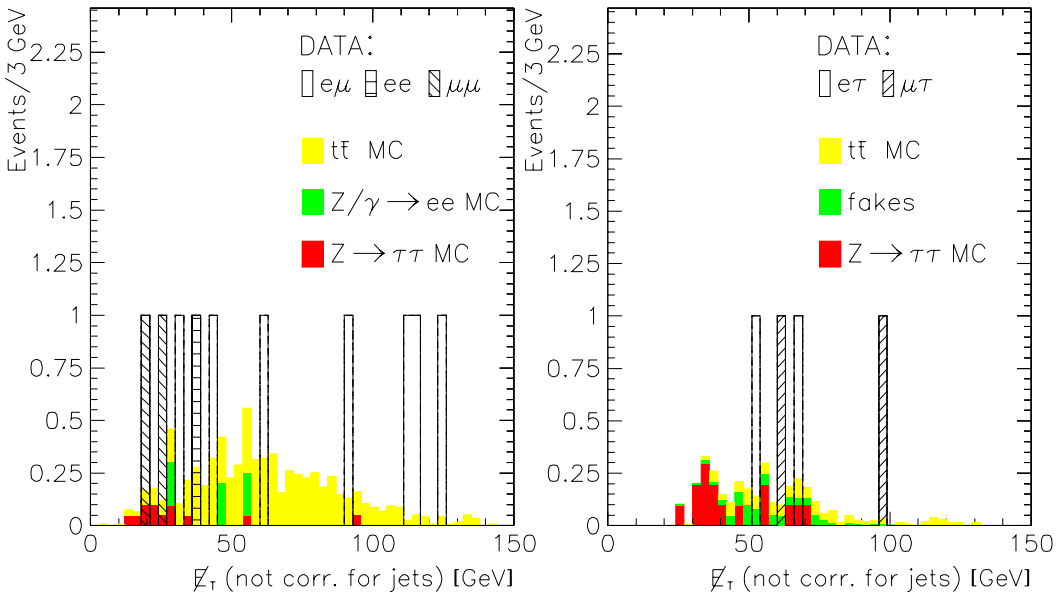

Figure 4.5: The $\not{E}_T$ spectrum without accounting for jet corrections for the candidate events compared with the expected spectra. Left: ee, $\mu\mu$, $e\mu$ candidates. Right: $e\tau$, $\mu\tau$ candidates. Background and top contributions have been normalized to the expected number of events.

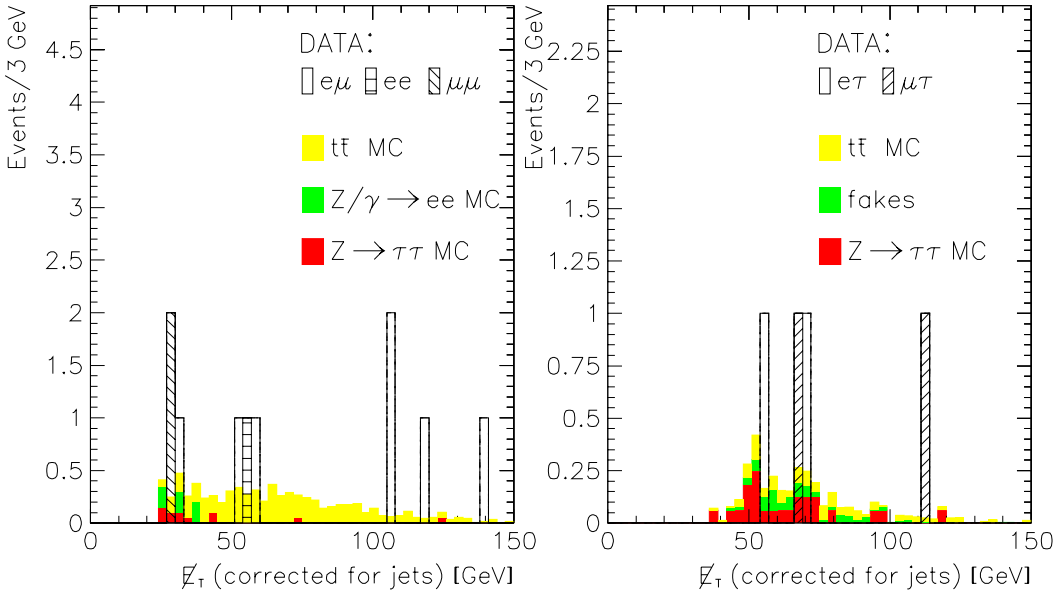

Figure 4.6: The $\not{E}_T$ spectrum after accounting for jet corrections for the candidate events compared with the expected spectra. Left: ee, $\mu\mu$, $e\mu$ candidates. Right: $e\tau$, $\mu\tau$ candidates. Background and top contributions have been normalized to the expected number of events.

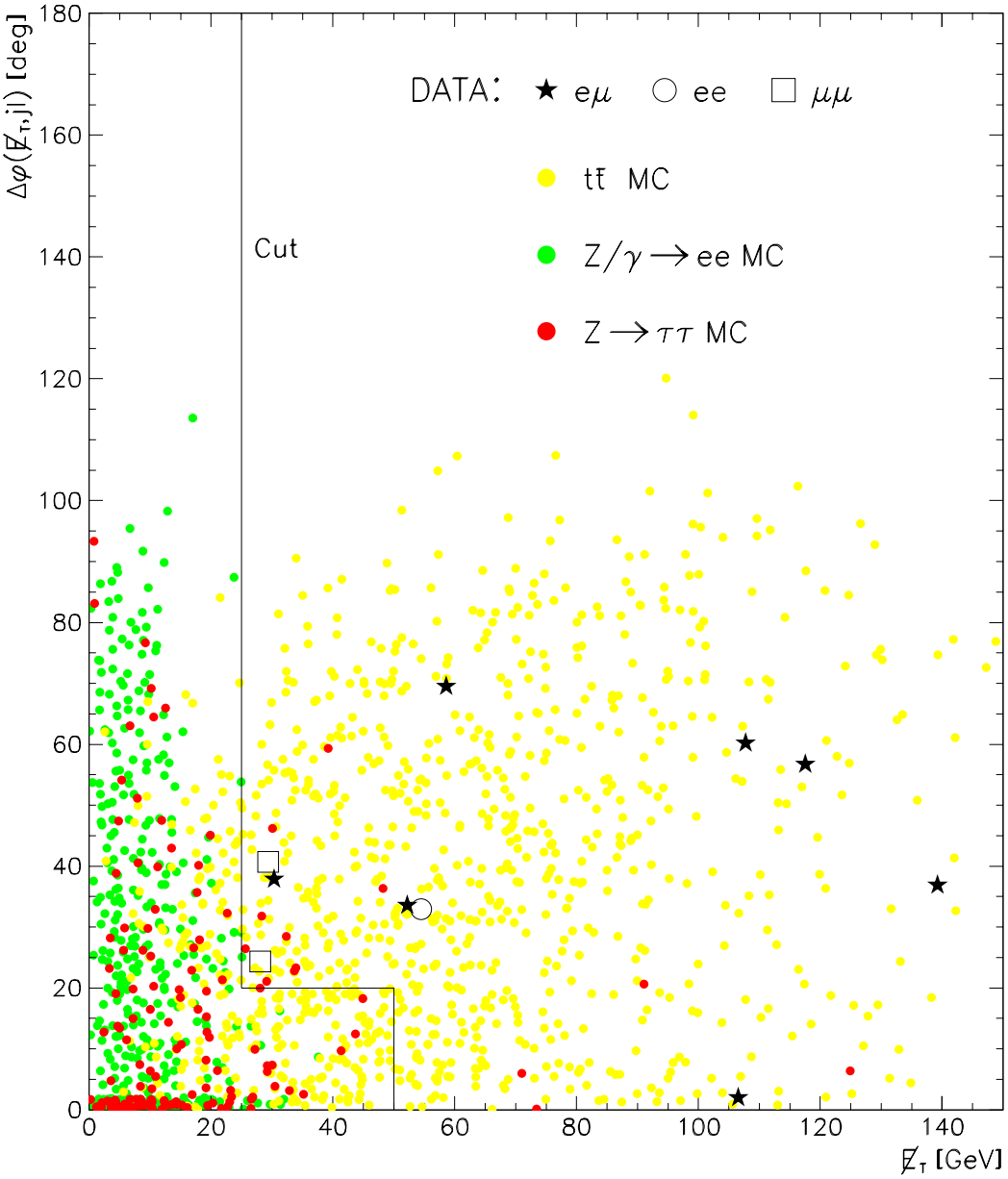

Figure 4.7: Scatterplot of the angle $\Delta\phi(\not{E}_T, \ell j)$ between the corrected $\not{E}_T$ and the closest lepton or jet versus corrected $\not{E}_T$ for the ee, $\mu\mu$, and $e\mu$ candidate events, compared with the expected distributions for $t\bar{t}$ and background. Background and top contributions are *not* normalized to the expected number of events.

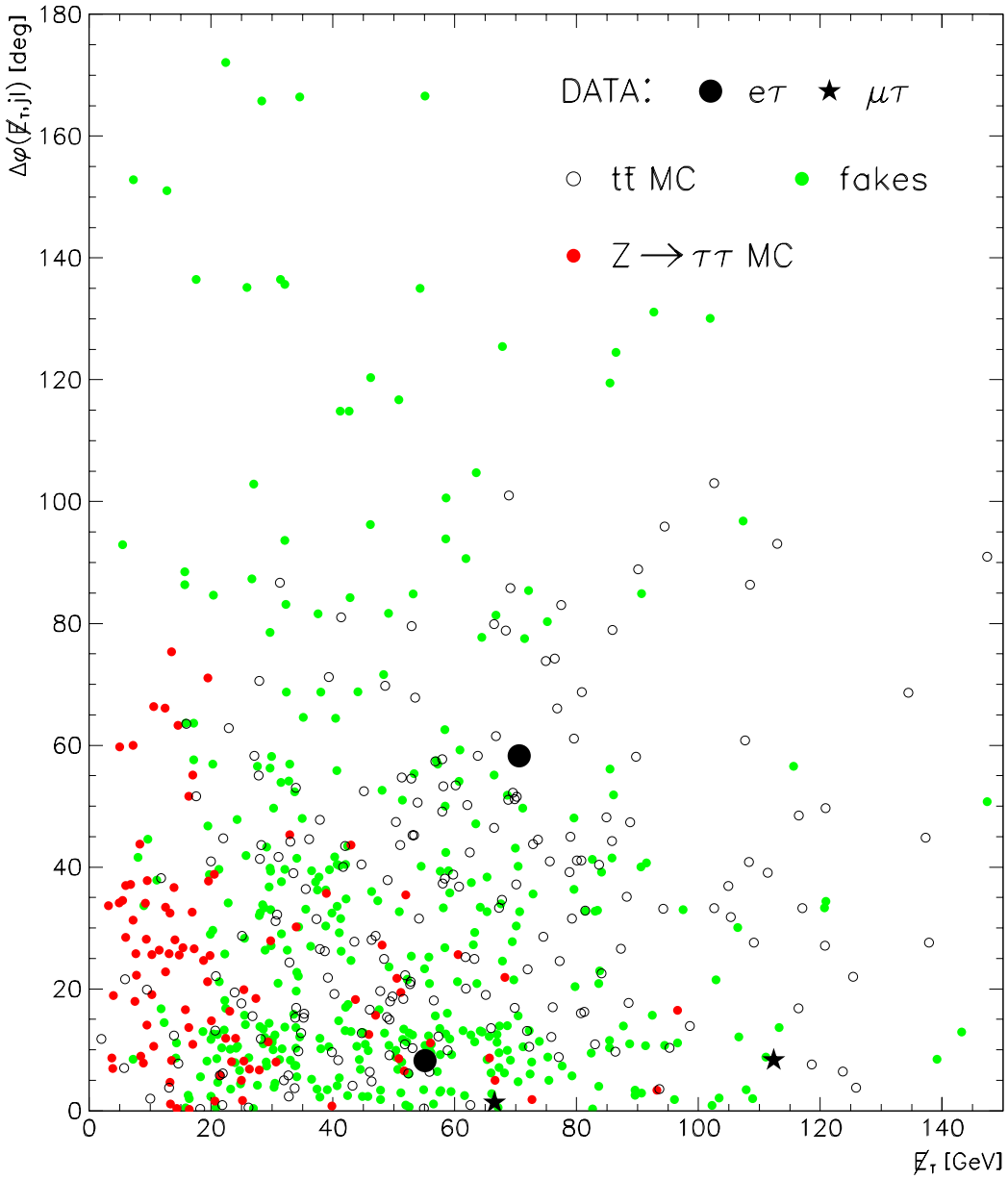

Figure 4.8: Scatterplot of the angle $\Delta\phi(\not{E}_T, \ell j)$ between the corrected $\not{E}_T$ and the closest lepton or jet versus corrected $\not{E}_T$ for the $e\tau$, and $\mu\tau$ candidate events, compared with the expected distributions for $t\bar{t}$ and background. Background and top contributions are *not* normalized to the expected number of events.

selection is indicated. Again it is apparent that the $\mu\mu$ events fall close to the cuts. One of them (Run 63700/Event 272140) sits right in the corner of the allowed region. The plot also shows that it is possible for $Z \rightarrow \tau\tau$ background to "spill" into this corner. We note again that 4 $e\mu$ events fall near the edge of the expected $t\bar{t}$ distribution because of the large $\not\!\!E_T$ in these events.

Even though we do not apply any cut in this plane for selecting the $e\tau$ and $\mu\tau$ events, we find that the 4 candidate events would pass such a cut. The distribution for the $\ell + \not\!\!E_T + \geq 3\ jets$ ($\ell = e, \mu$) data sample that is used to calculate the fake τ background and the distribution for $t\bar{t}$ Monte Carlo are similar. This is not surprising because a significant number of fakes are expected from real $t\bar{t}$ events decaying in the lepton + jets channel where a jet fakes a tau candidate.

$\not\!\!E_T$ significance

Figure 4.9 shows the spectrum for the $\not\!\!E_T$ significance, $S_{\not\!\!E_T}$. For the $e\tau$ and $\mu\tau$ events the data appear quite compatible with expectations. For the ee, $\mu\mu$, and $e\mu$ channel only the two Run Ia events with large $\not\!\!E_T$ end up on the tail of the distribution. The two Run Ib events that contain the very high E_T positrons are closer to the center of the distribution because the large E_T of the positron contributes a large fraction of the $\sum E_T$ in the denominator of the $S_{\not\!\!E_T}$ calculation. However, electron energies are much better measured than jet energies, which typically produce false $\not\!\!E_T$, when mismeasured. In the case of very large electron energies the $S_{\not\!\!E_T}$ variable can underestimate the significance of the $\not\!\!E_T$. In order to take this into account we take out the contribution of tight and loose central electrons (TCE, LCE) by defining a

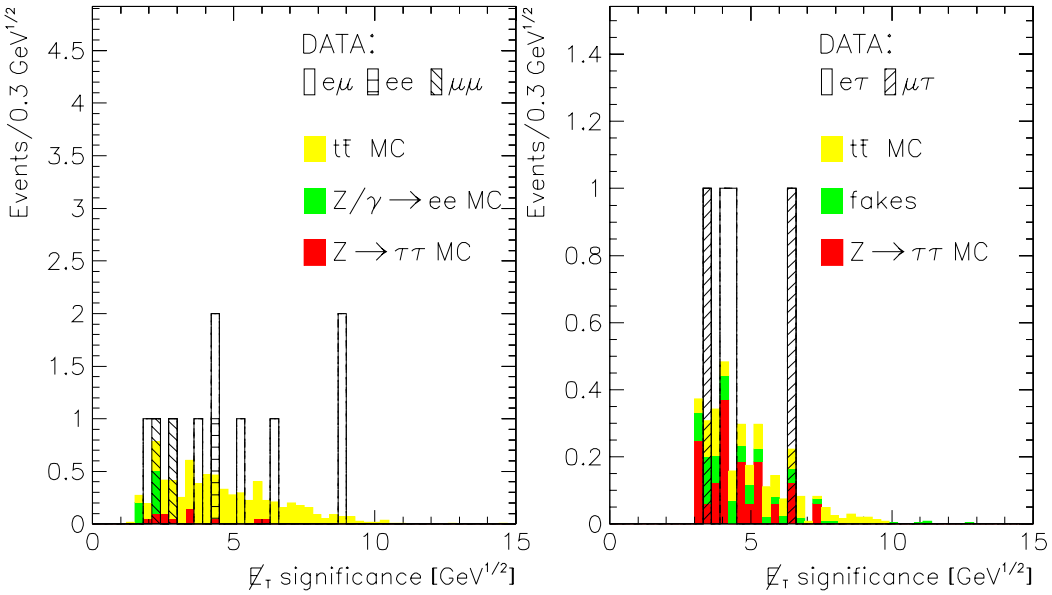

Figure 4.9: The spectrum of the $\not{E}_T$ significance after accounting for jet corrections for the candidate events compared with the expected spectra. Left: ee, $\mu\mu$, $e\mu$ candidates. Right: $e\tau$, $\mu\tau$ candidates. Background and top contributions have been normalized to the expected number of events.

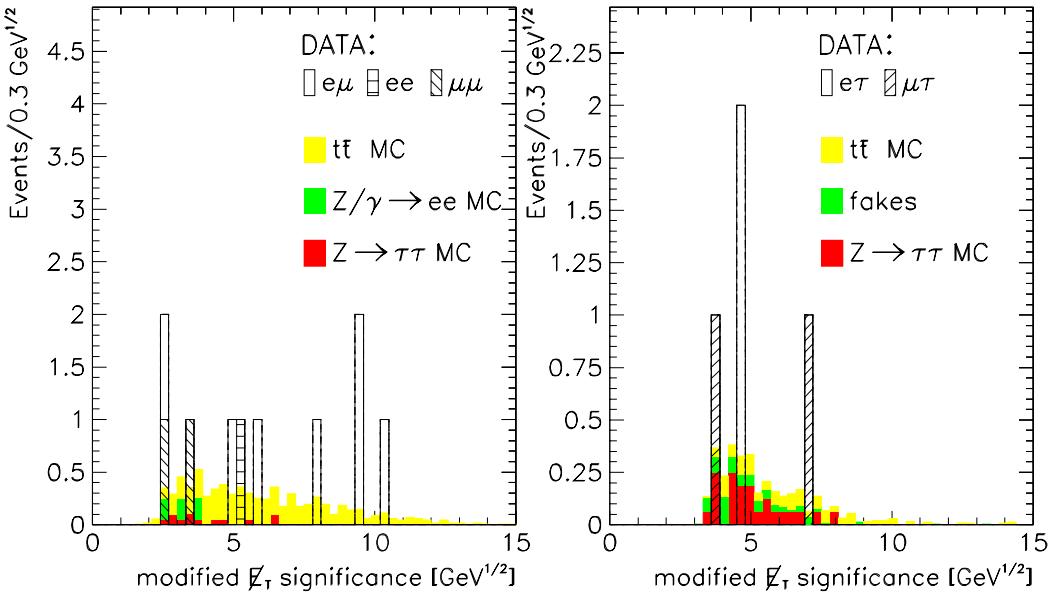

Figure 4.10: The spectrum of the modified $\not{E}_T$ significance (see equ. 4.1) after accounting for jet corrections for the candidate events compared with the expected spectra. Left: ee, $\mu\mu$, $e\mu$ candidates. Right: $e\tau$, $\mu\tau$ candidates. Background and top contributions have been normalized to the expected number of events.

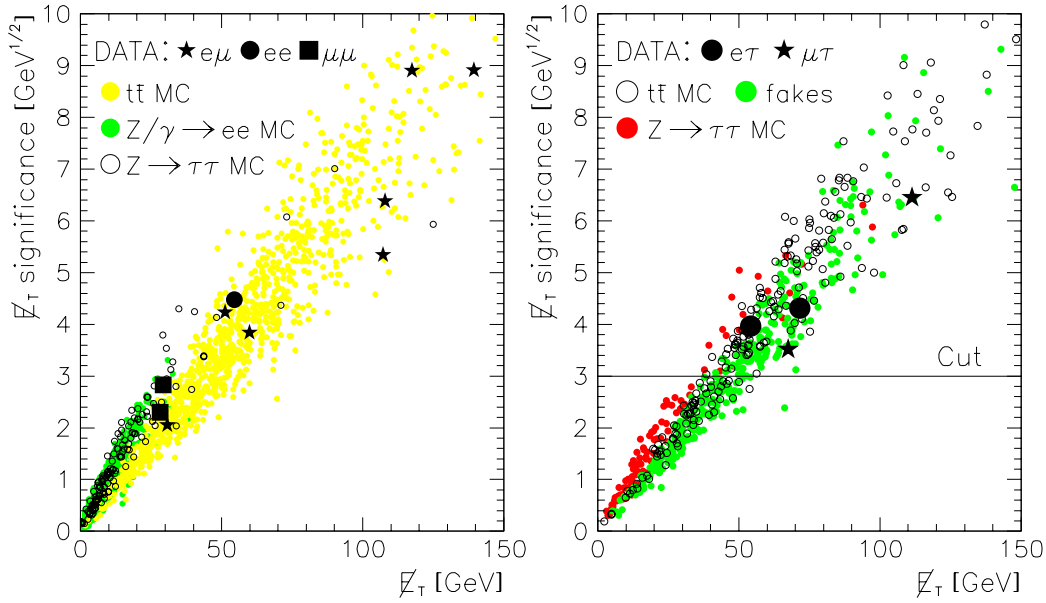

Figure 4.11: Scatterplot of the $\not\!\!E_T$ significance, $S_{\not\!\!E_T}$, versus $\not\!\!E_T$ for the candidate events compared with the expected distributions for top and background. Jet corrections are taken into account for calculating the $\not\!\!E_T$. Left: ee, $\mu\mu$, $e\mu$ candidates. Right: $e\tau$, $\mu\tau$ candidates. Background and top contributions are *not* normalized to the expected number of events.

second $\not\!\!E_T$ significance variable, $S'_{\not\!\!E_T}$:

$$S'_{\not\!\!E_T} \equiv \frac{\not\!\!E_T}{\sqrt{\Sigma E_T - \sum_e E_T^e}} \tag{4.1}$$

Figure 4.10 shows that in this case all 4 $e\mu$ events with large $\not\!\!E_T$ also exhibit large values of $S'_{\not\!\!E_T}$ and are found on the tail of the $t\bar{t}$ Monte Carlo distribution.

In Figure 4.11 $S_{\not\!\!E_T}$ is plotted versus $\not\!\!E_T$. Again, the 4 $e\mu$ events with $\not\!\!E_T >$ 105 GeV appear in the fringes of the expected $t\bar{t}$ distribution. If the topological cut from the tau dilepton analysis, $S_{\not\!\!E_T} >$ 3 GeV$^{1/2}$, is applied to the ee, $\mu\mu$, and $e\mu$ channel three events will be lost, including the 2 $\mu\mu$ events.

4.1.3 Jets

Figure 4.12 shows that the number of jets with $E_T > 10$ GeV, $|\eta| < 2.0$ found in the candidate events is compatible with the expectations. The same statement holds for the E_T spectra of the leading and second jet in the ee, $\mu\mu$, and $e\mu$ channel shown in Figures 4.13 and Figures 4.14. The jet corrections are not applied here. The 4 jets in the 2 $\mu\mu$ events all appear in the low E_T end of the spectrum where the jets from background events are expected.

The leading jets in the 2 $\mu\tau$ events are found in the tail of the expected distribution. Run 65471/Event 47719 has a very energetic leading jet with $E_T = 169$ GeV. We expect 0.009 ± 0.003 tau dilepton events containing a jet with $E_T > 169$ GeV from $t\bar{t}$ decays. Note that this is the only tau dilepton event without a b–tag. The distribution of the second jet in the tau dilepton events appears compatible with the expectations.

4.1.4 Summary of distributions with events in the tails

Table 4.1 lists the p_T of the leptons, the $\not\!\!E_T$, the $\not\!\!E_T$ significance (calculated both ways), and the H_T for all 14 candidate events. In Table 4.2 we summarize the information for those inclusive kinematical variables where events show up in the tails of the distributions, i.e. for the p_T of the leptons and the missing transverse energy. We list the mean expected number of events, m, above a threshold, the observed number of events, N, and the Poisson probability to observe $\geq N$ events when m events are expected.

Run	Event	'Name'	Type	$p_T(\ell_1), E_T(\ell_1)$ [GeV(/c)]	$p_T(\ell_2), E_T(\ell_2)$ [GeV(/c)]	corr. $\not\!\!E_T$ [GeV]	$S_{\not\!\!E_T}$ [GeV$^{1/2}$]	$S_{\not\!\!E_T}{}'$ [GeV$^{1/2}$]	H_T [GeV]
41540	127085	DPF $e\mu$	TCE–TCM	e: 22.2 (22.0)	μ: 47.7	138.1	9.0	9.3	360
45047	104393	Pseudo $e\mu$	TCM–LCE	μ: 40.7	e: 24.3 (24.6)	117.8	9.0	10.3	249
47122	38382	Ia CEMX	TCE–TCM	e: 50.6 (49.1)	μ: 37.2	60.0	3.9	4.9	225
57621	45230	Ib $e\mu$ 1	TCE–TCM	e: 49.0 (47.7)	μ: 25.4	52.0	4.2	5.9	177
58281	44805	$\mu\mu\gamma$	TCM–TCM	μ: 35.5	μ: 34.4	29.0	2.8	3.5	140
63700	272140	Ib $\mu\mu$	TCM–TCM	μ: 39.9	μ: 29.3	27.2	2.3	2.7	134
66046	380045	Ib CEMX	TCE–TCM	e: 105.6 (109.8)	μ: 52.5	107.7	6.3	9.4	326
67581	129896	trilepton	TCE–TCM	e: 181.8 (197.1)	μ: 27.3	106.8	5.4	7.8	413
68185	174611	Ib ee	TCE–TCE	e: 23.4 (24.5)	e: 20.5 (20.3)	54.6	4.5	5.3	165
69808	639398	Ib $e\mu$ 3	TCE–TCM	e: 42.3 (43.4)	μ: 55.7	30.7	2.0	2.6	222
45880	31838	Ia $e\tau$	TCE–TAU	e: 27.3 (27.1)	τ: 81.9	71.0	4.3	4.5	265
64721	229200	Ib $\mu\tau$ 1	TCM–TAU	μ: 46.1	τ: 33.9	112.1	6.5	7.0	346
64934	416715	Ib $e\tau$	TCE–TAU	e: 60.1 (61.3)	τ: 30.0	54.9	3.9	4.7	203
65471	47719	Ib $\mu\tau$ 2	TCM–TAU	μ: 22.3	τ: 45.5	66.1	3.5	3.7	353

4.1: Kinematic properties of the 14 top dilepton candidates. For electrons we list the corrected E_T^e in parentheses. The modified significance $S_{\not\!\!E_T}{}'$ is defined in equ. 4.1.

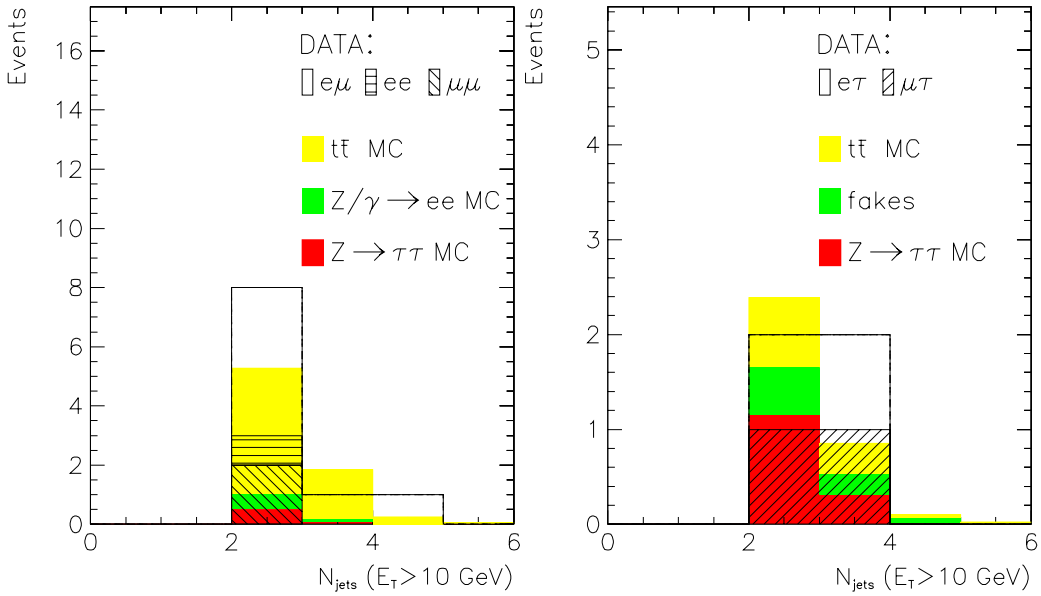

Figure 4.12: The number of jets with $E_T > 10$ GeV, $|\eta| < 2.0$ in the candidate events compared with the expected spectra. Left: ee, $\mu\mu$, $e\mu$ candidates. Right: $e\tau$, $\mu\tau$ candidates. Background and top contributions have been normalized to the expected number of events.

4.2 Global event kinematics

4.2.1 Total transverse energy H_T

Figure 4.15 shows the total transverse energy, $H_T = E_T^{\ell_1} + E_T^{\ell_2} + \not{E}_T + \sum E_T^{jets}$, of the candidate events. Due to the large mass of the top quark all its decay products are imparted with large transverse energies, so that we expect H_T values in the $200 - 400$ GeV range. In general, the data appear to be compatible with this expectation. The 7 $e\mu$ events all have larger H_T than the ee and the 2 $\mu\mu$ events. If one were to impose a cut $H_T > 180$ GeV as in the tau dilepton analysis, only 10 events, the 4 tau dilepton events plus 6 $e\mu$ events, would pass the cut. The H_T distribution for the tau dilepton events shows the two $\mu\tau$ events with $H_T \approx 350$ GeV. In this region the background contribution is expected to be small and the top contribution dominates.

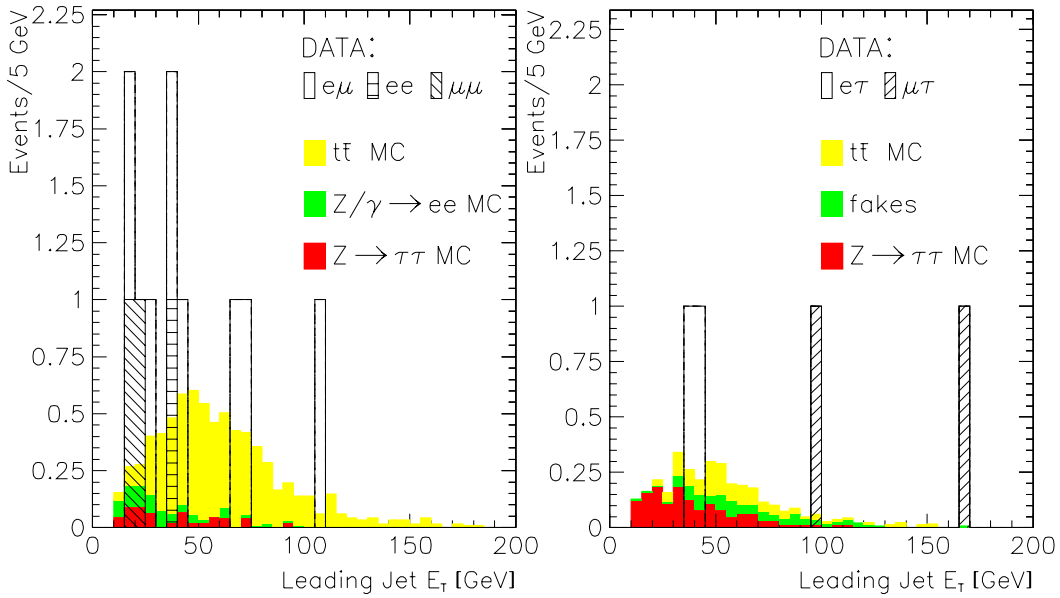

Figure 4.13: The E_T spectrum of the leading jet in the candidate events compared with the expected spectrum. No jet corrections are applied. Left: ee, $\mu\mu$, $e\mu$ candidates. Right: $e\tau$, $\mu\tau$ candidates. Background and top contributions have been normalized to the expected number of events.

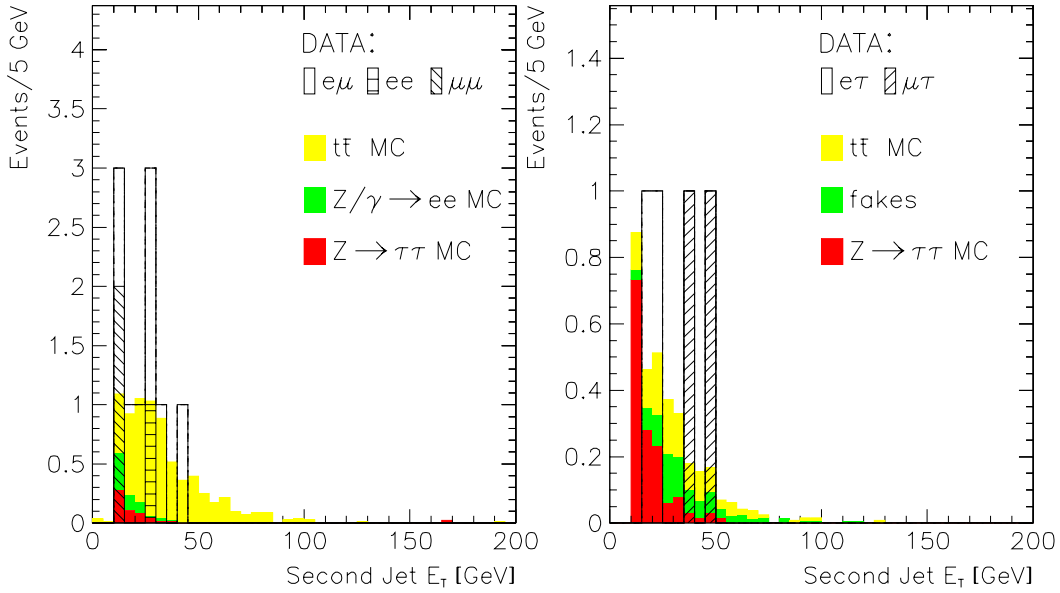

Figure 4.14: The E_T spectrum of the second jet in the candidate events compared with the expected spectrum. No jet corrections are applied. Left: ee, $\mu\mu$, $e\mu$ candidates. Right: $e\tau$, $\mu\tau$ candidates. Background and top contributions have been normalized to the expected number of events.

Distribution	mean expected number m	observed number N	$P(\geq N, m)$
$p_T^\ell > 105$ GeV	0.6 ± 0.1	2	12.2%
$p_T^\ell > 180$ GeV	0.06 ± 0.02	1	5.8%
$E_T^{jet} > 169$ GeV ($e\tau$, $\mu\tau$ only)	0.009 ± 0.003	1	0.9%
$\not{E}_T{}^{corr} > 105$ GeV (ee, $\mu\mu$, $e\mu$ only)	0.7 ± 0.1	4	0.6%
$\not{E}_T{}^{corr} > 105$ GeV (ee, $\mu\mu$, $e\mu$, $e\tau$, $\mu\tau$)	0.9 ± 0.1	5	0.2%

Table 4.2: Summary of the information for the kinematic distributions in which events are found in the tails. We give the mean expected number of events (m) above a kinematic threshold, the observed number of events (N), and the Poisson probability $P(\geq N, m)$ to observe $\geq N$ events when m events are expected.

4.2.2 Thrust analysis

Since the previous section showed that some candidate events have peculiar kinematical features we further analyze the general event shape of the candidate events by performing a "classical" thrust analysis. The idea is that this might be a way in which one could distinguish the pair production of particles with high mass at low to moderate p_T, e.g. top quarks, from pair production of particles with lower mass but higher p_T that decay with a signature similar to top dileptons. The latter event type would have higher thrust and lower invariant masses.

The thrust axis $\vec{a}$ of an event is defined as the unit 3-vector that maximizes the expression for the thrust

$$thrust = \frac{\sum_i \mid \vec{a} \cdot \vec{p}_i \mid}{\sum_i \mid \vec{p}_i \mid}, \tag{4.2}$$

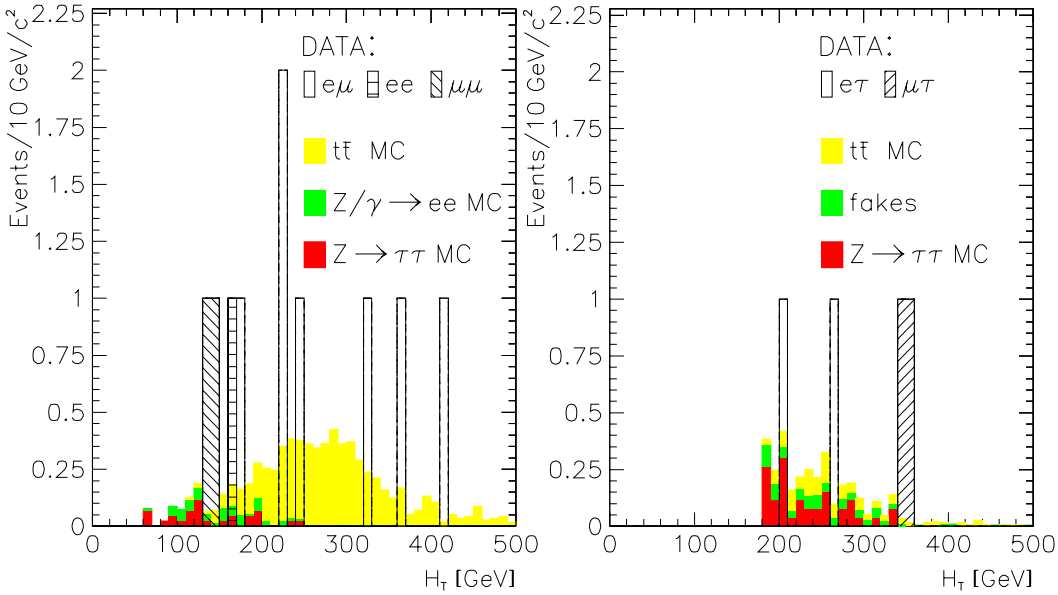

Figure 4.15: The H_T spectrum of candidate events compared with the expected spectrum. Left: ee, $\mu\mu$, $e\mu$ candidates. Right: $e\tau$, $\mu\tau$ candidates. Background and top contributions have been normalized to the expected number of events.

where $\vec{p}_i$ is the 3-momentum of the i-th particle in the event. It is that axis along which the sum of the projections of all particle momenta $\vec{p}_i$ is largest.

The oblateness is defined using the "major" and "minor" axis in the plane perpendicular to the thrust axis. The major axis is analogous to the thrust axis in this plane, i.e. it maximizes

$$major = \frac{\sum_i |\vec{m} \cdot \vec{p}_i^{\,proj}|}{\sum_i |\vec{p}_i^{\,proj}|}, \tag{4.3}$$

where $\vec{p}_i^{\,proj}$ is the projection of the particle 3-momenta onto this plane. The minor axis is the axis perpendicular to thrust axis and major axis. The oblateness is the difference of the above expressions for major and minor axis, $(major - minor)$. The 3-momenta $\vec{p}$ of the following objects are used in the calculation [76]: the two leptons, the four highest jets using uncorrected energy, and $\not{E}_T$, where we set $p_z = 0$.

We divide the event into 2 hemispheres using the plane perpendicular

Run	Event	'Name'	Thrust	m_{thrust} [GeV/c^2]	m_{opp} [GeV/c^2]	oblate-ness
41540	127085	DPF	0.94	62.28	64.79	0.20
45047	104393	Pseudo $e\mu$	0.83	95.02	57.30	0.24
47122	38382	Ia CEMX	0.70	100.03	84.11	0.24
57621	45230	Ib $e\mu$ 1	0.76	72.40	49.32	0.45
58281	44805	$\mu\mu\gamma$	0.92	21.38	26.65	0.23
63700	272140	Ib $\mu\mu$	0.79	49.68	22.74	0.19
66046	380045	Ib CEMX	0.87	107.95	61.97	0.29
67581	129896	trilepton	0.71	0.06	179.51	0.17
68185	174611	Ib ee	0.68	39.70	65.68	0.27
69808	639398	Ib $e\mu$ 3	0.68	65.49	107.21	0.12
45880	31838	Ia $e\tau$	0.64	80.04	142.96	0.28
64721	229200	Ib $\mu\tau$ 1	0.82	135.15	9.58	0.09
64934	416715	Ib $e\tau$	0.73	72.14	82.60	0.30
65471	47719	Ib $\mu\tau$ 2	0.86	68.74	105.23	0.07

Table 4.3: Thrust, oblateness and invariant masses for the 14 top dilepton candidates.

to the thrust axis and calculate 2 invariant masses: m_{thrust} is the invariant mass of all objects in the hemisphere that the thrust axis points into, and m_{opp} is the invariant mass of all objects in the hemisphere opposite to the thrust axis.

The thrust axes and thrust values are shown in the schematic (r, ϕ) views of the 10 ee, $\mu\mu$, and $e\mu$ candidate events in Figures 2.10 and 2.11 in Chapter 2. Figure 4.16 shows the corresponding information for the 4 tau dilepton candidates. In Table 4.3 we list the values for thrust, oblateness and invariant masses for the 14 candidate events. Note that we have used uncorrected electron and jet energies to calculate these.

In Figure 4.17 we compare the thrust and oblateness of the top dilepton candidates with $t\bar{t}$ Monte Carlo distributions that are normalized to the data. To quantify the consistency or inconsistency of distributions we use the Kolmogorov-Smirnov (KS) test. In the following we give the KS probability

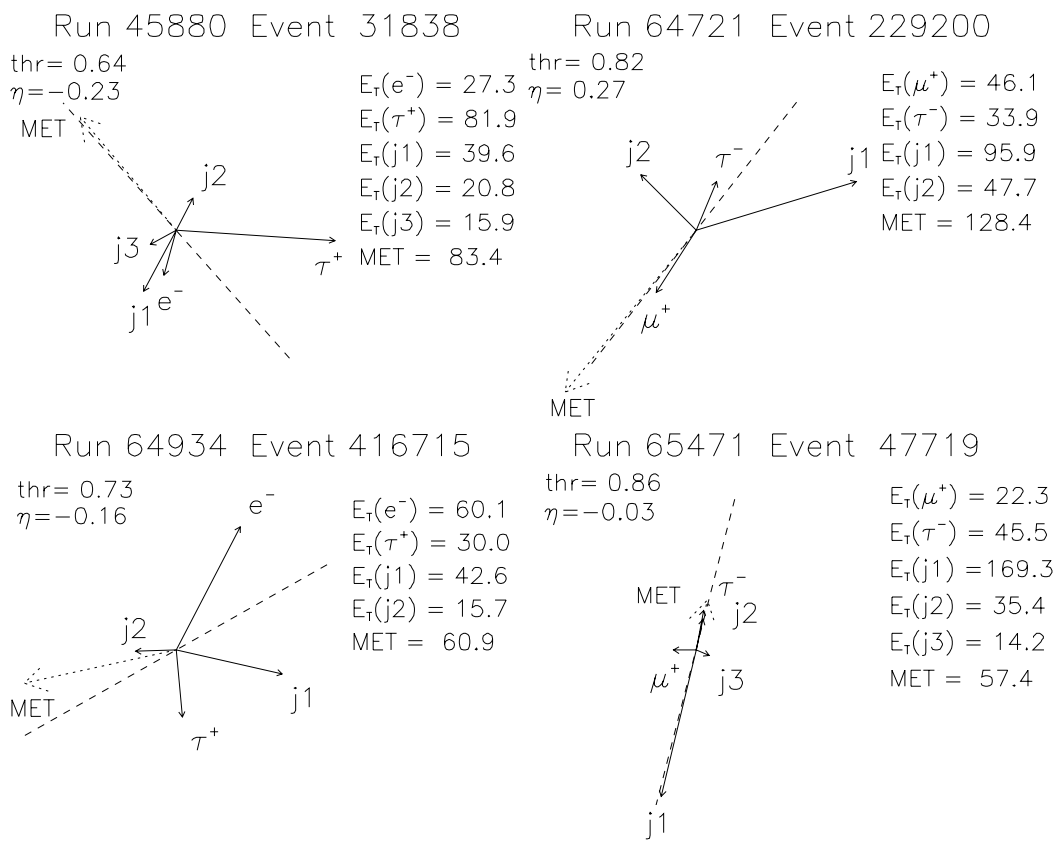

Figure 4.16: Schematic (r, ϕ) view of the topology for $e\tau$ and $\mu\tau$ top dilepton candidates including thrust axes (dashed line). The vector lengths represent the transverse momenta of the objects. Note that we plot quantities as used for the dilepton selection, i.e. electron and jet energies are not corrected, but $\not\!\!E_T$ is corrected for muons and jets.

for all distributions with the value for the tau dileptons in parentheses. The thrust distributions appear consistent with $t\bar{t}$ MC. The KS test returns a 70.2% (93.3%) probability for the 2 distributions to be from the same parent distribution. For the oblateness the KS test returns a 53.4% (70.3%) probability.

The event with the highest thrust of 0.94 is the DPF event. It is known that this event can only be successfully fitted to a top hypothesis if the neutrinos are assumed to go in the same direction and if the jets are pulled considerably [77]. The next highest thrust is found for a $\mu\mu$ event (Run 58281/Event 44805). As discussed in the following section this event can be interpreted as a radiative Z decay, which would explain the large thrust.

Plotting the thrust vs the invariant masses in Figure 4.18 we notice some peculiarities: For one $e\mu$ event (Run 67581/Event 129896) we find $m_{thrust} \approx 0$. This is due to the fact that there is only one object, the 182 GeV positron, in the thrust hemisphere. We also note that $m_{opp} \approx m_{top}$ for this event. The DPF and $\mu\mu$ event are again outliers and also Run 66046/Event 380045 appears in the tail of the top distribution.

There is also a more general unusual feature present in the data: Except for the opposite thrust side of Run 67581/Event 129896, the ee, $\mu\mu$, and $e\mu$ events do not have an invariant mass greater than 110 GeV, even though this region is well populated by $t\bar{t}$ MC events. The KS test for these events returns smaller probabilities, 25.1% and 24.1%, than for the one-dimensional thrust distribution. The probabilities for the tau dilepton events are higher: 83.1% and 98.6%.

If we plot m_{thrust} vs m_{opp} as shown Figure 4.19 the KS test yields an even smaller probability of 3.7% for compatibility with the $t\bar{t}$ MC. Both $\mu\mu$ events again look rather "untop–like" in this view. This is consistent with our finding that the inclusive distributions for these two events are background-

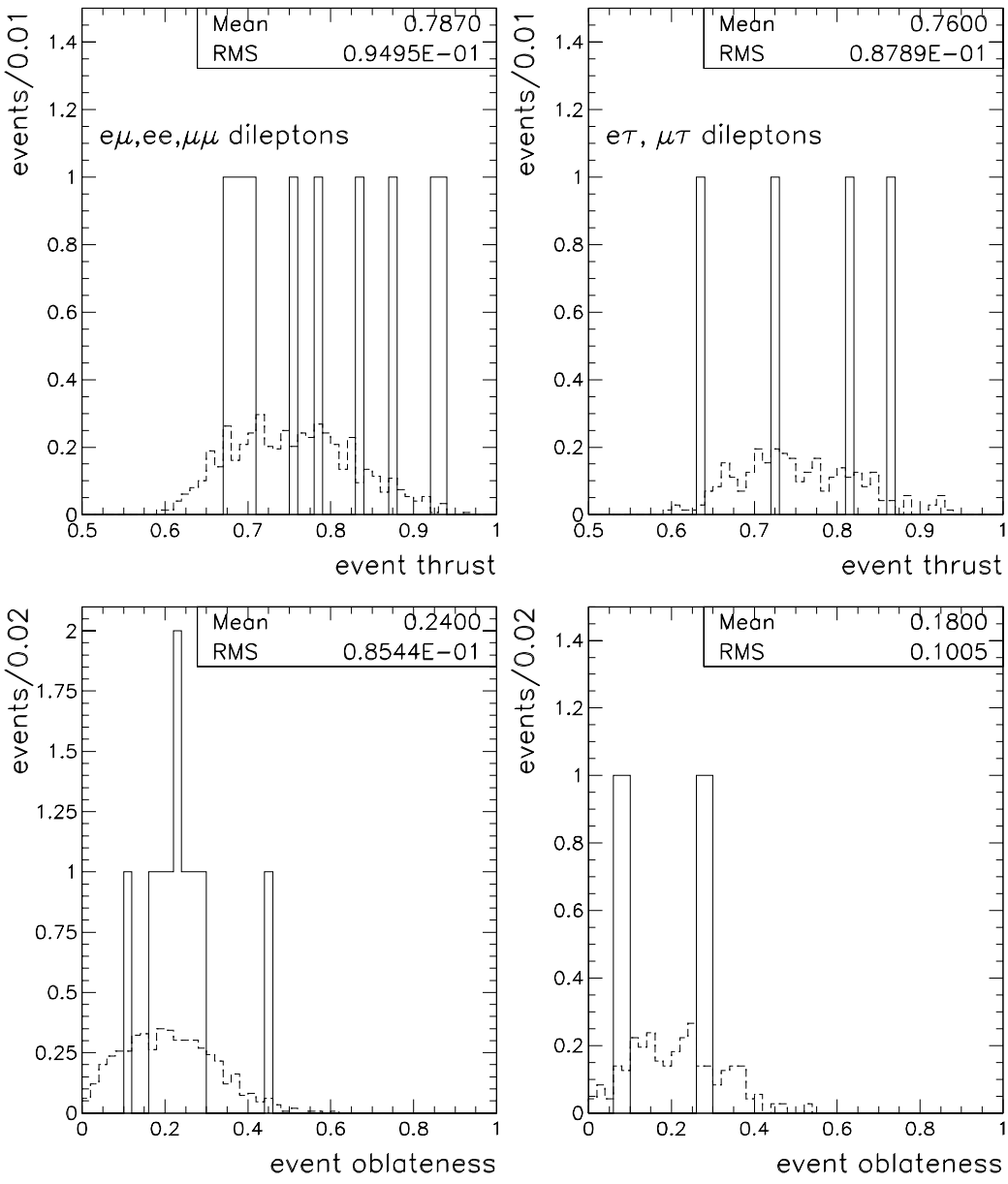

Figure 4.17: Thrust and oblateness of top dilepton candidates compared with $t\bar{t}$ 175 MC (dashed). Left: $e\mu, ee, \mu\mu$ candidates. Right: $e\tau$, $\mu\tau$ candidates. KS probability for thrust is 70.2% (93.3%), for oblateness is 53.4% (70.3%). Values in parentheses are for tau dileptons.

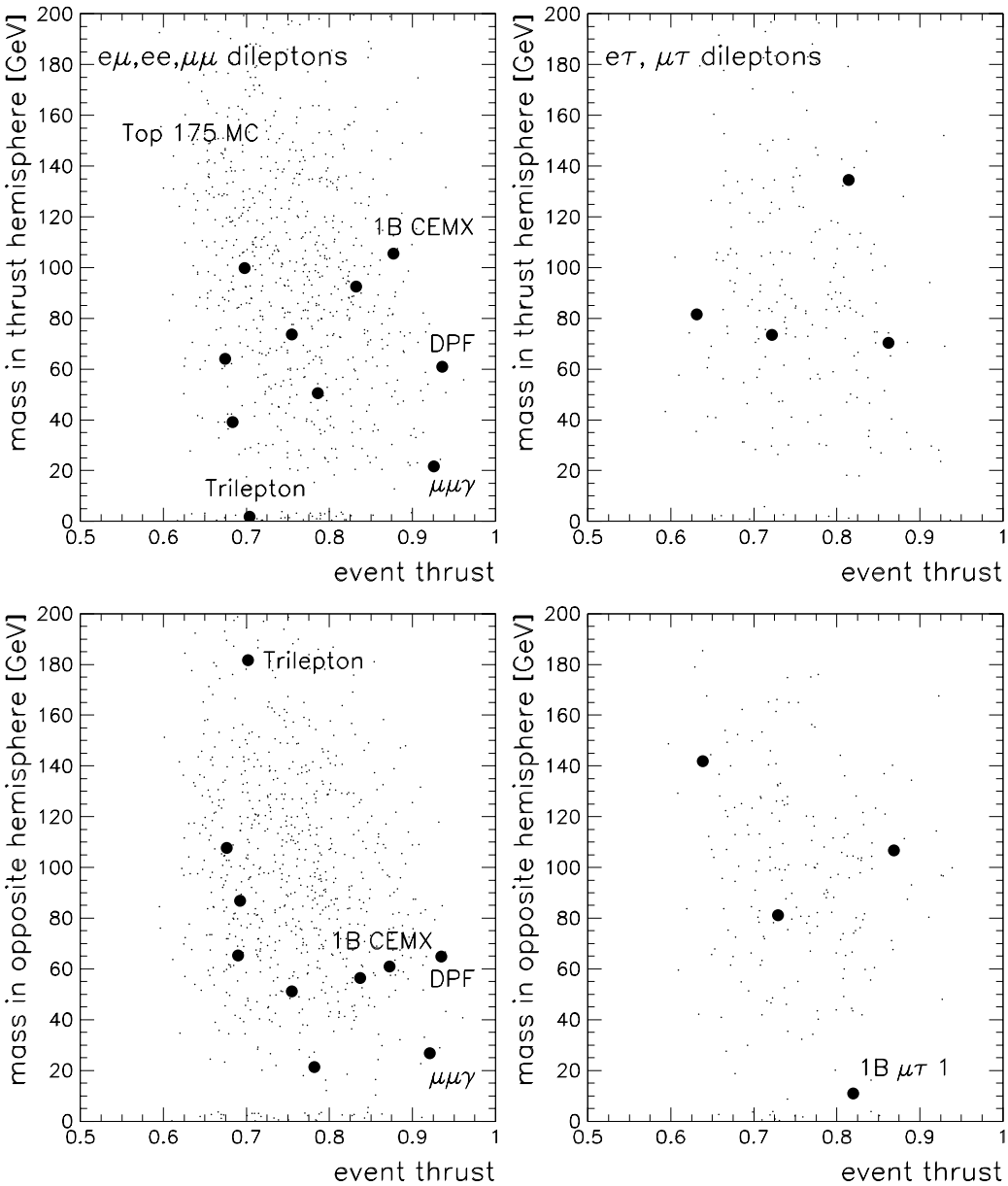

Figure 4.18: Top: Invariant mass in thrust hemisphere vs thrust [KS P = 25.1%, (P = 83.1%)]. Bottom: Invariant mass in hemisphere opposite the thrust vs thrust [KS P = 24.1%, (P = 98.6%)]. Left: $e\mu, ee, \mu\mu$ candidates. Right: $e\tau$, $\mu\tau$ candidates. Values in parentheses are for tau dileptons. Large dots are data, smaller dots are $t\bar{t}$ 175 MC.

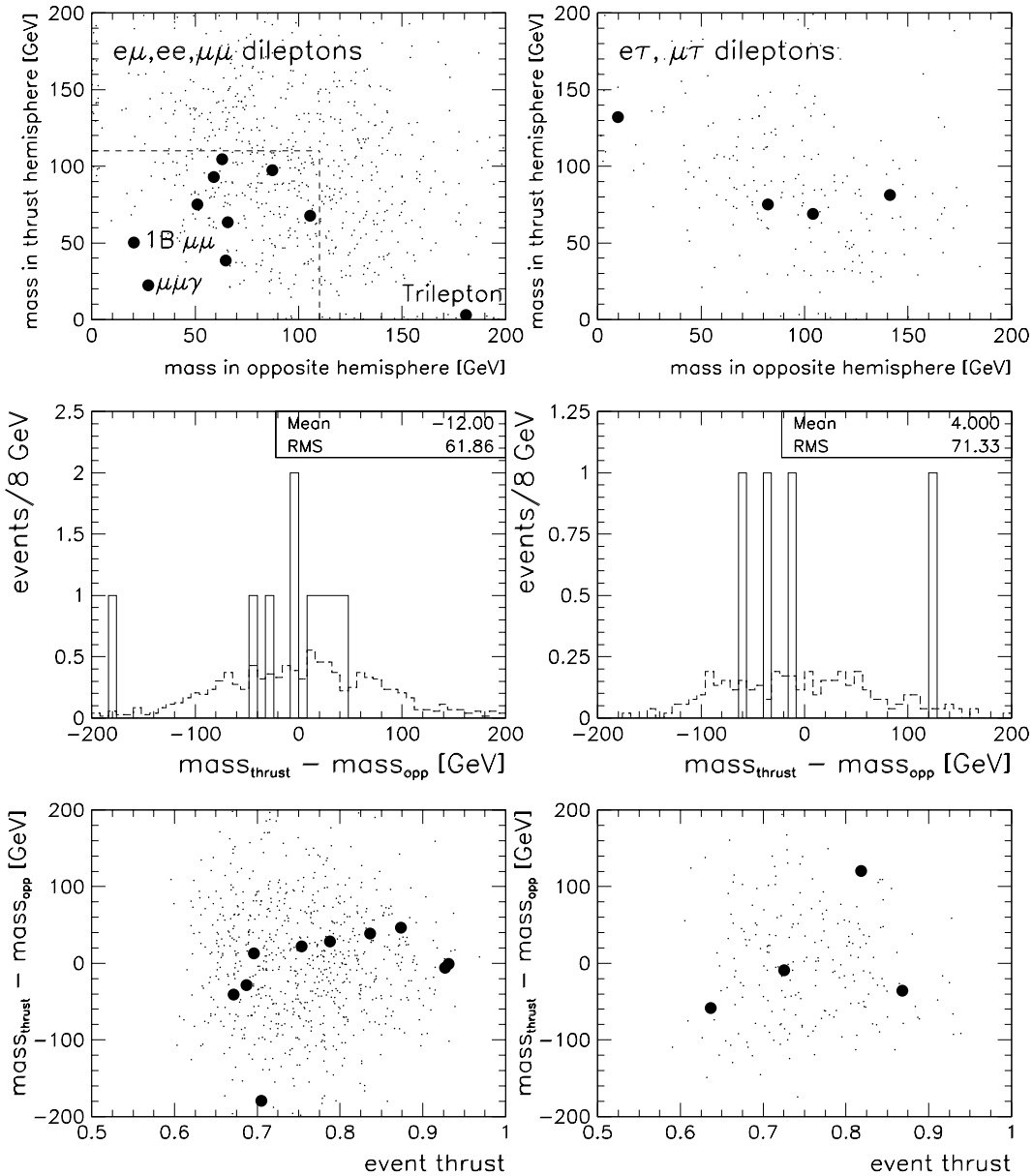

Figure 4.19: Top: Invariant mass in thrust hemisphere vs invariant mass in hemisphere opposite the thrust [KS $P = 3.7\%$ ($P = 95.3\%$)]. Center: $m_{thrust} - m_{opp}$ [KS $P = 44.1\%$ ($P = 95.4\%$)]. Bottom: $m_{thrust} - m_{opp}$ vs thrust [KS $P = 51.9\%$ ($P = 87.5\%$)]. Left: $e\mu, ee, \mu\mu$ candidates. Right: $e\tau$, $\mu\tau$ candidates. Values in parentheses are for tau dileptons. Large dots are data, smaller dots are $t\bar{t}$ 175 MC.

like. Interestingly, we observe a possible clustering of the 6 $e\mu$ events and the ee event in the mass range 40–110 GeV. The tau dileptons agree better with the top distributions at 95.3% probability. Plotting just the difference of the invariant masses we find a KS probability of 44.1% and 95.4% for ee, $\mu\mu$, and $e\mu$ dileptons and tau dileptons, respectively.

Given the low statistics evaluating the effect of background fluctuations is difficult. Instead of mixing in the background using Monte Carlo we choose to simply apply a strict H_T cut to suppress the background sufficiently and redo the analysis. We require $H_T > 220$ GeV, which is about 80% efficient for ee, $\mu\mu$, and $e\mu$ top dilepton events ($m_{top} = 175$ GeV/c^2) and 75% efficient for tau dilepton events. Note that we have required $H_T > 180$ GeV in the selection of tau dileptons.

The expected background with this cut is 0.4 events for the ee, $\mu\mu$, and $e\mu$ dileptons. About 4 events total are expected from top signal plus background. For the $e\tau$ and $\mu\tau$ channel we expect 1.1 background events and about 2 events total. Five $e\mu$ events of the ten standard dilepton events and three of the four tau dilepton events pass this cut. Note that neither of the two $\mu\mu$ events passes this cut.

In Figure 4.20 we plot m_{thrust} vs m_{opp} for the events passing the H_T cut as shown, which is the plot with the largest discrepancy between $t\bar{t}$ MC and data before applying the H_T cut. We find that the KS probability increases to 25.6%. The increase is basically due to the fact that the low-mass outliers – the 2 $\mu\mu$ events – do not pass the H_T cut. We conclude from this that the low KS value obtained before is not indicative of new physics. However, we still observe a clustering of 4 $e\mu$ events in the mass range 60-110 GeV.

In Table 4.4 we list the KS values for all comparisons of the data with $t\bar{t}$ Monte Carlo in the thrust analysis. We conclude that the distributions of

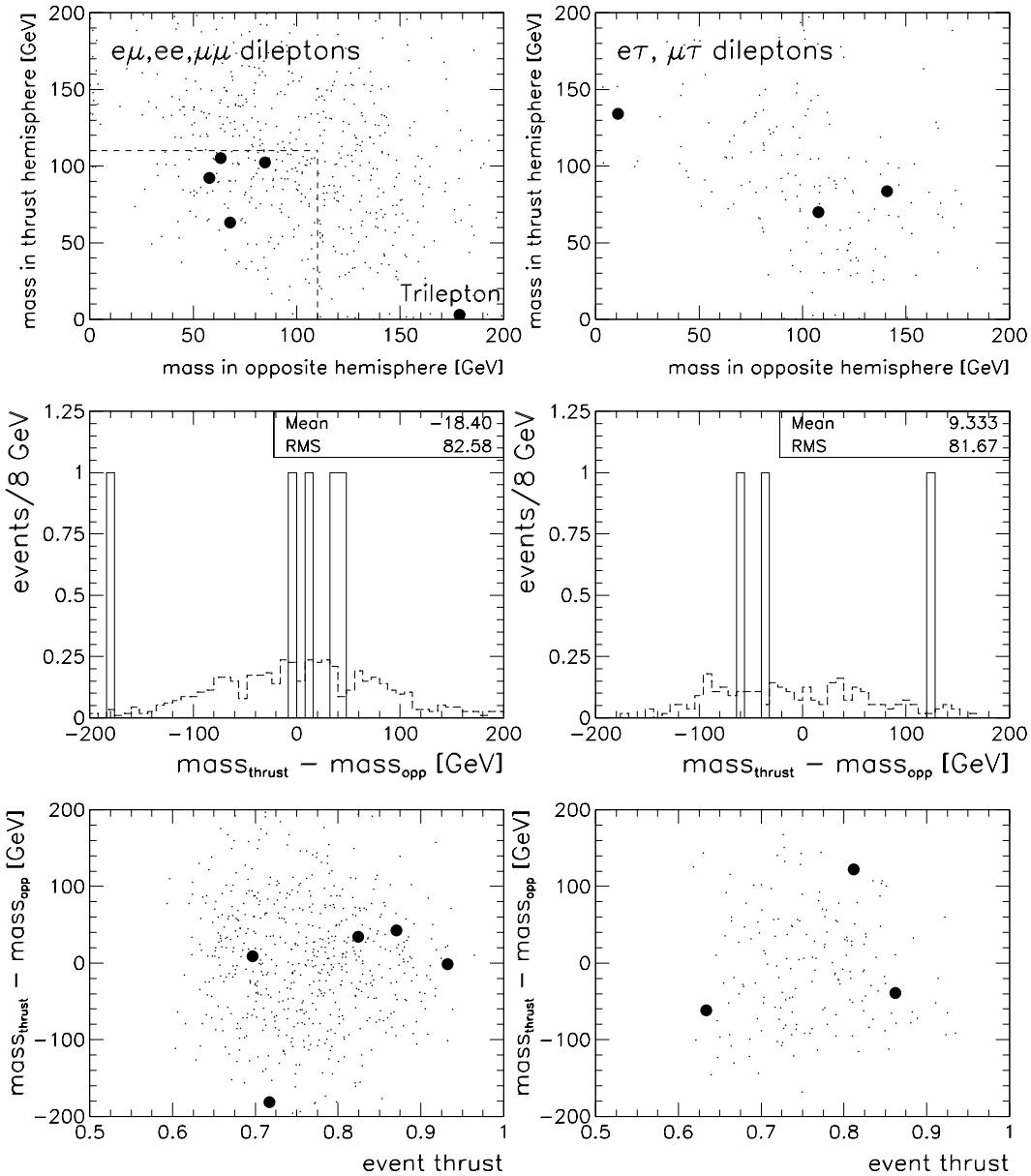

Figure 4.20: Same as previous figure, except with additional requirement $H_T >$ 220 GeV. Left: $e\mu$ candidates. Right: $e\tau$, $\mu\tau$ candidates. Top: Invariant mass in thrust hemisphere vs invariant mass in hemisphere opposite the thrust [KS $P = 25.6\%$ ($P = 93.9\%$)]. Center: $m_{thrust} - m_{opp}$ [KS $P = 81.7\%$ ($P = 97.5\%$)]. Bottom: $m_{thrust} - m_{opp}$ vs thrust [KS $P = 59.7\%$ ($P = 81.9\%$)]. Values in parentheses are for tau dileptons. Large dots are data, smaller dots are $t\bar{t}$ 175 MC.

Variables	KS values	
	$e\mu$, ee, $\mu\mu$	$e\tau$, $\mu\tau$
Thrust	70.2%	93.3%
Oblateness	53.4%	70.3%
m_{thrust} vs thrust	25.1%	83.1%
m_{opp} vs thrust	24.1%	98.6%
m_{thrust} vs m_{opp}	3.7%	95.3%
m_{thrust} vs m_{opp}, $H_T > 220$ GeV	25.6%	93.9%
$m_{thrust} - m_{opp}$	44.1%	95.4%
$m_{thrust} - m_{opp}$, $H_T > 220$ GeV	81.7%	97.5%
$m_{thrust} - m_{opp}$ vs thrust	51.9%	87.5%
$m_{thrust} - m_{opp}$ vs thrust, $H_T > 220$ GeV	59.7%	81.9%

Table 4.4: Probability for the compatibility of the data with the $t\bar{t}$ Monte Carlo for the variables in the thrust analysis using the Kolmogorov–Smirnov test.

the thrust and oblateness variables are in general quite compatible with expectations from top dilepton decays. The DPF event and the $\mu\mu$ event (Run 58281/Event 44805) are in the high tail of the thrust distribution. The distributions of invariant masses in the two hemispheres as defined by the thrust axis are less compatible with top dileptons in the ee, $\mu\mu$, and $e\mu$ channels, mostly due to the two $\mu\mu$ events. This is consistent with the fact that these two events appear more background–like in the analysis of the inclusive kinematic distributions. There is no evidence for new physics, but it is interesting that we observe a possible clustering of masses between 40 and 110 GeV. The mass distributions in the tau dilepton channel appear to be quite compatible with the top hypothesis.

4.3 Discussion of unusual candidate events

In this section we discuss the candidate events which have properties that are unusual for top dilepton events.

4.3.1 The $ee\mu$ trilepton event (Run 67581/Event 129896)

A closer look at this event which contains a positron with raw E_T = 181.8 GeV reveals an even more interesting feature. The second "jet" in the event with $E_T = 23.4$ GeV[2] at $\phi = 359°$ is highly electromagnetic, E_{had}/E_{em} = 0.001, and has a single track with $p_T = 25.2$ GeV/c pointing at it. Figure 4.21 shows the CTC display for this event.

The values of the isolation variables for the cluster are $I_{trk} = 0.02$ and $I_{cal} = 0.094$, i.e. it passes both calorimeter– and track–isolation cuts. The associated track originates from the same vertex at $z = -51.2$ cm as the e^+, the μ^- [3] and the leading jet. The track curvature indicates a negatively charged particle. Furthermore, the cluster passes all electron identification cuts for a tight central electron, i.e. this cluster looks very much like an isolated electron. Applying the electron corrections we find a corrected E_T = 26.5 GeV for this cluster. However, even though it has all the properties of a good electron, it is technically not considered an electron candidate because it fails the fiducial requirements: the wire cluster in the CES closest to the extrapolated track position is located 21.4 cm from the center of the CES

[2] This is the raw E_T based on the electron clustering algorithm (ELES bank), the jet clustering algorithm yields $E_T = 26.2$ GeV (JETS bank).

[3] We note that the z–intercept of the muon track differs by 3.2 cm from the z position of the vertex. However, the z–intercept is not very well measured because only the outer three stereo layers of the CTC have useful z–information for this track and there is no reconstructed track segment in the VTX. We estimate the uncertainty on the z–intercept to be a few centimeters. Since there are no other z–vertices nearby it appears reasonable to assume that the muon is attached to the same event vertex as the positron and the jet.

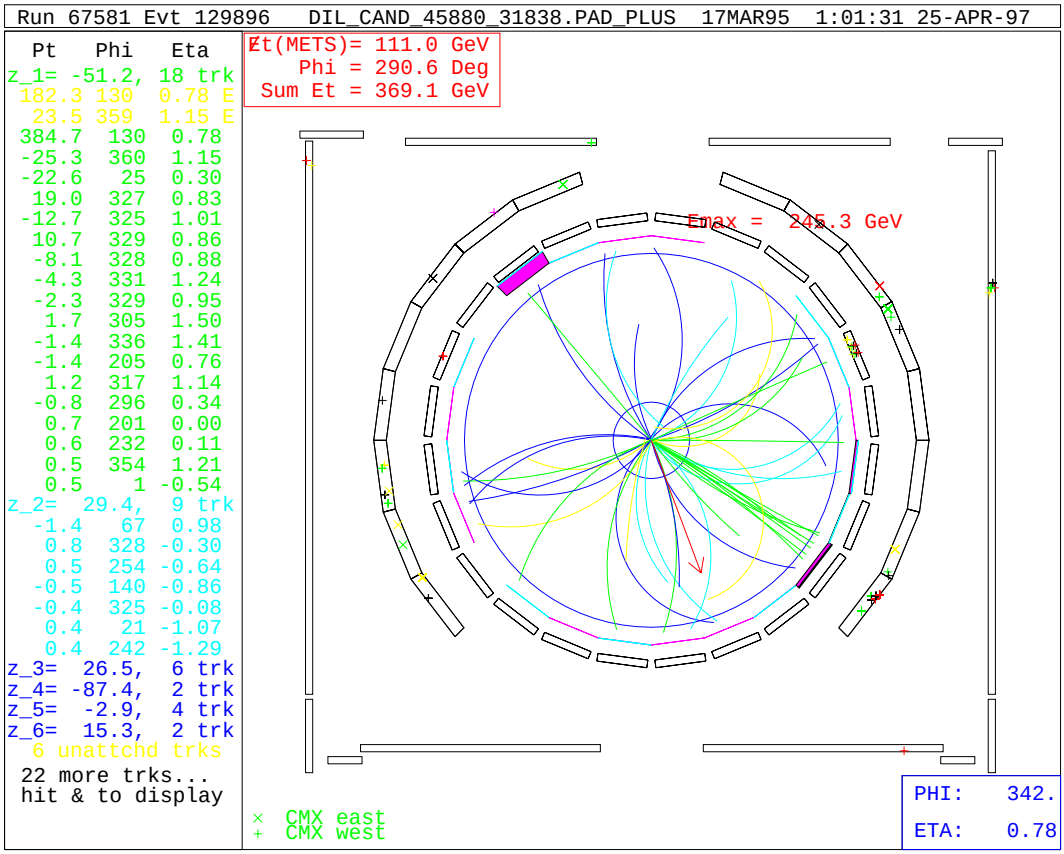

Figure 4.21: CTC display for the "trilepton" event (Run 67581/Event 129896). The additional third lepton is at $\phi = 359°$ (right). It is isolated and passes all TCE identification requirement, except the fiducial cut (because it is too close to the wedge boundary in ϕ).

chamber. For a fiducial electron the cluster is required to be located $< 21.0\ cm$ from the center, which corresponds to a minimum separation of 1° from the nominal ϕ bounday between wedges (see also the section on fiducial CEM coverage in the introduction).

The e^+ and μ^- are both isolated and would therefore originate most likely from W decays, if we interpret the event as $t\bar{t}$ production and decay. In that case the extra electron would have to be due to semileptonic b decay or c decay. We estimate the probability for observing an isolated electron

(or positron) from such decays from our $t\bar{t}$ Monte Carlo sample. In 80,000 simulated events we find 1739 central electrons with $E_T > 20$ GeV from b decays and 605 from c decays. Of these only 28 and 6, respectively, pass both isolation cuts. The probability for finding an isolated electron from b decays is $(3.5 \pm 0.7) \times 10^{-4}$ and $(7.5 \pm 3.1) \times 10^{-5}$ for c decays. This translates into $(2.2 \pm 0.4) \times 10^{-3}$ and $(4.7 \pm 1.9) \times 10^{-4}$ expected dilepton events with a third isolated electron in our data sample, respectively. Only statistical uncertainties are given here. These estimates include the geometrical and kinematical acceptance and the efficiency of the isolation cut. In addition, the efficiency for identifying electrons from b decays also needs to be taken into account. As discussed in Ref. [20], this is estimated to be only $(10 \pm 2)\%$, i.e. considerably smaller than for electrons from W decays, even if the electron is isolated.

This event has two features that are unusual for a dilepton from $t\bar{t}$ decay: a positron with very large E_T and an additional isolated electron. Multiplying the combined probabilities for b and c decays that produce isolated electrons with the electron identification efficiency and with a probability of 0.009 ± 0.002 to find a positron with $E_T > 180$ GeV in a dilepton event yields the total probability of $(3.9 \pm 1.4) \times 10^{-7}$ for such a dilepton event. In 109 pb^{-1} we expect $(2.4 \pm 0.9) \times 10^{-6}$ such events. We conclude that it appears quite unlikely that this candidate event is due to $t\bar{t}$ production.

Another possible Standard Model explanation for this event could be $WZ + jet$ production with the subsequent decays $Z \rightarrow e^+e^-$ and $W \rightarrow \mu\nu$. However, the positron and the electron form an invariant mass of 133.7 GeV/c^2 using corrected E_T, well above the Z peak. The transverse mass formed by the μ^- and the $\not{E}_T$ is $M_T = 92.7$ GeV, which is also higher than the W mass.

Exotic explanations that invoke supersymmetry have been proposed

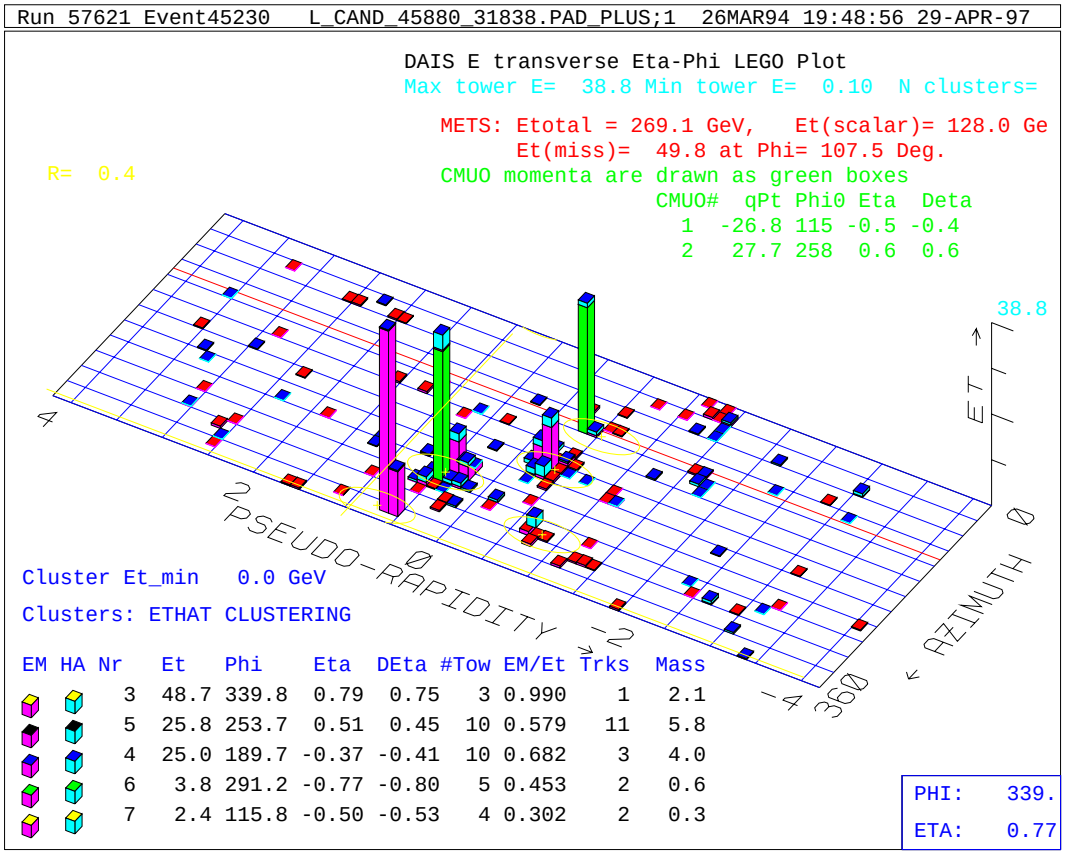

Figure 4.22: Lego display of transverse calorimeter energies for the "other" trilepton event (Run 57621/Event 45230). The p_T of the muons are also indicated (in medium gray scale). The additional third lepton, a muon, is very close to the jet at $\phi = 254, \eta = 0.5$, which is also b–tagged by the SVX.

for this event, such as chargino pair production and decay involving a stau particle [78], or squark pair production with the subsequent decay chain $\tilde{q} \to q\tilde{\chi}, \tilde{\chi} \to \nu\tilde{\ell}, \tilde{\ell} \to \ell\tilde{\chi}_1^0$ [79].

4.3.2 The $e\mu\mu$ trilepton event (Run 57621/Event 45230)

This is another event in the top dilepton data sample that contains a third high-p_T lepton: There is a second muon candidate with $p_T = 21.4$ GeV/c that passes all tight central muon identification cuts in this event. However,

this muon is not isolated at all ($I_{trk} = 1.30$, $I_{cal} = 0.88$) because it is very close to the leading jet as the event display of the calorimeter in Figure 4.22 shows. The proximity to this jet which is also b–tagged by the SVX indicates that the muon is most likely due to a semileptonic b decay. However, the event is unusual in that the muon has such high p_T. From our study in the previous section we expect only $(2.9 \pm 0.1(stat))\%$ of top events to contain a muon with $p_T > 20$ GeV/c from b or c decay.

4.3.3 The $\mu\mu\gamma$ event (Run 58281/Event 4805)

This event has the interesting feature that the leading "jet" at $\phi = 180°$ is 100% electromagnetic, which would be very unusual for a b-jet. Figure 4.23 displays the event in the CTC view. Since there is no high-p_T track ($p_T > 1$ GeV/c) within a cone of 0.4 of the cluster this "jet" is most likely due to a photon. The calculation of the invariant mass formed by the two muons plus the photon with $E_T = 17.9$ GeV gives $m_{\mu\mu\gamma} = 87.2$ GeV/c^2. Since this mass is close to the Z mass we interpret this event as a radiative Z decay: $Z \rightarrow \mu\mu\gamma$. Furthermore, the $\not\!\!E_T$ in this event points within 3° of a third jet with $E_T = 9.96$ GeV at $\phi = 356$, so that it is likely that the $\not\!\!E_T$ is due to a mismeasurement of this jet rather than due to escaping neutrinos. If the transverse energy of the third jet had been only 40 MeV bigger, the event would have been removed by the $\Delta\phi(\not\!\!E_T, \ell j) > 20°$ cut. These observations explain why the kinematics of this event do not look "top-like". We note that we expect only 0.07 events of this type in 109 pb^{-1} [20], which is why no specific removal cuts for radiative Z decays were made in our selection.

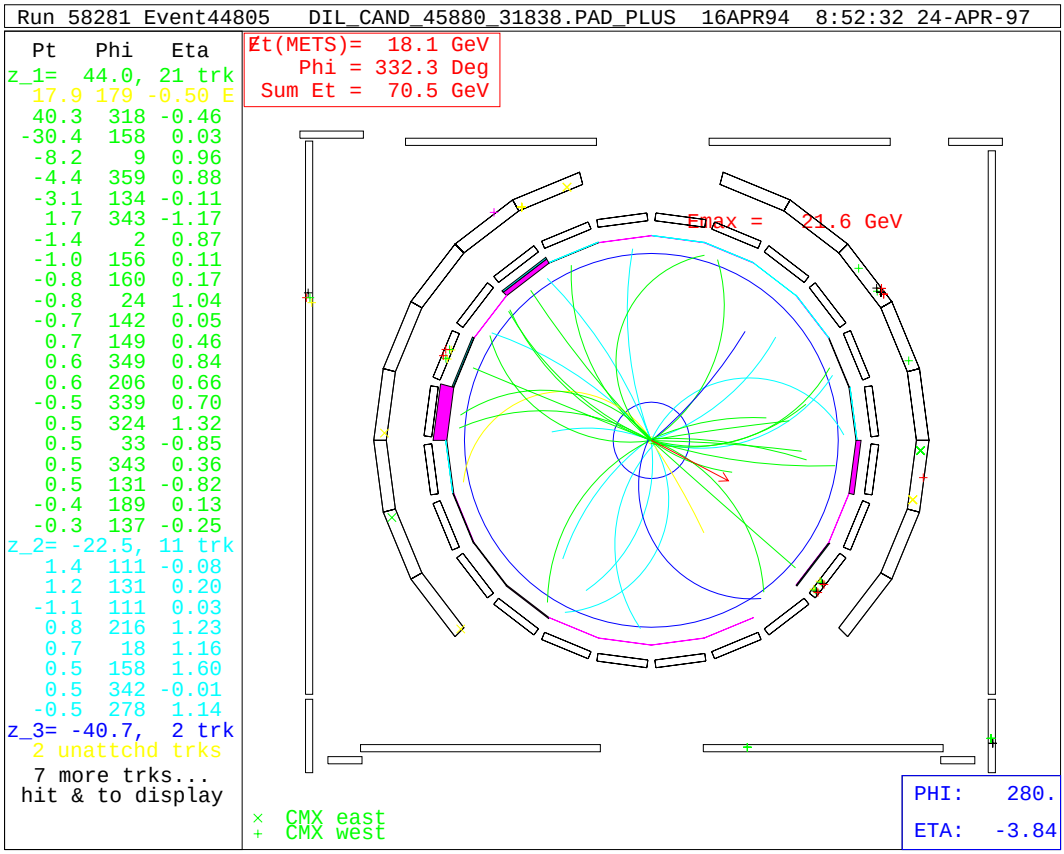

Figure 4.23: CTC display for the $\mu\mu\gamma$ event (Run 58281/Event 4805). The photon-like jet is near 180° (left) and forms a mass $m_{\mu\mu\gamma} = 87.2$ GeV/c^2 with the muon pair. The event is interpreted as a radiative Z decay.

4.4 Conclusions

From this study of the candidate events we draw several conclusions: Most of the candidate events exhibit kinematic features that are not untypical for $t\bar{t}$ events – with a few notable exceptions. The most interesting exceptions are the trilepton event, which appears to be a very unlikely top candidate, and the fact that 5 of the 14 candidate events have large $\not\!\!E_T$. A more mundane exception is the candidate event that appears to be a radiative $Z \rightarrow \mu\mu\gamma$ decay. In the end, only more data from the next run will help to answer the

question if these are just fluctuations or if we are beginning to observe some sort of "new physics" in the dilepton channel.

Another potential problem concerns the distribution of events among the three channels ee, $\mu\mu$, and $e\mu$, i.e. the branching ratios of $t\bar{t}$ decays. Our study of the kinematics indicates that not only the $Z \rightarrow \mu\mu\gamma$ event looks like background, but also that the other $\mu\mu$ candidate appears to be "soft" for a $t\bar{t}$ event. If we assume that this is one of the expected 2 background events, we are left with 6 $e\mu$ events (excluding the trilepton event), no $\mu\mu$ events, and 1 ee event. From our results in Chapter 2 we expect the distribution to be 57% $e\mu$ events, 27% $\mu\mu$ events, and 17% ee events. This corresponds to an expectation of 4 $e\mu$ events, 1.9 $\mu\mu$ events, and 1.2 ee events.

Finally, the kinematics of the 4 tau dilepton events appear somewhat stiffer than expected for a sample with ≈ 2 background events and ≈ 1 top signal event. This indicates a fluctuation towards a higher top fraction in the observed sample, which is consistent with the fact that the number of tagged events is also higher than expected.

Chapter 5

CONCLUSIONS

Da steh ich nun, ich armer Tor!
Und bin so klug als wie zuvor.

J.W. v. Goethe, *Faust I, Nacht*

5.1 Summary of results

We find a clear signal for $t\bar{t}$ production and subsequent decay in the ee, $\mu\mu$, and $e\mu$ dilepton channel using 109 pb^{-1} of data collected with the CDF detector. We observe 10 candidate events and expect 2.1 background events. The $t\bar{t}$ production cross section measured in this channel is

$$\sigma_{t\bar{t}}^{\ell\ell} = 8.5^{+4.1}_{-3.3}(stat)^{+1.6}_{-0.8}(syst)\ pb \quad (\ell = e, \mu). \tag{5.1}$$

In this thesis a method has been developed to identify tau leptons through their hadronic decays with good efficiency and a small fake rate from quark and gluon jets. Using this method we have searched for the $e\tau$ and $\mu\tau$ decay channels of $t\bar{t}$ pairs. We observe 4 candidate events, where we expect (2.5 ± 0.4) background events and (1.1 ± 0.4) top events. Three of the 4 candidate events also have b-tagged jets. Requiring tagged jets reduces the

expected background to 0.28 events. The probability for this background expectation to fluctuate up to ≥ 3 events is 0.3%, corresponding to a 3 σ effect. Two of the tau candidates in the 4 $e\tau$ and $\mu\tau$ events have SVX tracks with significant impact parameters ('τ–tag'), which supports the tau hypothesis. Each of the four events either has a b–tag or a τ–tag, and one has both. The kinematics of the four events also indicates that these events are more 'top-like' than 'background-like'.

We interpret this result as evidence for the presence of the $e\tau$ and $\mu\tau$ decay channels of $t\bar{t}$ pairs, which the Standard Model predicts. We calculate a $t\bar{t}$ production cross section from this channel based on all 4 candidate events and find

$$\sigma_{t\bar{t}}^{\ell\tau} = 10.2^{+16.3}_{-10.2}(stat) \pm 1.6(syst)\ pb \quad (\ell = e, \mu), \tag{5.2}$$

consistent with current measurements in other channels and theoretical predictions.

By including the $e\tau$ and $\mu\tau$ channel we have achieved our goal of enlarging the top dilepton data sample. The overall sample has been increased by 40% from 10 to 14 events, and the b–tagged sample by 75% from 4 to 7 events. The significance of the result after tagging is 5.1 σ for all 5 channels combined, compared with 3.2 σ for the ee, $\mu\mu$, and $e\mu$ channels alone.

Based on the theoretical $t\bar{t}$ cross section $\sigma_{t\bar{t}}^{theory} = 4.75\ pb$ we would expect 9.2$\pm$0.9 events from $t\bar{t}$ plus background. The probability for this to have fluctuated to 14 observed events is 14.8%. Since we observe 5 more events than predicted we have also studied the kinematics and topology of the candidate events to see how 'top-like' the data are. This study shows general consistency with the expectations, with a few notable exceptions. One $\mu\mu$ event appears to be more consistent with a radiative Z decay than with a $t\bar{t}$ event. Most

importantly, one $e\mu$ event contains an additional isolated positron. The probability for such a trilepton event to originate from $t\bar{t}$ production and decay is found to be very small. In 109 pb^{-1} we expect $(2.4 \pm 0.9) \times 10^{-6}$ such events. Furthermore, 5 of the 14 candidate events have unusually large $\not\!\!E_T$ of more than 105 GeV. Only 0.9 ± 0.1 such events are expected; the probability for such a fluctuation is 0.2%. These unexpected findings raise the intriguing possibility that we are observing something else besides top decays in this sample. However, only more data will reveal if these effects are simply fluctuations or a glimpse of "new physics".

5.2 Future Prospects

The CDF detector is currently being upgraded significantly for the next collider run, which will most likely begin in the year 2000. During that run CDF is expected to collect about 2 fb^{-1} of data, which is an increase by a factor of 20 compared with the data used in this thesis.

In this section we briefly examine how the increase in data and the detector improvements will affect the top dilepton analysis. The hardware improvements that will have the largest impact on the dilepton analysis are the new scintillating-tile fiber plug calorimeter, the extension of the muon system, and the new tracking system with the new SVX II detector and the intermediate silicon layers (ISL). Details on the hardware upgrade can be found in the Technical Design Report for the CDF II detector [80]. The new plug calorimeter together with good tracking in the more forward region using the ISL will provide clean identification of electrons in the region $1.0 < |\eta| < 2.0$. The muon coverage will be extended to the region $1.0 < |\eta| < 1.5$ with the new

Channel	Total Acceptance in Run I	Acceptance increase in Run II	Number of events in Run I $t\bar{t}$ exp.	obs.	Expected events from $t\bar{t}$ in Run II
$t\bar{t}$ events produced	-	-	520	-	13300
ee	0.12%	+70%	0.6	1	27
$\mu\mu$	0.20%	+25%	1.0	2	34
$e\mu$	0.42%	+43%	2.2	7	81
$ee, \mu\mu, e\mu$	0.74%	+45%	3.8	10	142
$e\tau$	0.065%	+33%(+70%)	0.3	2	12 (15)
$\mu\tau$	0.069%	+10%(+45%)	0.4	2	10 (13)
$e\tau, \mu\tau$	0.134%	+21%(+55%)	0.7	4	22 (28)

Table 5.1: Current total acceptances including all efficiencies and branching ratios in Run I and expected acceptance increases in Run II for top dilepton events. The numbers of expected events for Run I are based on the theoretical cross section at a c.m. energy of 1.8 TeV, $\sigma_{t\bar{t}}^{theory} = 4.75\ pb$ [25]. Estimates for Run II are based on $\sigma_{t\bar{t}}^{theory} = 6.65\ pb$ at a c.m. energy of 2 TeV and a data sample of 2 fb^{-1}. Numbers in parentheses for tau dileptons assume that tau identification in the plug region up to $|\eta| = 2.0$ is possible with efficiencies similar to those in the central region. All other numbers assume only extension of the acceptance region for electrons and muons.

Intermediate Muon System. The gaps in the existing coverage of the CMP (see chapter 1) will also be filled.

Based on our 80,000 event $t\bar{t}$ Monte Carlo sample we expect a relative increase of 45% in the kinematical and geometrical acceptance for ee, $\mu\mu$, and $e\mu$ top dilepton events due to the increase in detector coverage, if the same $E_T(p_T) > 20\ GeV(/c)$ cut is used in the more forward regions. In the individual channels we expect an increase in acceptance of +70% for ee, +25% for $\mu\mu$, and +43% for $e\mu$ events. Assuming that fiducial losses and lepton identification efficiencies in the more forward regions are similar to the

current values in the central region, we expect that the total acceptance for top events will increase by a corresponding amount from 0.74% to 1.07%.

Similarly, we expect an increase of 33% for $e\tau$ events and 10% for $\mu\tau$ events, for a total of 21% for tau dilepton events. This estimate is conservative and only takes the improved acceptance for electrons and muons into account. If the current tau identification method can be extended into the plug region, say up to $\eta = 2.0$, an increase of $\approx 70\%$ in the $e\tau$ channel and $\approx 45\%$ in the $\mu\tau$ channel might be achievable for a total increase of about 55% for tau dileptons. This will require good tracking out to $\eta = 2.0$ because of the importance of the track isolation in the tau identification. However, it would be a very useful addition to the analysis as the tau dilepton channel suffers from its small acceptance.

In Table 5.1 we summarize the expected increases in acceptance and compare the expected number of identified $t\bar{t}$ events in Run II with the currently observed events in Run I. In the $ee, \mu\mu$ and $e\mu$ channel we expect ≈ 60 background events. For the $e\tau$ and $\mu\tau$ channnel also ≈ 60 background events are expected if only central τ's are used, or ≈ 80 events if τ's can be identified in the plug region. For this estimate we have assumed that the acceptance for backgrounds in the plug region scales similar to the top acceptance, which is probably an underestimate. While the expected ratio of signal–to–background $S/B = 1:3$ for Run II in the τ channels will be similar to Run I, the significance $S/\sqrt{B}$ will improve from 1:2.5 to $\approx 3:1$.

The new SVX II vertex detector will cover a larger region than the current SVX and will allow 3D track reconstruction. The efficiency for tagging at least one b in a $t\bar{t}$ event with this new detector is expected to be about 65% [80], compared with 42% achieved with the current SVX. Consequently, we expect 14-18 tagged signal events in the tau channels. Assuming that the

rate for misidentifying light quark jets as b's with SVX II is similar to what is observed with the SVX detector we expect about 3-4 tagged background events. This might be an overestimate because the 3D capabilities of the SVX II should reduce the mistag rate. In an analysis that employs tagging we expect the background to be dominated by $W+ \geq 3\ jets$ events and $t\bar{t}$ events in the $\ell + jets$ channel, where a jet is misidentified as a tau candidate. With single b–tagging the signal–to–background ratio will improve to $S/B = 4.5 : 1$ compared with the expectation without tagging and the significance $S/\sqrt{B}$ is expected to be $\approx 9 : 1$.

For the measurement of the $t\bar{t}$ cross section, $\sigma_{t\bar{t}}$, we expect a statistical uncertainty of about 10% in the ee, $\mu\mu$, and $e\mu$ channel, with or without b-tagging. This is to be compared with the current 50% statistical uncertainty in Run I. If we assume that the magnitude of the systematics in Run II will be similar to those in Run I (8% on luminosity, 10% on acceptance, and 10% on backgrounds), we find that the cross section measurement in these channels will be limited by systematics. The total uncertainty for this measurement is expected to be about 20%.

In case of the $e\tau$ and $\mu\tau$ channels we expect the statistical uncertainty on the $\sigma_{t\bar{t}}$ measurement to be about 40% with central taus and about 37% if taus in the plug region can be included. Requiring at least one SVX b–tag will reduce the uncertainties to 30% and 25%, respectively, because of the large reduction of the background. Even though this means that the measurement will still be limited by statistics, it will be a large improvement over the current 160% uncertainty in this measurement. The measurement will have a precision similar to that of the Run I result in the $\ell + jets$ channel using SVX tagging. The expected uncertainties are summarized in Table 5.2.

Finally, since we observe a quite unusual event in the Run I data we

Channel	b–tagging used	plug τ's used	$(\frac{\Delta\sigma_{t\bar{t}}}{\sigma_{t\bar{t}}})^{stat}$ [%]	N_{95} [events]	σ_{95}^{new} pb
$ee, \mu\mu, e\mu$	no	-	10	70 (25)	3.3 (1.2)
	yes	-	10	35 (17)	2.5 (1.2)
$e\tau, \mu\tau$	no	no	40	34 (16)	10.5 (5.0)
	no	yes	37	43 (19)	10.3 (4.4)
	yes	no	30	11 (9)	5.2 (4.0)
	yes	yes	25	13 (9)	4.7 (3.4)

Table 5.2: The expected statistical uncertainty for the measurement of the $t\bar{t}$ cross section, $(\frac{\Delta\sigma_{t\bar{t}}}{\sigma_{t\bar{t}}})^{stat}$, and the expected sensitivity to new physics in the dilepton channels in Run II for 2 fb^{-1} of data. The listed 95% confidence limits N_{95} on the numbers of events due to new physics in the dilepton channels are calculated assuming that the expected number of $t\bar{t}$ events, based on the theoretical cross section, and background events will be observed. For the numbers in parentheses systematic uncertainties are ignored, for the numbers outside of parentheses we assume systematic uncertainties on the integrated luminosity (8%), acceptance (10% for ee, $\mu\mu$, and $e\mu$, 14% for $e\tau, \mu\tau$), and background (20%) similar to the results in Run I. The limits on the numbers of events are converted to cross section limits assuming that the acceptance for new physics is similar to the acceptance for $t\bar{t}$ events.

estimate the expected sensitivity to new physics in the dilepton channels for a data sample of 2 fb^{-1} in Run II. If the observed number of events will turn out to be similar or less than the sum of the expected $t\bar{t}$ events and expected background events, one will be able to set a limit on the number of events from other sources, e.g. new physics processes that contribute to the dilepton channels. We explore what limits CDF might be able to set by calculating a 95% confidence level on other sources. For this calculation we assume that the actually observed number of events in the Run II data will equal the expected number of $t\bar{t}$ events, based on the theoretical cross section $\sigma_{t\bar{t}} = 6.65\ pb$ at $\sqrt{s} = 2.0\ TeV$, plus the expected number of background events. The calculation is

done with and without taking b–tagging into account, assuming again a 65% tagging efficiency. We also evaluate the effect of systematics where we assume systematic uncertainties on the integrated luminosity (8%), acceptance (10% for ee, $\mu\mu$, and $e\mu$, 14% for $e\tau, \mu\tau$), and background (20%) similar to the results in Run I.

The results of the calculations are listed in Table 5.2. The limits on the numbers of events, N_{95}, are converted to cross section limits, σ_{95}^{new}, assuming that the acceptance of new physics is similar to the acceptance for $t\bar{t}$ events. Under our assumptions we find that the $ee, \mu\mu$ and $e\mu$ channels will be sensitive to new physics produced with a cross section of 2-3 pb after accounting for systematics. The $e\tau$ and $\mu\tau$ channels will have a sensitivity of about 10 pb, which can be improved to about 5 pb if b–tagging is employed.

REFERENCES

[1] S.W. Herb *et al.*, Observation of a Dimuon Resonance at 9.5 GeV in 400-GeV Proton-Nucleus Collisions, *Phys. Rev. Lett.* **39**, 252 (1977).

[2] W. Bartel *et al.*, A Measurement of the electroweak induced charge asymmetry in $e^+e^- \to b\bar{b}$, *Phys. Lett.* B **146**, 437 (1984).

[3] D. Decamp *et al.*, Measurement of the forward-backward asymmetry in $Z \to b\bar{b}$ and $Z \to c\bar{c}$, *Phys. Lett.* B **263**, 325 (1991).

[4] Particle Data Group, Phys. Rev. **D 54**, 1 (1996).

[5] Particle Data Group, Rev. Mod. Phys. **D 56**(2), 1 (1984).

[6] S. Glashow, J. Iliopolous, and L. Maiani, Weak Interactions with Lepton-Hadron Symmetry, *Phys. Rev.* D **2**, 1285 (1970).

[7] C. Berger *et al.*, Search for a 'top' threshold in hadronic e^+e^- annihilation at energies between 22 GeV and 31.6 GeV., *Phys. Lett.* B **86**, 413 (1979).

[8] B. Adeva *et al.*, Search for top quark and a test of models without top quark at the highest PETRA energies, *Phys. Rev. Lett.* **50**, 799 (1983).

[9] K. Abe *et al.*, Measurement of R and search for new quark flavors decaying into multi-jet final states in e^+e^- collisions between 54 GeV and 61.4 GeV c.m. energies, *Phys. Lett.* B **234**, 382 (1990).

[10] G. Arnison *et al.*, Associated production of an isolated large transverse momentum lepton (electron or muon), and two jets at the CERN $p\overline{p}$ collider, *Phys. Lett.* B **147**, 493 (1984).

[11] C. Campagnari and M. Franklin, The Discovery of the Top Quark, *Rev. Mod. Phys.* **69**, 137 (1997).

[12] C. Albajar *et al.*, Search for new heavy quarks at the CERN proton-antiproton collider, *Z. Phys.* C **37**, 505 (1988).
In this paper UA1 sets a limit $m_{top} > 44\ GeV/c^2$ at 95% C.L..

[13] F. Abe *et al.*, Top-Quark Search in the electron + jets channel in proton-antiproton collisions at $\sqrt{s} = 1.8$ TeV, *Phys. Rev.* D **43**, 664 (1991).
CDF's first limit was $m_{top} > 77\ GeV/c^2$ at 95% C.L..

[14] F. Abe *et al.*, Lower Limit on the Top Quark Mass from Events with Two Leptons in $p\overline{p}$ collisions at $\sqrt{s} = 1.8$ TeV, *Phys. Rev. Lett.* **68**, 447 (1992).
F. Abe *et al.*, Limit on the Top Quark Mass in $p\overline{p}$ collisions at $\sqrt{s} = 1.8$ TeV, *Phys. Rev.* D **45**, 3921 (1992).
Using dileptons CDF sets a limit $m_{top} > 91\ GeV/c^2$ at 95% C.L..

[15] S. Abachi *et al.*, Search for the Top-Quark in $p\overline{p}$ collisions at $\sqrt{s} = 1.8$ TeV, *Phys. Rev. Lett.* **72**, 2138 (1994).
The D0 limit presented here is $m_{top} > 133\ GeV/c^2$ at 95% C.L..

[16] F. Abe *et al.*, Evidence for top quark production in $\overline{p}p$ collisions at $\sqrt{s} = 1.8$ TeV, *Phys. Rev.* D **50**, 2966 (1994).

[17] F. Abe *et al.*, Observation of Top Quark Production in $\overline{p}p$ Collisions with the Collider Detector at Fermilab, *Phys. Rev. Lett.* **74**, 2626 (1995).

[18] S. Abachi *et al.*, Observation of the Top Quark. *Phys. Rev. Lett.* **74**, 2632 (1995).

[19] J.C. Romano, A Search for Top Quark Pair Production in the Dilepton Decay Mode, Ph.D. thesis, University of Chicago, August 1995.

[20] M. Kruse, Observation of top quark pair production in the dilepton decay channel from proton-antiproton collisions at $\sqrt{s} = 1.8$ TeV, Ph.D. Thesis, Purdue University, May 1996 (unpublished).

[21] For a definition and discussion of 'parton luminosities' see for example: V.D. Barger and R.J.N. Phillips, Collider Physics, 1988, p. 159.

[22] P. Nason, S. Dawson, and R.K. Ellis, The total cross-section for the production of heavy quarks in hadronic collisions. *Nucl. Phys.* B **303**, 607 (1988).

[23] R.K. Ellis, Rates for top quark production, *Phys. Lett.* B **259**, 492 (1991).

[24] E. Laenen, J. Smith, and W.L. van Nerven, Top quark production cross-section, *Phys. Lett.* B **321**, 254 (1994).

[25] E. L. Berger and H. Contopanagos, Perturbative gluon resummation of the top quark production cross section, *Phys. Lett.* B **361**, 115 (1995).

[26] S. Catani *et al.*, The top cross section in hadronic collisions, *Phys. Lett.* B **378**, 329 (1996).

[27] I. Bigi *et al.*, Production and decay properties of ultra-heavy quarks, *Phys. Lett.* B **181**, 157 (1986).

[28] L.H. Orr, Decay versus hadronization for top quarks produced in hadron colliders, *Phys. Rev.* D **44**, 88 (1991).

[29] The Collider Detector at Fermilab, A compilation of articles reprinted from *Nuclear Instruments and Methods in Physics Research – A*, North-Holland (1988).

[30] D. Amidei *et al.*, The Silicon Vertex Detector of the Collider Detector at Fermilab, *Nucl. Instrum. Methods* A **350**, 73 (1994).

[31] P. Azzi *et al.*, SVX′: The New CDF silicon vertex detector, *Nucl. Instrum. Methods* A **360**, 137 (1995).

[32] In the CDF coordinate system, θ and ϕ are the polar and azimuthal angles, respectively, with respect to the proton beam direction. Up corresponds to 90° in ϕ. The pseudorapidity η is defined as -ln tan($\theta/2$). The transverse momentum of a particle is $P_T = P \sin\theta$. The analogous quantity using energies, defined as $E_T = E \sin\theta$, is called transverse energy. The missing transverse energy $\not{E}_T$ is defined as $-\sum E_T^i \hat{r}_i$, where $\hat{r}_i$ are the radial unit vectors in the $r-\phi$ plane pointing from the interaction point to the energy deposition in the calorimeter.

[33] This quantity is also refered to as x_{local} because it is a local coordinate in a strip chamber.

[34] L. Balka *et al.*, The CDF Electromagnetic Calorimeter, *Nucl. Instrum. Methods* A **267**, 272 (1988). Also see ref. [29].

[35] T. Sjöstrand, Computer Physics Commun. **82**, 74 (1994).

[36] L. Nodulman and K. Byrum, CEM tower calibration and map trim, CDF note CDF/MEMO/CAL/PUBLIC/2487 (1994).

L. Nodulman and K. Byrum, CEM calibration for 1B (but not for 1A), CDF note CDF/MEMO/CAL/PUBLIC/3477 (1996).
The calibrations are available for analyses via the CDF routines `CEMFIX`, `MAPFIX`, and `CEMTWK`. In this thesis the versions of `MAPFIX` and `CEMTWK` as of October 1996 are used.

[37] E. Kovacs, Jet energy resolutions from dijet balancing, CDF note CDF/JET/ANAL/PUB/2608 (1995).

[38] D. A. Glenzinski, Observation of the Top Quark in Proton-Antiproton Collisions at a Center of Mass Energy of 1.8 TeV, Ph.D. thesis, The Johns Hopkins University, (1995).

[39] S. Jadach et al., TAUOLA version 2.5 (June 1994); CERN-TH-5856(1990), CERN-TH-6195 (1991), CERN-TH-6793 (1992)
C. Loomis, Using TAUOLA, A Decay Library for Polarized τ Leptons, at CDF, CDF/DOC/EXOTIC/CDFR/2796 (1994).

[40] set PYTHIA switch MSTJ(27)=2

[41] set PYTHIA switch MSTJ(11)=3

[42] We use the jet correction routine JTC96S. Underlying event correction and out–of–cone corrections are not applied ('NN'). Default corrections for the relative and absolute energy scale are employed ('DD').

[43] D. Saltzberg, High-E_T Central Electron Datasets, CDF/DOC/ELECTRON/CDFR/2213 (1993).
M. Krasberg, High P_T Central Muon Data Sets, CDF/ANAL/ELECTROWEAK/CDFR/2326 (1993).

[44] This was done by Dave Toback and myself. Thanks to Dave for his invaluable help with this large task.

[45] Top group, Sample Selection for Run 1B Top Search,CDF/TOP/ANAL/CDFR/2966 (1996). This sample was made by A. Gordon and D. Glenzinski at Fermilab. Detailed comparison of the Chicago sample with the Fermilab sample helped to fix some problems with the Fermilab sample.

[46] C. Campagnari, D. Kestenbaum, A. Yagil, Soft Electron Reconstruction for Run 1b, CDF/TOP/ANAL/CDFR/2960 (1995).
C. Campagnari, D. Kestenbaum, A. Yagil, Soft Muon identification in Run 1b for the SLT analysis, CDF/TOP/ANAL/CDFR/2968 (1995).

[47] CDF Collaboration, The CDF II Detector, Technical Design Report, FERMILAB-PUB-96/390-E (1996)

[48] A. Roodman, Ph.D. Thesis, The University of Chicago, August 1991.

[49] T. Baumann, M. Franklin, J. Konigsberg, A Top Dilepton Analysis Using Hadronic Taus, CDF/DOC/TOP/CDFR/2325 (1993). See appendix A for jet selection with minimal bias.
T. Baumann, M. Franklin, J. Konigsberg, A Calorimetry-based Algorithm for Tau/Jet Separation in Top Searches at CDF, CDF/DOC/TOP/CDFR 2042 (1993).

[50] Sacha Kopp, A $t\bar{t}$ Dilepton Search Using Hadronic Decays of τ Leptons, CDF/ANAL/TOP/CDFR/2952 (1995).

[51] The `ANALYSIS_CONTROL` module `TAUFND`, which implements the τ selection described in this thesis, has been incorporated into the development version of the CDF offline code in `c$top`. For details on the module see:

M. Hohlmann and S. Kopp, A Description of the Tau-Tagging Routine TAUFND, CDF/ANAL/TOP/CDFR/2953 (1995).

[52] Particle Data Group, Phys. Rev. **D 50**, 1173 (1994).

[53] M. Gallinaro, Osservazione del quark top a CDF nel canale a due leptoni con elettroni, muoni e tau, Ph.D. thesis, University of Rome II, (1996). M. Gallinaro, M. Hohlmann, Observation of Top dileptons with hadronically decaying tau leptons, CDF/ANAL/TOP/CDFR/3461 (1996). The second part of this CDF note describes the track–based tau dilepton analysis.

[54] We use the standard `ANALYSIS_CONTROL` module `FINDTAU.CDF` in `c$tau` to implement this algorithm. The information is stored in so–called TAUO banks.

[55] C. Loomis, Comparison of Run 1B isolated pions to previous studies and QFL Monte Carlo, CDF/ANAL/JET/CDFR/3554 (1996).

[56] J. Conway, L. Groer, C. Loomis, Reprocessing, Preselection, and Validation of TAUX1B Data set for CDF Tau Analyses, CDF/ANAL/EXOTIC/CDFR/3463 (1996).

[57] Such a vertex requires more than 180 associated hits in the VTX and is known within CDF as a 'class 12' vertex.

[58] The level 2 trigger performs a search for energy clusters in the calorimeter for triggering on jets and electrons. Technically, we have required the Level 2 trigger 'MET_35(_TEX_2)_NOT_GAS' to have fired. A list of all triggers used in Run I is available online at FNALD in the area `trigger$tables`.

[59] M. Hohlmann, Tau Identification in $W \rightarrow \tau\nu$ events with TAUFND, CDF/ANAL/TOP/CDFR/3688 (1996).

[60] F. Abe *et al.*, Measurement of $\sigma \cdot BR(W \rightarrow e\nu)$ and $\sigma \cdot BR(Z^0 \rightarrow e^+e^-)$ in $p\overline{p}$ Collisions at $\sqrt{s} = 1.8\ TeV$, *Phys. Rev. Lett.* **76**, 3070 (1996).

[61] Both algorithms for removing background from $Z^0 \rightarrow e^+e^-$ decays are implemented in the routine `TAUZEE.CDF` that is available in the development version of the CDF offline code in `c$top`. It is modeled after the standard Z^0 removal routine `ELEZEE.CDF`.

[62] T. Chikamatsu, T. Uchida, J. Romano, M.T. Cheng, G.P. Yeh, H_T in Top Dilepton Analysis, CDF/ANAL/TOP/CDFR/3001 (1995).

[63] L. Demortier, Q. Wang, N. Giokaris, A Search for the Top Quark Using Kinematic Variables, CDF/PHYS/TOP/CDFR/2502 (1994).

[64] S. E. Kopp, A Measurement of the Ratio $R = \sigma \cdot B(p\overline{p} \rightarrow W \rightarrow e\nu)/\sigma \cdot B(p\overline{p} \rightarrow Z^0 \rightarrow e^+e^-)$ in $p\overline{p}$ Collisions at $\sqrt{s} = 1800\ GeV$, Ph.D. thesis, University of Chicago, August 1994.

[65] `c$top:SIM_MUTRIG.CDF` in development.

[66] F. Abe *et al.*, Inclusive Jet Cross–Section in $p\overline{p}$ Collisions at $\sqrt{s} = 1.8\ TeV$, *Phys. Rev. Lett.* **77**, 438 (1996).

[67] These sets have been provided by the Rutgers group (Leslie Groer; Cal Loomis). They use the routine `MIXEVT` which combines tracks and calorimeter tower energies from minimum bias data with Monte Carlo tracks and energies into new QTRK and TOWE banks. The number of minimum bias events used is picked according to a Poisson distribution

with a mean that corresponds to the average number of minimum bias events per crossing in Run 1B (0.6 events).

[68] K. Tollefson, The Top Quark Mass Measurement in the Lepton + Jets Channel from CDF, Proceedings, DPF 1996.

[69] F. Abe *et al.*, Measurement of the $t\bar{t}$ Production Cross Section in $p\bar{p}$ Collisions at $\sqrt{s} = 1.8$ TeV, PRL in preparation.

[70] R. A. Dunn, Using Precision Tracking To Identify Semileptonic Decays of Tau Leptons in $p\bar{p}$ Collisions at $\sqrt{s} = 1.8$ TeV, Ph.D. thesis, University of Michigan, 1994.

[71] The samples used are the Stream B JET_20, JET_50 and JET_70 samples. Thanks to Ping Yeh for collecting the relevant 1B data from the plethora of Stream B tapes into a small number of JET20,50,70 tapes.

[72] The VECBOS package currently supports only $Z \rightarrow e^+e^-$ decays. To produce the $Z \rightarrow tau^+tau^-$ sample we replace the generated e^+e^- from the Z decay with $\tau^+\tau^-$, decay the τ's with TAUOLA and resimulate the complete event with the detector simulation QFL. Thanks to Tom Baumann from Harvard University for supplying us with a corresponding routine.

[73] Thanks to the Duke group for supplying these samples (tapes ZE1JD1, ZE1JD2, ZE3JD1).

[74] H. Frisch, Separating Top and Z's in Dilepton events inside the Z mass window, CDF/ANAL/TOP/CDFR/3387 (1995).

[75] Guillaume Unal, $Wb\bar{b}$ and $Wc\bar{c}$ Backgrounds in Top SVX Channel, CDF/ANAL/TOP/CDFR/3389 (1995).

[76] We calculate the thrust of the events using the subroutine `LUTHRU` of the PYTHIA 5.7 package. The routine does not uniquely specify the direction of the axis (it returns $\vec{a}$ or $-\vec{a}$), so we define the axis to point into the upper half plane of the (r, ϕ) plane.

[77] K. Kondo and S.H. Kim, A DLM analysis of the DPF event as $t\bar{t}$ production, CDF/ANAL/TOP/CDFR 2412 (1994).

[78] J. Berryhill, R. Culbertson, H. Frisch, D. Toback, and P. Wilson, Minimal Zoosy: Four Events, CDF/ANAL/EXOTIC/CDFR 3571 (1996).

[79] R.M. Barnett and L.J. Hall, A Multi–Lepton Signal for Supersymmetric Particles in Tevatron Data ?, *Phys. Rev. Lett.* **77**, 3506 (1996).

[80] CDF II collaboration, The CDF II Detector – Technical Design Report, FERMILAB-PUB-96/390-E (1996).